THE HENRYK NIEWODNICZANSKI INSTITUTE OF NUCLEAR PHYSICS
POLISH ACADEMY OF SCIENCES

DOCTORAL THESIS

Search for extended scenarios of electroweak symmetry breaking with the ATLAS experiment at LHC

Author:
Marzieh BAHMANI

Supervisor:
Dr hab. Paweł BRÜCKMAN DE RENSTROM
Co-supervisor:
Dr Andrzej SIÓDMOK

A thesis submitted in fulfillment of the requirements for the degree of PhD

in the

The ATLAS Experiment Department
Division of Particle and Astroparticle Physics

Cracow, September 25, 2019

Acknowledgements

First, I would like to express my deepest gratitude to my supervisor, Dr hab. Paweł Brückman. Since I arrived to Poland, he has been helping me not only in my scientific issues but also in everyday normal life. His guidance allowed me to master many things in the field. Dr hab. Anna Kaczmarska also supported me in these matters, her guidance and suggestion helped me a lot. They both provided me with very important background and inspiration to develop my own ideas. I always appreciated our discussions and truly think that I could not have had better advisers, who where fully devoted since the first moment to answer any possible question I could have.

I also want to thank all the members of `TauSpinner` group and Higgstool project, Professor Zbigniew Wąs, Professor Elżbieta Richter-Wąs, Professor Jan Kalinowski and Doctor Wojciech Kotlarski, for their support and guidance. Special thanks go to Professor Elżbieta Richter-Wąs, who not only helped me in the project and answered all my questions, but also taught me how to be well organized, and have plan for everything. I would like to thank Professor Nigel Glover for his support in HiggsTools project. The `TauSpinner` work has been supported in part by the Research Executive Agency (REA) of the European Union under Grant Agreement PITNGA2012316704 (HiggsTools) and in part from funds of Polish National Science Center under decisions UMO-2014/15/B/ST2/00049, by PLGrid Infrastructure of Academic Computer center CYFRONET AGH in Krakow, Poland.

I would like to express my gratitude to all members of ATLAS Higgs Beyond-the-SM (HBSM) H^+ to tau nu search group, including Doctor Paweł Klimek, Doctor Blake Oliver Burghgrave, Doctor Sina Bahrasemani, Doctor Arnaud Ferrari and Doctor Michael Pitt for their support and help in the analysis, and fake factor estimation. My work in the analysis was supported in part by National Science Center grant 2017/25/B/ST2/01234.

I am also very grateful to all my colleagues, Doctor Paweł Malecki, Dr hab. Marcin Wolter, Doctor Rafał Staszewski, Doctor Bartłomiej Żabinski, Doctor Andrzej Siódmok and Janina Krzysiak for their help and support.

Last but not least, I want to thank all my family and friends for their constant support and love. They have encouraged and supported me, allowing me to overcome all the obstacles I found during these years and to meet my objectives.

Contents

List of Figures

List of Tables

Chapter 1

Introduction

1.1 Introduction

The Higgs boson discovery by the ATLAS [1] and CMS [2] experiments at CERN in 2012, opens the question of whether this is the Higgs mechanism (and its corresponding boson) of the Standard Model (SM) or there are other theories that can alter the electroweak symmetry breaking. The SM is currently the most complete theory of fundamental particles and their interactions. Although it is to a large extent successful, the SM fails to explain many observed phenomena, which include neutrino masses, matter-anti-matter asymmetry and cosmic dark matter, and suffers from severe fine-tuning of some of its parameters. This makes it obvious that the SM must be extended with a compatible "Beyond the Standard Model" (BSM) theory if we want to have a complete and unified description of particle physics. There are other theories which produce different distinguishable particles. Such theories as two-Higgs-doublet models (2HDM) and the Minimal Supersymmetric Standard Model (MSSM) which require an additional Higgs doublet.

As part of the search for extended scenarios of electroweak symmetry breaking in this thesis, studies were preformed on tools, phenomenology and analysis techniques used in the search for charged Higgs bosons with the ATLAS experiment. This thesis is divided in two parts. In the first part the focus is on the development of tools used for high precision predictions for processes containing τ leptons in the final state, including signal, background and their interference in the SM and BSM electroweak symmetry breaking scenarios. The studies include the development of the `TauSpinner` program [3]. `TauSpinner` is a tool for modifying the physics model of Monte Carlo generated samples in case of the changed assumptions about the event production dynamics without needing to re-generating events. With the help of weights the τ lepton production or decay processes can be modified according to a new physics model. In this study a new version of `TauSpinner` has been presented which includes a mechanism for introducing non-standard states and couplings and studying their effects in vector-boson-fusion processes. This method exploits the spin correlations of τ lepton pair decay products in processes where final states include also two hard jets.

The second part of the thesis presents a search for charged Higgs bosons decaying to a τ lepton and its neutrino with the ATLAS experiment at the Large Hadron Collider (LHC). The experimental observation of charged Higgs bosons, H^+, which are predicted by several models with an extended Higgs sector, would indicate physics beyond the SM. This part of the thesis is dedicated to the search for H^+ in the τ+jets and τ+lepton final state using 2015+2016 and full Run-II (2015-2018) ATLAS data-set.

This dissertation is organized in the following way. Chapter 2 briefly introduces the SM and BSM related to further discussions, and describes τ lepton properties and

signatures. In Chapter 3, precision calculations of non-SM Higgs boson scenarios are discussed in the context of `TauSpinner` tool and its development. Chapter 4 is dedicated to the experimental setup of the LHC and the ATLAS experiment while Chapter 5 gives a short introduction to multivariate analysis in particle physics. Chapter 6 presents the search for a charged Higgs boson decaying to $\tau\nu$ in τ+jet and τ+lepton final states with 36.1 fb^{-1} of proton proton collision data recorded at $\sqrt{s}$ =13 TeV with the ATLAS experiment. Chapter 7 is dedicated to the data-driven fake factor method for background estimation, in the ongoing analysis of the full Run-II worth of data.

1.2 Statement of the Author's Contribution

The author contributed significantly in both part of presented thesis. In the first part describing `TauSpinner` development, the work was done in the contex of HiggsTools project, in collaboration with Wrasaw and Jagiellonian Universities. In the second part describing a search for $H^+ \to \tau\nu$ with the ATLAS experiment, the work was done in collaboration with other members of the ATLAS Higgs Beyond-the-SM (HBSM) search group. The author's personal contributions are as follows:

- The author contributed to a study of systematic uncertainties of `TauSpinner` for variation of its input parameters, and study of an interference between QCD and electroweak subprocesses. The results were published in Ref. [4].

- In the development of the `TauSpinner` program for non-SM processes with spin-2 particle, the author contributions included generating matrix elements with `MadGraph`, modifying of the matrix elements in order to prepare them for implementation into `TauSpinner` source code, using symmetries for reducing the number of processes, and finally successfully testing the implementation of new matrix elements. The results were published in Ref. [5]. As part of the ATLAS authorship qualification for ATLAS experiment, the application of `TauSpinnerTool` which is an ATLAS specific interface to the `TauSpinner` library, was studied.

- In the search for $H^+ \to \tau\nu$ with 2015 and 2016 data, the author main contributions were study of τ polarization sensitive variable Y, its introduction to the BDT discriminant and evaluation of its imapct on the analysis sensitivity. The author also contributed in the evaluation of systematic uncertainty in V+jet background. The results were published in Ref. [6].

- In the search for $H^+ \to \tau\nu$ using the full Run-II data-set, the author contributed mainly in the detailed study of fake τ background estimation using data-driven fake factor method. The author was responsible for investigation of an alternative variable used for discriminanting between quark- and gluon-initiated jets, validating the fake factor methods using Monte Carlo samples and full evaluation of systematic uncertainties of fake τ estimation. The author also contributed in testing new matrix elements in `MadGraph` setup in H^+ generation. The result of this work will be used in the currently ongoing analysis and the future publication of the ATLAS collaboration.

1.3 Conventions

The symbol ℓ refers to either an electron or a muon. The symbol l refers to any lepton: an electron, muon or τ lepton.
In the following τ^+ and τ^- are indicated as τ, unless otherwise stated. The same applies to other charged particles. Charged Higgs bosons are denoted as H^+, with the charged conjugatevH^- always implied.
The natural units are used, where the proton carries a positive unit of charge and the speed of light is set to c=1.

Chapter 2

Theory

2.1 The Standard Model of particle physics

The theory of the Standard Model of particle physics represents our current understanding of particle physics, by describing the elementary particles and their associated interactions currently known in the nature. It successfully predicts and describes many phenomena of particle physics and so far has been confirmed experimentally to large extent.

The SM unravels the invisible hidden symmetries chosen for the design of our universe. It is a quantum field theory which has been developed since 1960s based on gauge invariance which naturally introduces interactions. The Higgs mechanism [7–9] breaks the gauge symmetry [10, 11] to generate masses of the weak force carriers (W and Z bosons). The general structure of the SM provides an elegant theoretical framework constructed with the symmetry group $SU(3)_C \times SU(2)_L \times U(1)_Y$, where the $SU(3)_C$ group represents the strong interactions, with subscript C denoting the color charge, while the $SU(2)_L \times U(1)_Y$ group describes the electroweak interaction, with L and Y denoting the left-handed fermions and weak hypercharge, respectively.

2.1.1 Elementary particles in the Standard Model

The elementary particles in the SM are associated into three generations of fermions (particles with spin 1/2) and vector bosons (spin-1 force carriers) and a scalar (spin 0 Higgs boson) as shown in Figure 2.1 [12].

The fermions include three generations of left-handed lepton doublets: the electron (e) and electron neutrino (ν_e); the muon (μ) and muon neutrino (ν_μ); the tau (τ) and tau neutrino (ν_τ). Additionally there are three generations of left-handed quark doublets: up (u) and down (d); charm (c) and strange (s); top (t) and bottom (b). The leptons e, μ and τ carry an electric charge of -1 (in the unit of elementary charge e), while the neutrinos ν_e, ν_μ and ν_τ are electrically neutral. All leptons participate in the electroweak interaction. Quarks u, c and t carry electric charge of $2/3$ while d, s and b carry electric charge of -1/3. Quarks carry another charge called the color charge, therefore they can interact via strong interaction as well. Thus quarks are able to participate in all the three types of interaction described by the SM (Section 2.1.2). The quarks are always bound together via strong interaction to form color-neutral composite particles called hadrons, which either contain a quark and antiquark (mesons) or three and five quarks (baryons).

There are three types of spin 1 gauge bosons in the SM, including 8 massless gluons (g) as the strong force carriers, and a massless photon (γ) as the electromagnetic force carrier, and Z and $W^\pm$ massive bosons (91.2 GeV and 80.4 GeV [13] respectively) as the weak force carriers.

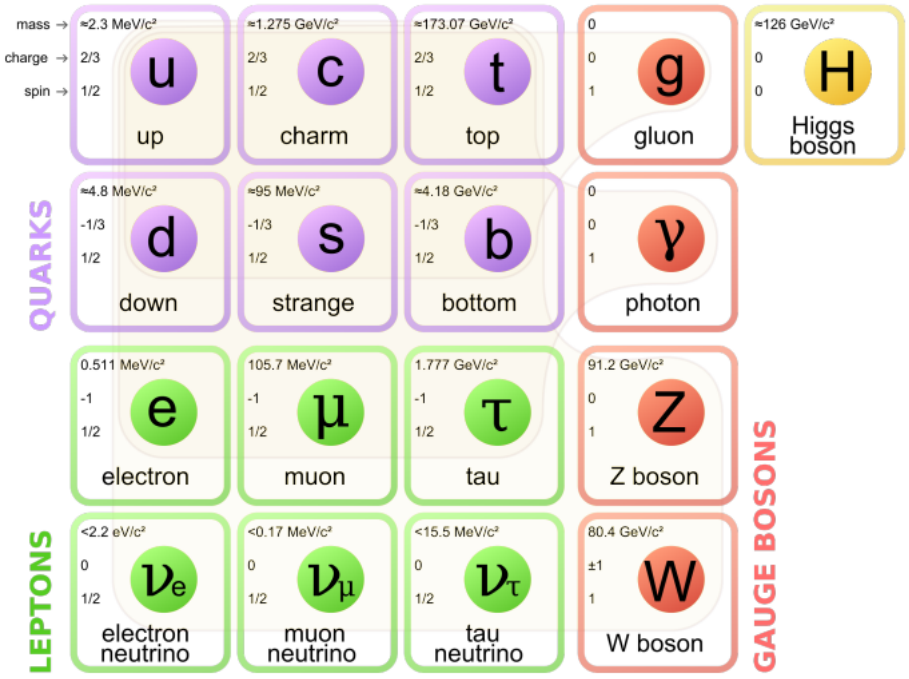

FIGURE 2.1: The elementary particles of the SM.

Interaction	Gauge boson	Particle sensitive to the interaction
Weak	W^+, W^-, Z^0	Quarks and leptons
Electromagnetic	γ (photon)	Electrically charged leptons and quarks
Strong	g (gluon)	Quarks

TABLE 2.1: The boson sector of the SM and the interactions.

2.1.2 Fundamental interactions

There are four known interactions between particles and, as mentioned in previous Section, three of them are described by the SM. They are listed in Table 2.1. Each one of them has an associated symmetry group. A fundamental property of the SM is the gauge invariance which means the theory is invariant under local gauge transformations. These interactions are discussed in the following Sections.

Electromagnetic interaction

The interaction between electrically charged particles are described by the electromagnetic force. The photon, γ is a massless, electrically neutral and not self-interacting gauge boson. This interaction is described by a relativistic quantum field theory which is called Quantum Electrodynamics (QED). It is based on local symmetry U(1). The QED Lagrangian density describes the coupling of a charged fermion field ψ to the boson field A^μ:

$$\mathscr{L}_{QED} = \overline{\psi}(i\gamma^\mu D_\mu - m)\psi - \frac{1}{4}F_{\mu\nu}F^{\mu\nu} \tag{2.1}$$

where γ^μ are Dirac matrices and m is mass of fermions. The covariant derivative and the field strength are as follows:

$$D_\mu = \partial_\mu - ieA_\mu, \tag{2.2}$$

$$F_{\mu\nu} = \partial_\mu A_\nu - \partial_\nu A_\mu. \tag{2.3}$$

Because $\mathscr{L}_{QED}$ is invariant under U(1) gauge symmetry ($\psi \to e^{ie\xi(x)}\psi$, where $\xi(x)$ is a function of space-time) the electrical charge is conserved locally. The elemental electrical charge e is given by $e = \sqrt{4\pi\alpha_{QED}}$, where α_{QED} is the electromagnetic coupling constant. It is a fundamental parameter of the theory which determines the strength of the electromagnetic interaction. In QED, observables are usually expressed as a function of α_{QED}. By using perturbation theory to calculate those observables, divergences appear in the calculations involving Feynman diagrams with loops including virtual particles. To avoid these divergences, a method called re-normalization is used [14]. It redefines measurable observables at a given energy scale, called the re-normalization scale μ_0, to include the virtual particle corrections and in this way the infinities are absorbed. Imposing the independence of the physical observable from μ_0 reveals that α_{QED} depends on the energy scale. The $\alpha_{QED}(Q^2)$ increases with the energy Q^2. It varies from $1/137$ at $Q^2 = 0$ to $1/127$ at Q^2 corresponding to the mass of Z boson.

Weak interaction

The weak interaction affects all fermions, including neutrinos, and has several massive mediators, unlike the electromagnetic and strong forces, called Z^0 and $W^\pm$ bosons. The weak interaction has very short range because of the heaviness of its mediator. The lifetime of a particle is proportional to the inverse square of the coupling constant of the force which causes the decay, therefore the lifetime of particles relying on weak force for their decay processes is large. The weak interaction is the only interaction able to change the flavor of a quark or a lepton. It also breaks the parity symmetry, because in the relativistic limit $W^\pm$ boson only couples to left-handed particles, i.e. particles with spin and momentum of opposite direction, and right-handed antiparticles.

The electroweak theory

In modern particle theory, electromagnetism and the weak force are unified under the Glashow-Weinberg-Salam (GSW) model [7–9]. The gauge theory [15] that describes both interactions is called the unified electroweak theory, and it is based on the $SU(2)_I \times U(1)_Y$ symmetry group. The generator of the $U(1)$ group is the weak hypercharge operator, $\hat{Y}$, and the generators of the $SU(2)$ group are the weak isospin operator $\hat{T}$. Leptons are represented according to their chirality: right-handed leptons are isospin singlets (T = 0), while left-handed leptons are isospin doublets ($T = \frac{1}{2}$, $T_3 = \pm\frac{1}{2}$) :

$$\psi_L = \frac{1-\gamma_5}{2}\begin{pmatrix}\psi_{\nu_l}\\ \psi_l\end{pmatrix}, \psi_R = \frac{1+\gamma_5}{2}\psi_l \tag{2.4}$$

where L, R refers to left- and right-handed fermions. The local gauge invariance requirement leads to the existence of four bosons: A^i_μ(i=1,2,3) from SU(2) and B_μ from U(1). The fields of the electroweak bosons are mixtures of these gauge boson fields. The Lagrangian density of the electroweak interaction is:

$$\mathscr{L}_{EW} = \overline{\psi}_L(i\gamma^\mu(D_\mu))\psi_L + \overline{\psi}_R(i\gamma^\mu(D_\mu))\psi_R - \frac{1}{4}A^i_{\mu\nu}A^{i\mu\nu} - \frac{1}{4}B_{\mu\nu}B^{\mu\nu}. \tag{2.5}$$

The gauge fields $A^i_{\mu\nu}$,$B_{\mu\nu}$ and the covariant derivative, D_μ are given by:

$$D_\mu = \partial_\mu + \frac{1}{2}\tau_{L,R}A^i_\mu - \frac{1}{2}ig'Y_{L,R}B_\mu, \tag{2.6}$$

$$A^i_{\mu\nu} = \partial_\mu A^i_\nu - \partial_\nu A^i_\mu + g\epsilon_{ijk}A^j_\mu A^k_\nu, \tag{2.7}$$

$$B_{\mu\nu} = \partial_\mu B_\nu - \partial_\nu B_\mu. \tag{2.8}$$

where g and g' are the coupling constant associated with SU(2) and U(1) respectively. They are related to α_{QED} as follows:

$$\alpha_{QED} = g\sin\theta_w = g'cos\theta_w \tag{2.9}$$

where θ_w is known as the weak mixing angle. The τ_i are generators associated with the SU(2) symmetry group (the Pauli matrices), and Y=Q-I_3 (hypercharge) is the generator of U(1), Q is the electric charge, and I_3 is the third component of weak isospin. So far the theory predicts massless SU(3) gauge fields, contradicting the experimental observations. The photon and the gluons are massless as a consequence of the exact conservation of the corresponding symmetry generators: the electric charge and the eight color charges. The fields for the the photon, $A^{(\gamma)}$, and for the physical bosons of weak interaction Z and $W^\pm$ are mixtures of A^i_μ and B_μ :

$$A^{(\gamma)}_\mu = \cos\theta_w B_\mu + \sin\theta_w A^3_\mu, \tag{2.10}$$

$$Z_\mu = -\sin\theta_w B_\mu + \cos\theta_w A^3_\mu, \tag{2.11}$$

$$W^\pm_\mu = \frac{1}{\sqrt{2}}(A^1_\mu \mp A^2_\mu). \tag{2.12}$$

Strong interaction

The strong interaction is responsible for holding quarks together in hadrons and binding protons and neutrons together to form the atomic nucleus. This interaction is described by Quantum Chromodynamics (QCD) [16], a gauge theory with the symmetry group SU(3). In this representation the gluon is the gauge field, i.e. the QCD equivalent of the QED photon. QCD introduces its own charge (just as electric charge in electromagnetism), known as "color". The color charge comes in three varieties called red, green and blue. Antiquarks have corresponding anticolor. Quarks

and antiquarks are combined in such a way that they always form colorless hadrons. Leptons have no color charge. The gluon is not a charge-neutral force carrier (as its QED counterpart), it can be thought of as carrying both color charge and anticolor charge. There are eight possible different combinations of (anti) color for gluons, which form an octet in color SU(3) [17]. Due to their non-Abelian nature, the gluon gauge fields exhibit self-couplings that allow for self-interactions.

The QCD Lagrangian density is given by:

$$\mathscr{L}_{QCD} = \Sigma_q \overline{\psi}_{q,j}(i\gamma^\mu(D_\mu)_{jk} - m_q\delta_{jk})\psi_{q,k} - \frac{1}{4}G^a_{\mu\nu}G^{\mu\nu}_a \tag{2.13}$$

where ψ^i_q are quark-field spinors for a quark q with a mass of m_q, and a color index of i which runs form i=1 to N_c=3, N_c is number of colors, $\overline{\psi}^i_q = \psi^\dagger\gamma^0$ is its Dirac adjoint, γ^μ are the Dirac matrices, $G^a_{\mu\nu}$ is the gluon field-strength tensor and a is the color charge (a=1 ...8=N_c^2-1) , $G^a_{\mu\nu} = \partial_\mu G^a_\nu - \partial_\nu G^a_\mu + g_s f^{abc} G^b_\mu G^a_\nu$ where f^{abc} is the structure constant.

The term D_μ is the covariant derivative that maintains gauge invariance under SU(3) given by:

$$(D_\mu)_{ij} = \delta_{ij}\partial_\mu - ig_s\lambda^a_{ij}G^a_\mu \tag{2.14}$$

where G^a_μ is the field of a gluon with the color a, λ^a_{ij} are the traceless and Hermition matrices (generators of fundamental representation of SU(3) known as the Gell-Mann matrices) and finally the $g_s = \sqrt{4\pi\alpha_s}$, where α_s is the coupling constant of strong interaction. An interesting property of QCD is the dependency of α_s on the energy scale (Q), which can be determined by the re-normalization group Equation:

$$\beta(\alpha_s) \equiv Q^2\frac{\partial\alpha_s}{\partial Q^2} = -\alpha_s^2(b_0 + b_1\alpha_s + b_2\alpha_s^2 + ...) \tag{2.15}$$

where b_0, b_1, ... are the coefficients of perturbation expansion. The α_s falls with increasing Q hence asymptotic freedom. Self interaction results in confinement.

The Higgs mechanism

The Higgs mechanism is an essential part of the SM. It describes how the gauge fields in the Lagrangian $\mathscr{L}_{EW}$, Equation 2.5, can be massive. The Higgs mechanism is generally described as a case of spontaneous symmetry breaking [18]. It adds a new field that breaks the $SU(2)_I \times U(1)_Y$ gauge symmetry of the GSW model and dynamically gives masses to the vector bosons. Consider the Higgs field, a weak isospin doublet (T=1/2 , $T_3 = \pm 1/2$) of the complex scalar field

$$\phi = \begin{pmatrix} \phi^+ \\ \phi^0 \end{pmatrix} \tag{2.16}$$

where $\phi^{+(0)}$ has a positive (neutral) electric charge and Y=1 hypercharge. The Higgs Lagrangian is then given by:

$$\mathscr{L}_{Higgs} = |D_\mu\phi|^2 - U(\phi) \tag{2.17}$$

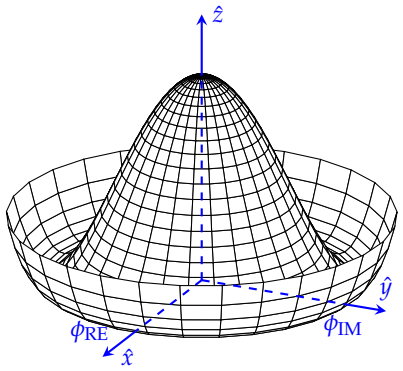

FIGURE 2.2: The Higgs potential with its non-zero vacuum expectation value.

where D_μ is the covariant derivative of Equation 2.6 and the energy potential $U(\phi)$ is given by:

$$U(\phi) = -\mu^2|\phi|^2 + h\phi^4 \tag{2.18}$$

where $\mu^2 > 0$ and $h > 0$. The Higgs potential from Equation 2.18 has a "Mexican hat" shape as shown in the Figure 2.2. For such a potential, minima occur for non-zero values of the field. Therefore, the Higgs field is said to have a positive vacuum expectation value. Without losing generality, we can set the top isospin component to zero, by a suitable gauge choice. In this gauge, the Higgs doublet is given by :

$$\phi' = \frac{1}{\sqrt{2}}(\lambda + \chi(x)) \begin{pmatrix} 0 \\ 1 \end{pmatrix} \tag{2.19}$$

where $\lambda = \sqrt{\frac{\mu^2}{h}}$ is the non-zero vacuum expectation value of the field, and $\chi(x)$ are local deviations from it. Thus Equation 2.18 becomes:

$$U(\lambda) = h\lambda^2\chi^2 + h\lambda\chi^3 + \frac{h}{4}\chi^4. \tag{2.20}$$

The field $\chi(x)$ corresponds to the excitation of the field around the vacuum expectation value, and represents a new boson called the Higgs boson. Equation 2.20 shows that the Higgs boson has a mass ($m_h = \sqrt{2h\lambda^2}$) and is self-interacting. The Higgs field vacuum expectation value can be obtained from Fermi's constant and is approximately 246 GeV. The electroweak scale is commonly associated with this value.
The Higgs field interaction with fermions dynamically generating the fermion masses, the Yukawa interaction, is given by:

$$\mathscr{L}_{l-Higgs} = -\sqrt{2}m_f(\overline{\psi}_R\phi\dagger\psi_L + \overline{\psi}_L\phi\psi_R) \tag{2.21}$$

in which m_f is the charged fermion mass and ψ_L and ψ_R are left- and right-handed fermions (see Equation 2.4). The Yukawa interaction is a general interaction between a scalar field and a Dirac (fermionic) field, so that there is also a Yukawa term for

quarks. By adding the Higgs sector, the Lagrangian of the SM becomes:

$$\begin{aligned}\mathscr{L}_{SM} &= \mathscr{L}_{QCD} + \mathscr{L}_{EW} + \mathscr{L}_{Higgs} = \overline{\psi}_q^i \gamma^\mu i(D_\mu)_{ij}\psi_q^j - m_q\overline{\psi}_q^i\psi_{qi} \\ &- \frac{1}{4}G^a_{\mu\nu}G_a^{\mu\nu} + \overline{L}_l\gamma^\mu iD_\mu L_l + \overline{R}_l\gamma^\mu iD_\mu R_l - \frac{1}{4}A_{\mu\nu}A^{\mu\nu} \\ &- \frac{1}{4}B_{\mu\nu}B^{\mu\nu} + |D_\mu\phi|^2 + \mu^2|\phi|^2 - h\phi^4.\end{aligned} \tag{2.22}$$

Using the perturbation expansion of Equation 2.19, combined with Equation 2.6, this becomes:

$$\begin{aligned}\mathscr{L}_{SM} &= \Sigma_q[\overline{\psi}_q^i(i\gamma^\mu)(\delta_{ij}\partial_\mu - \frac{1}{2}ig_s\lambda^a_{ij}G^a_\mu)\psi_q^j - f_q\overline{\psi}_q^i\psi_{iq}(\lambda+\chi)] - \frac{1}{4}G^a_{\mu\nu}G_a^{\mu\nu} \\ &- \Sigma_q i[g\overline{\psi}^L_{qi}\gamma^\mu(\frac{g}{6}B_\mu + \frac{g'}{2}A_\mu)\psi^L_{qi} - ig\overline{\psi}^R_{qi}\gamma^\mu Y^R g B_\mu\psi^R_{qi}] \\ &- \frac{1}{4}A_{\mu\nu}A^{\mu\nu} - \frac{1}{4}B_{\mu\nu}B^{\mu\nu} - e\Sigma_l\overline{\psi}_l\gamma^\mu\psi_l A^\gamma_\mu \\ &+ \Sigma_l i[\overline{\psi}_{\nu_l}\gamma^\mu\frac{1}{2}(1-\gamma_5)\partial_\mu\psi_{\nu_l} + i\overline{\psi}_l\gamma^\mu\partial_\mu\psi_l - f_f\overline{\psi}_l\psi_l(\lambda+\chi)] \\ &+ \frac{g}{2\sqrt{2}}\Sigma_l[\overline{\psi}_l\gamma^\mu(1-\gamma_5)\psi_{\nu_l}W^-_\mu + \overline{\psi}_{\nu_l}\gamma^\mu(1-\gamma_5)\psi_l W^+_\mu] \\ &+ \frac{6}{4cos\theta}\Sigma_l[\overline{\psi}_{\nu_l}\gamma^\mu(1-\gamma_5)\psi_{\nu_l} - \overline{\psi}_l\gamma^\mu(g'_V-\gamma_5)\psi_l]Z_\mu \\ &+ \frac{h\lambda^4}{4} + \frac{1}{2}(\partial_\mu\chi)^2 - h\lambda^2\chi^2 - h\chi^2(\lambda\chi + \frac{1}{4}\chi^2) + \frac{g^2}{8}(2W^+_\mu W^{-\mu} + \frac{Z_\mu Z^\mu}{cos^2\theta})(\lambda+\chi)^2\end{aligned} \tag{2.23}$$

where ψ_q^L and ψ_q^R are the left-handed quark doublets and right-handed quark singlets respectively, $Y^R = \frac{4}{3}(\frac{2}{3})$ is the hypercharge of up-type (down-type) right-handed quarks, $e = qsin\theta$, $f_f = \frac{m_f}{\lambda}$ is the coupling of the fermions to the Higgs field, the coupling of the Higgs field to quarks is $f_q = \frac{m_q}{\lambda}$ and $g'_V = 1 - \sin^2\theta_w$. Note that the coupling of fermions to the Higgs field scales with fermion mass. The last part contains the mass terms for $W^\pm$ and Z bosons given by :

$$M_W = \frac{g\lambda}{2} \tag{2.24}$$

and

$$M_Z = \frac{M_W}{cos\theta_w}. \tag{2.25}$$

The Higgs field does not couple to the electromagnetic field $A^{(\gamma)}_\mu$ which leads to the desired result of photon being massless. The masses of gauge bosons and the Weinberg mixing angle can be grouped together to a parameter traditionally denoted as ρ:

$$\rho = \frac{M_W^2}{M_Z^2 cos^2(\theta_w)} \tag{2.26}$$

which upon substitution of Equation 2.24 into Equation 2.25 gives the (tree-level) result:

$$\rho = 1, \tag{2.27}$$

an important prediction of the SM, and a good test for various BSM models.

2.2 Beyond the Standard Model

So far, the Standard Model has been widely successful in describing the phenomena currently known in nature. However, several limitations prevent the SM from being regarded as the complete and ultimate theory. Some of these limitations are as follow:

- **Hierarchy of particle masses**
  Experimental data show a clear hierarchy of the lepton and quark masses that are distributed in three families, the properties of which with respect to interactions seem universal. The most important questions are why they have different masses and how to understand the effective Yukawa couplings in the theory with unpredicted magnitudes. The reason is expected to be found in a more fundamental theory.

- **Matter-antimatter asymmetry**
  According to the Lambda-CDM model of cosmology, matter and antimatter should have been produced in equal abundance during the Big Bang, because the SM interactions are producing new particles in matter-antimatter pairs. However, the current Universe is clearly dominated by matter and therefore, in order to explain its current structure, it is necessary to suppose that a matter-antimatter symmetry must have been broken in the evolution of the Universe.

- **Gravity**
  The gravitational force is the only interaction which is not included in the Standard Model description. The main reason is that the combination of the quantum mechanical formalism with general relativity generates infinities which cannot be absorbed by any re-normalization process. In other words, the current SM-based theories of gravitational forces are ill-defined. The corresponding mediating particle of this interaction would be the so-called graviton, which is a spin-2 tensor boson.

- **Neutrino masses**
  On contrary to what the Standard Model predicts, it is now known that neutrinos are massive [19]. This is a major issue for the original SM, but the model can be easily extended in order to take neutrino masses into account. It is sufficient to add a new right-handed neutrino ν_R for every generation and introduce a Dirac mass term. The only conceptual problem with this solution is that the resulting ν_R would be sterile, i.e. it would not interact at all with other SM particles (except gravitationally). However, one can also treat neutrino masses as a hint when looking for an extension of the SM. For example, if neutrinos are Majorana particles, which indicates that they are their own antiparticles, the smallness of their masses can be elegantly explained via the see-saw mechanism [20]. This idea can also lead to thermal leptogenesis as a very promising mechanism for producing the baryon asymmetry [21].

Moreover, after the discovery of a Higgs-like boson in 2012 by ATLAS [22] and CMS [23] which was compatible with the prediction of SM, the focus of the experiment at the Large Hadron Collider (LHC) [24] has shifted on the one hand towards performing precision Higgs rate measurement, in order to establish indirect evidence for BSM physics. And on the other hand towards direct BSM discovery, for example other neutral or charged Higgs bosons present in the theories with an extended Higgs sector. One of the well-motivated class of models, which is in agreement with the SM Higgs, is obtained by extending the SM Higgs sector by a second scalar $SU(2)_L$ doublet, the so called two-Higgs doublet model (2HDM) [25]. The minimal supersymmetric extension of the SM (MSSM) [26] is a prominent example of this category of models.

2.2.1 2HDM models

There are at least three fermion families and two left-handed SU(2) doublets in each family but the SM has just one scalar doublet of the Higgs field (the "standard" Higgs doublet). However there is no reason why there should be only one Higgs doublet, there are some arguments that favor several such doublets. Motivations for models including two Higgs doublet instead of one, include the following [25]:

- Supersymmetry (SUSY): supersymmetry requires at least two Higgs doublets [27], because scalars come in chiral multiplets and the complex conjugates come in multiplets of opposite chirality.
- Cancellation of anomalies: in the SM the fermion families need to be complete in order for guage anomalies to be canceled. In SUSY the introduction of a single Higgsino (the supersymmetric partner of the Higgs boson) introduces anomalies. There are canceled when the second doublet is introduced.
- Axion models: according to axion models [28] in the QCD possible CP-violating terms (that are experimentally known to be very small) in $\mathscr{L}_{QCD}$ may be rotated away if the Lagrangian exhibits a global U(1) symmetry. Such a symmetry exists only if there are two Higgs doublets.
- Baryon asymmetry of the universe: baryon asymmetry of the universe is not properly described by the SM. 2HDMs, however, may explain this asymmetry thanks to the flexibility of the scalar mass spectrum as well as additional new sources of CP violation.

The scalar potential and the field content

Complex scalar doublets have four degrees of freedom so with two (Higgs) doublets ϕ_1, ϕ_2 there are eight degrees of freedom. Three of these are just Goldstone bosons that give masses to the $W^{\pm}$ and Z bosons and the remaining five are the physical scalars: the Higgs fields. Of these five there is a charged scalar (with two physical states $H^{\pm}$), two neutral scalars and a pseudoscalar (see e.g Ref. [29]):

$$(h^0, H^0, A^0, H^{\pm}) \tag{2.28}$$

with masses $(m_h, M_H, m_A, M_{H^{\pm}})$. Here h^0, H^0 are scalars (CP-even particles) and A^0 is pseudoscalar (CP-odd). The SM Higgs sector has only one free parameter, the Higgs mass. However, 2HDMs contain several free parameters and the vacuum

structure is much richer. The most general scalar potential contains several parameters and it has CP-conserving, CP-violating and charge-violating minima. The potential reads ([25]) :

$$V = m_{11}^2 \boldsymbol{\phi_1^\dagger \phi_1} + m_{22}^2 \boldsymbol{\phi_2^\dagger \phi_2} - m_{12}^2 (\boldsymbol{\phi_1^\dagger \phi_2} + \boldsymbol{\phi_2^\dagger \phi_1}) + \frac{\lambda_1}{2} (\boldsymbol{\phi_1^\dagger \phi_1})^2 + \frac{\lambda_2}{2} (\boldsymbol{\phi_2^\dagger \phi_2})^2 + \lambda_3 \boldsymbol{\phi_1^\dagger \phi_1 \phi_2^\dagger \phi_2} + \lambda_1 \boldsymbol{\phi_1^\dagger \phi_2 \phi_2^\dagger \phi_1} + \frac{\lambda_5}{2} [(\boldsymbol{\phi_1^\dagger \phi_2})^2 + (\boldsymbol{\phi_2^\dagger \phi_1})^2] \tag{2.29}$$

for $\boldsymbol{\phi_1}$, $\boldsymbol{\phi_2}$ the two doublets of hypercharge +1. All the parameters of the potential are real. A region of parameter space minimizing the potential Equation 2.29 gives the vacuum expectation values:

$$< \boldsymbol{\phi_1} >_0 = \frac{1}{\sqrt{2}} \begin{pmatrix} 0 \\ v_1 \end{pmatrix}, < \boldsymbol{\phi_2} >_0 = \frac{1}{\sqrt{2}} \begin{pmatrix} 0 \\ v_2 \end{pmatrix}. \tag{2.30}$$

For the vacuum described by Equation 2.30 the fields have the following mass terms in the Lagrangian for charged scalar $\phi^\pm$, pseudoscalar η and neutral scalar ρ, respectively :

$$\mathscr{L}_{\phi^\pm}^{mass} = [m_{12}^2 - (\lambda_4 + \lambda_5) v_1 v_2] (\phi_1^-, \phi_2^-) \begin{pmatrix} \frac{v_2}{v_1} & -1 \\ -1 & \frac{v_1}{v_2} \end{pmatrix} \begin{pmatrix} \phi_1^+ \\ \phi_2^+ \end{pmatrix} \tag{2.31}$$

$$\mathscr{L}_{\eta}^{mass} = \frac{m_A^2}{v_1^2 + v_2^2} (\eta_1, \eta_2) \begin{pmatrix} v_2^2 & -v_1 v_2 \\ -v_1 v_2 & v_1^2 \end{pmatrix} \begin{pmatrix} \eta_1 \\ \eta_2 \end{pmatrix} \tag{2.32}$$

$$\mathscr{L}_{\rho}^{mass} = -(\rho_1, \rho_2) \begin{pmatrix} m_{12}^2 \frac{v_2}{v_1} + \lambda_1 v_1^2 & -m_{12}^2 + \lambda_{345} v_1 v_2 \\ -m_{12}^2 + \lambda_{345} v_1 v_2 & m_{12}^2 \frac{v_1}{v_2} + \lambda_2 v_2^2 \end{pmatrix} \begin{pmatrix} \rho_1 \\ \rho_2 \end{pmatrix} \tag{2.33}$$

The mass-squared matrices of Equations 2.31, 2.32 each have a zero eigenvalue, corresponding to the massless Goldstones that give the masses to the $W^\pm$ and Z, respectively. Besides the zero eigenvalues, these matrices also give the physical masses for the charged and pseudoscalar Higgs:

$$m_\pm^2 = [\frac{m_{12}^2}{(v_1 v_2)} - \lambda_4 - \lambda_5](v_1^2 + v_2^2), \tag{2.34}$$

$$m_A^2 = [\frac{m_{12}^2}{(v_1 v_2)} - 2\lambda_5](v_1^2 + v_2^2). \tag{2.35}$$

The mass matrices of Equations 2.31, 2.32 and 2.33 can be diagonalized, but in general not simultaneously. Two important parameters in the study of 2HDMs are α and β, the rotation angles that diagonalize the mass-squared matrices of the pseudoscalr and charged scalar sector and neutral scalar sector, respectively. The angle β is defined using the vacuum expectation values of the two doublets $\boldsymbol{\phi}_1$, $\boldsymbol{\phi}_2$:

$$\tan\beta \equiv \frac{v_2}{v_1}. \tag{2.36}$$

Flavor conservation

The mass-squared matrices of the various Higgs fields in general may not be diagonalized at the same time. This leads to tree-level flavor-changing neutral currents (FCNCs). Since FCNCs have not been observed in nature, their existence poses a problem for such models with several scalar multiplets. In order to illustrate this, we consider the Lagrangian describing the mass of down-type quarks [25]:

$$\mathscr{L}_Y^d = y_{ij}^{(1)}\overline{\psi_i}\psi_j\boldsymbol{\phi_1} + y_{ij}^{(2)}\overline{\psi_i}\psi_j\boldsymbol{\phi_2}. \tag{2.37}$$

where i, j are a family indices. The corresponding mass matrix reads:

$$M_{ij}^d = y_{ij}^{(1)}\frac{v_1}{\sqrt{2}} + y_{ij}^{(2)}\frac{v_2}{\sqrt{2}} \tag{2.38}$$

In the SM, with just one Higgs multiplet, the diagonalization of the mass matrix M implies the diagonalization of the Yukawa couplings y. This is not the case in Equation 2.38, where $y^{(1)}$ and $y^{(2)}$ usually do not have the same set of eigenvectors, and so in general the Yukawa interactions in Equation 2.37 will have FCNCs at the tree level (e.g. couplings $\bar{d}s\phi$). Getting rid of these is customarily done by introducing some additional, continuous or discrete symmetries [25].

There are different ways to introduce the symmetries that hinder the FCNCs. One option is to introduce a discrete symmetry:

$$\boldsymbol{\phi_1} \to -\boldsymbol{\phi_1}, \tag{2.39}$$

which is done for example in the so called type I 2HDM, where $\boldsymbol{\phi_1}$ is chosen to couple to all fields of the theory, and $\boldsymbol{\phi_2}$ to none.
Another option is to have transformations

$$\boldsymbol{\phi_1} \to -\boldsymbol{\phi_1},\ d_R^i \to -d_R^i, \tag{2.40}$$

as may be done in the type II 2HDM, where the right-handed down-type quarks couple to $\boldsymbol{\phi_1}$ and the right-handed up-type quarks couple to $\boldsymbol{\phi_2}$.

Here, we shall concentrate on the type II 2HDM since in the Chapter 4 of this thesis, in the search for charged Higgs boson, the benchmarks of this model which is explained in Section 2.2.2, is used.

Yukawa couplings of the type II 2HDM

In the type II 2HDM the Yukawa terms in the SM Lagrangian can be given by [25]:

$$\begin{aligned}\mathscr{L}_{Yukawa}^{2HDM} &= -\Sigma_{f=u,d,l}\frac{m_f}{v}(\xi_h^f\overline{f}fh + \xi_H^f\overline{f}fH - i\xi_A^f\overline{f}\gamma_5 fA)\\ &-(\frac{\sqrt{2}V_{ud}}{v}\overline{u}(m_u\xi_A^u P_L + m_d\xi_A^d P_R)dH^+ + \frac{\sqrt{2}m_l}{v}\xi_A^l\overline{v_L}l_R H^+ + h.c.),\end{aligned} \tag{2.41}$$

where the f are fermion fields with Yukawa couplings ξ^f as in Table 2.2 and, $P_{L,R}$ are the projection operators on left- and right-handed helicities, respectively. The coupling of the neutral, scalar Higgses h^0, H^0 to the massive vector bosons Z and $W^\pm$ are proportional to the SM coupling of the single Higgs, namely

$$g(hWW, hZZ)|_{2HDM} = \sin(\beta-\alpha)g(hWW, hZZ)|_{SM}. \tag{2.42}$$

/	h	H	A
u	$\xi_h^u \cos\alpha/\sin\beta$	$\xi_H^u \sin\alpha/\sin\beta$	$\xi_A^u \cot\beta$
d	$\xi_h^d -\sin\alpha/\cos\beta$	$\xi_H^d \cos\alpha/\cos\beta$	$\xi_A^d \tan\beta$
l	$\xi_h^l -\sin\alpha/\cos\beta$	$\xi_H^l \cos\alpha/\cos\beta$	$\xi_A^l \tan\beta$

TABLE 2.2: Yukawa coupling of u,d,l to the neutral Higgs boson h,H,A in the type II 2HDM. The coupling to the charged Higgs bosons are obtained from Equation 2.32. Values from Ref. [25].

$$g(HWW, HZZ)|_{2HDM} = \cos(\alpha - \beta) g(HWW.HZZ)|_{SM} \tag{2.43}$$

The coupling of the pseudoscalar A to the vector bosons is zero.

2.2.2 The charged Higgs production and decay

In general, there are four types of 2HDM commonly discussed. Type-I and type-II were already discussed. In the lepton-specific type, all leptons couple to one of the Higgs doublets, and the quarks to the other. In the flipped-model, up-type quarks and charged leptons couple to the same doublet. In a type-II 2HDM, which corresponds to the Higgs sector of the Minimal Supersymmetric Standard Model (MSSM) [26], the production and decays of the charged Higgs boson partly depend on its mass m_{H^+}. For low masses ($m_{H^+} < m_{top}$, where m_{top} is the top-quark mass), the primary production mechanism at the LHC is through the decay of the top quark, $t \to bH^+$. The leading source of top quarks at the LHC is $t\bar{t}$ production. For H^+ masses above the top-quark mass ($m_{H^+} > m_{top}$), the leading H^+ production mode at the LHC is in association with a top quark which can be described as either $gb \to tH^+$ (referred to as the 5-flavor scheme, or 5FS) or $gg \to tbH^+$ (referred to as the 4-flavor scheme, or 4FS). Diagrams illustrating the leading-order production mechanisms of a charged Higgs boson in 5FS and 4FS are shown in Figure 2.3.

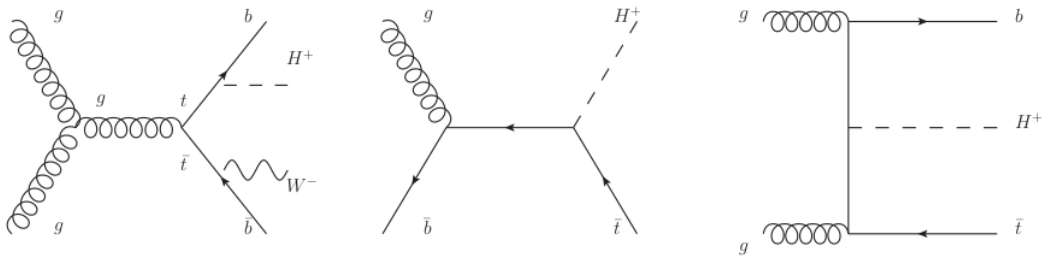

FIGURE 2.3: Leading Feynman diagrams for the charged Higgs boson production processes in the proton-proton collision: (a) top quark decay, (b) associated top quark in five-flavour (5FS) and (c) four-flavour (4FS) scheme.

The production and decays of the charged Higgs boson are also controlled by the parameter tanβ. Figure 2.4 shows typical production cross-sections for heavy

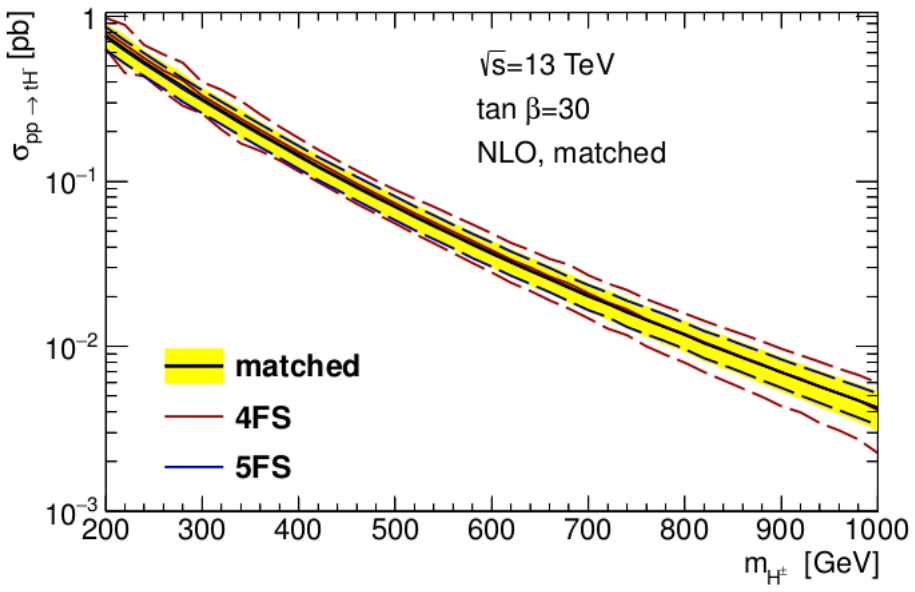

FIGURE 2.4: Production cross-section for charged Higgs bosons as a function of m_{H^+} for tanβ=30 at a center of mass energy of $\sqrt{s}$ = 13TeV. The values are shown for 5FS and 4FS schemes and matched, where the red and blue dashed lines indicate the systematic uncertainties on the 4FS and 5FS, respectively, the yellow band shows the uncertainty on the matched cross-sections [30].

charged Higgs bosons in a type II 2HDM at $\sqrt{s}$ = 13 TeV. In order to avoid a dependence on the chosen approximation, the cross-sections calculated in the 4FS and 5FS approximations are combined and matched [30]. The difference between the two schemes is logarithmic. Therefore, the dependency of the relative weight is controlled by a logarithmic term. In the following Equation 2.44 the matched cross-section is presented, with weight $w = \log\frac{m_{H^+}}{m_b} - 2$, where m_b is the mass of the b-quark,

$$\sigma_{matched} = \frac{\sigma_{4FS} + w\sigma_{5FS}}{1 + w}. \tag{2.44}$$

The theoretical uncertainties are combined according to:

$$\Delta\sigma_{matched} = \frac{\Delta\sigma_{4FS} + w\Delta\sigma_{5FS}}{1 + w}. \tag{2.45}$$

An overview of the cross-section estimation in the intermediate-mass region is given in Ref. [31], where several production modes and their interference are taken into account. Figure 2.5 shows a two-dimensional plot of production cross-section as a function of tanβ and m_{H^+} for 4FS in the 2DHM along with its average relative uncertainty.

In the MSSM, a number of benchmark scenarios have been defined, which keep a low number of free parameters in the theoretical model, even when taking higher-order corrections into account [33]. The m_h^{max} scenario is constructed to yield the highest possible mass for the CP-even Higgs boson h at any given tanβ . Following the discovery of a Higgs boson with a mass close to 125 GeV, the m_h^{max} scenario

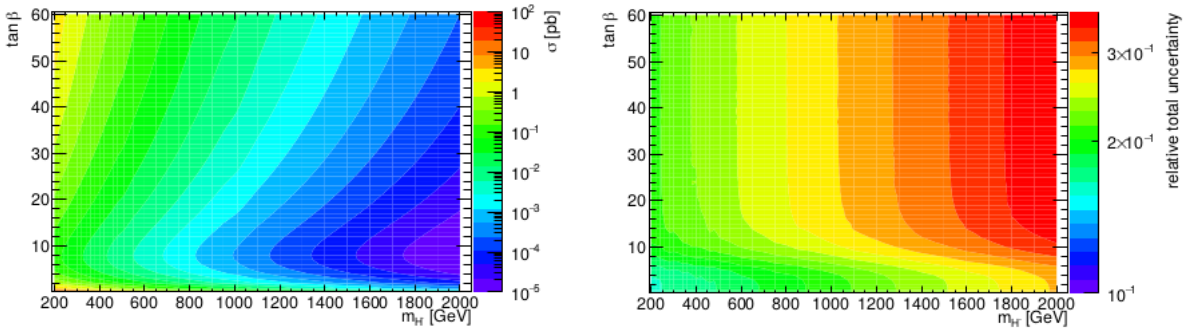

(a) (b)

FIGURE 2.5: Two-dimensional plots of the charged Higgs boson production cross-section (a) and average relative uncertainty (b) as a function of tanβ and m_{H^+} values in the 4FS of the 2DHM [32].

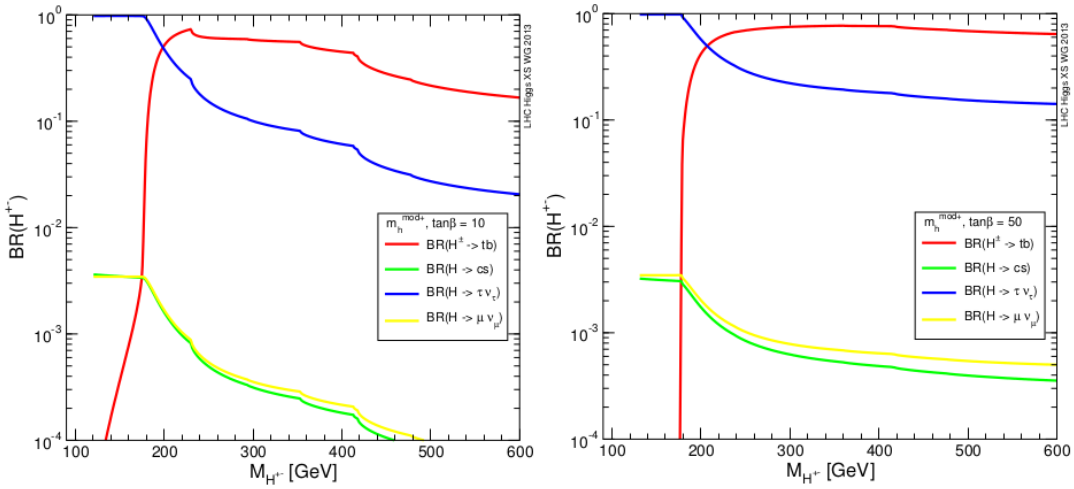

(a) (b)

FIGURE 2.6: Branching fractions of the charged Higgs boson as a function of m_{H^+}, for tanβ values of 10 (a) and 50 (b), in the m_h^{mod+} scenario of the MSSM [32].

becomes less relevant, and new benchmark scenarios have been proposed. These include e.g. the so-called m_h^{mod+} and m_h^{mod-} scenarios, in which h can be interpreted as the LHC signal in a large part of the parameter space (mod stands for modified theory) [31]. Another model, the hMSSM [34], is also considered, where the lighter h boson has a mass of 125 GeV and the non-observation of super particles at the LHC is taken into account by setting the SUSY-breaking scale to $M_S > 1$ TeV. The branching fractions for H^+ decays into SM particles are displayed in Figure 2.6, as a function of m_{H^+} , for tanβ = 10 and tanβ = 50, in the m_h^{mod+} scenario. H^+ decays to SUSY particles are taken into account, but are not shown in the plots (their effects are visible as kinks in the lines of other channels, in particular for tanβ =10). For tan$\beta > 3$, light charged Higgs bosons decay mainly via $H^+ \to \tau\nu$ [35]. Above the top-quark mass, the branching fraction BR ($H^+ \to \tau\nu$) can still be substantial (at least

10%), depending on the value of tanβ.

In Chapter 4 of this dissertation the search for the charged Higgs boson with the ATLAS experiment [1] is presented.

2.3 τ lepton properties and its signature (polarization)

The τ lepton and its characteristics are going to be used widely in this thesis, therefore this Section is dedicated to its general overview. The τ lepton was discovered in 1975 at the Stanford Linear Accelerator by Martin Perl and his collaborators [36]. It is the first discovered member of the third quark-lepton family. It has a rest mass of 1776.82 $\pm$ 0.16 MeV [13] and a very short life time of 290.6 $\pm$ 1.0$\times 10^{-15}$ s [13]. The τ lepton is sufficiently heavy to decay to an up quark and a Cabibbo-mixed down quark, unlike its lighter counterparts (the electron and muon). Hence the τ lepton has two different decay modes: it can decay either leptonically or hadronically. Figure 2.7 depicts the two decay modes of the τ lepton. The branching fractions for both hadronic and leptonic decays are shown in Table 2.3. In hadronically decaying τ leptons, decays with only one charged particle (so-called 1-prong decays) occur about 72% of the time and with three charged particles (so-called 3-prong decays) about 23% of the time. The τ lepton can decay to pseudo-scalar, vector or axial-vector resonances which are either Cabibbo-favored (π^-, ρ^-, a^-) or Cabibbo-suppressed (K^-, K^{*-}, K_l^-). The leptonic decays have a total branching fraction of about 35 % and the hadronic decays have a total branching fraction of about 65%. Table 2.4 summarizes the masses and the quark composition of mesons from hadronically decaying τ leptons.

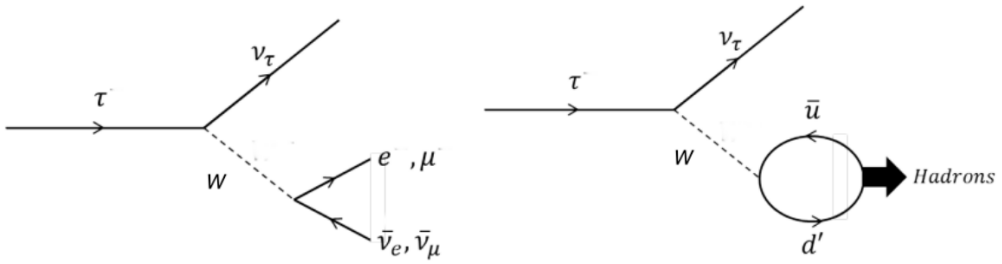

(a) (b)

FIGURE 2.7: Leptonic (a) and hadronic (b) decays of the τ lepton

The τ lepton plays an important role in the physics program of the LHC. Among others, it is relevant for identifying properties of the 125 GeV Higgs boson as well as makes an important signature in searches for BSM physics.

2.3.1 τ lepton polarization

In the year 1971, four years before the discovery of the τ lepton, it was predicted that if the lepton were heavy enough to decay to quarks its helicity would be accessible through the kinematics of its decay products, due to the maximal parity violation in the weak decay of the heavy lepton [37]. The spin correlations depends on the nature of decaying resonance (scalar, pseudo-scalar, vector). The Z vector boson decays to fermions are parity violating i.e. the left-handed fermions (and right-handed anti-fermions) are favored, inducing polarization and spin correlation between its decay

Decay modes	Branching fraction [%]
$e^-\overline{\nu}_e\nu_\tau$	17.82 $\pm$0.04
$\mu^-\overline{\nu}_\mu\nu_\tau$	17.39 $\pm$ 0.04
$\pi^-\nu_\tau$	10.91 $\pm$ 0.07
$\rho^-\nu_\tau$	25.94$\pm$0.09
$K^-\nu_\tau$	0.696$\pm$ 0.023
$K^{*-}\nu_\tau$	0.429$\pm$ 0.015
$h^-2\pi^0\nu_\tau$	10.85$\pm$ 0.11
$h^- \geq 3\pi^0\nu_{tau}$	1.34 $\pm$ 0.07
$h^-h^+h^-\nu_\tau$	9.80$\pm$ 0.07
$h^-h^+h^- \geq 1\pi^0\nu_\tau$	5.38 $\pm$ 0.07

TABLE 2.3: Decay modes and branching ratios of the τ lepton.

Mesons	Quark Composition	Mass [MeV]	Dominating decay mode
π^-	$\overline{u}d$	139.6	-
ρ^-	$\overline{u}d$	775.5	$\pi^-\pi^0$
a_1^-	$\overline{u}d$	1230	$\rho^-\pi^-$
K^-	$\overline{u}s$	493.7	-
K^{*-}	$\overline{u}s$	891.6	$K^-\pi^0$
K_1^-	$\overline{u}s$	1403	$K^{*-}\pi^0$

TABLE 2.4: Quark compositions of mesons, mass and dominating decay mode of mesons from main hadronically τ decays 2.4.

products. On the other hand, the Higgs is a scalar, and the Yukawa coupling does not distinguish handedness, therefore fermions originating from Higgs decay are unpolarized. Hence in the decay to a pair of τ leptons, polarization can be used as an additional information helping to distinguish between Higgs and Z bosons.
The longitudinal polarization is the asymmetry of the cross-section for positive ($\lambda = 1$) and negative ($\lambda = -1$) helicity τ lepton production:

$$P_\tau = \frac{N_R - N_L}{N_R + N_L} = \frac{\sigma_\tau(\lambda = 1) - \sigma_\tau(\lambda = -1)}{\sigma_\tau(\lambda = 1) + \sigma_\tau(\lambda = -1)} \tag{2.46}$$

At the Z pole the integrated polarization is given by

$$< P_\tau >= -\frac{2\overline{g}_v^\tau \overline{g}_A^\tau}{\overline{g}_v^{\tau 2} + \overline{g}_A^{\tau 2}} = -\mathcal{A}_\tau, \tag{2.47}$$

$$< P_\tau > \approx -\frac{2\overline{g}_A^\tau}{\overline{g}_v^\tau} = -2(1 - 4\sin^2_{eff}\theta_w), \tag{2.48}$$

by considering that $\overline{g}_A^\tau \gg \overline{g}_v^\tau$. According to Equation 2.48, the polarization is therefore a measure of the effective mixing angle. The so called chiral coupling asymmetry $\mathcal{A}_\tau$ was measured very precisely at LEP, from which the effective mixing angle $\sin^2\theta_{eff}$=0.23147 $\pm$ 0.00057 was derived [38]. The positive and negative helicity states and right- or left-handed chiral states are equivalent in the assumed relativistic limit.

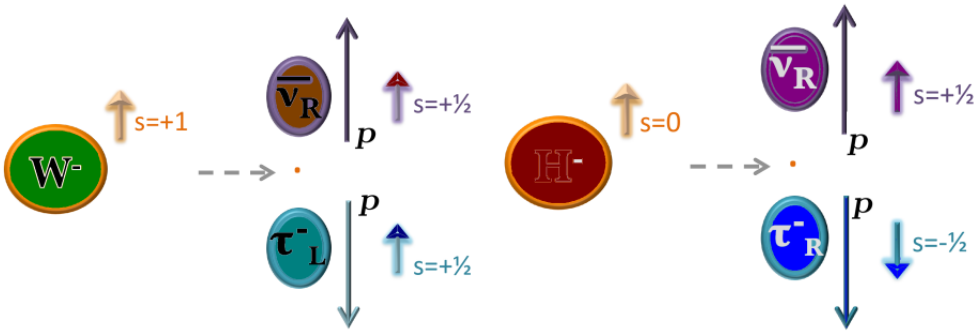

(a) (b)

FIGURE 2.8: The $W^- \to \tau_L \nu$(a) and $H^- \to \tau_R \nu$ (b), in the rest frame of the bosons. Since W boson has spin 1, the $\frac{1}{2}$-spin directions of the subsequent leptons must be compensated. Moreover, since the state of the ν is fixed by nature, the spin of the τ lepton has to be oriented opposite to the direction of flight. However, the H^- spin=0 causes the spin vectors of the subsequent leptons to be in opposite directions [39].

The τ polarization, P_τ, is a measure of the degree of parity violation in the interaction. In $W^\pm \to \tau^\pm \nu$ decays, the W^- is expected to couple solely to a left-handed τ^- and the W^+ to a right-handed τ^+ which corresponds to the τ polarization $P_\tau = -1$. In the case of the SM scalar Higgs boson decay to τ lepton pairs, the parity-conserving decay, P_τ=0. On the other hand, an MSSM charged Higgs boson decaying via $H^+ \to \tau^\pm \nu$, being a spin-0 particle, would lead to a prediction of P_τ=1. Due to the angular momentum conservation, the angular distribution of the τ decay products depends strongly on the τ spin orientation. Since there is only one neutrino in the final state in the hadronic decay modes, these models are especially well-suited to determine the τ spin orientation. The decays of $W^- \to \tau_L \nu$ and $H^- \to \tau_R \nu$ are shown in Figure 2.8. The angle θ between the τ flight direction and the hadronic decay products in its rest frame is the basic observable sensitive to τ polarization. In the relativistic limit , i.e E$\gg m_\tau$, the angle θ is related to the ratio of the energy of the hadronic decay products to the τ energy in the laboratory frame. However, the cosθ parameter is difficult to measure experimentally. There is an additional observable, cosΨ, sensitive to the polarization state of τ in one-prong hadronic decays $\tau \to \rho\nu \to \pi^+\pi^-\nu$, where Ψ is the angle between the flight direction of the ρ meson and the neutral pion [40]:

$$\cos\Psi = \frac{m_\rho}{\sqrt{m_\rho^2 - 4m_\pi^2}} \frac{E_{\pi^-} - E_{\pi^0}}{|P_{\pi^-} + P_{\pi^0}|} \tag{2.49}$$

where the particle energies and momenta are measured in the laboratory frame and m_ρ, m_π denote the masses of ρ and π mesons, respectively. However, the width of ρ is large and its mass cannot be well measured at the LHC. At the expense of sensitivity, the first part of Equation 2.49 is dropped, and the charged energy asymmetry,

Y, is used instead:

$$Y = \frac{E_T^{\pi^\pm} - E_T^{\pi^0}}{p_T} \approx 2\frac{p_T^{trk}}{p_T} - 1 \tag{2.50}$$

It measures the energy sharing between the $\pi^\pm$ and π^0 in the τ decay relative to the visible momentum of the τ. Experimentally, the energy associated with $\pi^\pm$ is given by the transverse momentum of the single track (p_T^{trk}) associated with the hadronically decaying τ candidate. The energy ascribed to π^0 is calculated as the difference between the transverse momentum of the track of the τ candidates. It should be noted that for angular momentum to be conserved, in $\tau^\pm \to \rho^\pm \nu_\tau$ decays, transversely polarized ρ mesons are favored in left-handed τ decays, which is leading to a symmetric energy sharing between $\pi^\pm$ and π^0, while right-handed τ leptons preferably decay to longitudinally polarized ρ which leads to an asymmetric energy sharing. The Y observable is optimized for the ρ decay, but in practice, it is studied inclusively for all τ lepton decays with one charged meson in the final state.

2.3.2 The τ lepton transverse spin effect as an observable for CP test

Transverse spin effects can be helpful for distinguishing between scalar and pseudoscalar natures of spin-zero particles in their decays to τ pairs. The spin density matrix for the two τs resulting from the decay of the state which is a mixture of the scalar and pseudoscalar is given by:

$$\Gamma(H/A^0 \to \tau^+\tau^-) \sim 1 - s_{||}^{\tau^+} s_{||}^{\tau^-} \pm s_{\perp}^{\tau^+} s_{\perp}^{\tau^-}. \tag{2.51}$$

The transverse spin correlation carries information on Higgs parity which can be translated into observables such as acollinearity in the $H \to \tau^+\tau^-$, $\tau^\pm \to \pi^\pm \nu$ decay chain in the rest frame of H. We can define the acollinearity angle, $\Theta_{\text{acollinearity}}$, as illustrated in Figure 2.9:

$$\Theta_{\text{acollinearity}} = \cos^{-1}\left(\frac{\overrightarrow{p_{\pi^+}}.\overrightarrow{p_{\pi^-}}}{|\overrightarrow{p_{\pi^+}}||\overrightarrow{p_{\pi^-}}|}\right) \tag{2.52}$$

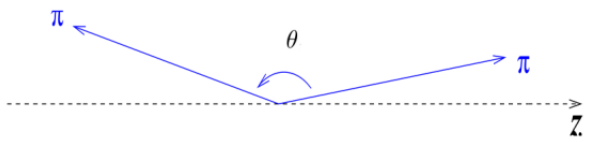

FIGURE 2.9: Simple illustration of $\Theta_{\text{acollinearity}}$ shown as the angle between two charged pions.

A θ_{plane} parameter is defined as an angle between planes defined by: the $\tau^\pm$ momentum and the beam momentum (first plane); and $\tau^\pm$ momentum and the momentum of the $\pi^\pm$ (second plane). In the presence of transverse polarization in the sample, the acollinearity distribution after applying a cut on the $\cos(\theta_{\text{plane}})$ is modified. This is illustrated in Figure 2.10 [41] .

For the $H \to \tau^+\tau^-$, $\tau^\pm \to \rho^\pm \nu$, $\rho^\pm \to \pi^\pm \pi^0$ decay chain, the $\rho^+\rho^-$ rest frame is used, which has the advantage that it can be constructed only from directly visible

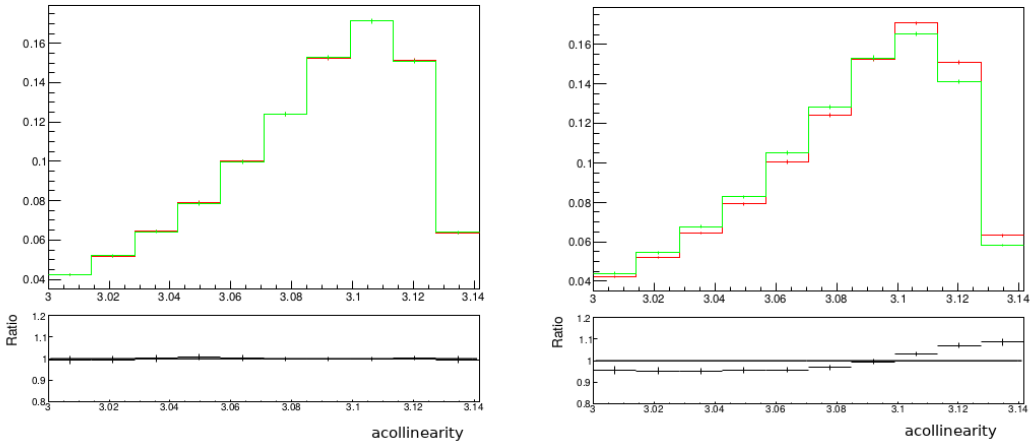

(a) (b)

FIGURE 2.10: The reference plots for transverse polarization [41]: acollinearity distributions with (red line) and without (green line) the cut $\cos(\theta_{\text{plane}}) > 0.5$ for samples without transverse polarization (a) and with transverse polarization (b).

decay products. In that case the one-dimensional angular distribution of acoplanarity [41], the angle between $\pi^+\pi^0$ and $\pi^-\pi^0$ decay plane in the $\rho^+\rho^-$ rest frame (see Figure 2.11) was proposed as CP sensitive observable:

$$\theta_{\text{acoplanarity}} = \cos^{-1}\left(\frac{\overrightarrow{n_+}\overrightarrow{n_-}}{|\overrightarrow{n_+}||\overrightarrow{n_-}|}\right), \tag{2.53}$$

where

$$\overrightarrow{n_\pm} = \overrightarrow{p_{\pi^\pm}} \times \overrightarrow{p_{\pi^0}}. \tag{2.54}$$

This distribution is CP-sensitive if events are separated into two categories, according to the sign of the product $y_+ \cdot y_-$, where, y_+ and y_- variables are defined as follows:

$$y_+ = \frac{E_{\pi^+} - E_{\pi^0}}{E_{\pi^+} + E_{\pi^0}};\ y_- = \frac{E_{\pi^-} - E_{\pi^0}}{E_{\pi^-} + E_{\pi^0}}. \tag{2.55}$$

In the case of $y_+ \cdot y_- > 0$, both π^+ and π^- are more energetic or less energetic than π^0 which is known as fast-fast and slow-slow configuration respectively. For the case of $y_+ \cdot y_- < 0$, π^+ or π^- is more or less energetic than π^0 which leads to the fast-slow configuration. The distribution of acoplanarity without applying any selection cuts, should be flat, independently of the sign of $y_+ \cdot y_-$. In Figure 2.12 events are split into two separate categories and compared to the case of the scalar (red) and the mixed scalar-pseudo scalar state (blue dashed) with assumed mixing angle θ=0.2. The $\theta_{\text{acoplanarity}}$ distribution relies on a measurement of the four-momenta (in the laboratory frame) of the $\pi^+\pi^0$ and $\pi^-\pi^0$ only, no reconstruction of the rest frame of the Higgs boson and/or $\tau^\pm$ is required. The nature of the observable is at least three dimensional and the multi-dimensional fit in the space ($\theta_{\text{acoplanarity}}$,$y_+$,$y_-$) offers an additional increase in the sensitivity of this measurement.

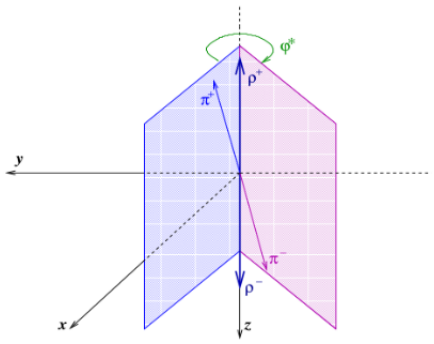

FIGURE 2.11: Schematic of angles between the $\pi^+\pi^0$ (blue) and $\pi^-\pi^0$ (red) decay planes in the $\rho^+\rho^-$ rest frame.

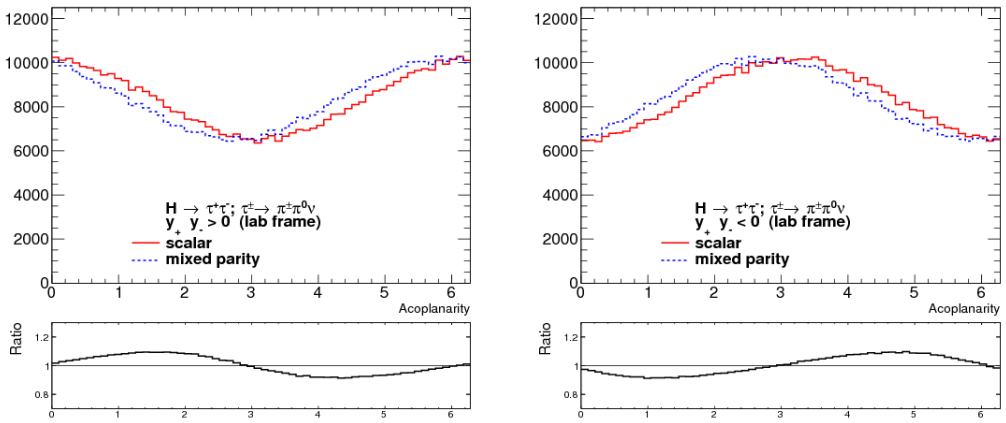

(a) (b)

FIGURE 2.12: The acoplanarity distribution for the $H \to \tau^+\tau^-$, $\tau^\pm \to \pi^\pm\pi^0\nu$ decays. (a) Events with $y_+ \cdot y_- > 0$, (b) $y_+ \cdot y_- < 0$. The scalar (red) and mixed scalar-pseudoscalar (blue dashed), with mixing angle θ=0.2, are compared, the y_+ and y_- variables are calculated in the laboratory frame [41].

All these observables were used in the study of the `TauSpinner` program. The $H^+ \to \tau\nu$ search analysis used the Y variable to improve signal-background discrimination.

2.4 Hadronic collision and Monte Carlo event generators

The LHC is a machine producing primarily proton-proton (pp) collisions. A proton consists of quarks and gluons. At the LHC, the parton interactions can be divided into hard and soft scattering processes depending on the momentum transferred between partons. A pp collision event at the LHC can be illustrated as shown in Figure 2.13.

The theoretical model for a hadron-hadron collision event is described below:

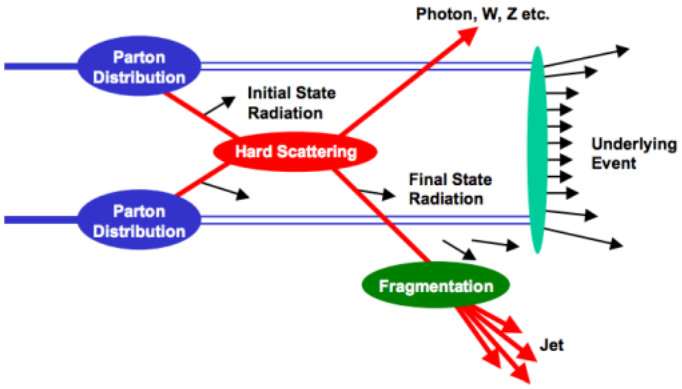

FIGURE 2.13: Schematic view of a hadron-hadron collision.

- **Parton Distribution Function (PDF)** at leading order quantifies the probability of finding a certain type of quark or gluon with momentum fraction x at an energy scale Q.
- **Hard Scattering** shows the event produced by proton interactions. A hard scattering process transfers a large momentum among partons, which could be either a violent scatter or the creation of a large mass system. For example, the Higgs boson production from gluon-gluon fusion and the final state of Higgs boson decay for underlying physics process such as vector bosons or quark pairs.
- **Jet Fragmentation** produces the hadronic jets in the final state from the partons (quarks and gluons) which are produced in the hard scattering.
- **Initial and Final State Radiation** represents the QCD radiation, in form of gluons or QED radiation, in form of photons, from incoming and outgoing particles.
- **Underlying Event** contains the particles produced by proton remnants.

One of the physical quantities to connect the theory and experimental measurements is the cross-section (σ) of a certain physics process. According to the QCD factorization theorem [42] the cross-sections for hard scattering can be factorized into a parton level hard scattering convoluted with the parton distribution functions. For example, for the scattering of two hadrons A and B producing a final state X, a general form to calculate the hadronic cross-section can be written as:

$$\sigma_{AB} = \int dx_a dx_b f_{a/A}(x_a, \mu_F^2) f_{b/B}(x_b, \mu_F^2) \widehat{\sigma}_{ab\to X}(\alpha_S, \mu_R, \mu_F) \tag{2.56}$$

where μ_F is the factorization scale, which can be also understood as the scale that separates the short- and long-distance physics and μ_R is the re-normalization scale for the QCD running coupling. The $f_{a/A}(x_a, \mu_F^2)$ and the $f_{b/B}(x_b, \mu_F^2)$ represent the PDF for the incoming particles. The $\widehat{\sigma}_{ab\to X}(\alpha_S, \mu_R, \mu_F)$ is the parton level cross-section, which can be calculated by perturbative QCD, in form of a fixed-order

expansion in α_S

$$\widehat{\sigma}_{ab\to X}(\alpha_S, \mu_R, \mu_F) = (\alpha_S)^n[\widehat{\sigma}^{(0)} + (\alpha_S/2\pi)\widehat{\sigma}^{(1)}(\mu_R, \mu_F) + (\alpha_S/2\pi)^2\widehat{\sigma}^{(2)}(\mu_R, \mu_F) + ...] \tag{2.57}$$

where $\widehat{\sigma}^{(0)}$ denotes the leading-order (LO) partonic cross-section, and $\widehat{\sigma}^{(1)}$ the next-to-leading-order (NLO), $\widehat{\sigma}^{(2)}$ (NNLO).

The choice of μ_F and μ_R is arbitrary. To avoid unnaturally large logarithms reappearing in the perturbation series, it is sensible to choose μ_F and μ_R values of the order of the typical momentum scales of the hard scattering process. The scale μ_F=μ_R is often assumed. Taking the Higgs production through gluon-gluon fusion and decay to ZZ^* as an example, the standard choice is $\mu_F = \mu_R = \frac{m_{ZZ^*}}{2}$.

2.4.1 Monte Carlo event generators

Monte Carlo (MC) event generators are software for simulating particle physics events using Monte Carlo methods. MC event generators [62, 63, 66]play a crucial role throughout the whole process of an experiment, including the design of the experiment, detector simulation and calibration, data analysis and comparison of the experimental results and theoretical predictions. The structure of a proton-proton collision at the LHC as built up by event generators can be described by a few main steps which follow the theoretical model for an event from hadron-hadron collisions as mentioned above. These steps are illustrated in Figure 2.14. It is worth to mention that sometimes MC generators do not model spin structure correctly and programs like `TauSpinner` are able to make up for it by appropriate reweighting of the final state kinematics. Throughout this thesis, MC generator samples were used. More information about MC samples used in this dissertation is provided in the corresponding Chapter.

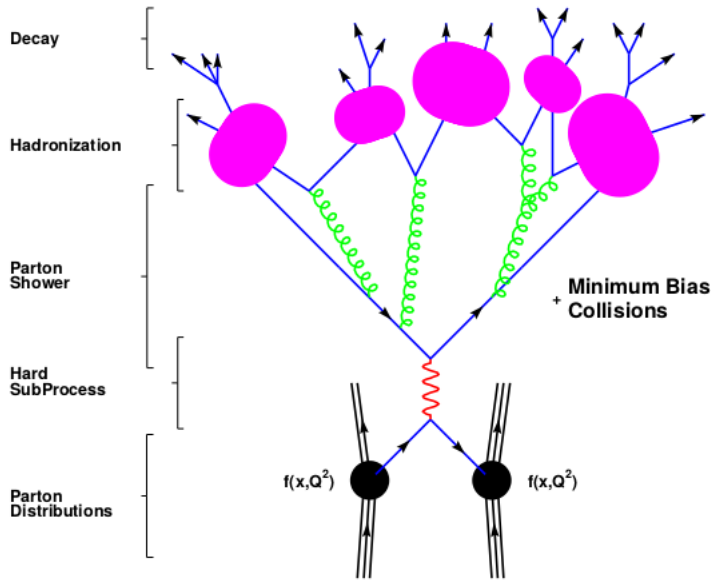

FIGURE 2.14: The basic structure of a showering and hadronization generator event is shown schematically [43].

Chapter 3

The TauSpinner studies in SM and non-SM processes

3.1 TauSpinner algorithm

The τ-lepton plays an important role in the physics program at the LHC. It offers a powerful probe in searches for new physics and can be used to measure parameters of the Standard Model. Polarization of τ lepton represents an interesting phenomenological quantity which can be used for the sake of separation of signal from background or in measuring properties of particles decaying to τ leptons. A proper treatment of τ spin effects in the Monte Carlo simulations is important for understanding the detector acceptance as well as for the measurements and use of τ polarization and τ spin correlations in experimental analysis.

Exploring final states with τ leptons becomes even more important with increasing amount of data taken by experiments at the LHC. The `TauSpinner` package represents a tool which can be used to modify τ spin effects in any sample containing τ leptons. Moreover, the matrix element responsible for the production processes can be modified with the help of `TauSpinner`. The algorithm relies on kinematics of outgoing particles (or partons) only, and averages over all possible initial states to assumed parton distribution and cross-sections. The `TauSpinner` program can be used to calculate appropriate event weights, whereby correction spin effects could be included into or removed from the generated events sample. It started with modeling of $2 \to 2$ production processes matrix elements; two incoming and two outgoing particles matrix elements [44]. Then the new implementation of hard processes $2 \to 4$ matrix elements; two incoming and two outgoing partons with two τ leptons at the final state was introduced [3].

In this Chapter, the general idea behind `TauSpinner` program is presented. The physics processes of interest of `TauSpinner` $2 \to 4$ and the systematic uncertainty related to variation of its input parameters are discussed in Section 3.2. In Section 3.3 the new matrix element implementation for the case of non-SM spin 2 particle is presented. Finally, Section 3.4 is dedicated to `TauSpinnerTool` and its application for validation of τ polarization in MC generated samples.

3.1.1 Theoretical basis

Here, following the documentation [45] the theoretical basis of the `TauSpinner` program is presented. For the process $pp \to \tau^+\tau^-\chi$; $\tau^+ \to \mathrm{Y}^+\overline{\nu}$; $\tau^- \to \overline{\mathrm{Y}'}^-\nu$, where χ is outgoing partons, the basic cross-section formula reads:

$$d\sigma = |\mathcal{M}|^2 d\Omega = |\mathcal{M}|^2 d\Omega_{prod} d\Omega_{\tau^+} d\Omega_{\tau^-} \tag{3.1}$$

where $\mathcal{M}$ is the complete matrix element and Ω is the element of phase space, where $d\Omega_{prod}$ corresponds to production phase space and $d\Omega_{\tau^\pm}$ to the $\tau^\pm$ decay. The terms related to averaging over initial state spin degrees of freedom and flux factor are dropped out. Since the τ lepton width is very small, its propagator module squared, reduces to the Dirac δ function in lepton virtuality, thus the infinitesimal element in the kinematical phase space factorizes into $d\Omega_{prod} d\Omega_{\tau^+} d\Omega_{\tau^-}$.

There are more than 20 possible τ decay channels which lead to 400 distinct processes and matrix elements. This makes the Equation 3.1 inconvenient. Fortunately, because of narrow width of the τ, matrix element can be expressed as product of amplitudes of production $\mathcal{M}^{prod}$ and decays $\mathcal{M}^{\tau^\pm}$, summed over each τ spin projection (λ=1,2):

$$\mathcal{M} = \sum_{\lambda_1,\lambda_2=1}^{2} \mathcal{M}^{prod}_{\lambda_1\lambda_2} \mathcal{M}^{\tau^+}_{\lambda_1} \mathcal{M}^{\tau^-}_{\lambda_2}. \tag{3.2}$$

Then, the cross-section with the help of Fierz identity can be rewritten as the decoupled summations of decays and production matrix elements. It introduces the correlations in a form of spin weight wt_{spin}:

$$d\sigma = \Big(\sum_{\lambda_1,\lambda_2} |\mathcal{M}^{prod}_{\lambda_1\lambda_2}|^2\Big)\Big(\sum_{\lambda_1} |\mathcal{M}^{\tau^+}_{\lambda_1}|^2\Big)\Big(\sum_{\lambda_2} |\mathcal{M}^{\tau^-}_{\lambda_2}|^2\Big) wt_{spin}\, d\Omega_{prod} d\Omega_{\tau^+} d\Omega_{\tau^-}. \tag{3.3}$$

The Equation 3.3 is the core of `TauSpinner` algorithm. The wt_{spin} is dimensionless, and contains information of all spin effects transmitted from the production to the decay of τ leptons:

$$wt_{spin} = \sum_{i,j=t,x,y,z} R_{ij} h^i_{\tau^+} h^j_{\tau^-}. \tag{3.4}$$

The indices i and j of the adjoint (1/2 representation of fermions) rotation group representation run over time space coordinates; t, x, y, z. The polarimetric vector $h^i_{\tau^\pm}$ is represented by:

$$h^i_{\tau^\pm} = \sum_{\lambda,\bar{\lambda}} \sigma^i_{\lambda\bar{\lambda}} \mathcal{M}^{\tau^\pm}_{\lambda} \mathcal{M}^{\tau^\pm\dagger}_{\bar{\lambda}} \tag{3.5}$$

where $\sigma^i_{\lambda\bar{\lambda}}$ are Pauli matrices. The $h^i_{\tau^\pm}$ are normalized to set their time-like component to 1.

The spin correlation matrix R_{ij} is calculated from Equation:

$$R_{ij} = \sum_{\lambda_1,\bar{\lambda_1}\lambda_2\bar{\lambda_2}} \sigma^i_{\lambda_1\bar{\lambda_1}} \sigma^j_{\lambda_2\bar{\lambda_2}} \mathcal{M}^{prod}_{\lambda_1\lambda_2} \mathcal{M}^{prod\dagger}_{\bar{\lambda_1}\bar{\lambda_2}} \tag{3.6}$$

and also it is normalized to set its time-like component to 1. Equation 3.4 is universal, derived without any approximation. It can be shown that: $0 < wt_{spin} < 4$ and weight average $< wt_{spin} >= 1$. The R_{ij} matrix describes the full spin correlation between the two τ leptons as well as their individual spin states. The R_{ij} depends on kinematics of production process only, and $h^i_{\tau^+} h_{\tau^-}$ on the kinematics of decay products of $\tau^\pm$. The explicit definition of the matrix R_{ij} and vectors $h^i_{\tau^\pm}$ are well known, see [46, 47] for detailed definitions.

So far, the case of τ pair in the final state, that is the case of $H \to \tau\tau$ or $Z/\gamma^* \to \tau\tau$ processes, was discussed. For the case of only one τ in the final state, such as

$W^{\pm}/H^{\pm} \to \tau\nu$, calculation is much simpler. For $W^{\pm}$ decay the R_{ij} matrix is replaced by a vector of components R_t, R_x, Ry, R_z= 1, 0, 0, ±1. Sum over two indices is thus reduced to sum over one index only, axis z is the direction of $\tau\nu$ from $W^{\pm}$ or $H^{\pm}$ decay as seen from τ-lepton rest-frame. Therefore, spin weight can be written as $wt_{spin} = 1 \pm h^z_\tau$.

The parton level amplitudes used for TauSpinner weight formula

Following factorization theorems, the cross-section can be presented with the help of parton level (PL) amplitudes, $\mathcal{M}^{prod\ PL}$, convoluted with the parton density functions (PDF's) and summed over all flavour configurations of incoming partons, see Equation 2.56.

We would like to define the wt_{spin} as independent from the PDF's as possible. For the H or W mediated processes, spin polarization state does not depend on flavours of incoming partons. For the Z/γ^* the R_{ij} used in calculation of wt_{spin} is taken as weighted average (with PDF's and production matrix elements squared) over all flavour configurations.

To introduce corrections due to different spin effects and modified production process or decay model in the already generated MC sample (i.e. without re-generation of events) one can define the weight WT, representing a ratio of new to old cross-sections at each point in the phase-space. Then from Equation 3.3, the modified cross-section can be written as:

$$d\sigma = \sum_{flavours} \int dx_1 dx_2 f(x_1,...) f(x_2,..) d\Omega^{prod\ PL} (\sum_{\lambda_1,\lambda_2} |\mathcal{M}^{prod\ PL}_{\lambda_1\lambda_2}|^2) \\ (\sum_{\lambda_1} |\mathcal{M}^{\tau^+}_{\lambda_1}|^2) d\Omega_{\tau^+} (\sum_{\lambda_2} |\mathcal{M}^{\tau^-}_{\lambda_2}|^2) d\Omega_{\tau^-} \times wt_{spin} \times WT. \tag{3.7}$$

In general the weight WT factorizes into multiplicative components and weights: production (wt_{prod}), decay ($wt^{\tau^\pm}_{decay}$) and ratio of spin correlation and polarization weights, new to old one $wt_{spin\ new}/wt_{spin\ old}$:

$$WT = wt_{prod} wt^{\tau^+}_{decay} wt^{\tau^-}_{decay} wt_{spin\ new}/wt_{spin\ old}. \tag{3.8}$$

The first three terms of the weight, represent modification of matrix elements for production and decays:

$$wt_{prod} = \frac{\sum_{flavours} f(x_1,...) f(x_2,..) (\sum_{\lambda_1,\lambda_2} |\mathcal{M}^{prod\ PL}_{\lambda_1\lambda_2}|^2)|_{new}}{\sum_{flavours} f(x_1,...) f(x_2,..) (\sum_{spin} |\mathcal{M}^{prod\ PL}_{\lambda_1\lambda_2}|^2)|_{old}}, \tag{3.9}$$

$$wt^{\tau^\pm}_{decay} = \frac{\sum_\lambda |\mathcal{M}^{\tau^\pm}_{new}|^2}{\sum_\lambda |\mathcal{M}^{\tau^\pm}_{old}|^2}. \tag{3.10}$$

The eventual changes in the PDFs parametrizations should be taken into account in calculation of wt_{prod} and also in ratio $wt_{spin\ new}/wt_{spin\ old}$ in Equation 3.8. Ratio of spin weights $wt_{spin\ new}/wt_{spin\ old}$ allows for introduction of new spin effects. In the case of originally unpolarized sample, the $wt_{spin\ old}$ =1 and $wt_{spin\ new}$ alone allows to introduce desired spin effects.

3.1.2 `TauSpinner` functionality

In this Section the functionality of `TauSpinner` is discussed. In the program there are couple of steps which are done automatically before calculating the spin weight. The first step identifies the flavour of the intermediate boson: $W^{\pm}$, Z/γ^*, H or H^+. The four-momenta of outgoing τ leptons and their decay products, with the four-momenta of intermediate boson are used to calculate the polarimetric vectors. The τ polarization is randomly generated and set to ± 1 corresponding to pure τ helicity states. In the case of longitudinal polarization, the probability of helicity state for τ leptons coming from $W^{\pm}$, H and H^+ bosons is constant. For $Z/\gamma^* \to \tau\tau$, the probability is a function of τ scattering angle, θ, and the center of mass squared of the hard process, s, denoted as $P_\tau^Z = f(\theta, s)$. In the `TauSpinner` $2 \to 2$ the quark configuration of the initial state is attributed randomly from the kinematics of intermediate boson and PDFs, in the following order. From the intermediate boson four-vector, the invariant mass of Z/γ^* is calculated. Then, the scattering angle is calculated in the τ pair rest frame from the angle between the direction of τ^+ and the direction of the one of incoming partons boosted to the rest frame of the τ pair, or direction of τ^- and second incoming parton boosted to the rest frame of the τ pair. In the final step the angle is taken as the average of the two. Next, the fraction of momenta taken from proton by each parton: x_1 and x_2 are calculated from the relations: $x_1 x_2 E_{CM}^2 = s$ and $(x_1 - x_2)E_{CM} = p_z$, where E_{CM} and p_z are the center of mass energy of collision and the longitudinal component of the Z/γ^*, respectively. A probabilistic choice is preformed on the basis on the leading order the $2 \to 2$ born level cross-section to attribute the flavours to the incoming quarks and the sign of the scattering angle θ.

The P_τ^Z is calculated as weighted average over all possible quark configuration of initial state [48].

In the `TauSpinner` $2 \to 4$ with two τ leptons and 2 jets in the final state, the baseline of algorithm remains the same. There are a few differences, for instance for sums $\Sigma_{flavour}$ as defined in Section 3.1.1 should read as sum over flavours of incoming and outgoing partons. Also, the matrix element squared is calculated for a given helicity state of τ leptons and flavours of incoming and outgoing partons. For more detail see Ref. [3].

The `TauSpinner` outputs a spin weight given for each event separately. From Equation 3.4, neglecting the transverse spin degree of freedom, in the ultra-relativistic limit, for $Z/\gamma^* \to \tau^+\tau^-$ events the Equation reduces to:

$$wt_{spin} = 1 + sign\ h_{z^+} h_{z^-} + P_\tau h_{z^+} + P_\tau h_{z^-} \tag{3.11}$$

where *sign* equals +1 for left-handed τs and -1 for right-handed τs and P_τ is the polarization of the single τ in a mixed quantum state. Within this approximation, P_τ is a linear function of the probability P_τ^z

$$P_\tau = 2P_\tau^z - 1. \tag{3.12}$$

For a neutral and spin zero Higgs boson decaying to $\tau^+\tau^-$, Equation 3.11 is further simplified to:

$$wt_{spin} = 1 + sign\ h_{z^+} h_{z^-}. \tag{3.13}$$

Here *sign* is +1 for the Z/γ^* boson and -1 for the neutral Higgs boson, showing the opposite spin correlations in the two processes.

3.2 TauSpinner 2→4

The Standard Model processes in pp collision with two opposite-sign τ leptons and two outgoing partons (hereafter, parton is referred to as jet or j) in the final state are the physics processes of interest. Such processes are described by $(2 \to 4)$ matrix elements at the tree level, with single or double intermediate states Z,W, γ^*, H or fermion exchange in the s- or t-channel.

By considering the dynamical structure of the amplitudes, there are in general seven different topologies of Feynman diagrams. It is worth to mention that, regardless of their origin, in all processes the polarization of τ leptons are strongly correlated due to the helicity-conserving couplings to the vector bosons. The matrix elements at tree-level, depending on the initial state, are of the order of $\alpha_S\alpha_{EW}$ or α_{EW}^2, involving sometimes triple WWZ couplings. Figure 3.1 shows two examples of such subprocesses. More details about topologies and the dynamical structure of subprocesses can be found in the Appendix A.

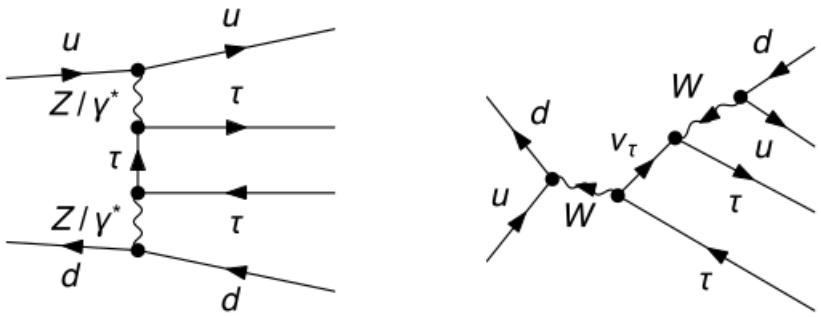

(a) (b)

FIGURE 3.1: Typical topologies of diagrams contributing to the Drell-Yan–type SM process in $u\bar{d} \to \tau^+\tau^- u\bar{d}$: multi-peripheral (a), t-cascade (b)

This version of TauSpiner implementation considers the tree-level only, and the focus is on the spin configurations. Note that there are automated programs for generating codes for spin amplitudes calculation such as MadGraph5 [51].

3.2.1 Input parameters of TauSpinner

In the current version of TauSpinner, one has the freedom to change the input parameters by using the initialization for QCD factorization and renormalization scale and the electroweak scheme. Anomalous parameters can be provided by the user, as well. In the process of calculating the spin weight, in the case of $2 \to 2$ process, the main option is an effective electroweak scheme, using the lowest order matrix element for the $q\bar{q} \to Z/\gamma^* \to \tau\tau$ process, with the effective value for the $\sin(\theta_W^{eff})$ and running of Z boson width in the propagator [49]. In the case of $2 \to 4$ processes, more options are available [3].

In TauSpinner, one can either include dominant EW loop corrections simultaneously with QCD corrections or use an effective scheme which takes into account the τ lepton polarization at the Z boson peak and physical W boson mass. TauSpinner uses by default the second option. Since the effects of WW box diagrams

can be numerically significant for τ lepton pairs with large invariant mass, option for including weak loop effects into TauSpinner effective born level is also available. There are four EW schemes implemented in TauSpinner $2 \to 4$, listed in Table 3.1. Schemes 1 and 3 use tree level definition of the weak mixing angle $\sin^2(\theta_w) = 1 - M_W^2/M_Z^2$=0.222246 which is different from the measured value [49]. Since the τ lepton polarization is sensitive to the weak mixing angle, these schemes are not sufficient. In scheme 2 the predicted tree level value of W boson mass is different from the measured value. This leads to distortion of jet's spectra coming from W boson decays, and shift in the structure of resonance matrix elements. Therefore using EWSH=4 is recommended. In this scheme the effects of loop correction are also taken into account, which makes the result of τ lepton polarization close to the result of LEP experiments. Note that, first three schemes have three input parameters, while the last one has four input parameters.

Type	EWSH=1 input:G_F,α_{QED},M_z	EWSH=2 input:G_F,$\sin^2(\theta_w)$,M_z	EWSH=3 input:G_F,M_W,M_z	EWSH=4 input:G_F,M_W,M_z,$\sin^2(\theta_w)$
M_z	91.1882 GeV	91.1882 GeV	91.1882 GeV	91.1882 GeV
M_W	80.4190 GeV	79.9407 GeV	80.4189 GeV	80.4189 GeV
$\sin^2(\theta_w)$	0.222246	0.231470	0.222246	0.231470
$1/\alpha_{QED}$	132.5070	128.7538	132.5069	127.2272
G_F	1.6639 10^{-5} GeV^{-2}	1.6639 10^{-5} GeV^{-2}	1.6639 10^{-5} GeV^{-2}	1.6639 10^{-5} GeV^{-2}

TABLE 3.1: EW scheme implemented in TauSpinner matrix element for processes (2→4), see [3] for details.

3.2.2 QCD factorization and re-normalization scales and strong coupling constant

The default implementation imposes QCD scales, factorization and renormalization to be equal to $\mu_R = \mu_F = Q^2$, where μ_R is renormalization and μ_F is factorization scale. For the $2 \to 4$ process, several choices of scalePdDFOpt parameters are possible as specified below:

scalePDFOpt=0 Q=200 GeV
scalePDFOpt=1 Q=$\sqrt{\hat{s}}$
scalePDFOpt=2 Q=$\sum m_T$, $m_T^2 = m^2 + p_\perp^2$
scalePDFOpt=3 Q=$\sum E_\perp$, $E_\perp = E \times p_\perp / |\overrightarrow{p}|$

where $p_\perp$ is the transverse momentum of outgoing partons and τ leptons.
The default option is scalePDFOpt=1. For the $\alpha_s(Q^2)$, a simple choice of the Q^2 dependence is provided by the following leading logarithmic Equation:

$$\alpha_s(Q^2) = \frac{\alpha_s(M_Z^2)}{1 + 4\pi\alpha_s(M_Z^2)(11 - 2N_f/3) ln\frac{Q^2}{M_Z^2}} \tag{3.14}$$

with the starting point $\alpha_s(M_Z^2)$=0.118, where M_Z is mass of Z boson. The same value of α_s is used for the case of the fixed coupling constant, that is for scalPDFOpt=0.
In the LHAPDF package [50] which is used for providing parameterization of the

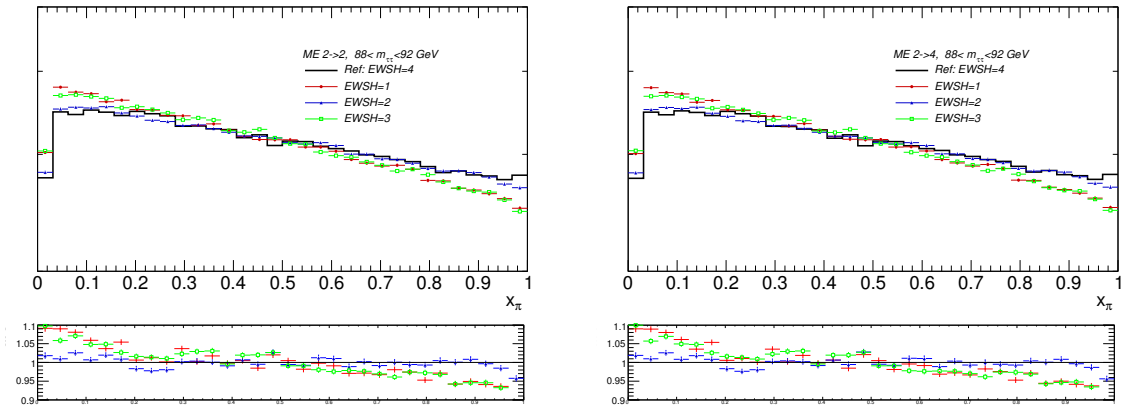

(a) (b)

FIGURE 3.2: Distribution of visible energy fraction (x_π) in the $\tau \to \pi\nu$ decays in the invariant mass window of τ pairs between 88 and 92 GeV, for different EW schemes for $2 \to 2$ (a) and $2 \to 4$ (b) matrix elements [4].

structure functions, the calculation of α_s is implemented for each set of parameters. It is therefore possible to use the definition of the strong coupling consistent with the choice of the structure functions parameterization. The code of TauSpinner is interfaced to the LHAPDF library, therefore any other parameterization of parton density function is easy to install.

3.2.3 Systematic uncertainties

In this Section, systematic uncertainties on the average τ lepton polarization and other polarization sensitive observables like visible energy fraction in the $\tau \to \pi\nu$ decays are discussed. In the last part of this Section the result of a study on the interference between QCD and electroweak sub-processes in the TauSpinner algorithm is presented. For the numerical results discussed here, long series (about 10^6) of Drell-Yan events of $pp \to \tau\tau + jj$ process generated with MadGraph5 package [51] were used. Table 3.2, gives the average τ lepton polarization obtained with different EW schemes used for spin weight calculations for $2 \to 2$ and $2 \to 4$ matrix elements with invariant mass of τ pairs between 88 and 92 GeV. Figure 3.2 shows the distribution of the visible energy fraction in the $\tau \to \pi\nu$ decays, $x_\pi = \frac{E_\pi}{E_\tau}$, an observable sensitive to τ polarization. One can clearly notice the impact of different EW schemes on the average polarization and sensitive observables.

	EWSH=1	EWSH=2	EWSH=3	EWSH=4
$2 \to 4$	-0.2048 ± 0.0015	-0.1385 ± 0.0015	-0.2014 ± 0.0015	-0.1331± 0.0015
$2 \to 2$	-0.2063 ±0.0015	-0.1407±0.0015	-0.2055 ±0.0015	-0.1412± 0.0015

TABLE 3.2: τ-lepton polarization in the invariant mass window of τ pairs between 88 and 92 GeV for different EW schemes [4]. Errors are statistical only.

In Table 3.3 and 3.4 the average τ lepton polarization with different QCD scale option and different PDF sets which is used for spin weight calculations for $2 \to 2$ and

2→ 4 matrix elements are shown, respectively. The variation of TauSpinner results with respect to different QCD scale option is 3.6% and 1.7% with respect to different PDF sets.

	scalePDFOpt=0	scalePDFOpt=1	scalePDFOpt=2	scalePDFOpt=3
$2\to4$	-0.1362 ± 0.0015	-0.1331 ± 0.0015	-0.1380 ± 0.0015	-0.1363 ± 0.0015
$2\to2$	-0.1368 ± 0.0015	-0.1412 ± 0.0015	-0.1377 ± 0.0015	-0.1378 ± 0.0015

TABLE 3.3: τ-lepton polarization in the invariant mass window of τ pairs between 88 and 92 GeV for different QCD scales [4], the errors are statistical only.

PDF sets	TauSpinner $2\to4$	TauSpinner $2\to2$
cteq6ll.LHpdf	-0.1331 ± 0.0015	-0.1412 ± 0.0015
MSTW2008nnlo90cl.LHgrid	-0.1354 ± 0.0015	-0.1379 ± 0.0015
CT10.LHgrid	-0.1338 ± 0.0016	-0.1368 ± 0.0016

TABLE 3.4: τ-lepton polarization in the invariant mass window of τ pairs between 88 and 92 GeV for different PDF sets [4], the errors are statistical only.

3.2.4 Interference between QCD and Electroweak subprocesses

For generating matrix element using MadGraph5, the calculation is preformed up to 4th order in the electroweak couplings. In the case of calculation to the second order of electroweak couplings, some of the diagrams which include QCD couplings are not present. However there can be a significant interference between those diagrams and EW diagrams. By default in the Standard Model, the square of matrix element is calculated from the Equation:

$$|ME|^2 = |\alpha_S\alpha_{EW}M_1 + \alpha_{EW}^2 M_2|^2 = |\alpha_S\alpha_{EW}M_1|^2 + |\alpha_{EW}^2 M_2|^2 + \alpha_{EW}^3\alpha_S(M_1M_2^* + M_1^*M_2) \tag{3.15}$$

where $\alpha_S\alpha_{EW}M_1$ is the component of matrix element related to processes with QCD couplings, while the $\alpha_{EW}^2 M_2$ related to processes with only electroweak couplings. Without QCD contribution, the first and last terms in Equation 3.15 will vanish. However if α_S is set to be large, one must check if the interference terms (last terms) have any effect on matrix element calculation. TauSpinner allows to calculate a weight which is a ratio of non-SM/SM cross-section. In order to estimate the effect of interference term, for non-SM we set α_{QCD} parameter (strong coupling constant) to be 0, α_s and $2\alpha_s$. For the SM, the nominal value α_s is used. In the case of α_{QCD}=0, only EW diagrams contribute, with $Z \to \tau\tau$ and $W \to q\bar{q}$ leading to $\tau\tau$ in the final state. It results in cross-section of the EW diagrams only in the ME calculation. In TauSpinner α_{QED} can not be set to zero, but as the α_S is much larger than α_{QED}, setting for non-SM option α_{QCD}= $2\alpha_S$ in calculation of matrix element strongly enhance contribution of QCD diagrams with respect to EW ones.

In presented test, two MadGraph samples of Z→ $\tau\tau j_1 j_2$ were used, the sample 1 has cut on invariant mass of τ leptons (30 GeV $< M_{\tau\tau} <$ 160 GeV) at the generation

level. The sample 2 has kinematical cuts both at generation and analysis level, which are shown in Table 3.5.

Selection at generation level for sample 1
30 GeV $< M_{\tau\tau} <$ 160 GeV
Selection at generation level for sample 2
$p_T(j_1)$+$p_T(j_2) > 50$ GeV
$p_T(\tau_1)$+ $p_T(\tau_2) > 30$ Gev
invariant mass of jets $M_{jj} > 120$ GeV
invariant mass of τs $M_{\tau\tau} > 120$ GeV
Selection at analysis level for sample 2
$p_T(j_1) > 30$ GeV or $p_T(j_2) > 30$ GeV
$\eta(j_1)$ -$\eta(j_2) > 3.0$
$p_T(\tau_1) > 25$ GeV or $p_T(\tau_2) > 25$ GeV
$p_T(\tau_1)$+ $p_T(\tau_2) > 35$ GeV
$\lvert\eta_{\tau_1}\rvert < 2.5$ or $\lvert\eta_{\tau_2}\rvert < 2.5$

TABLE 3.5: Kinematical selection for Z→ $\tau\tau j_1 j_2$ samples at generation and analysis level [4], p_T is the transverse momentum and η is Pseudorapidity.

One can quantify the interference term with simple math as following. In the SM case, α_{QCD}=α_S :

$\sigma^{tot} = \sigma^{QCD} + \sigma^{EW} + \sigma^I = |ME|^2 = |\alpha_{EW}(\alpha_S M_1 + \alpha_{EW} M_2)|^2 = |\alpha_S \alpha_{EW} M_1|^2 + |\alpha_{EW}^2 M_2|^2 + \alpha_{EW}^3 \alpha_S (M_1 M_2^* + M_1^* M_2)$.

For the non-SM case with enhance QCD diagrams, α_{QCD}=2α_S, the cross section is:

$|ME|^2 = 4\sigma^{QCD} + \sigma^{EW} + 2\sigma^I$.

For non-SM case with no QCD diagram, α_{QCD}=0, the cross section is:

$|ME|^2 = |\alpha_{EW}^2 M_2|^2 = \sigma^{EW}$.

The interference term σ^I can be expressed as the function of cross-sections, and its ratio to nominal cross-section:

$$\frac{\sigma^I}{\sigma^{tot}} = \frac{1}{2}[4 - 3\frac{\sigma^{QCD}_{\alpha=0}}{\sigma^{tot}} - \frac{\sigma^{QCD}_{2\alpha_S}}{\sigma_{tot}}]. \tag{3.16}$$

Obtained cross-sections for different α_{QCD} used for matrix element calculation and the fraction of interference term for two samples are presented in Table 3.6. The fraction of interference term for the sample 1 is around 1% and for the sample 2, is around 2%. In TauSpinner this effect is neglected.

Sample 1	σ(pb)	(σ^I/σ^{tot})
$\alpha^{QCD}=\alpha_s$	474581 $\pm$ 688	0.01
$\alpha^{QCD}=2\,\alpha_s$	1897110 $\pm$ 2753	0.02
$\alpha^{QCD}=0$	416 $\pm$ 7	0.0
Sample 2	σ(pb)	(σ^I/σ^{tot})
$\alpha^{QCD}=\alpha_s$	120602 $\pm$ 347	-0.02
$\alpha^{QCD}=2\,\alpha_s$	437487$\pm$ 1272	-0.04
$\alpha^{QCD}=0$	16461 $\pm$ 76	0.0

TABLE 3.6: The cross-section for different α_{QCD} used for matrix element calculation, and fraction of the interference term for two different samples [4].

3.3 Development of `TauSpinner` for non-SM processes with spin-2

Introducing non-standard states and couplings and studying their effects in the vector-boson-fusion processes and exploiting the spin correlations of τ lepton pair decay products can be useful in the search for new physics. This is why, a possibility to implement external matrix element for non-SM theories was introduced into `TauSpinner`.

In Section 3.2 an extended version of `TauSpinner` $2\to4$ [5] was presented which now includes hard processes featuring tree-level parton matrix elements for production of a τ lepton pair and two jets. The tool was prepared to be used for studying spin effects in processes of the Standard Model and searches of new physics like in Ref. [52, 53], and in experimental applications for the Standard Model measurements [54–58]. In this Section the application of the `TauSpinner` algorithm for physics model chosen by user is presented. A case study of non-SM spin-2 object coupled to SM particles have been taken. This work is documented in Ref. [5].

3.3.1 Physics model of $2\to4$ process with spin-2 object

A simplified model of a massive gauge singlet spin-2 object X coupled to the SM gauge bosons is considered. This model is used as a case study to show how to prepare and test external matrix element to be used by the `TauSpinner` algorithm.

Continuing the previous study [44] dedicated to Drell-Yan-like production of τ leptons through a hypothetical spin-2 object X, here we focus on the X production in the VBF topology $pp\to jjX$, followed by $X\to\tau^+\tau^-$ decay.

An extension of the Lagrangian of Ref. [44] by a set of gauge invariant dimension five operators, coupling the field X to gauge boson field strength tensors B, W and G is given as:

$$\mathcal{L}\ni\frac{1}{F}X_{\mu\nu}\left(g_{XBB}\,B^{\mu\rho}B_{\rho}{}^{\nu}+g_{XWW}W^{\mu\rho}W_{\rho}{}^{\nu}+g_{Xgg}G^{\mu\rho}G_{\rho}{}^{\nu}\right),\tag{3.17}$$

where group indices are implicitly summed over (where appropriate). For keeping the coupling constants dimensionless, the parameter F is introduced and set to 1 TeV.

The state X does not couple to the entire energy momentum tensor and couplings g_X are kept as free parameters. In this work the focus is on technical aspects of incorporating the couplings of X to the EW gauge bosons. Relevant diagram topologies

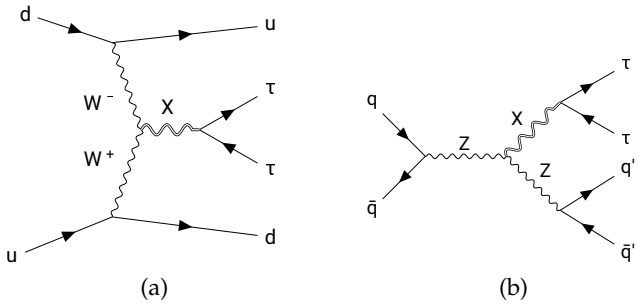

FIGURE 3.3: Topologies of Feynman diagrams for X production through its coupling to gauge bosons VBF process (a) and X-Strahlung process (b). Similar diagrams, with different combinations of $W^{\pm}$'s, Z's, photons and quark flavours also exist.

are shown in Figure 3.3: for the VBF process (a) and the X-strahlung process (b). The squared matrix elements of this model are generated by using MadGraph5, using the spin-2 support of the HELAS library [59]. This is done with the following set of commands:

(a) `import model spin2_w_CKM_UFO`

(b) by default, "multiparticles" containers already include all massless partons
```
p = g u c d s u~ c~ d~ s~
j = g u c d s u~ c~ d~ s~
```

(c) generate spin 2 matrix elements
```
generate p p > j j x QED<=99 QCD<=99 NPgg<=99 NPqq<=99 NPVV<=99, x >
ta+ ta-
```

(d) write the output to disk in MadGraph's standalone mode using
`output standalone "directory name"`

NPgg, NPqq and NPVV parameters control the maximum number of g_{Xgg}, $g_{Xq\bar{q}}$ and g_{XWW}, g_{XBB} couplings, respectively. Limiting them to 99 effectively means that their number is not restricted. The model includes the CKM matrix in the Wolfenstein parametrization. Note that, the matrix element, coded as an example for user, contains all of couplings.

3.3.2 Integrating example matrix-element code into TauSpinner

The matrix element code is based on automatically produced FORTRAN subroutines by MadGraph5[1] package, similarly as it was done for processes of the Standard Model [3]. In the spin-2 case they were also manually modified and adapted to avoid name clashes. Also, as a consequence of the fact that C++ user function for the spin-2 matrix element calls FORTRAN code created by MadGraph5, the `name space` functionality of C++ can not be used as a natural solution to this problem and therefore, some subroutine names changes were necessary.

The generated codes for the individual sub-processes are grouped together into subroutines, depending on the flavour of initial state partons, and named accordingly. For example, `SUBROUTINE DSX_S2(P,I3,I4,H1,H2,ANS)` encompasses the X production processes initiated by the $d\bar{s}$ partons. The previous convention [3] is

[1] version MG5_aMC_v2.4.3

used, where symbol X in the subroutine or internal function name after the letter U,D,S or C means that the corresponding parton is an antiquark, i.e. UXCX corresponds to processes initiated by $\bar{u}\bar{c}$ partons, while GUX to processes initiated[2] by $g\bar{u}$. The S2 stands explicitly for the production of spin-2 X state. The input variables are: real matrix P(0:3,6) for four-momenta of incoming and outgoing particles, integers I3,I4 for the Particle Data Group (PDG) [13] identifiers for final state parton flavours and integers H1,H2 for the outgoing τ helicity states. A number of modifications have been done, before integrating these subroutines into the TauSpinner program which is documented in Ref. [5].

3.3.3 Tests of implementation of external matrix elements

Once the user-provided external matrix elements are prepared, numerical tests are necessary to test proper implementation into the TauSpinner environment. A single event with fixed kinematic configuration at the parton level has been chosen, to check the consistency of the implemented codes generated with MadGraph5 and modified as explained in previous Section. For that event, the matrix elements squared were calculated for all possible helicity and parton flavour configurations, using the code implemented as user example. By comparison of results with the numerical values obtained directly from MadGraph5, the agreement on the level of at least 6 significant digits were confirmed.

Further tests of the internal consistency of external matrix element implementation have been explored by comparing a number of kinematic distributions obtained directly or reweighted with $wt_{prod}^{H\to X}$ which is the ratio of the matrix element used in the generation of the sample for process ($H \to \tau\tau$jj) to the matrix elements corresponding to a new physics model ($X \to \tau\tau$jj) [3]. Samples of 10^7 events generated by MadGraph5 for Higgs boson and X particle, for pp collisions at 13 TeV with CTEQ6L1 PDFs were used. The masses of both X particle and Higgs boson were set to 125 GeV and the width to 5.75 MeV.

Figure 3.4 shows the weight distributions for H sample reweighted to X (a) and for X sample reweighted to H (b). One can see that there is a constant slope on this double logarithmic plot with clear sharp upper end. With such spectrum of weights it may be possible statistically to have sensible calculation of the cross-sections. The large weights are correspond to subset of phase space where matrix element of X state has zero value. Therefore, they can not be removed by increasing the size of sample. Even though contribution of such events to the weighted distribution is formally finite and integrable, the error estimate of the MC generated distribution will not get reduced with the increasing statistical sample. The ratio of the matrix element with respect to the one of the original sample is too large in comparison to the typical event. Therefore, to eliminate excessive weight regions of phase space on the generated events the following selections were applied: invariant mass of outgoing particles $m_{jj\tau\tau} < 1500$ GeV, transverse momentum of τ leptons $p_T^{\tau\tau} < 600$ GeV and invariant mass of outgoing partons $m_{jj} < 800$ GeV (loose selection) In addition for eliminating $Z \to jj$ or $W \to jj$ resonance peaks $100 < m_{jj} < 800$ GeV (tight selection) cut was applied.

Several kinematical distributions were compared: pseudorapidity of outgoing parton j, rapidity of $\tau\tau$ and jj systems, invariant mass of $\tau\tau$ system, pseudorapidity of $\tau\tau$ system, opening angle between jets, opening angle between τ leptons, angle between incoming parton and outgoing parton in the rest frame of jets and angle

[2] X in this context should not be confused with the spin-2 field X.

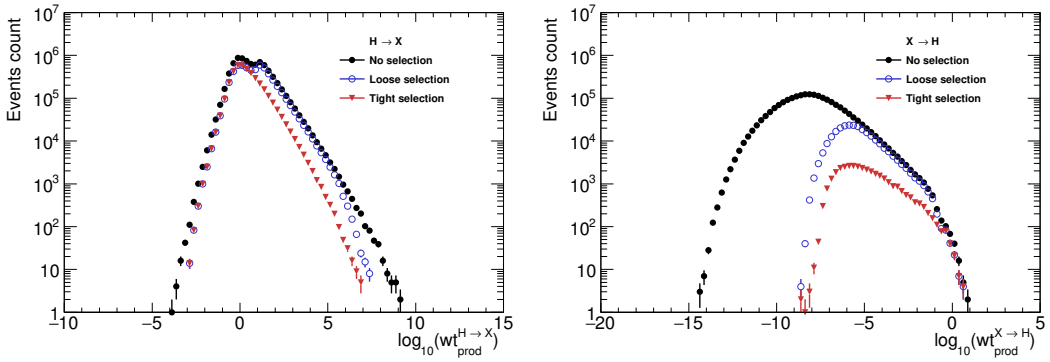

(a) (b)

FIGURE 3.4: Weight distribution for H sample reweighted to X (a) and for the X sample reweighted to H (b) [5]. The black points correspond to sample without selection, the red triangles correspond to sample with loose selection and blue circles correspond to sample with tight selection.

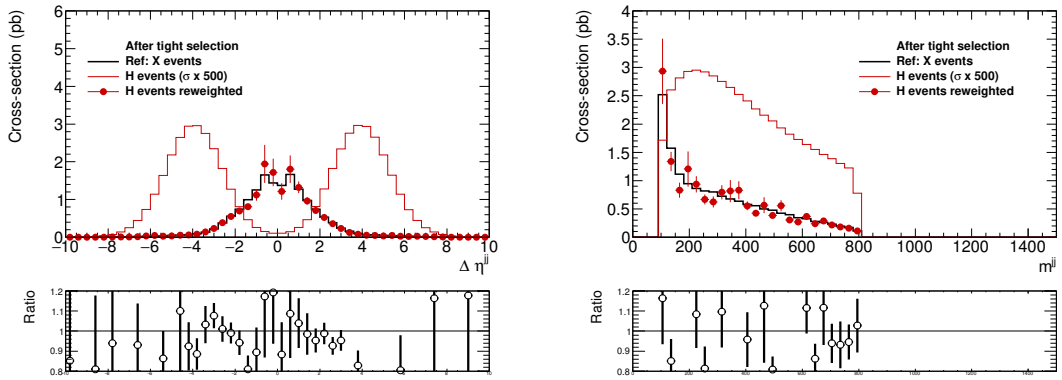

(a) (b)

FIGURE 3.5: The H sample reweighted to the X and compared with the X sample for the difference of jets rapidities $\Delta\eta^{jj}$ (a) and the invariant mass of the jet pair m_{jj} (b) [5]. The distribution `Ref`, for the reference process, is shown as a black histogram while the red histogram is the original distribution of generated events which is reweighted using `TauSpinner` weight to red filled circles. The tight selection was used.

between resonance and outgoing parton in the rest frame of jets. For all these variables, plots can be found in Appendix A. Here, in Figure 3.5 and Figure 3.6, we show only plots for difference of jet's rapidities $\Delta\eta^{jj}$ and invariant mass of the jet pair, m_{jj}. In each plot the distribution `Ref`, for the reference process, is shown as a black histogram while the red histogram is the original distribution of generated events which is reweighted using `TauSpinner` weight to obtain the distribution represented by the red points with error bars. For the test to be successful, the red points should follow the black histogram; the ratio of `Ref` and reweighted distributions is shown in the bottom panel of each Figure.

The reweighted distributions follow the reference histograms, `Ref`, in both Figure 3.5 and 3.6. For reweighting of X to H (see Figure 3.6), the distributions show

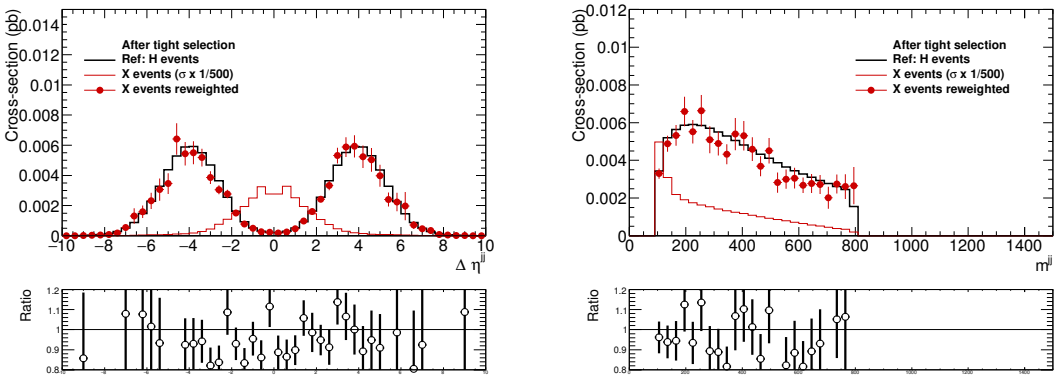

(a) (b)

FIGURE 3.6: The X sample reweighted to the H and compared with the H sample for the difference of jets rapidities $\Delta\eta^{jj}$ (a) and the invariant mass of the jet pair m_{jj} (b) [5]. The distribution `Ref`, for the reference process, is shown as a black histogram while the red histogram is the original distribution of generated events which is reweighted using `TauSpinner` weight to red filled circles. The tight selection was used.

larger statistical errors than in the case of H to X reweighting (Figure 3.5). This is because tight selection cuts leave only 1.7% of X events due to eliminating configurations with small m_{jj}. The tests validating reweighting algorithm were complemented with the ones monitoring overall normalizations (integrated cross-sections).

3.3.4 Spin dependent characteristics

In the previous Sections we were discussing observables relying on the kinematics of final states consisting of four momenta of τ leptons and accompanying two jets. If we include the τ decay products, the phase space dimensionality will increase substantially, making the analysis much more difficult, especially when dependence on selection cuts is taken into account. In this Section, a few spin dependent results obtained for the H and X samples with the tight selection cuts is presented. By using `TAUOLA++` [60] these samples are supplemented with τ decays in the mode $\tau \to \pi\nu$ only with no spin effects included. With the help of `TauSpinner` weights, the spin effects calculated according to the production and decay kinematics are introduced [48, 61]. The spin weight histograms for the H and X samples in Figure 3.7 shows the comparison of spin weights calculated using the matrix element for X productions as described in Ref. [44], that is featuring effective born level $2 \to 2$ kinematic (open red circles), and using new way in which amplitudes featuring two jet kinematics are taken into account (blue full circle points). The same $X - \tau\tau$ couplings were used in both cases. As expected (see Equation 3.13), for the $2 \to 2$ case the range of spin weights is limited to $[0, 2]$ since in this process there are no couplings which could lead to individual τ polarization. In the $2 \to 4$ case the spin weight distribution shows a tail which extends beyond 2 and covers most of the allowed $[0, 4]$ range. One of the reasons can be the presence of the sub-process $W^+W^- \to X \to \tau^+\tau^-$ in which W's are polarized and can has impact on τ polarization. Although the tail above 2, is not so much pronounced, it will manifest itself in the distribution of τ decay products.

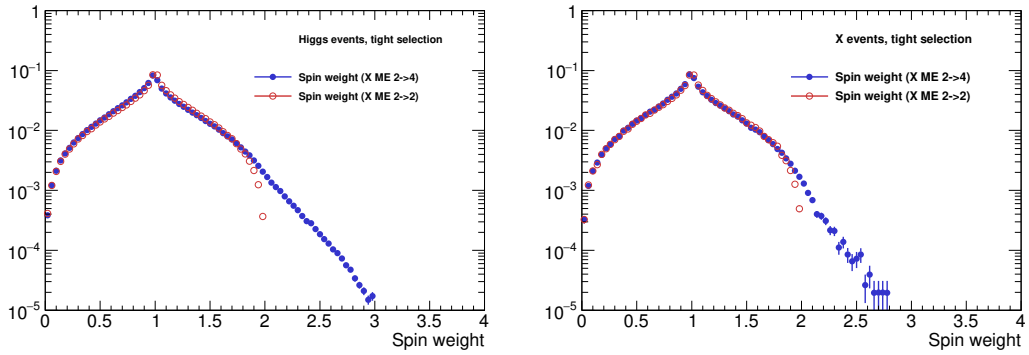

(a) (b)

FIGURE 3.7: Spin weight distributions, normalized to unity, obtained from X matrix elements for H sample (a) and X sample (b) the red circles correspond to $2\to 2$ matrix element and the blue circles correspond to $2\to 4$ matrix element. The tight selection was used.

The τ polarization can originate from the X production via VBF process, which is asymmetric over the phase-space regions. To show the polarization effects we have to sort out events according to the τ polarization; otherwise the effects will average out. In the proton there are more u-type quarks than d-type, therefore, the X particle produced in the VBF preferentially will follow the direction of W^+ which is right-handed and imparts its polarization on X bosons. One can expect that τ lepton from X decay will have polarization dependent on its direction with respect to the X flight direction. Thus it is suggested to sort events according to positive and negative value of $C = Y_X \cdot (p_z^{\tau^-} - p_z^{\tau^+})$, where Y_X is the τ lepton pair rapidity and $p_z^{\tau^-}$, $p_z^{\tau^+}$ are the z components of $\tau^\pm$ four-momenta. Distributions of $E_{\pi^\pm}/E_{\tau^\pm}$ (x_π) after applying tight selection for positive and negative C are plotted in Figure 3.8 . We observe that spin weights, calculated with the X production amplitude, when applied to the H sample lead to a larger spin effect, than when applied to the X sample. In the second case the spin effect is barely visible. The results indicates that even within tight selection there is a sizable difference between events of X and H production, which is reflected in τ polarization effects greater for the H sample than for X sample, even though the same $pp \to \tau\tau jj$ matrix elements featuring intermediate X are used in both cases.

The reason might be that such small spin effect present in Figure 3.8 for the X case is a consequence of substantial contribution from other than VBF channel in our samples, therefore, our cuts may need to be refined. However, because of the weight distribution, as seen in Figure 3.7 (b), such a refinement is unlikely to be found within our tight selection, since the tail of events with spin weight exceeding 2 is very small. Nonetheless τ polarization may offer help in exclusion of X hypothesis, even in the case when $X\tau\tau$ couplings are insensitive to parity.

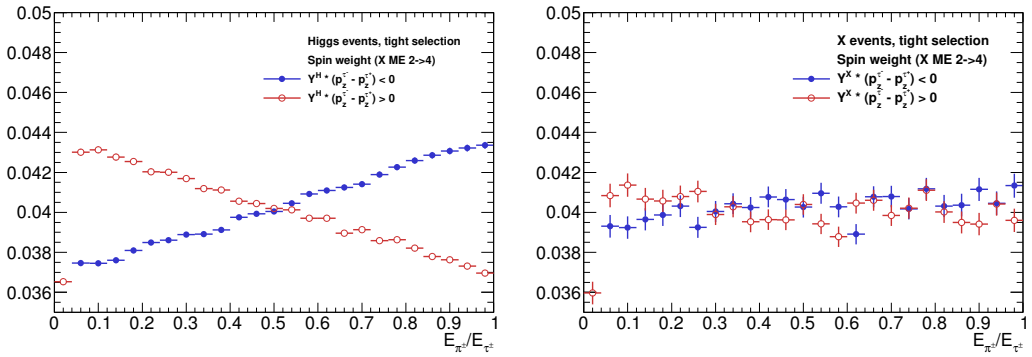

(a) (b)

FIGURE 3.8: Distributions of $E_{\pi^\pm}/E_{\tau^\pm} = x_\pi$ spectra, normalized to unity, for the H sample (a) and for the X sample (b) after applying tight selection. In all cases $2 \to 4$ matrix elements of X exchange are used to implement spin effects. Red open circle points correspond to additional cut $Y_X \cdot (p_Z^{\tau^-} - p_Z^{\tau^+}) > 0$ and the blue, full circle points to $Y_X \cdot (p_Z^{\tau^-} - p_Z^{\tau^+}) < 0$.

3.4 Application of `TauSpinnerTool` in ATLAS

In this Section, `TauSpinnerTool` [61], an ATLAS specific interface to the `TauSpinner` library is used for validation of τ polarization in different Monte Carlo samples.

The following MC data sets containing Z+jets events with $Z \to \tau\tau$ decay were used:

- An inclusive sample generated using `Powheg & Pythia8` [62, 63]. The CT10 PDF set is used in the matrix element while the A14 set of tuned parameters [64] is used together with the NNPDF2.3LO PDF set [65] for the modeling of the nonperturbative effects. The total number of generated events is 20×10^6.
- Events containing W or Z bosons with associated jets are simulated using the `Sherpa2.2.0` [66] event generator. Matrix elements are calculated for up to 2 partons at NLO and 4 partons at LO using Comix [67] and OpenLoops [68] and merged with the Sherpa parton shower [69] according to the $ME + PS@NLO$ prescription [70]. The CT10nlo PDF set is used in conjunction with dedicated parton shower tuning developed by the Sherpa authors. These sample were split into non overlapping streams containing b-, c- and light-quarks and various Z boson transverse momenta. The total number of generated events was 12×10^6.

The samples were unpolarized with use of the spin weight, wt_{spin}, obtained from `TauSpinner`. If the generated sample has proper polarization after applying weight=$1/wt_{spin}$, the distribution of x_π should become flat. In Figure 13, x_π distributions for `Sherpa2.2` and `Powheg & Pythia8` are shown with overlapped unpolarized distributions obtained by applying `TauSpinner` weight. One can see that the reweighted distribution are not flat. Distribution of x_π with and without reweighting were fitted with the semi-analytic formula [46]:

$$1 + P_\tau(2x - 1) \tag{3.18}$$

where P_τ is τ polarization and x is x_π. The result of fitted P_τ values are presented in Table 3.7.

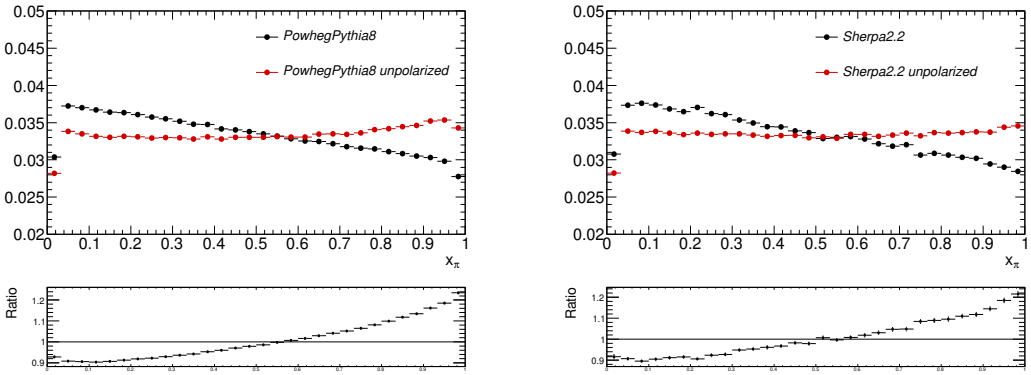

(a) (b)

FIGURE 3.9: x_π distribution with red circles are before and with black circles after reweighting with `TauSpinner` for `Powheg & Pythia8` (a) and `Sherpa2.2` (b) samples.

MC generators	x_π	x_π unpolarized
`Sherpa2.2`	-0.144 $\pm$0.003	0.002 $\pm$ 0.003
`Powheg & Pythia8`	-0.121$\pm$ 0.001	0.027$\pm$ 0.001

TABLE 3.7: P_τ from fitting x_π and x_π unpolarized distributions

The polarization value of about -12 % obtained with `Powheg & Pythia8` sample is not in agreement with the expected value -14.5 %$\pm$ 0.3 from LEP experiments [38]. Also the unpolarized distribution after reweighting by `TauSpinner` still has 2% polarization. Thus, one can conclude that polarization is not exact in samples generated by `Powheg & Pythia8`. Additionally, the spin correlation of τ pairs decaying to $\pi^\pm\nu$ final state are presented in two dimensional plots of x_{π^-} versus x_{π^+} variable in Figures 3.10 and 3.11. One can see that the spin correlation after reweighting has been removed.

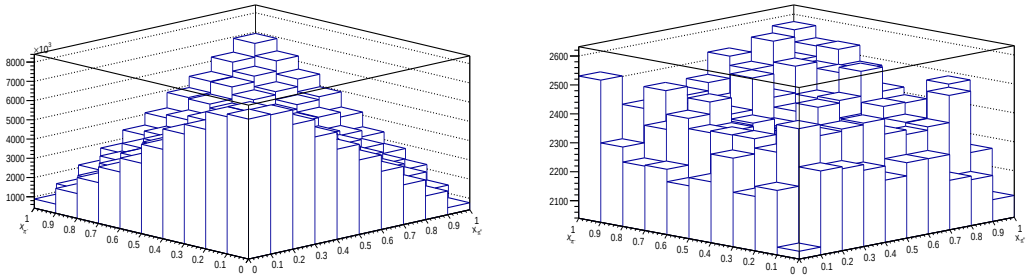

(a) (b)

FIGURE 3.10: Distribution of x_π^+ versus x_π^- before (a) and after (b) reweighing for `Powheg & Pythia8`.

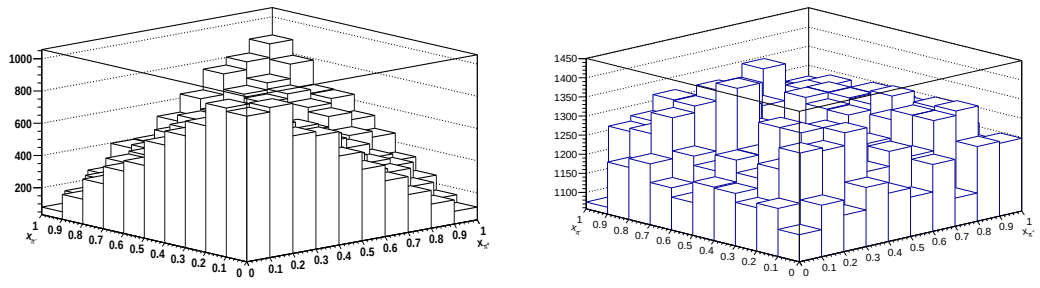

(a) (b)

FIGURE 3.11: Distribution of x_{π}^{+} versus x_{π}^{-} before (a) and after (b) reweighing for `Sherpa 2.2`.

3.5 Summary

In this Chapter, the `TauSpinner` algorithm for manipulation of spin effects in MC samples where τ lepton is present in the final state and in particular the development of the algorithm for production of $\tau\tau jj$ final states for non-SM model has been described. Detailed theoretical basics and the systematic uncertainties on the average τ lepton polarization and other sensitive variables for different input parameters (QCD scale option and different PDF sets) have been discussed. The effect of interference term between QCD and electroweak sub-processes for matrix elements calculation has been estimated and it shows a negligible effect. In the second part of this Chapter, the complete algorithm of the development of `TauSpinner` has been presented. The main purpose of this part was to demonstrate how the new (with respect to the ones used for sample generation) matrix elements for the production of τ lepton pair accompanied with two jets in pp collisions can be used in `TauSpinner` environment to reweight events. For that purpose, the new physics matrix element for spin-2 X particle was implemented as a user example. The numerical tests of the algorithm, demonstrating that starting from the $H \to \tau\tau jj$ sample (or $X \to \tau\tau jj$ sample), the other one can be obtained by applying event-by-event weight calculated from the implemented matrix elements were preformed. Finally, the validation of `TauSpinnerTool` on samples obtained from various MC generators, used by ATLAS collaboration for τ polarization validation has been discussed as one of the applications of this program.

Chapter 4

The experimental setup

4.1 The Large Hadron Collider

The Large Hadron Collider is the world's largest and most powerful particle accelerator. It first started up on 10 September 2008, and remains the latest addition to CERN's accelerator complex. The LHC consists of a 27 km ring equipped with superconducting magnets and a number of accelerating structures to boost the energy of the particles along the way. It is designed to collide proton beams at a maximum center-of-mass energy of 14 TeV with the nominal instantaneous luminosity of $10^{34}\,\mathrm{cm}^{-2}\mathrm{s}^{-1}$. Additionally, ion beams can also accelerated by the LHC at energies up to 2.8 TeV per nucleon and the maximum instantaneous luminosity of $\approx 10^{27}\mathrm{cm}^{-2}\mathrm{s}^{-1}$. The tunnel is composed of eight straight sections and eight arcs and lies between 45 m and 170 m below the surface on a geological plane inclined at 1.4% towards the Leman lake. The LHC beams collide in four interaction points (IP) around the accelerator ring providing data for two large experiments searching for general new high energy phenomena, **ATLAS** and **CMS** [2], and two other large detectors which test more specific physics: **LHCb** [71] to study heavy flavour; and **ALICE** [72] to investigate quarks and gluons behavior at temperatures five times hotter than the sun core (quark-gluon plasma). Three smaller experiments are installed at the LHC:

- The **TOTEM** experiment [73] is dedicated to measuring precisely the total pp interaction cross-section as well as diffractive proton-proton physics. It is placed on both sides of the CMS interaction point.
- The **LHCf** experiment [74] devoted to studying large energy cosmic-rays physics. Particles emitted in the forward region of the proton beam are used to simulate such cosmic particles. It is placed on both sides of the ATLAS interaction point, 140 meters away.
- The **MoEDAL** experiment [75] is devoted to the search for significant signals of magnetic monopoles.

The positioning of the major experiments on the LHC ring is shown in Figure 4.1.

Protons are created from ionized hydrogen atoms, then they are accelerated by a series of accelerators that progressively increase their energy, starting by the **LINAC** which is a linear accelerator and rises the energy of beam up to 50 MeV, then the protons are accelerated in three further steps by the circular pre-accelerators to 1 GeV(**PSB**), 26 GeV (**PS**) and 450 GeV (**SPS**), respectively. The minimum energy of the beam for LHC in order to maintain a stable beam is 450 GeV. At the nominal conditions, protons are arranged into bunches of 1.15×10^{11} particles. These bunches are organized in several "bunch trains". The spacing between bunches within a bunch

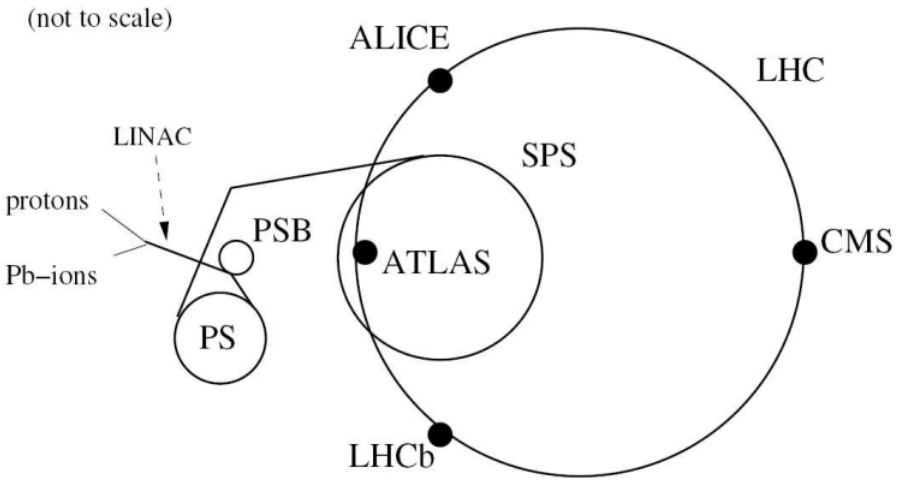

FIGURE 4.1: LHC layout with the positioning of the four experiments and the structure of the SPS+LHC acceleration system.

train is approximately 25 ns at the design conditions, while bunch trains are further apart. The minimum distance between bunches is about 7 m, which for a 27 km tunnel gives approximately 3550 bunches. However the effective number of bunches is 2808 in order to leave room for beam injection and abort procedure.

After protons are organized into bunches the **SPS** injects them into the LHC, both in clockwise and counter-clockwise directions. Once beams are accelerated to the desired energy, stable beams are declared and the LHC experiments can start taking physics data. The intensity of beams decreases with time due to loss of protons through collisions or through other effects influencing the trajectories of individual protons in the ring. It results in an expected beam lifetime of approximately 10 hours at the design conditions. When the intensity of the beam is too low, it is "dumped" or directed out of the accelerator into a large metal block where it is absorbed. The dipole magnets are then ramped down to 0.54 T and they stay at flat bottom for some 20-40 minutes. Meanwhile beam injection is repeated before the magnets are ramped up again to 8.3 T for another cycle of high energy collisions. This beam cycle is called a "fill". The machine is designed to withstand some 20,000 such cycles in a 20 years lifetime.

4.1.1 Luminosity

In most LHC searches, the production of large statistics data is primordial to have a chance of observing very rare new physics processes. The performance of the accelerator is characterized by the energy at which particles are accelerated and also by the number of collisions that it provides per unit of time. During Run II (years 2015-2018), the LHC is operating at the center of mass energy of 13 TeV. For each interaction point, the number of events for a given process, $N_{process}$, is:

$$\frac{dN_{process}}{dt} = L\sigma_{process} \tag{4.1}$$

where σ_{process} is the process cross-section which represents the probability that such process occurs, and L is the instantaneous luminosity delivered by the LHC, presented as inverse cross-section unites, e.g. $\text{cm}^{-2}\text{s}^{-1}$. The luminosity is a parameter that depends on the features of the accelerator, and determines the rate of collisions.

The total amount of data from pp collisions delivered by the LHC and recorded by the ATLAS experiment during the Run II at 13 TeV center-of-mass energy during stable beams is 158 fb^{-1}, is presented in Figure 4.2. The delivered luminosity is the luminosity evaluated before any trigger decision, which the accelerator delivered to certain experiment. The recorded luminosity is the actual data recorded on disk accounting for the data acquisition system dead time and operational problems data taking efficiency. The good for physics luminosity corresponds to data passed the criteria which require all reconstructed physics objects to be of good data quality. Precise measurement of the luminosity is an essential task, since the uncertainty on the delivered luminosity influences precision of the physics processes cross-section determination.

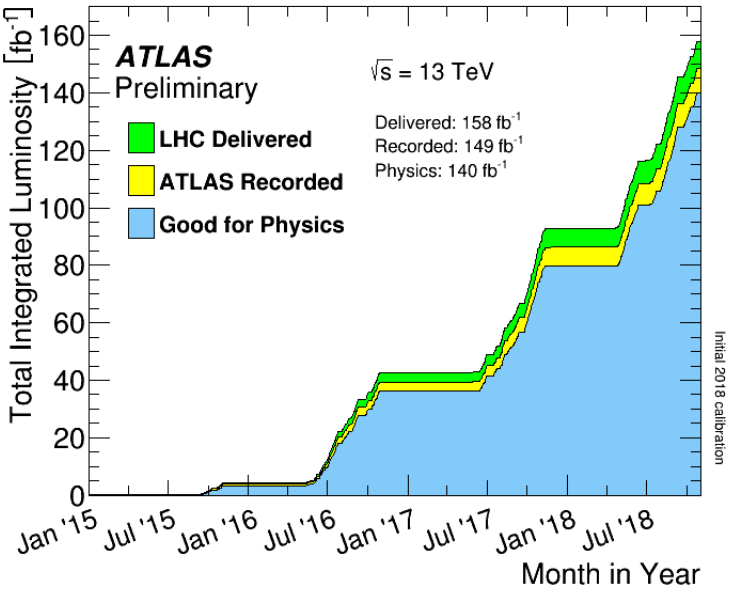

FIGURE 4.2: Integrated luminosity from pp collisions at $\sqrt{s}$= 13 TeV during stable beams entire Run II. The total integrated luminosity delivered by the LHC is shown in green, the amount of data recorded by ATLAS is shown in yellow and the subset that is used for physics analyses is shown in blue [76].

The larger the instantaneous luminosity, the larger the number of pp collisions. However, this increase in luminosity implies that multiple interactions pp collisions may occur inside the same bunch crossing. These interactions, overlap with products of other interactions, either issued from collisions in the same bunch crossing (in-time) or from interactions between remnants of previous bunch crossings (out-of-time). These multiple interactions are referred to as pileup and described by the number of pp interactions per bunch crossing, μ. For stable data taking conditions μ has a Poisson distribution and is conveniently described by the average number of interactions per bunch crossing ($< \mu >$). Figure 4.3 presents the distribution of the $< \mu >$ value during Run II data taking.

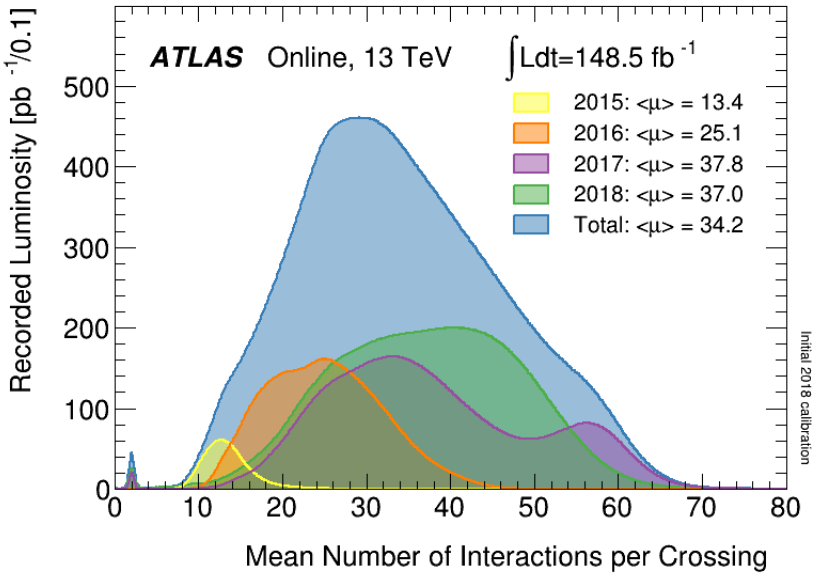

FIGURE 4.3: The luminosity-weighted distribution of the mean number of interactions per crossing for Run II data taking pp collision data at 13 TeV center-of-mass energy [76].

4.2 ATLAS detector

ATLAS (**A** **T**oroidal **L**HC **A**pparatu**S**) is one of the experiments located in the LHC ring. It was designed to study the Standard Model physics, and to search for any hint of physics Beyond Standard Model in the new high energy regime allowed by the LHC. ATLAS detector is composed of several subsystems as shown in Figure 4.4.

ATLAS coordinate system

ATLAS uses a right-handed coordinate system with the origin at the nominal interaction point (IP), in the center of the detector. The z-axis is defined along the beam direction while the transverse plane is defined by the x-axis pointing from the nominal IP to the center of the LHC ring and the y-axis pointing upwards. Usually, particle direction is defined in polar coordinates (r,ϕ,θ), where r is the distance between the particle and the IP, ϕ is the azimuthal angle in the transverse plane around the beam pipe and θ is the polar angle with respect to the z-axis. This is defined in terms of the polar angle as $\eta = -\ln[\tan(\theta/2)]$. The rapidity is defined as $y = 0.5\times \ln[(E+p_z)/(E-p_z)]$, where E denotes the energy and p_z is the z component of the momentum. For massless or ultra-relativistic objects, the rapidity and pseudorapidity are equal. The variable ϕ and η define the pseudorapidity-azimuthal angle space ($\eta-\phi$) and parameterize the different directions in which particles are emitted/detected with respect to the IP. In this space the distance is defined as $\Delta R = \sqrt{(\Delta\eta)^2+(\Delta\phi)^2}$. The pseudorapidity also helps in the description of the general features of the detector. In the following, the central detector region (generally up to $|\eta| < 1.6$) is referred to as barrel, the more forward region (up to $|\eta| < 2.5$ unless otherwise noted) as end-cap and the forward-most pseudorapidities are simply called forward region.

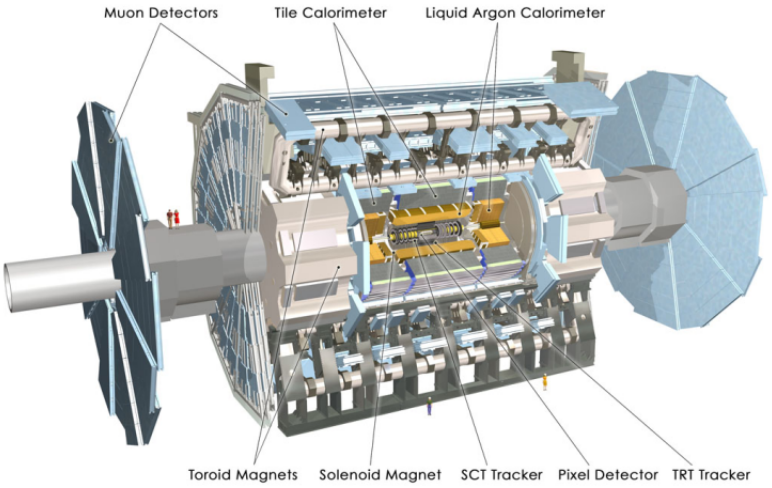

FIGURE 4.4: Schematic of the ATLAS detectors and the different sub-detectors [1].

In a collision the overall boost along the z-axis is not known since the partons that give rise to a given process carry an unknown fraction of the proton momentum. This is why mostly boost-invariant quantities are used in most analyses. Differences in pseudorapidity and rapidity are invariant under boosts along the z axis, as well as the transverse momentum (p_T, projection of the particle momentum on the $x-y$ plane).

4.2.1 ATLAS subsystems

The ATLAS detector consists of many sub-detectors as shown in Figure 4.4. From the innermost layer, it consists of the inner detector (ID), the tracking system. The main components of the Inner Detector are: Pixel Detector, SemiConductor Tracker (SCT) and Transition Radiotor Tracker (TRT). It provides precise reconstruction of charged-particle trajectories and of decay vertices of long-lived particles. Together with the magnetic field from the surrounding solenoid, it allows the measurement of the momenta of the different charged particles produced by the pp collisions. It also allows to discriminate electrons from charged hadrons thanks to the transition radiation tracker measurements.

Next layer is lead/liquid-argon (LAr) electromagnetic sampling calorimeter which measures the energy and the position of electromagnetic showers (electrons and photons) in the end-cap and forward regions. After electromagnetic calorimeter a steel/scintillator-tile calorimeter is placed which measures hadronic showers in the central region. The ATLAS detector provides discriminant detection power and identification between electrons, photons, muons and products from hadronic processes, leaving wide signals in the different detector subsystems called jets. Figure 4.5 illustrates the typical interaction that each of these particles has in the subsequent ATLAS sub-detectors. The combination of all signals allow an identification of the various particles together with an estimation of their energy and direction.

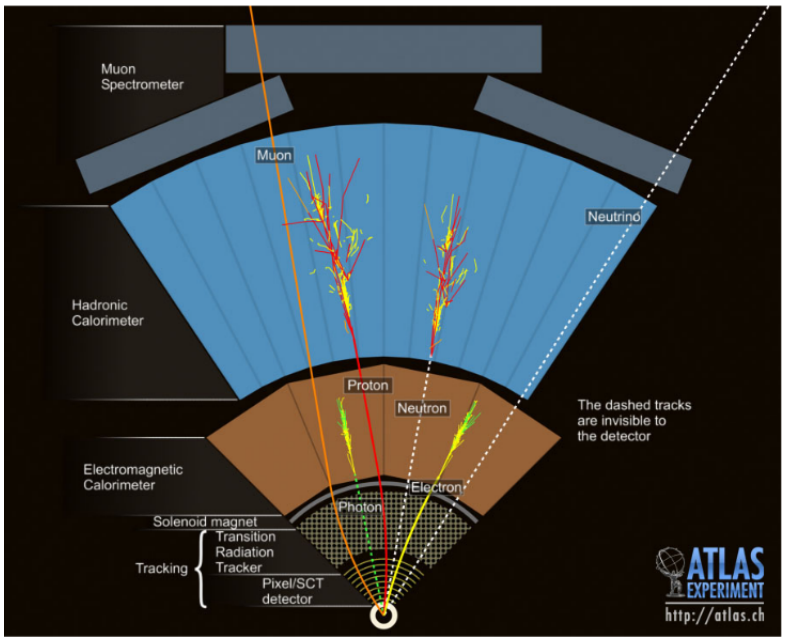

FIGURE 4.5: The illustration of energy deposits expected for each measured particle (particle detection in the subsystems) in the ATLAS detector [1].

4.2.2 Magnet system

The magnet system of ATLAS as shown in Figure 4.6 is composed of a central solenoid, providing magnetic field to the inner tracking system, and a toroidal system providing magnetic field to the muon spectrometer. The total size of the system is 22 m in diameter and 26 m in length.

Solenoid magnet system

The solenoid system is composed of a single central barrel surrounding the inner detector and providing 2 T axial field at a nominal operational current of 7730 kA.

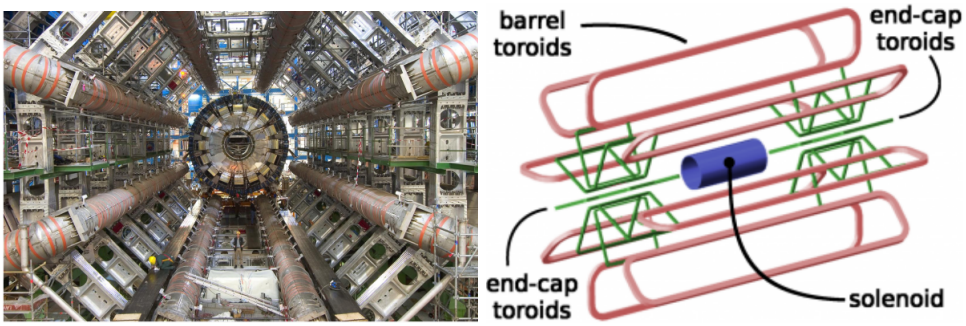

(a) (b)

FIGURE 4.6: Illustration of the magnet system layout (b), and photograph of the final installation of the ATLAS detector (a), where barrel toroids may be observed in the foreground [1].

To improve object measurements and reduce the rate of interactions upstream the calorimeter, the solenoid layout was optimized to keep the material thickness as low as possible. It consists of a single superconductive coal layer wrapped internally around a support cylinder. The inner and outer diameters of the solenoid are 2.46 m and 2.56 m, and its axial length is 5.8 m.

Toroidal magnet system

The toroidal system consists of a barrel and two end-caps providing a magnetic field to the muon spectrometer in the central region and the end-caps of approximately 0.5 and 1 T, respectively. The barrel toroid consists of eight coils encased in individual race track-shapped vacuum vessels made of stainless-steel which are distributed symmetrically around the calorimeter. The muon spectrometer is installed in the core and around these vessels. The end-cap toroids are also composed of eight coils placed at both ends of the toroidal barrel and aligned with the central solenoid. Coils are distributed radially and symmetrically around the beam axis and they are rotated by 22.5° with respect to the barrel coils in order to provide radial overlap and to optimize the bending power at the interface. The end-cap muon spectrometer is placed upstream each end-cap toroid.

4.2.3 Inner detector

The inner detector is the ATLAS sub-detector closest to the beam axis, where the density of particles is the largest, therefore high granularity and good radiation tolerance are its important requirements. The purpose of the ID is to reconstruct the trajectories of charged particles and traversing it to identify vertices and measure the momenta of charged particles. The ID achieves high precision measurements using three independent sub-detectors and an insertable layer distributed around the beamline under 2 T magnetic field as shown in Figure 4.7 [77].

These layers are ordered from the innermost to the outermost as:

- **Insertable B layer (IBL)**: The IBL [79] is an additional innermost pixel layer that has been built around the beam pipe and then inserted in the core of the ATLAS detector. The reason of introducing it, was because of enchantment of luminosity in Run II, which could provoke significant radiation damage to the inner layers of detector. The ATLAS detector could loose tracking efficiency, especially in tagging the decay of the beauty quark. Therefore this layer was build so that it can easily replace the missing information from pixel detector layers. It consists of 14 carbon fibers staves each 64 cm long and 2 cm wide surrounding the beam-pipe with the radius of 3.3 cm from the beamline and it covers $|\eta| < 3$. Each stave is equipped with 32 front-end chips FE-14, bump bonded to 26880 pixel cells of 50 μm $\times$ 250 μm which is ordered in 80 columns and 336 rows.

- **Pixel detector**: The pixel detector is designed to provide a very high-granularity and high-precision set of measurements as close to the interaction point as possible. It covers the full ID pseudorapidity range ($|\eta| < 2.5$) and consists of three barrels of pixel sensors at a radius of $\sim$ 5.05 cm, 8.85 cm and 12.25 cm and three end-cap disks placed between at 49.9 cm, 55.4 cm and 79.9 cm from the interaction point. All disks are identical, with an inner radius of 11.5 cm and an outer radius of 21.2 cm from the beamline. There are 1744 identical sensors for a total of 80.4 millions of pixels covering a total surface of 1.7 m^2. They

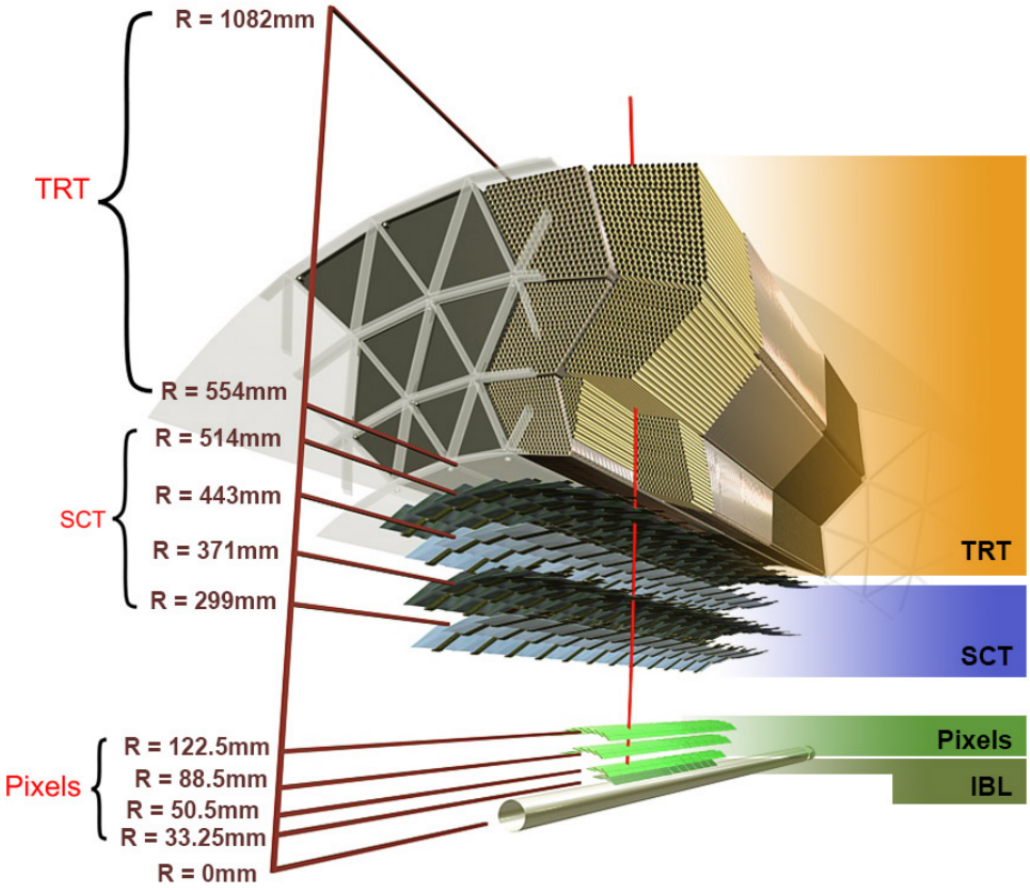

FIGURE 4.7: Illustration of the barrel region of the inner tracker showing the different sub-detector layers and structures traversed by a charged particle created in collision point during Run II [78].

provide 80 million channels used in the identification and reconstruction of secondary vertices from the decay of particles like hadrons containing b quark or τ leptons. Moreover, it provides excellent spatial resolution for reconstructing primary vertices coming from pp interaction region. The nominal pixel size is 50×400 μm^2 , allowing around 46080 readout channels per sensor.

- **Semiconductor tracker (SCT)**: The semiconductor tracker is located after the pixel detector. The SCT uses 15912 silicon strip sensors grouped into 4088 two-sided modules representing 63 m^2 with approximately 6.3 million readout channels (silicon strips). It is organized into a barrel with 4 coaxial cylindrical layers and two end-caps containing 9 disk layers. Barrel layers are located radially at 29.9 cm, 37.1 cm, 44.3 cm and 51.4 cm from the beamline, containing in total 2112 modules. The end-cap strips instead extend radially from 80 cm to 280 cm from the interaction point (z=0) grouped in 988 modules per end-cap. The design of such corresponding layout can realize that each charged particle crosses at least four layers, which leaves four space points anywhere in SCT's acceptance region.

- **Transition Radiation Tracker (TRT)**: This is the outermost subsystem of the ID. It is located between 0.554 m and 1.082 m from the beamline and comprises many layers of drift tubes with a diameter of 4 mm interleaved with

transition radiation material. Tubes are filled with a gas mixture of Xe, CO_2 and O_2. When a particle enters the TRT, it ionizes the gas inside the straws. In the center of each tube, there is a gold-plated tungsten wire of 31 μm diameter for readout [80]. The straw tubes of the TRT can provide a large number of hits normally 36 hits for each track. The TRT can only provide R -ϕ information, for which it achieves an intrinsic accuracy of 130 μm for each straw. The joint system of the precision trackers at small radii and the TRT at a larger radius provides robust pattern recognition and also high precision in both r-ϕ and z coordinates. The straw hits at the larger radius make significant contributions to the momentum measurement, due to the fact that the lower precision per point compared to the silicon can be compensated by the large number of measurements and longer measured track length. Particles passing through the tubes ionize the gas inside the tube, and the charged atoms and electrons are pulled apart by the electric field existing between the walls of the tube and the thin wire going through the center of the tube. The X-ray range transition radiation is emitted as a charged particle crosses a boundary between the media of differing dielectric constants, and can be subsequently absorbed by the gas in the straw tube. Since the transition radiation depends on the radiating particle Lorentz gamma factor, then typically it is the largest for electrons allowing their discrimination from other particles.

The spatial resolution of all subsystems of ATLAS inner detector are summerized in the Table 4.1.

Subdetector	Element size	Intrinsic resolution [μm]	Radius barrel layers [mm]
IBL	50 μm×250 μm	8×40	33.2
Pixel	50 μm×400 μm	10×115	50.5, 88.5, 122.5
SCT	80 μm	17	299, 371, 443, 514
TRT	4 mm	130	from 554 to1082

TABLE 4.1: Summary of the main characteristics of the ID subdetectors. The intrinsic resolution of the IBL and the Pixel is reported along r–ϕ and z, while for SCT and TRT is only along $r-\phi$. For SCT and TRT the element size refers to the spacing of the readout strips and the diameter of the straw tube, respectively.

4.2.4 Calorimetric system

The ATLAS calorimeters contain number of sampling calorimeter with full ϕ coverage around the beam axis as it is illustrated in Figure 4.8. They are divided into electromagnetic and hadronic part with the goal of performing precise measurements on the position and energy of electromagnetic and hadronic particles from pp collisions [1]. The energy resolution of a calorimeter can be parametrized as:

$$\frac{|\sigma(E)|}{E} = \frac{a}{\sqrt{E}} \oplus \frac{b}{E} \oplus c \tag{4.2}$$

where a is the stochastic term, b is the electronic noise term and c is the constant term that includes effects of detector instabilities and mis-calibration. The stochastic term takes into account the statistical fluctuations in the shower detection and it is small for homogeneous calorimeters and larger for sampling calorimeters, but its effect decreases with growing energy.

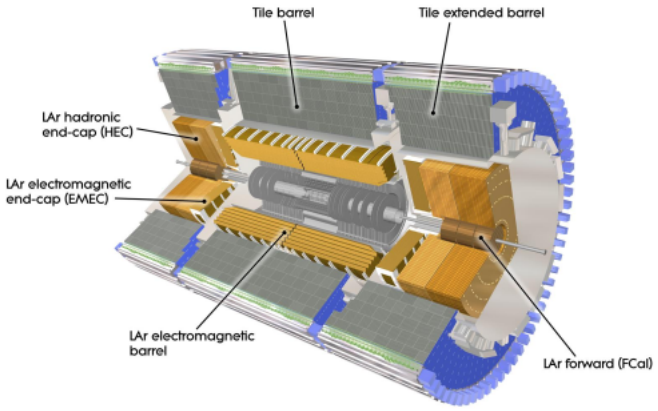

FIGURE 4.8: View of the ATLAS calorimeter geometry with the different sub-detectors [1].

- **Electromagnetic calorimeter**: is a lead/liquid argon sampling calorimeter as it shown in Figure 4.9, divided into a barrel ($|\eta|$ <1.475) and two end-caps (1.375 < $|\eta|$ < 3.2). The barrel (EMB) is divided into two half barrels with an interface at z=0. Each symmetrical half-barrel is divided into 16 modules covering each a $\Delta\phi = 2\pi/16$ region, each containing 64 absorbers interleaved with kapton-copper electrodes. The end-caps (EMEC) are two wheels located at each side of the barrel calorimeter. Each end-cap consists of two different wheels, an outer wheel covering the 1.375 < $|\eta|$ < 2.5 and an inner wheel covering 2.5 < $|\eta|$ <3.2. Absorbers and electrodes are shaped following an accordion structure. In the barrel, the accordion waves are axial and run in r and z. In the end-caps, the waves are parallel to the radial direction and run axially. Each end-cap wheel is further divided into 8 azimuthal modules. It is designed for the identification and measurement of photon and electron energy and position. They are placed in front of hadronic calorimeters, in part because particles that interact only electromagnetically require less material to be absorbed. Liquid argon was chosen as the active material due to its resistance to radiation and its uniformity, which translates into spatial uniformity in the energy measurement. Charged particles traversing the calorimeter ionize the LAr, and the resulting electrons drift towards the copper electrodes in the read out cells because of the presence of an electric field. The energy resolution is parametrized by $\sigma_E/E \sim 10\%/\sqrt{E} \oplus 170\ \text{MeV}/E \oplus 0.7\%$.

- **Hadronic calorimeter**: system is composed of four subsystems covering different ranges in η. A scintillating tile calorimeter covers the region in $|\eta| < 1.7$ and is divided into two central barrels (LB) and two extended barrels (EB). Scintillating tiles are ordered radially and normal to the beamline, interleaved with stainless-steel absorbers and fibres, which collect scintillation light from tiles. Fibres are connected to readout photomultiplier tubes (PMT's). The end-cap region of the hadronic calorimeter (HEC) is a sampling liquid argon calorimeter covering the range $1.5 < |\eta| < 3.2$. The HEC consists of two wheels, a front and a back wheel, each divided into 32 wedge-shaped modules. Front wheel modules are made of 24 copper plates, each 25 mm thick, plus a 12.5 mm thick front plate. In the rear wheels, modules are made of 16 copper plates, each

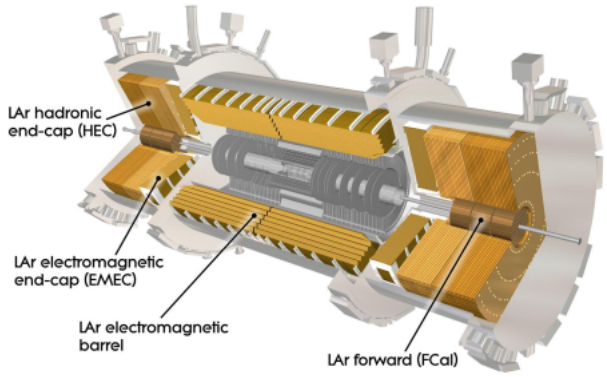

FIGURE 4.9: View of the liquid argon calorimeters, containing the electromagnetic calorimeter (on barrel and two end-caps) and the hadronic calorimeter end-caps (HEC) and forward calorimeters (FCal) [1].

50 mm thick, plus a 25 mm thick front plate. And finally, two liquid argon calorimeters are placed in the forward regions ($3.1 < |\eta| < 4.9$). They are located at 4.7 m of the interaction point and are segmented into three longitudinal deep modules: one electromagnetic module (FCal1) and two hadronic modules (FCal2 and FCal3). The FCal1 is made of copper rods parallel to the beamline arranged inside an outer tube with 250 μm liquid argon gap in between. These rods and tubes are inserted in a matrix of copper plates also made of copper. The FCal2 and FCal3 absorbers have the same structure as the FCal1, with the difference that tungsten rods are used in order to increase the radiation length to absorb the huge amount of radiation expected at these forward regions. The energy resolution obtained in test beams for single pions is $\sigma_E/E \sim 52.9\%/\sqrt{E} \oplus 5.7\%$.

The liquid argon calorimeter barrel and the end-caps (composed of the EMEC, HEC and FCal) are placed in separate cryostats, instrumented with a cooling system based on liquid nitrogen which ensures a nominal LAr temperature of 88.5 K.

4.2.5 Muon spectrometer

The ATLAS muon spectrometer (MS), shown in Figure 4.10, is the outermost part of the ATLAS detector. It detects mainly muons, since all other charged particles should be absorbed in the calorimeters. The MS uses the high precision tracking chambers to measure the muon tracks which are bent in the toroidal magnetic field. The measurement of the track curvature is used to determine the muon transverse momentum, from a few GeV up to the TeV, and charge of the muons. The MS is composed of three regions: the barrel, the end-cap and the transition region between the two aforementioned ones. The barrel toroid provides the magnetic field of about 1.5 to 5.5 T and covers the range of $0 < |\eta| < 1.4$, the end-cap region covers $1.6 < |\eta| < 2.7$ with the magnetic field of 1 to 7.5 T and the transition region covering the $1.4 < |\eta| < 1.6$ region where magnetic fields of both systems are used. In the barrel region three layers of muon chambers are used, whereas four wheels perpendicular to the beam axis are installed in the end-cap region. In most parts of

the MS the trajectories of the muons are measured by monitored drift tubes, which provide a spatial resolution of 35 μm per chamber. The one exception is the range of $2.0 < |\eta| < 2.7$ in the forward region, where the cathode strip-chambers are used in the innermost layer and provide a higher rate capability and better time resolution. The MS is also designed to trigger on muons with dedicated trigger chambers for particles in the range $|\eta| < 2.4$. In order to achieve a response time of a few nanoseconds, the resistive plate chambers are used in the barrel region and thin gap chambers in the end-cap regions.

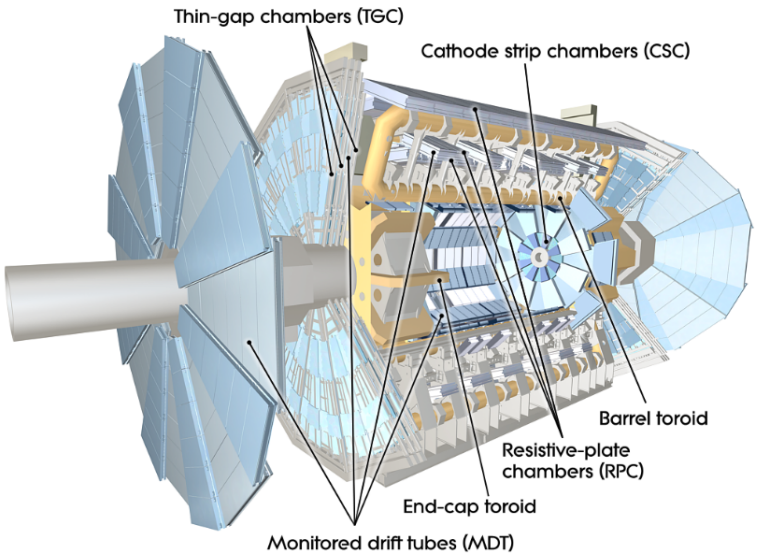

FIGURE 4.10: The ATLAS muon spectrometer with its different regions and the toroid system [1].

4.2.6 Trigger

The trigger system is a crucial component for the ATLAS experiment. It is designed to select interesting events created with very high rate in pp interactions at the LHC and to read out the detector information with minimal dead time due to hardware and software limitations [81]. The trigger system is composed of the hardware-based level-1 trigger (L1) and the software-based high- level trigger (HLT). The L1 trigger consists of the L1 calorimeter trigger system (L1Calo), the L1 muon trigger system (L1Muon) and L1 topological trigger modules (L1Topo). The L1Calo triggers on high-E_T objects coming from electrons, photons, jets and τ leptons, and events with large total E_T^{miss}. The L1Muon triggers on muons for each of the predefined p_T thresholds. The L1Topo combines information from L1Calo and/or L1Muon into topological variables, which are based on geometric properties of the event. The maximum L1 accept rate is 100 kHz. The L1 trigger defines also the Region-of-Interest (RoI), which determines the locations in η and ϕ where relevant features are identified. The L1 trigger decision and RoI are passed to the HLT trigger, where the event recording rate of around 1.5 kHz is achieved with the decision time of 200 ms. The HLT runs on computing cluster accessing data from the RoI, applying offline-like algorithms using the full event information. Events accepted by the HLT

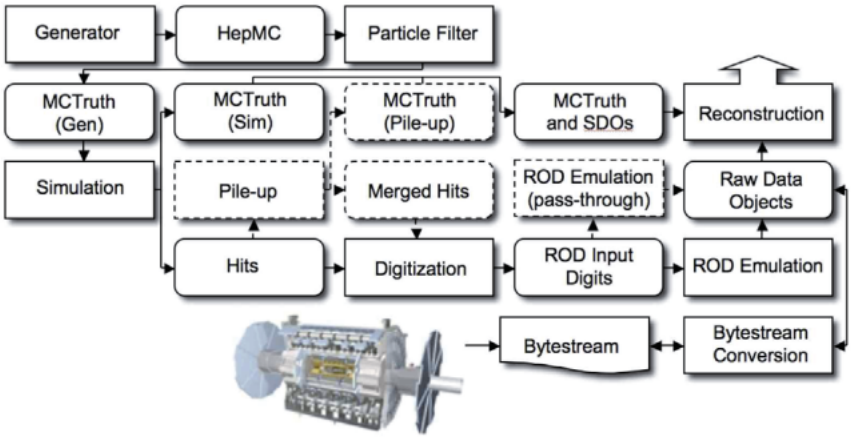

FIGURE 4.11: The flow of the ATLAS simulation software, from event generators (top left) through reconstruction (top right) [84].

are transferred to local storage at the experimental site and exported to the Tier-0 facility at CERN's computing center for offline reconstruction.

4.2.7 Detector simulation

The ATLAS detector simulation is performed by using the `Geant4` simulation toolkit [82, 83]. The simulation software chain is generally divided into three steps, as shown in Figure 4.11: generation of the events and immediate decays, simulation of the detector and physics interactions, and digitization of the energy deposited in the sensitive regions of the detector into voltages and currents for comparison to the readout of the ATLAS detector. The output of the simulation chain can be presented in either an object-based format or in a format identical to the output of the ATLAS data acquisition system (DAQ), which can then be run through the ATLAS trigger and reconstruction packages in the same way as the real data.

The ATLAS detector geometry used for simulation, digitization, and reconstruction is built from databases containing the information describing the physical construction and conditions data. The latter contains all the information needed to emulate a single data-taking run of the real detector, such as the detector misalignment or temperatures. With the same geometry and simulation infrastructure, it is able to reproduce the installation configurations of the ATLAS detector. These events can be filtered during the generation process so that only events with a certain property (e.g. leptonic decay or within a specific kinematics phase space) are kept. The generated events are then read into the simulation. A record of all particles produced by the generator is retained in the simulation output file, but cuts can be applied to select only certain particles to process in the simulation. Each particle is propagated through the full ATLAS detector by `Geant4`. It provides models for physics and infrastructure for particle transportation through a geometry in the `Geant4` format. In both event generation and detector simulation, information called "truth" is recorded for each event, which is a history of the interactions from the generator, including incoming and outgoing particles. A record is kept for every particle, whether the particle is to be passed through the detector simulation or not.

4.2.8 Data format in ATLAS

The output of the trigger (the Event Filter- final stage of the HLT) are the so-called RAW data organized into inclusive streams. Here, the term inclusive means that events can end up in one or more streams, depending on which triggers they pass. Then, after the physics objects reconstruction step Event Summary Data, ESD, are produced. Their reduced content, used in analyses is called Analysis Object Data, AOD. They contain physics objects and other elements of analysis interest. AODs are further brought under selection called derivation resulting in Derived Analysis Object Data, DAOD, to obtain events with the physical observables with appropriate features for further analysis but with reduced size.

4.3 Physics Objects Reconstruction and Identification

In this Section, the general procedures for reconstructed and identyfing the physics objects like electrons, jets, hadronically decaying τ leptons, muons, missing transverse energy used in the analysis presented in this thesis are described.

Electron

Electrons are reconstructed by matching clustered energy deposits in the electromagnetic calorimeter to tracks reconstructed in the inner detector [85, 86]. Electron candidates are required to meet quality requirements based on the shower shape, enclosed in the definition of a loose (tight) likelihood-based identification selection point. The transverse energy E_T is required to be greater than 20 GeV, and the pseudorapidity range is $|\eta| < 2.47$ (with $1.37 < |\eta| < 1.52$ excluded).

Muons

Muon candidates are required to contain matching inner detector and muon spectrometer tracks [87], as well as to have p_T >20 GeV and $|\eta| < 2.5$. Only muons that satisfy loose (tight) identification and isolation working points, are accepted.

In order to ensure that electrons or muons originate from primary vertex which is the vertex with the highest sum of p_T^2 of its associated tracks, the track associated with the lepton is reqiured to have a longitudinal impact parameter and transverse impact parameter significance that fulfil, respectively, $|z_0 \sin\theta| <$0.5 mm and $|d_0/\sigma(d_0)| < 5(3)$. In order to reduce contamination by leptons from hadron decays or photon conversion, isolation requirements are applied. The calorimeter-based isolation relies on energy deposits within a cone of size ΔR= 0.2 around the electron or muon, while the track-based isolation uses a variable cone size starting at ΔR= 0.2 for electrons or ΔR= 0.3 for muons, and then decreasing as p_T increases.

Jets

Jets are reconstructed from energy deposits in the calorimeters using the anti-k_t algorithm [88] implemented in the FastJet package [89] with a radius parameter value of R = 0.4. Jets are corrected for pile up energy and calibrated using energy- and η-dependent corrections [90]. Only jets with a transverse momentum $p_T > 25$ GeV and within $|\eta| < 2.5$ are considered in the following. A multivariate technique (jet vertex tagger) that allows identification and selection of jets originating from the hard-scatter interaction through the use of tracking and vertexing information is applied to jets with $p_T < 60$ GeV and $|\eta| < 2.4$ [91].

τ objects

A τ lepton decays as mentioned in Section 2.3 can decay hadronically and leptonically. The τ leptons considered in this analysis are identified through their hadronic decays, which are characterized by the presence of mostly one or three charged tracks, accompanied by a neutrino and possibly neutral pions. Although electrons and muons can mimic a hadronic τ decay, with just one charged hadron, the main source of background for $\tau_{\text{had-vis}}$ identification are quark- or gluon-initiated jets, because of their large production cross-section. The jets originated by $\tau_{\text{had-vis}}$, have a lower track multiplicity and a larger electromagnetic energy component since one or more π^0s are present in 60% of $\tau_{\text{had-vis}}$ decay. Unlike gluons and light quarks, τ leptons can decay relatively far from the interaction point, therefore have a track with an impact parameter which is incompatible with the primary or a displaced secondary vertex.

The ATLAS $\tau_{\text{had-vis}}$ algorithm is made of two steps [92]. First the $\tau_{\text{had-vis}}$ candidates are seeded by jets with $p_T > 10$ GeV and $|\eta| < 2.5$, reconstructed with anti-k_T algorithm with a distance parameter value of 0.4 applied to clusters of calorimeter cells, also calibrated using a local hadronic calibration [93]. The candidate can have associated tracks if they are within a cone of ΔR= 0.2 from the candidate direction and have $p_T > 10$ GeV. The candidates with 1 or 3 tracks are considered. The candidate momentum is built using only clusters of calorimeter cells within a cone of radius 0.2. For both one and three prong decays, as it shown in Figure 4.12 (a), the efficiency to reconstructed $\tau_{\text{had-vis}}$ is roughly 70% for $p_T(\tau_{\text{had-vis}})$ below 250 GeV. For three prong at high-p_T the efficiency slightly decreases because of the increased collimation of the decay products that cause an increased probability to miss a track because of overlapping trajectories.

The second identification step is based on a boosted decision tree (BDT). Training has been done separately for one and three prong decays to discriminate $\tau_{\text{had-vis}}$ from jets. It is using variables related to calorimeter deposits and the reconstructed tracks. The variables exploited are related to the collimation of tracks and calorimeter cells, the balance of track momentum and calorimeter energy measurements, the fraction of energy deposited in the electromagnetic calorimeter, the presence of a significant impact parameter or secondary vertex and the invariant mass of the hadronic τ decay products. The input variables are corrected for pileup. Figure 4.12 (b) shows the misidentification probability as a function of selection efficiency for one and three prong $\tau_{\text{had-vis}}$ candidates together with several identification working points.

The BDT discriminant is transformed to have a flat acceptance for prompt ("signal") $\tau_{\text{had-vis}}$ candidates. For the nominal definition of $\tau_{\text{had-vis}}$ candidates, the working point meduim, which has a reconstruction and identification efficiency of 55% (40%) for 1-prong (3-prong) hadronic τ decays in $Z \to \tau\tau$ events, is chosen, leading to a rejection factor of about 50-200 for jets [92]. This rejection factor depends on the p_T and η of the candidate, as well as the number of associated tracks. Only the highest-p_T $\tau_{\text{had-vis}}$ candidate that passes the pre-selection requirements (associated number of tracks, p_T, η and overlap removal against electrons and muons) is considered as a potential $\tau_{\text{had-vis}}$ in the analysis. Identification is applied later at the event level selection. A looser selection of $\tau_{\text{had-vis}}$ candidates is also used in the analysis, with the BDT working point loose instead of medium. The corresponding efficiency for hadronically decaying τ-leptons in $Z \to \tau\tau$ events is about 70%, with a jet rejection factor about 2-5 times smaller than medium [92].

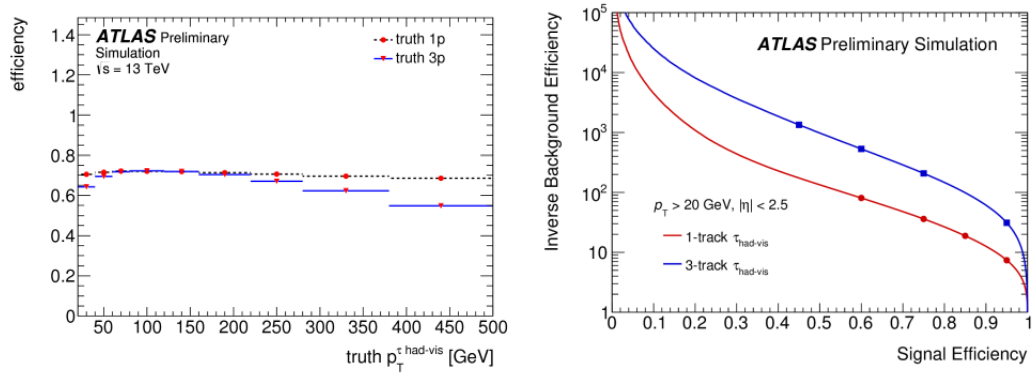

(a) (b)

FIGURE 4.12: ATLAS reconstruction efficiency for with one or three prongs $\tau_{\text{had-vis}}$ as a function of the $p_T(\tau_)$had-vis (a) [92] and efficiency and misidentification rate of jets $\rightarrow \tau_{\text{had-vis}}$ for different requirements on the BDT, the ponits on the curves correspond to different working point (b) [94].

Removal of geometric overlaps between objects

When several objects selected using the criteria above overlap geometrically, an overlap removal procedure is applied. The "Heavy-flavour" scheme is applied to the selected objects:

- A $\tau_{\text{had-vis}}$ object is rejected if found within $\Delta R < 0.2$ of either electron or muon with loose identification criteria with p_T above 20 GeV or 7 GeV respectively.
- A $\tau_{\text{had-vis}}$ object is rejected if matches a reconstructed electron with a log-likelihood value above a pre-determined threshold, chosen in order to maintain a flat 95% $\tau_{\text{had-vis}}$ efficiency in p_T and $|\eta|$.
- Remove any calorimeter-tagged muon sharing an inner-detector track with an electron.
- Jets are removed if they are within $\Delta R < 0.2$ of the highest-p_T pre-selected $\tau_{\text{had-vis}}$ candidate.
- Non-b-tagged jets are removed if they are within $\Delta R < 0.2$ of any selected electron.
- Non-b-tagged jets are removed if they are within $\Delta R < 0.2$ of any muon.
- Electrons and muons are rejected if they are found within $\Delta R < 0.4$ of the remaining non-pile-up jets.

4.3.1 The *b*-jet tagging

Since the top quark usually decays into a W boson and a *b*-quark, it is very important to efficiently identify the jets resulting from hadronization and decays of the *b*-quark. In order to identify the *b*-jets, the multivariate-based algorithm MV2c10 is used in the presented analysis [95, 96]. This algorithm exploits the fact that *b*-flavoured hadrons

have long mean life time $\sim$ 1.5 ps and combines the information of impact parameter with the explicit identification of secondary (several millimeters away from the primary vertex due to time dilation) and tertiary vertices, where the secondary vertex is reconstructed with the tracks of the charged particles within a jet, as it shown in Figure 4.13 selection based on the MV2c10 output, which gives 70% efficiency of tagging b-jets from $t\bar{t}$ process, is found to be the best choice for fitting working point for the analysis. The rejection factors of b-jets against c-jet, hadronic τ decays and jets form light quarks or gluons are 13, 56 and 380 respectively. In order to compensate for differences between data and simulation in b-tagging efficiency for b-, c- and light-quark jets correction factors are applied to the simulated events.

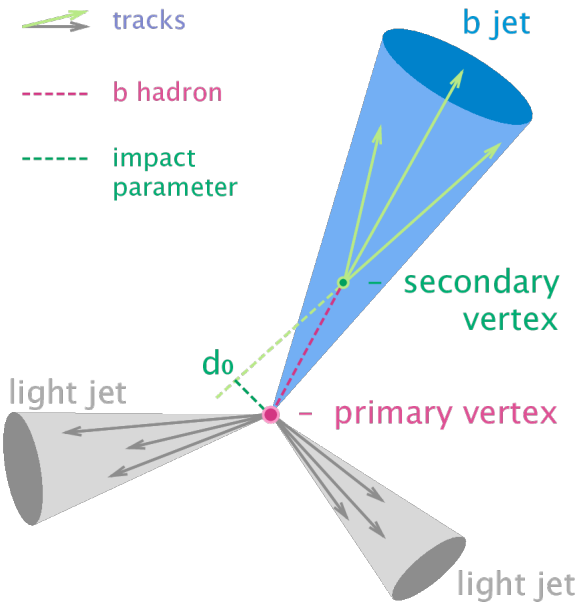

FIGURE 4.13: Illustration of an event with a b-jet, which shows the b hadron formed from the b quark decays at a secondary vertex.

Chapter 5

Multivariate analysis in particle physics

5.1 Introduction

In data analysis, one of the most challenging task is to identify events that are rare and simultaneously obscured by the wide variety of processes, known as background, which mimic the searched process, known as signal. This is like "finding needles in a haystack" for which the conventional approach that is selecting events by using cuts on individual kinematic variables can be insufficient. The multivariate analysis (MVA) is a set of statistical methods that simultaneously analyze multiple measurements or variables describing a given object that can be dependent or correlated in various ways. In order to provide predictions for future data, in conventional statistical techniques, parameters of a given mathematical model are found either analytically or numerically. However, dealing with a large amount of data puts pressure on the development of automated algorithms for learning from data, named *machine learning* (ML). The multivariate analysis in particle physics is mainly used for : *classification*- the process of assigning objects or events to one of the possible discrete classes and *parameter estimation* or *regression*- extraction of one or more parameters by fitting a model to data such as measurements of track parameter, vertices or physical parameters like production cross-section, branching ratios and masses [97]. Classification is used in the identification of particles (e.g. electrons, τ leptons, etc) and in signal and background discrimination as can be seen in several completed analysis [98–100]. One of the most important tasks in high energy physics is the classification of objects, for example discrimination of signal events from those coming from background processes. The optimal discrimination between classes is crucial to obtain the signal-enhanced samples for precision physics measurements. Therefore, it is important to remember that good understanding of the input before starting playing with multivariate techniques is very desirable, for example, finding observables with a good separation power between signal and background with little correlations amongst each other. However, for deep neural networks the trend is different, it can take plenty of variables and let the net construct the features.

5.2 Multivariate analysis

In comparison to the classical rectangular cut selection, that is the sequential application (not in specific order) of requirements to the individual observables in an event, modern classification methods have become increasingly sophisticated and powerful. The so-called multivariate analysis or algorithm, are very closely related to what is called pattern recognition or data mining in general statistical context.

They use the multi-dimensional observable space rather than each observable separately. Multivariate methods use the statistical distributions of the events in the observable space to decide on a class membership of a particular event. Instead of assigning a definite class to an event, it is also common to attribute a probability for it to belong to a certain class.

In case of two class discrimination, multivariate techniques combine the information of all observables of an event, often referred to as the feature vector **x** of an event, into one single variable, γ. This MVA variable can then be used in order to decide if the event is selected as signal or rejected as background, depending on whether the variable passes a previously set threshold or not, as shown in Figure 5.1.

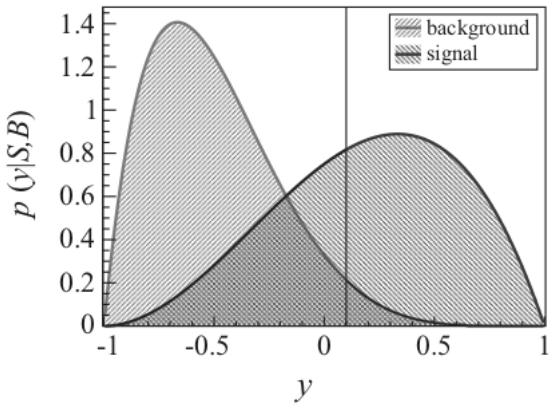

FIGURE 5.1: Distributions of an MVA variable γ for signal and background events. If the measured γ is above the indicated threshold value (vertical line) then the event is selected as signal, otherwise it is rejected as background [101]

In general, one can consider a multivariate selection algorithm as a mapping function of the D-dimensional feature space of the observables to a real number, $R^D \rightarrow R : \gamma = \gamma(x = x_1, ..., x_D)$. Each constant value $\gamma(x) = c$ represents a hypersurface in the original observable space. Simply classifying all events with $\gamma(x) > c$ as signal corresponds to classifying all events on one side of this, possibly very complicated, hypersurface as signal and rejecting the others as background.

Some classifiers, for example the naive Bayes classifiers (a family of simple "probabilistic classifiers" based on applying Bayes' theorem with strong (naive) independence assumptions between the features) that are often referred to as likelihood-selection techniques in high energy physics, are simple to code. When applying more advanced techniques using of standard program packages that offer either individual classifiers (e.g. JETNET [102]) or a collection of many different classifiers (e.g. Scikit [103] and TMVA [104]) have become increasingly popular. The latter group of packages, even though in some cases less sophisticated for the individual classifiers, offers the possibility to easily compare different MVA techniques against each other, allowing the user to choose the simplest technique without sizable sacrifice in performance. Comparison of different statistical approaches in data mining shows that it is impossible to identify the best-performing classifier without considering the specific features of the problem at hand.

	Reject H_0 (select as signal)	Accept H_0 (select as background)
H_0 is false (event is signal)	Right decision with probability 1-β =power = efficiency	Wrong decision; type II error with probability β
H_0 is true (event is background)	Wrong decision; type I error with probability α = size = significance	Right decision with probability 1-α= background rejection

TABLE 5.1: The different types of errors that are made when either failing to classify a signal event as such (type II error) or misclassifying a background event as signal (type I error).

Going from classical cuts to MVA techniques is motivated by the better performance of the latter in terms of higher efficiency for the same misclassification rate. Obviously individual cuts in each observable are not able to exploit possible correlations among the different observables. In addition, a signal event that might look background-like in only a single observable will inevitably be misclassified as background in a cut-based analysis. However, it might be correctly classified with a multivariate classification approach that is able to compensate for this one background-like feature by exploiting all the other observables that might look very signal-like.

Constructing the perfect multivariate classifier would be easy if we had access to the full differential cross-section in the actually observed event features, which is theoretical differential cross-section in the observables, folded with the detector response for both signal and background events. Then the differential cross-section is the probability density function (pdf) $p(x|C)$, where C can be either signal (S) or background (B).

Classification from a Statistical Perspective

In statistical literature one typically talks about hypothesis testing. These tests are usually done by formulating a null hypothesis (H_0). In the context of event classification, where we want to select the (signal) events we are interested in, the null hypothesis which means an event is 'background'. The null hypothesis is then either rejected or not, depending on the value of a test statistic $\gamma(x)$ which in our case is the MVA variable.

In most cases the probability densities of the observables for signal and background events overlap. This means that there are regions in phase space where one can find both signal and background events, leading to unavoidable errors in the decisions made to classify the events. One either misclassifies background events as signal (type I error), or one fails to identify a signal event as such and classifies it as background (type II error). Their probabilities of occurrence are denoted as α (the size of the test or significance) and β, where (1-β) is called power of the test or signal efficiency. The quantity (1-α) is referred to as background rejection. Table 5.1 shows the various situations that occurrence when testing for a hypothesis, and the corresponding error types.

For each individual classification problem, one has to find the optimal working point, that is the best balance between type I and type II errors. It is not always sufficient to simply choose the classification that gives the smallest number of misclassifications (sum of type I and type II errors). Instead, a figure of merit has to be defined that reflects the nature of the respective analysis.

In the critical region, - the part of the parameter space where $\gamma(x) > c$ - the null hypothesis is rejected and the events are accepted as signal; the type I(II) error rates $\alpha(\beta)$ are given by :

$$\alpha = \int_C p(x|H_0)dx = \int_C p(x|B)dx = \int_{\gamma(x)>C} p(x|B)dx. \tag{5.1}$$

Similarly we have

$$\beta = \int_{\gamma(x)<C} p(x|S)dx. \tag{5.2}$$

The boundary of the critical region C is also called the *decision boundary*. Rather than integrating over the multi-dimensional observable space, we can also revert to using the distributions of the test statistic $\gamma(x)$. Once the distribution $p(\gamma|S)$ and $p(\gamma|B)$ have been determined, the integrals 5.1 and 5.2 can easily be evaluated :

$$\int_{\gamma=C}^{\infty} p(\gamma|B)d\gamma = \alpha \quad \text{and} \quad \int_{-\infty}^{\gamma=c} p(\gamma|S)d\gamma = \beta \tag{5.3}$$

Rather than defining hard decision boundaries, the probability densities, expressed either in terms of the multi-dimensional observables $p(x|S(B))$ or the one-dimensional projection $p(\gamma = \gamma(x)|S(B))$, can also be used to calculate the probability of an observed event to be of either signal or background origin. For this one needs the prior probabilities of randomly picking either a signal or a background event given by the relative fraction of signal (f_S) and background events ($f_b = 1 - f_s$) in the sample. The probability of an event observed with features x, resulting in $\gamma(x) = \gamma$, is then given by:

$$P_s(\gamma) \equiv P(S|\gamma) = \frac{p(\gamma|S) \cdot f_s}{p(\gamma|S) \cdot f_S + p(\gamma|B) \cdot (1 - f_s)} \tag{5.4}$$

Assuming $\nu_{s(b)}$ to be expected number of signal (background) events in the sample on which the classification algorithm is run, the relative abundance f_s is given by $f_s = \nu_s/(\nu_s + \nu_b)$.

5.2.1 Receiver-Operating-Characteristic curve

Both type I and type II errors can be made arbitrarily small individually, at the expense of the other one becoming large. As indicated earlier, the best working point, that is the cut value c, has to be found for each analysis individually. This is equivalent to choosing a particular cut value C on the MVA output variable $\gamma(x) = C$, which in turn is equivalent to picking a particular point on the so-called Receiver-Operating-Characteristic (ROC) curve which is often used to display the performance of a classification algorithm. It shows the relation between the signal efficiency and the background rejection. An example is shown in Figure 5.2 since typically the MVA variable distributions for signal and background overlap (as is also the case for the example shown in Figure 5.2a), the background rejection becomes worse for higher signal efficiency, and vice versa.

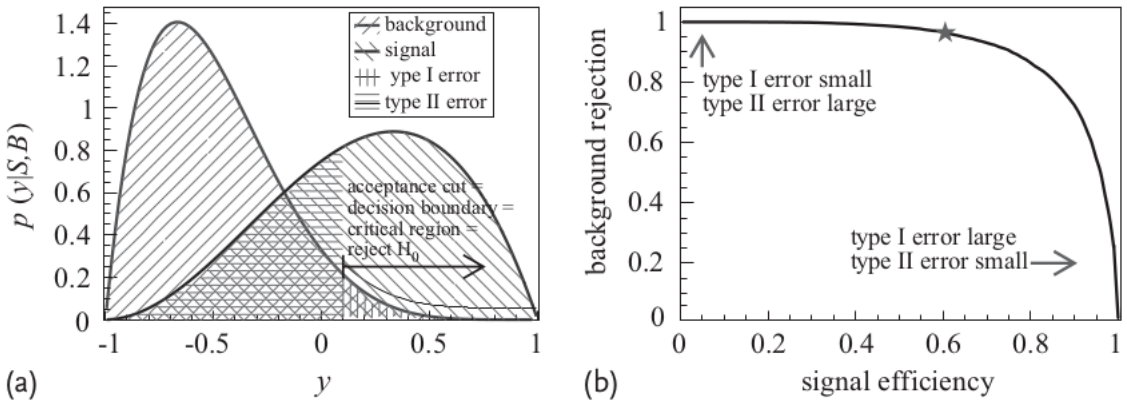

FIGURE 5.2: The distributions $p(\gamma|S)$, $p(\gamma|B)$ of an MVA variable γ for signal and background events. The classification is based on a cut on the MVA variable γ which in this example is chosen to be at $\gamma = 0.1$ (a) The ROC curve, showing the background rejection as a function of the signal efficiency achieved by varying the cut on the MVA output variable (b). The working point according to the cut value of 0.1 is indicated by a star [101].

This is also illustrated by the ROC curve in Figure 5.2b. For a hypothetical cut value of $\gamma = 0.1$, the areas which lead to type I and type II errors, respectively, are also indicated in Figure 5.2a. The hatched areas of the pdfs for signal and background are proportional to the number of misclassified signal and background events, respectively. In case the total number of signal and background events are the same, the sum of the hatched areas is directly proportional to the total number of misclassified events. This area, and hence the misclassification error, is minimized for a cut where the two curves intersect, which for the given example would be at -0.175. The overall performance for all possible cut values for a given classification algorithm is easily visualized using the ROC curve: the algorithm with the largest area underneath the curve has on average the best performance. Note that for a particular analysis with specific requirements on the type I or type II error, an algorithm with excellent performance in special regions of the ROC curve might be more suited, even if its overall performance is worse.

5.2.2 Supervised machine learning

Machine learning refers to the automated determination of the decision boundary according to a chosen algorithm. Supervised machine learning uses so-called training events for which the class memberships are known. The decision boundary is chosen by minimizing a loss function - a process which is referred to as the training of the classifier. The resulting decision boundary is used in the following for the classification of events with yet unknown class membership. Conversely, unsupervised learning techniques do not exploit training events and are typically used to find clusters in a distribution or, in general, to approximate the overall probability density of a given data sample. One example are self-organizing maps [105]. In this thesis, the interest is in classifying events into signal or background, and the training events are available from Monte Carlo simulations or from data sidebands. Therefore, the focus is on supervised machine learning.

The choice of the classifier which is best suited for a given classification task is very much dependent on the particular problem at hand. There are very simple classifiers with a small number of degrees of freedom that, for example, allow only for a linear decision boundary. Others allow for very complicated, non-linear features in the decision boundary and feature a large number of degrees of freedom. Obviously, it is best to use a linear discriminator rather than one with more freedom if, according to the underlying true probability density, the classes are separable by a linear boundary. More complex classifiers will result in boundaries that are not exactly linear but tend to follow the statistical distribution of the training sample along the boundary. Conversely, if the training data already show a clear non-linearity beyond statistical uncertainties, a simple linear classifier would certainly under-perform and systematically misclassify events in certain regions of the phase space.

Classifiers with a small number of degrees of freedom are naturally less prone to statistical fluctuations in the training sample: decision boundaries calculated from different sets of training data which were all drawn from the same underlying pdf would be very similar, i.e. they would have small variance. However, these decision boundaries will systematically deviate from the ideal ones given by the underlying probability density if the latter has more complicated features which cannot be described with the limited number of degrees of freedom of the classifier. This systematic deviation is referred to as the bias of the classifier. Conversely, a classifier with many degrees of freedom, allowing for very detailed decision boundaries, will have a larger dependence on the statistical fluctuations of the training sample, i.e. it will have a large variance (variation of the decision boundary when using different training samples), but typically a smaller bias. Defining the necessary flexibility of the model and fixing the model configuration parameters is an optimization procedure that can also be automated, but is typically performed by the experimenter. This includes, for example, choosing the number of nodes and layers in an artificial neural network. Finding a balance between variance and bias is often referred to as the bias-variance trade-off. In order to find an adequate model flexibility, one can use a so-called validation sample, which like the training data-set contains events with known class memberships. Starting with very low model flexibility and moving to ever increasing flexibility, the separation between signal and background will become better and better on the training sample because the decision boundary will become better adapted to the actual data sample. The performance of the classification tested on the independent validation sample, however, will increase only up to a certain point and will then decrease again once one starts to overtrain. The term 'overtraining' refers to the scenario where small-scale features in the decision boundary are dominated by statistical fluctuations in the training sample rather than by actual features of the underlying pdfs. This obviously leads to a worse performance of the trained classifier compared to properly trained classifiers with an appropriate degree of flexibility. An overtrained classifier also does not generalize properly as it does not capture the general features of the underlying distribution, and vice versa. It is worth mentioning that, with more training data available, more flexible models can be applied and properly fitted. Once the best model flexibility has been determined and the model has been trained, both the validation and the training sample have been used. In order to get a truly unbiased estimate of the final performance of the classifier, a third sample typically referred to as the testing sample is used.
Within the particle physics community several methods are particularly relevant and popular, i.e.: Naive Bayes classifier, K-Nearest Nieghbour, Fisher Linear Discriminant, Neural Networks and Boosted Decision Trees. We used in the presented analysis the last two examples (for review see [101] and [106]). All of listed classifiers

are trained using "*simulated data*" (MC samples), where the class membership of an event is known and from these training data the classifier "*learn*" how the parameters of the decision boundaries are chosen to get optimal separation between the signal and background events.

5.2.3 Artificial neural networks, feed-forward multi-layer perceptrons

An artificial neural network (ANN) is an interconnected group of nodes, inspired by simplification of network of neurons in a brain [107, 108]. The original goal of the ANN approach was to solve problems in the same way that a human brain would. A graphical representation of neural network is illustrated in Figure 5.3. Each circular node represent an artifitial neuron and a connection from the output of one artifitial neuron to the input of another represented by an arrow. An ANN is made up of 3 components:

- Input Layer which is a vector, since it consists of many components.
- Hidden Layer
- Output Layer.

In general a simple neuron model is as following:

- Input vector has x_i components which is multiplied by the appropriate weights w_i and weighted sum : $\sum_i w_i x_i$.
- Nonlinear mapping f defines the scalar output y: $y = f(\sum_i w_i x_i)$.
- The model is made of a set of synapses (hidden layer) each of which is charectrized by a weight or strength of its own, an adder, an activation function and a bias.
- A nueral network is charectrized by its pattern of connections between the neurons (called its architecture), its method of determining the weights on the connections (its training or learning algorithm) and its activation function.

Neural network consists of processing units, the neurons, and directed, weighted connections between those neurons. The reactions of the neurons to the input values depend on the activation state. The activation state indicates the extent of a neuron's activation and is often shortly referred to as activation (neurons get activated if the network input exceeds their threshold value). The threshold value θ_j is assigned to neuron j and markes the position of maximum gradient value of the activation function.

With simplification the learning happens in two steps:

- *Forward-proagation* which is making guess about the answer.
- *Back-propagation* minimizing the error between actual answer and guessed answer.

In the first step, data at input layer is weighted by randomly initialized weight to form hidden layer, then the output of hidden layer is passed through a non-linear function also known as activation function to form guessed output. In the *Back-propagation* [109] the total error is calculated by the difference between value $y_{expected}$

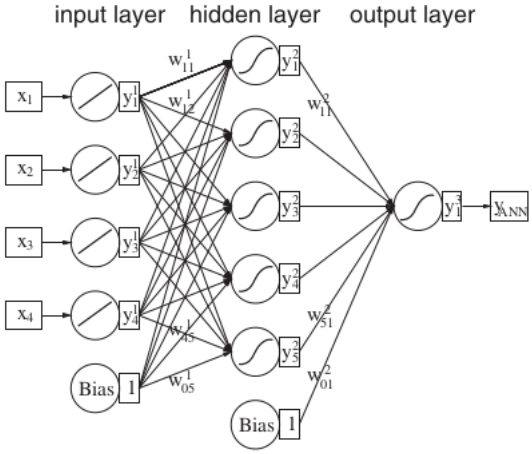

FIGURE 5.3: Graphical representation of the architecture of a feed-forward neural network with four input observables, one hidden layer of five nodes and one output node. The constant input (bias) at each layer allows a certain offset to be given to each node of the following layer [101].

(value in trianing set) and observed value y_{ANN} (the value obtained from *Forward-prpagation* by passing them through a lost function. Then, the contribution of each weight is measured in total loss, the result is subtracted from the respective weight.

It is straightforward to enlarge the architecture by adding more layers of neurons. For the output node, an activation function for instance sigmoidal $h(t) = 1/(1+e^{-t})$, maps the output value onto a range between 0 and 1. In applications where signal and background processes have to be separated, neural networks are typically trained such that signal events peak close to 1 and background events close to 0. Networks with this kind of architecture, where the output of one layer of nodes is only used as input for the following layer(s), not allowing for feedback loops into previous layers, are called feed-forward networks or (multi-layer) perceptrons (MLPs). This method is used for optimization of fake factor methods in the Chapter 7.

5.2.4 Boosted decision trees

Decision trees are tree-structured classifiers that consist of a series of binary splits as displayed in Figure 5.4. The tree starts from a root node and is built up of repeating splits and nodes down to the final or leaf nodes. The set of nodes and splits leading to a given leaf node is called a branch. An event is classified according to the class label of the leaf node at the end of the tree branch in which it ends up. For most decision trees the split criteria are simple cuts on individual observables (features). Each branch of a decision tree corresponds to a sequence of cuts which classifies an event as either signal or background, depending on the leaf node class label. A decision tree hence splits up the multi-dimensional observable space into many (rectangular) volumes that are attributed to either signal or background.

An individual decision tree is trained by sequentially splitting the training data sample. At each step, starting from the root node which sees the whole data sample, one determines the one variable and the corresponding cut value that provide the

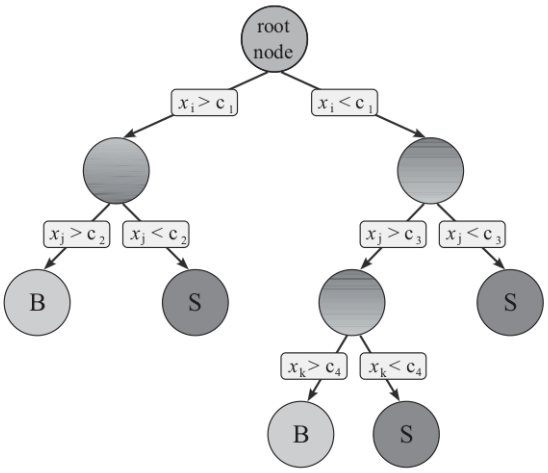

FIGURE 5.4: A decision tree is typically a two-dimensional structure with a single root node, followed by a set of yes/no decisions (binary splits) that finally result in a set of leaf nodes. For classification, a test event is passed from the root node down the tree and will end up in a certain leaf node depending on how it responded to the various split criteria. The event is then classified according to the class label of this leaf node [101].

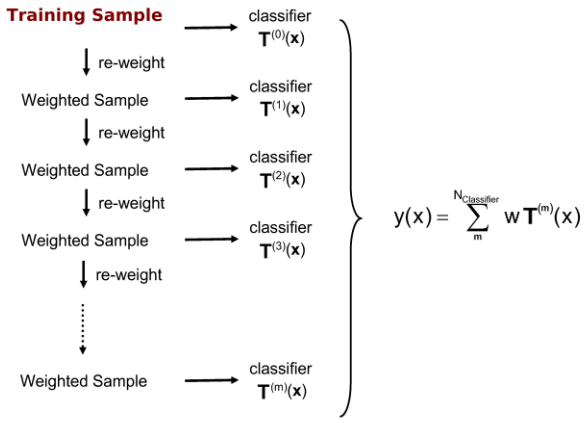

FIGURE 5.5: Scheme of the boosting procedure. Note that this method can be applied also to classifiers other than trees [110].

best separation of the data. Separation is typically measured in terms of the Gini index p·(1-p) [111], where p denotes the purity. This index has maximum values when the sample is totally mixed, and they decrease monotonically for samples that become purer in either signal or background, note that a population is pure if all of its members belong to a single class. The best split variables and values are determined by comparing the separation index before and after the split. The latter is defined by the sum of the indices of the two daughter nodes, weighted by the respective fraction of events in the nodes. The best split is then performed in order to split the training sample into two daughter nodes, for which the whole procedure is re-iterated. Despite the aforementioned similarity with simple cuts and the easy interpretability of a decision tree, they have hardly been used in high energy physics.

The way they are typically constructed (grown or trained) makes them fairly sensitive to statistical fluctuations in the training data sample, and as a multivariate classification algorithm they are typically less powerful than others. However, this changed with the advent of BDTs that combine many different decision trees which together form a forest. All trees are trained with data samples that are derived from the training events by reweighting the events according to the boost recipe as it shown in Figure 5.5, i.e. trees are trained in sequence, and misclassified events are reweighted (boosted) in the training subsequent tree. The classification of a test event is then obtained by a (weighted) average of the responses of each of the individual decision trees in the forest, note that this method can be applied also to other classifires. While a 'standard' decision tree is best grown during the training to full size - that is until the training sample is (almost) fully divided into clean signal and background nodes - and then cut back in a pruning procedure to avoid overtraining, this does not hold for boosted decision trees. As the boosting procedure is designed to work with so-called weak classifiers, it is advantageous here to stop the individual tree growing at quite an early stage already, resulting in trees which only have a few split levels and therefore do not require pruning. The optimal tree depth depends on the degree of correlations between the variables and will have to be optimized for each use case. Boosted decision trees are very robust and powerful classifiers and have hence been referred to as the best-suited 'off-the-shelf' classifiers [110].

K-Fold cross-validation

Generally, it is necessary to validate the stability of chosen machine learning technique, which gives a kind of assurance that the algorithm has got most of the patterns from the data correctly (it is low on bias and variance). In an ideal situation, i.e having enough data, one would set aside a validation set and use it to assess the performance of the chosen prediction model. But data are often scarce and this is simply not possible. To solve this issue, K-Fold Cross-Validation method uses a part of the available data to fit the model and a different part to test it, the data are divided into k subsets and each time one of the k subsets of data is used as the test set (validation set) and the other k-1 subsets are put together to form a training set as it shown in Figure 5.6. Hence, every data point gets to be in a validation set exactly once and gets to be in a training set k-1 times. Then the error estimation is averaged over all k trials to get the total effectiveness of the prediction model. This significantly reduces the bias since all of the data are used for training, and also significantly reduces variance the all of the data are also being used in the validation set [112].

	Fold 1	Fold 2	Fold 3	Fold 4	Fold 5	Background
Partition 1	Evaluation	Train	Train	Train	Train	Fold 1
Partition 2	Train	Evaluation	Train	Train	Train	Fold 2
Partition 3	Train	Train	Evaluation	Train	Train	Fold 3
Partition 4	Train	Train	Train	Evaluation	Train	Fold 4
Partition 5	Train	Train	Train	Train	Evaluation	Fold 5

FIGURE 5.6: For the k-th part, the model is fitting to the other k-1 parts of the data, and calculation of the prediction error of the fitted model during predicting the k-th part of the data is done. The procedure is repeated for k=1,2, .., k and combination of the k estimates of prediction error is prepared [111].

Chapter 6

Search for a charged Higgs boson

6.1 Introduction

The discovery of the Higgs boson at the LHC in 2012 [24], with a measured mass close to 125 GeV [113, 114], opens the question of whether this is the Higgs boson of the SM or part of an extended scalar sector. Charged Higgs bosons are predicted in several extensions of the SM as discussed in Section 2.2.2. Searches for charged Higgs bosons in pp collisions at $\sqrt{s}$ = 7-8 TeV by the ATLAS and CMS Collaborations were done, probing the mass range below the top-quark mass with the $\tau\nu$ [115–119] and cs [120, 121] decay modes, as well as the mass range above the top-quark mass with the $\tau\nu$ and tb decay modes [117, 119, 122]. Later, using 3.2fb^{-1} of data collected at $\sqrt{s}$ = 13 TeV, searches for charged Higgs bosons heavier than the top-quark were performed by the ATLAS [123] and CMS [124] in the $\tau\nu$ decay mode. Moreover, $H^+ \to WZ$ in the vector-boson-fusion production mode was searched at 8 TeV by ATLAS Collaboration [125] and at 13 TeV by the CMS Collaboration [126]. No evidence of charged Higgs bosons was found in any of these searches.

A search for charged Higgs boson decaying via $H^+ \to \tau\nu_\tau$ in the τ+jets and τ+lepton final states, using pp collision data at $\sqrt{s}$ = 13 TeV with integrated luminosity of 36.1 fb^{-1}, recorded by the ATLAS detector [6] is described in this Chapter. Similar search for charged Higgs boson was done by the CMS Collaboration for the H^+ in the mass range of 80 GeV to 3 TeV with integrated luminosity of 35.9 fb^{-1} [127].

The search for charged Higgs bosons in the $H^+ \to \tau\nu_\tau$ decay was done assuming the subsequent hadronic decay of the τ-lepton, in the mass range 90-2000 GeV, including the intermediate mass region close to the mass of the top quark. The reconstructed candidate of a hadronic τ decay will be hereafter referred to as $\tau_{\text{had-vis}}$. Depending on the assumption made for the decay mode of the W boson originating from the top-quark produced together with H^+, two channels were studied: $\tau_{\text{had-vis}}$+jets, if the W boson decays into a $q\bar{q}$ pair, or $\tau_{\text{had-vis}}$+lepton, if the W boson decays into an electron or a muon and at least one neutrino (directly or via a leptonically decaying τ).

In Section 6.2, the data and simulated samples are summarized. The analysis strategy and event selection are discussed in Section 6.3. The data-driven estimation of backgrounds with misidentified τ objects is presented in Section 6.4. Finally, Section 6.6 presents the statistical interpretation of the obtained results.

6.2 Data and simulated event samples

The data-set used in this analysis, collected during stable beam conditions and with all ATLAS subsystems fully operational, corresponds to an integrated luminosity of

36.1 ± 0.8 fb^{-1}, derived using a methodology similar to that detailed in Ref. [129]. Data-quality criteria are applied in order to remove events where reconstructed jets are consistent with noise in the calorimeter or with non-collision backgrounds [90].

Signal events with the $H^+ \to \tau\nu$ decay are generated with MadGraph5_aMC@NLO [51] in three distinct mass regions:

- In the mass range below the top-quark mass (90–150 GeV), $t\bar{t}$ events with one top-quark decaying into a charged Higgs boson and a b-quark are generated at leading order (LO). Both $t\bar{t}$ events with two $t \to bH^+$ decays and single-top-quark events with a subsequent decay $t \to bH^+$ have a negligible contribution and are not simulated.
- In the intermediate-mass region (160-180 GeV), the full $pp \to H^+Wbb$ process is generated at LO.
- In the mass range above the top-quark mass (200-2000 GeV), H^+ production in association with a top-quark is simulated at next-to-leading order (NLO).

In all cases, the parton-level generator is interfaced to PYTHIA v8.186 [130] with the A14 set of tuned parameters for the underlying event [64], and the NNPDF2.3 [131] parton distribution function (PDF) sets. The SM background processes include the production of $t\bar{t}$ pairs, single top quarks, W+jets, Z/γ^*+jets, electroweak gauge-boson pairs ($WW/WZ/ZZ$), as well as multijet events (MJ). The $t\bar{t}$ events constitute the main background in the low- and intermediate-mass H^+ searches, while multijet events dominate for large charged Higgs boson masses. All backgrounds arising from a quark- or gluon-initiated jet misidentified as a hadronically decaying τ-lepton are estimated with a data-driven method, described in Section 6.4.

The generation of $t\bar{t}$ and single top-quarks in the Wt- and s-channels uses the POWHEG-BOX v2 [132–134] generator, with the CT10 [135] PDF set in the matrix-element calculations. Electroweak t-channel single-top-quark events are generated using the POWHEG-BOX v1 generator. This generator uses the 4-flavour scheme for the NLO matrix-element calculations together with the fixed 4-flavour PDF set CT10f4 [136].

For all processes above, top-quark spin correlations are preserved (MadSpin [137] is used for top-quark decays in the t-channel). The parton shower, fragmentation and the underlying event are simulated using PYTHIA v6.428 [138] with the CTEQ6L1 [139] PDF set and the corresponding Perugia 2012 tune [140]. The top-quark mass is set to 172.5 GeV. The sample of $t\bar{t}$ events is normalized to the next-to-next-to-leading order (NNLO) cross-section, including soft-gluon resummation to next-to-next-to-leading-log (NNLL) order [141]. The normalization of the sample of single-top-quark events uses an approximate calculation at NLO in QCD for the s- and t-channels [142–144] and an NLO+NNLL calculation for the Wt-channel [144].

Events containing a W or Z boson with associated jets are simulated using SHERPA v2.2.1 [66] together with the NNPDF3.0NNLO [145] PDF set. Matrix elements are calculated for up to two partons at NLO and four partons at LO using COMIX [67] and OPENLOOPS [146], and they are merged with the SHERPA parton shower [69] according to the ME+PS@NLO prescription [70]. The W/Z+jets events are normalized to the NNLO cross-sections calculated using FEWZ [147–149]. Diboson processes (WW, WZ and ZZ) are simulated at NLO using the POWHEG-BOX v2 generator, interfaced to the PYTHIA v8.186 parton shower model. The CT10nlo PDF set is used for the hard-scatter process, while the CTEQL1 PDF set is used for the parton shower. The non-perturbative effects are modeled using the AZNLO [150] tune. EVTGEN v1.2.0 [151] is used for the properties of bottom- and charm-hadron decays, except in samples generated with SHERPA. All simulated events are overlaid with additional minimum-bias

Background process	Generator & parton shower	Cross section(in pb)
$t\bar{t}$ with at least one lepton	POWHEG& PYTHIA6	451.66
$t\bar{t}$ all had	POWHEG& PYTHIA6	729.77
Single top-quark t-channel	POWHEG & PYTHIA6	70.43$*$
Single top-quark s-channel		3.35$*$
Single top-quark Wt-channel		71.67
W($l\nu$)+jets	SHERPA	2.0×10^4
Z/$\gamma^*(ll)$+jets	SHERPA	2.1×10^3
WW	POWHEG & PYTHIA8	54.81
WZ		16.3
ZZ		8.95

TABLE 6.1: MC generators and cross sections for the main SM background samples at $\sqrt{s}$ = 13 TeV. Here, l refers to the three lepton families e, μ and τ. All background cross sections are normalized to NNLO predictions, except for diboson events, where the NLO prediction is used. A $'*'$ indicates that the quoted cross section for the sample is without leptonic/hadronic branching ratios [32].

events generated with `PYTHIA v8.186` using the `A2` [152] tune and the `MSTW2008LO` [153] PDF set to simulate the effect of multiple pp collisions per bunch crossing (pile-up). Simulated events are then weighted to have the same distribution of the number of collisions per bunch crossing as the data. All signal and background events are processed through a simulation [154] of the detector geometry and response based on `GEANT4` [155] and they are reconstructed using the same algorithms as the data. The full list of simulated SM backgrounds with their cross-sections and names of generators used is presented in Table 6.1.

6.3 $H^+ \to \tau\nu$ analysis strategy

As mentioned before two channels are targeted in this analysis: $\tau_{\text{had-vis}}$+jets or $\tau_{\text{had-vis}}$+lepton. The corresponding signal regions are described below.

Event selection in the $\tau_{\text{had-vis}}$+jets channel

The analysis of the $\tau_{\text{had-vis}}$+jets channel is based on events accepted by an E_T^{miss} trigger with a threshold at 70, 90 or 110 GeV, depending on the data-taking period and thereby accounting for different pile-up conditions. The efficiency of these triggers is measured in data and used to reweight the simulated events, with the same method as in Ref [156]. At least one vertex with two or more associated tracks with p_T above 400 MeV is required, and the following event selection criteria are applied:

- at least one $\tau_{\text{had-vis}}$ candidate with $p_T^\tau > 40$ GeV, (which must pass the medium identification criteria);
- no lepton (electron or muon) with $p_T > 20$ GeV;
- at least three jets with $p_T > 25$ GeV, of which at least one is b-tagged;

- $E_T^{miss} > 150$ GeV;
- $m_T > 50$ GeV.

Here, the transverse mass m_T of the highest-p_T $\tau_{\text{had-vis}}$ candidate and E_T^{miss} is defined as

$$m_T = \sqrt{2p_T^{\tau}E_T^{miss}(1-\cos\Delta\phi_{\tau,miss})} \tag{6.1}$$

where $\Delta\phi_{\tau,miss}$ is the azimuthal angle between the $\tau_{\text{had-vis}}$ candidate and the direction of the missing transverse momentum.

Event selection in the $\tau_{\text{had-vis}}$+lepton channels

The $\tau_{\text{had-vis}}$+electron and $\tau_{\text{had-vis}}$+muon channels are based on events accepted by single-lepton triggers. Triggers for electrons or muons with low E_T or p_T thresholds respectively (24-26 GeV depending on the data-taking period, for both electrons and muons) and isolation requirements are combined in a logical OR with triggers having higher (E_T, p_T) thresholds (60-140 GeV for electrons, 50 GeV for muons) and looser isolation or identification requirements in order to maximize the efficiency. Following the same vertex requirement as in the $\tau_{\text{had-vis}}$+jets channel, events are selected as follows:

- exactly one lepton matched to the single-lepton trigger object, with p_T above 30 GeV and passing the loose identification critera. Depending on whether the lepton is an electron or a muon, two signal regions, $\tau_{\text{had-vis}}$+electron and $\tau_{\text{had-vis}}$+muon are considered;
- exactly one $\tau_{\text{had-vis}}$ candidate with $p_T^{\tau} > 30$ GeV and an opposite electric charge with respect to that of the lepton (it fulfills the loose identification criteria);
- at least one b-tagged jet with $p_T > 25$ GeV;
- $E_T^{miss} > 50$ GeV.

6.3.1 Multivariate discriminant in the $H^+ \to \tau\nu_\tau$ search

The output score of the Boosted Decision Trees method is used to separate the H^+ signal from the SM background processes, following the event selections described in Section 6.3. Training of the BDT is performed using the FastBDT [157] library via the TMVA toolkit [104]. The signal samples are divided into five H^+ mass bins, in which the kinematic distributions of the input variables and the event topology are found to be similar enough to ensure that the higher statistics from an inclusive training improves the performance:

- 90–120 GeV,
- 130–160 GeV (using the low-mass 160 GeV sample),
- 160–180 GeV (using the intermediate-mass 160 GeV sample),
- 200–400 GeV,
- 500–2000 GeV.

The BDTs are trained separately for $\tau_{\text{had-vis}}$+jets and $\tau_{\text{had-vis}}$+lepton events, and depending on whether the leading $\tau_{\text{had-vis}}$ candidate has one or three associated tracks (1- and 3-prong cases, respectively). The variables enetring the BDT training differ for the two types of final states considered in this search, and are summerized in Table 6.2.

BDT input variable	$\tau_{\text{had-vis}}$+jets	$\tau_{\text{had-vis}}$+lepton
E_T^{miss}	✓	✓
p_T^{τ}	✓	✓
p_T^{b-jet}	✓	✓
p_T^{l}		✓
$\Delta\phi_{\tau,E_T^{miss}}$	✓	✓
$\Delta\phi_{b-jet,E_T^{miss}}$	✓	✓
$\Delta\phi_{l,E_T^{miss}}$		✓
$\Delta R_{\tau,l}$		✓
$\Delta R_{b-jet,l}$		✓
$\Delta R_{b-jet,\tau}$	✓	✓
$\mathcal{Y}$	✓	✓

TABLE 6.2: The variables used in BDT training for the $\tau_{\text{had-vis}}$+jets and $\tau_{\text{had-vis}}$+lepton channels [6]

Here, the focus will be on the $\tau_{\text{had-vis}}$+jets channel, since the majority of the author's contribution is related to this channel. The k-fold method is used for training and classification: events are divided into k sets, and they are classified using a BDT trained on the signal and backgrounds from the other k-1 sets, thereby allowing every event to be classified with a BDT that does not include this event in its training set. While k = 2 is sufficient to ensure independence of training and classification of the sets, k = 5 is used in this analysis to increase the size of the training set for each BDT (see the previous chapter for more details).

All available H^+ signal samples corresponding to a given mass bin are combined into one inclusive signal sample. The BDT is trained on $H^+ \to \tau\nu$ signal and top ($t\bar{t}$ and single-top quark) background MC samples using the final (SR) selection defined in Section 6.3. For the first four H^+ mass ranges, events arising from $j \to \tau$ fakes are taken from the simulated background samples. In the H^+ mass range 500–2000 GeV, the misidentified $\tau_{\text{had-vis}}$ candidates estimated with a data-driven method are included in the training, as the multijet background with a misidentified $\tau_{\text{had-vis}}$ candidate dominates in this mass range. At the same time, the $j \to \tau$ fakes in the simulated background samples are excluded from the training to avoid double-counting.

The transverse mass of the $\tau_{\text{had-vis}}$ candidate and E_T^{miss} is known to strongly discriminate the signal from background, particularly for high H^+ masses. In the MVA approach, this quantity is replaced by its three components p_T^{τ} , E_T^{miss} and $\Delta\phi_{\tau,E_T^{miss}}$ carrying equivalent information. This way the MVA can also benefit from potential additinal descrimination of those three constituents. At low H^+ masses the polarization of the τ lepton $\mathcal{Y}$ is used as an additional discriminating variable. The $\mathcal{Y}$ variable and its impact on the discriminant is described in detail in Section 2.3.1.

The importance of the other kinematic variables in the BDT training becomes dominant at large H^+ masses, in which case the BDT discriminant is inclusive in the number of tracks associated to the $\tau_{\text{had-vis}}$ candidate and does not contain the $\mathcal{Y}$

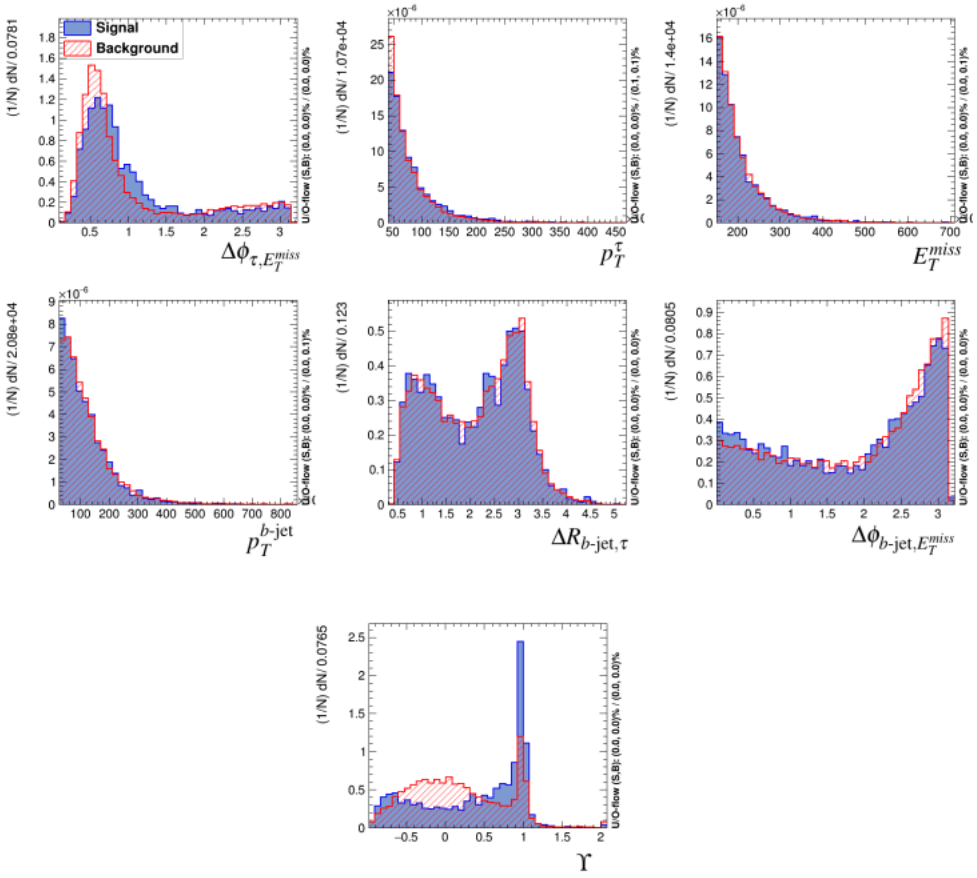

FIGURE 6.1: Distributions of input variables for BDT training within 90-120 GeV. Signal is presented as a blue, solid histogram; top production background (as estimated from MC) is presented as a red, dashed histogram. Histograms are arbitrarily normalized.

variable. In total, seven variables are used as an input to the BDT in the $\tau_{\text{had-vis}}$+jet channel:

- p_T^{τ}, the transverse momentum of τ;
- p_T^{b-jet}, the transverse momentum of b-jet;
- E_T^{miss}, the missing transverse energy;
- $\Delta\phi_{\tau,E_T^{miss}}$, the azimuthal angle between $\tau_{\text{had-vis}}$ candidate and the direction of the missing transverse energy;
- $\Delta\phi_{b-jet,E_T^{miss}}$, the azimuthal angle between b-jet candidate and the direction of the missing transverse energy;
- $\Delta R_{b-jet,\tau}$, the distance between reconstructed b-jet candidate and $\tau_{\text{had-vis}}$;
- Υ only for 1-prong $\tau_{\text{had-vis}}$ candidates in mass ranges from 90 to 400 GeV.

In the above definition the b-jet with the largest p_T in the event is considered. Optimization of the hyperparameters described above was done using "grid-search",

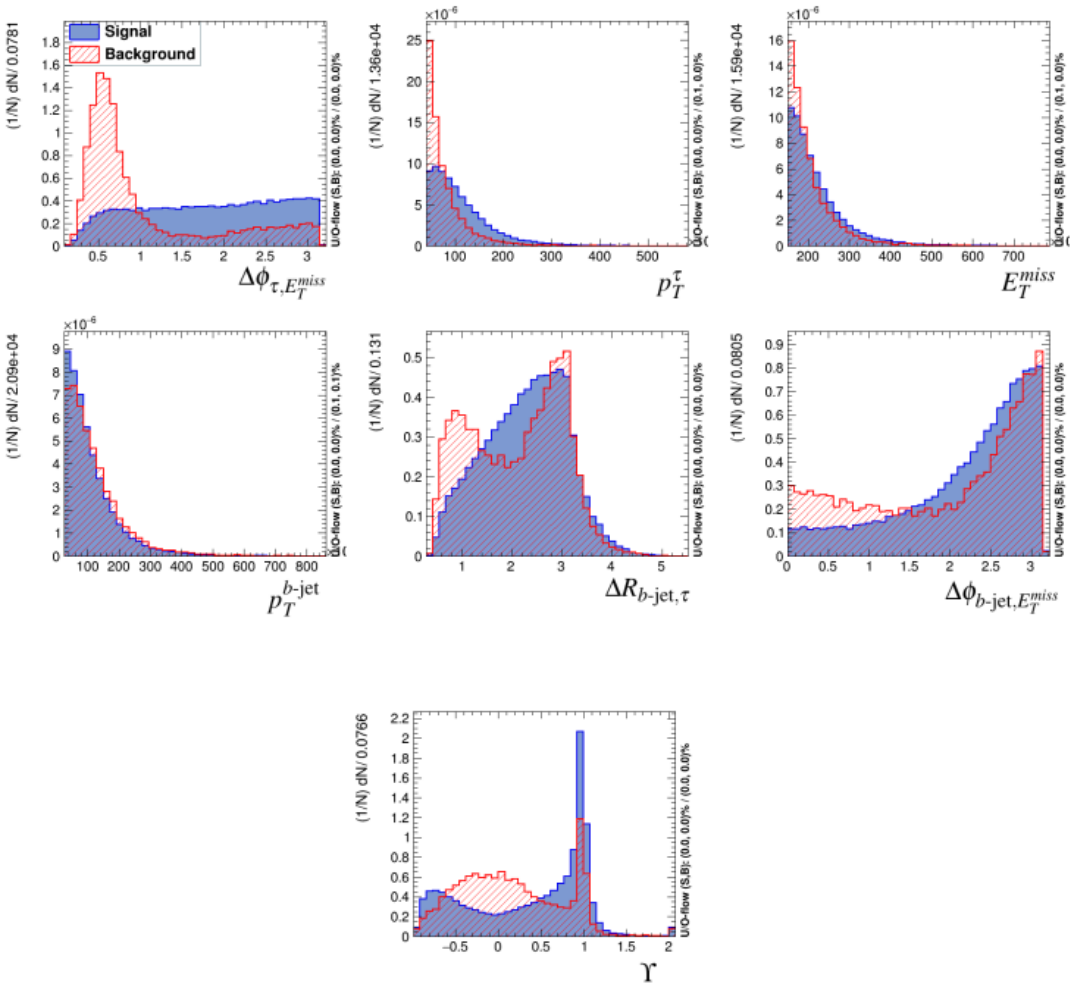

FIGURE 6.2: Distributions of input variables for BDT training within 200-400 GeV . Signal is presented as a blue, solid histogram; top production background (as estimated from MC) is presented as a red, dashed histogram. Histograms are arbitrarily normalized.

i.e. by constructing all possible combinations of the hyperparameters and choosing the setup for which the FastBDT algorithm turned out to have the largest area underneath the ROC curve. As a result of optimization the chosen hyperparameters are:

- for 1-prong: number of trees= 1000; shrinkage= 0.05; RandRatio= 0.6; number tree layers= 3; NCutLevel= 7,
- for 3-prong: number of trees= 500; shrinkage= 0.02; RandRatio= 0.4; number tree layers= 5; NCutLevel= 9.

The distribution of input variables for mass ranges of 90-120 GeV and 200-400 GeV are shown in Figures 6.1 and 6.2. The correlation matrices of input variables are presented in Figures 6.3, 6.4 and 6.5 for the top production backgrounds and signal. It can be seen that the Υ variable is uncorrelated with the other variables used in the training. Table 6.3 shows the ranking of the variables used in the BDT training for

each H^+ mass range. Note that this is a measure of how often a given variable is used to split decision tree nodes. Thus, a variable can be ranked lower or higher in a specific set and a value of "Variable Importance" (VI) gives some information on whether the impact of a variable on the BDT output is significant. It can be seen that for the low mass H^+ search Υ is the most important variable, while for high mass the components of m_T are the most important variables.

Variable	mass 90-120		mass 130-160		mass 160-180		mass 200-400		mass 500-2000	
	Rank	VI	Rank	VI	Rank	VI	Rank	VI	Rank	VI
Υ	1	0.210	2	0.180	3	0.165	4	0.093	-	
$\Delta\phi_{\tau,E_T^{miss}}$	2	0.190	1	0.276	1	0.319	1	0.385	2	0.276
p_T^{τ}	3	0.140	3	0.125	2	0.167	2	0.234	1	0.522
$\Delta\phi_{b-jet,E_T^{miss}}$	4	0.122	7	0.099	5	0.098	6	0.052	5	0.029
p_T^{b-jet}	5	0.115	4	0.118	7	0.063	7	0.049	6	0.022
E_T^{miss}	6	0.113	6	0.100	6	0.091	5	0.090	3	0.122
$\Delta R_{\tau,b-jet}$	7	0.110	5	0.103	4	0.098	3	0.098	4	0.030

TABLE 6.3: Ranking of variables used in the BDT training for the all mass range. The ranking is shown for trainings with 1-prong $\tau_{\text{had-vis}}$ candidates.

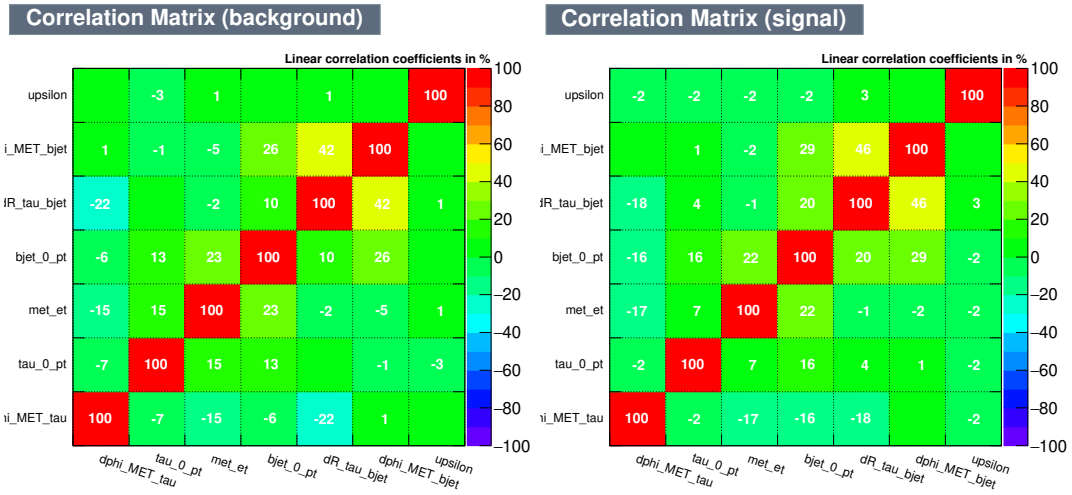

FIGURE 6.3: Correlation matrix of BDT input variables for the background (left plot) and signal (right plot), the H^+ mass range, 90-120 GeV. Here: upsilon= Υ; $dphi\_MET\_bjet$= $\Delta\phi_{b-jet,E_T^{miss}}$; dR_tau_bjet= $\Delta R_{b-jet,\tau}$; $bjet\_0\_pt$=p_T ; met_et= E_T^{miss}; tau_0_pt= p_T^{τ} and $dphi\_MET\_tau$= $\Delta\phi_{\tau,E_T^{miss}}$.

The pre-fit BDT score distributions in the signal region in the $\tau_{\text{had-vis}}$+jet for the five signal mass range trainings are shown in Figures 6.6 and 6.7. The good modelling of BDT score distributions can be observed in the SR for five H^+ mass ranges.

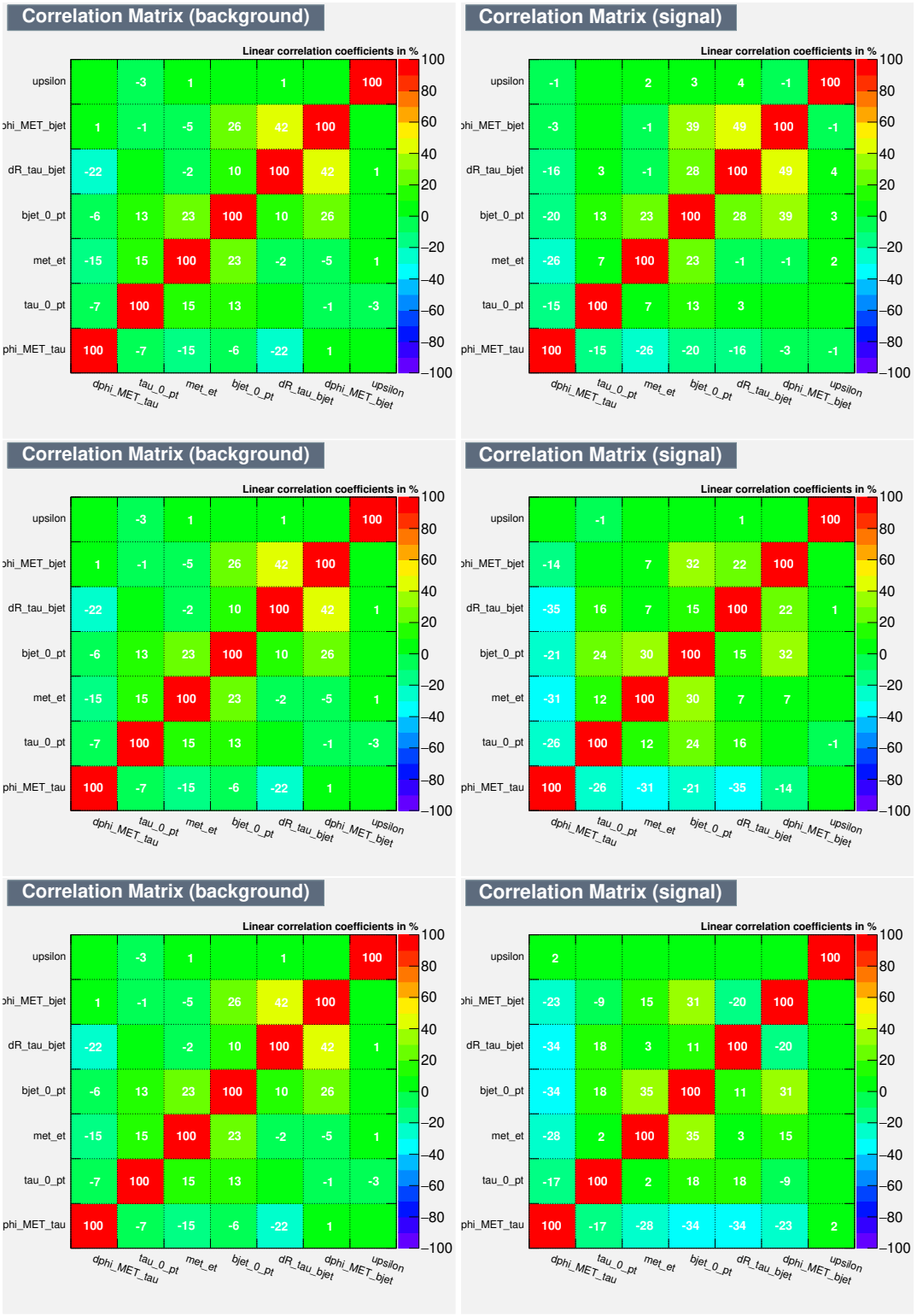

FIGURE 6.4: Correlation matrix of BDT input variables for the backgrounds (left plots) and signal (right plots), the H^+ mass ranges, 130-160 GeV (top), 160-180 GeV (middle), 200-400 GeV (bottom). Here: upsilon= Υ; *dphi_MET_bjet*= $\Delta\phi_{b-jet,E_T^{miss}}$; *dR_tau_bjet*= $\Delta R_{b-jet,\tau}$; *bjet_0_pt*=p_T; *met_et*= E_T^{miss}; *tau_0_pt*= p_T^{τ} and *dphi_MET_tau*= $\Delta\phi_{\tau,E_T^{miss}}$.

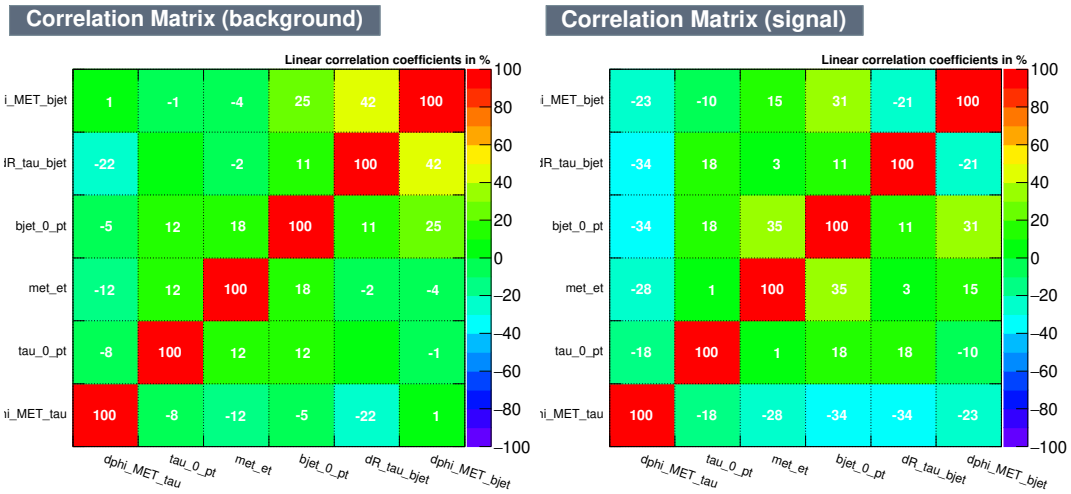

FIGURE 6.5: Correlation matrix of BDT input variables for backgrounds (left plot) and signal (right plot), the H^+ mass ranges 500-2000 GeV. Here: upsilon= Υ; $dphi\_MET\_bjet$= $\Delta\phi_{b-jet,E_T^{miss}}$; dR_tau_bjet= $\Delta R_{b-jet,\tau}$; $bjet\_0\_pt$=p_T ; met_et= E_T^{miss} ; tau_0_pt= p_T^{τ} and $dphi\_MET\_tau$= $\Delta\phi_{\tau,E_T^{miss}}$.

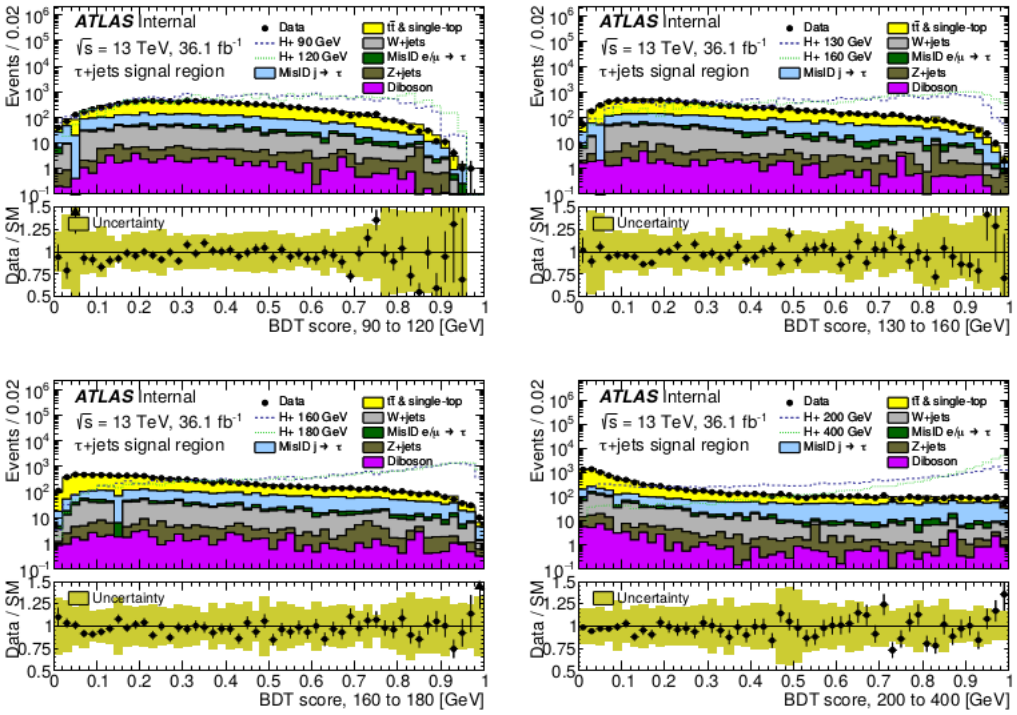

FIGURE 6.6: BDT score distributions in the signal region of the $\tau_{\text{had-vis}}$+jet channel. Shown are results for four H^+ mass ranges. The uncertainty bands in the ratio plots include both the statistical and systematic uncertainties of simulated events. The normalisation of the signal samples corresponds to the integral of the background.

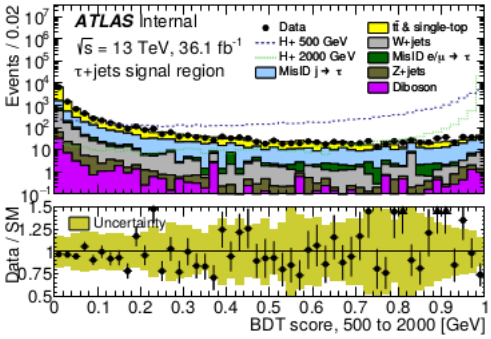

FIGURE 6.7: BDT score distributions in the signal region of the $\tau_{\text{had-vis}}$+jet channel. Shown is the result for the H^+ mass range 500-2000 GeV training. The uncertainty bands in the ratio plots include both the statistical and systematic uncertainties of simulated events. The normalisation of the signal samples corresponds to the integral of the background.

6.3.2 The impact of the Υ variable

As mentioned before, at low H^+ masses, the kinematics of the $t \to bH^+$ and $t \to bW$ decay products are similar. Therefore using only kinematical variable results in poor separation between the signal and the background. In that case, the polarization of the τ -lepton is employed as an additional discriminating variable. In all SM background processes, the $\tau_{\text{had-vis}}$ object originates from a vector-boson decay, while in the case of H^+ it stems from the decay of a scalar particle. The variable Υ is used as a measure of polarization of the $\tau_{\text{had-vis}}$ candidate for the 1-prong τ-lepton decay (see also Section 2.3.1):

$$\Upsilon \approx 2\frac{p_T^{\tau-track}}{p_T^{\tau}} - 1. \tag{6.2}$$

The distribution of Υ for predicted background, data and signal with mass of 110 GeV and 150 GeV are shown in Figure 6.8. For H^+ masses in the range 90-400 GeV, the BDT training is performed separately for events with selected 1- and 3-prong $\tau_{\text{had-vis}}$ candidate. In order to check the impact of using the Υ variable on the BDT discriminant, two trainings were performed on the 1-prong event candidates, one configuration including Υ as an input variable in the final BDT discriminant and the other one without Υ. The plots of the BDT score distribution for the mass range 90-120 GeV are shown in Figure 6.9. The ROC curve plots in Figure 6.10 (a) correspond to the two configurations, with Υ (red curve) and without Υ (black curve) for the mass range 90-120 GeV. One can see that the erea under the ROC-curve for training with Υ is larger, so it has a better performance.

Figure 6.10 (b) shows results of the full statistical analysis, background-only fit to the background+signal hypothesis, i.e. the expected limits $\sigma(pp \to [b]tH^+) \times BR(H^+ \to \tau^{\pm}\nu)$ using the two training configurations defined above. More details will be given in Section 6.5. Only statistical uncertainty is taken into account. The plots clearly show an improvement of the analysis sensitivity when Υ is added as one of the input variable to the BDT discriminant. It is particularly significant at the lowest H^+ masses, as expected.

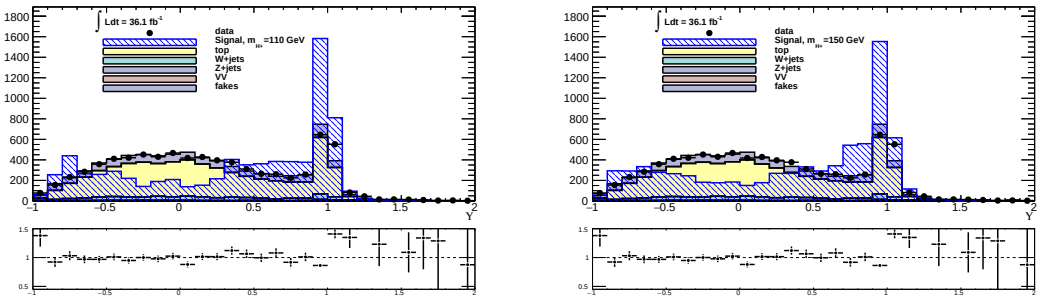

(a) (b)

FIGURE 6.8: Distribution of Υ variable for the predicted backgrounds, data and signal with m_{H^+} in the range 90-120 GeV (a), 130-160 GeV (b) for 1-prong $\tau_{\text{had-vis}}$.

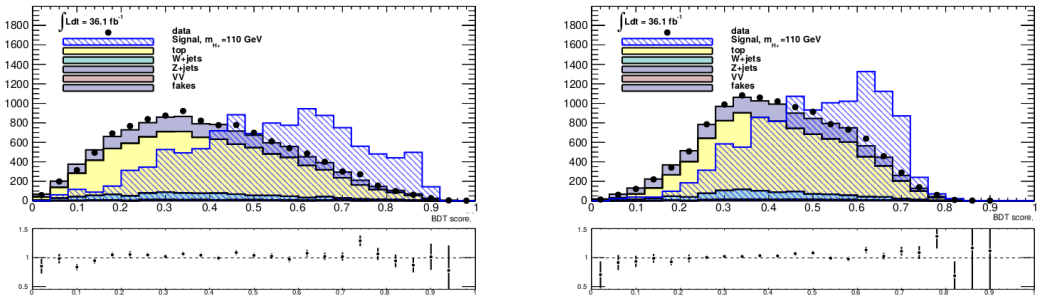

(a) (b)

FIGURE 6.9: BDT score distributions for the predicted backgrounds and data for m_{H^+} 90-120 GeV (a) with Υ and (b) without Υ.

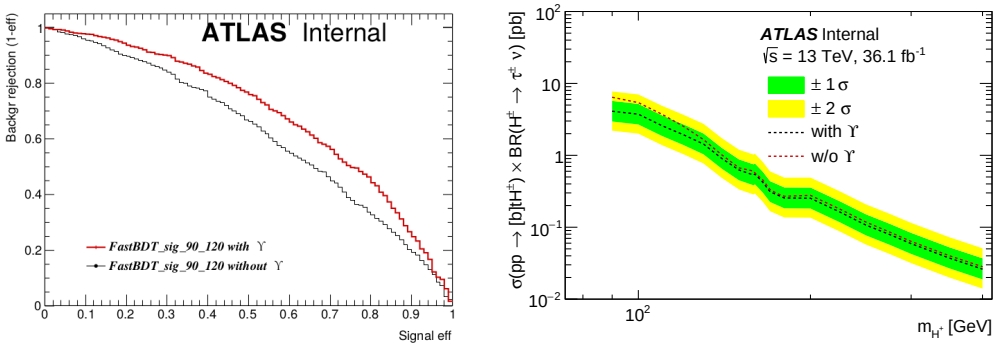

(a) (b)

FIGURE 6.10: ROC curve, showing the background rejection as a function of the signal efficiency achieved by the MVA output variable trained on m_{H^+} in the range 90-120 GeV with and without Υ (a); Expected 95% CL exclusion limits on $\sigma(pp \to btH^+) \times BR(H^+ \to \tau^{\pm}\nu)$ for charged Higgs boson production as a function of m_{H^+} in 36.1fb^{-1} of pp collision data at $\sqrt{s}$ = 13 TeV for BDT output when Υ is used as an input variable in comparison with the case without Υ for 1 prong τ leptons (b).

6.4 Background estimation

The dominant background processes are categorized based on the object that gives rise to the identified $\tau_{\text{had-vis}}$ candidate. Simulation is used to estimate backgrounds in which $\tau_{\text{had-vis}}$ comes from an electron, muon or a hadronically decaying τ-lepton. Otherwise, a data-driven method is employed. Electrons faking $\tau_{\text{had-vis}}$ candidates are not guaranteed to be well modeled in simulation. In order to study this background component, a dedicated control region enriched in Z→ee events is defined, using the following event selection:

- single-electron trigger, the same as used in the $\tau_{\text{had-vis}}$+lepton signal region;
- exactly one tight electron with $E_T > 30$ GeV matched to the trigger;
- exactly one medium $\tau_{\text{had-vis}}$ candidate with $p_T^{\tau} > 40$ GeV and an electric charge opposite to that of the selected electron;
- no b-tagged jets or muons;
- at least one jet with $p_T > 25$ GeV.

The topology of the selected events has a prompt electron that is reconstructed and identified as a medium $\tau_{\text{had-vis}}$ candidate, but not as an electron. The distribution of the e-$\tau_{\text{had-vis}}$ visible mass, as well as the transverse mass of the $\tau_{\text{had-vis}}$+ E_T^{miss} system, as obtained with the event selection described above, are shown in Figure 6.11. The modeling of electrons faking a $\tau_{\text{had-vis}}$ candidate is found to be satisfactory in the Sherpa Z→ee samples. Therefore, no additional corrections are applied, beyond the $e \to \tau_{had-vis}$ scale factors.

6.4.1 Fake factor data-driven method

An important source of background in physics analyses is object misidentification. Jets genuinely fake hadronically decaying τ leptons, and all τ-related analyses suffer from such backgrounds. These are quark- or gluon-initiated jets fulfilling the selection criteria of the signal region. The fake τ background is not well modeled by MC simulation. Therefore, data-driven techniques had to be developed. There are different approaches for the estimation of jet-to-τ misidentified contribution. In this analysis, we focus on the fully data-driven fake factor (FF) method. In this method, an anti-τ selection is defined by requiring the τ candidate to fail the identification criteria of the nominal selection. The fake factor is defined as the ratio between the number of jets reconstructed as τ candidates and fulfilling the nominal τ identification criteria to the number of corresponding candidates failing the identification criteria (anti-τ) and is measured in a dedicated control region (CR) enriched with fake τ leptons:

$$\text{FF} = \frac{\text{N}^{\text{CR}}_{\tau-ID}(\text{data}) - \text{N}^{\text{CR}}_{\tau-ID}(\text{MC}, \tau \neq j)}{\text{N}^{\text{CR}}_{\text{anti}-\tau-ID}(\text{data}) - \text{N}^{\text{CR}}_{\text{anti}-\tau-ID}(\text{MC}, \tau \neq j)}. \tag{6.3}$$

The contribution from true τ events in either category is subtracted using simulation. The fake factors are usually measured in bins of lepton p_T and the number of associated tracks in the τ hadronic decay (1-prong, 3-prong). In order to estimate the yield of fake τ background in the signal region, an anti-τ region is defined. This region is identical to the signal region, but the τ candidate fails the τ identification

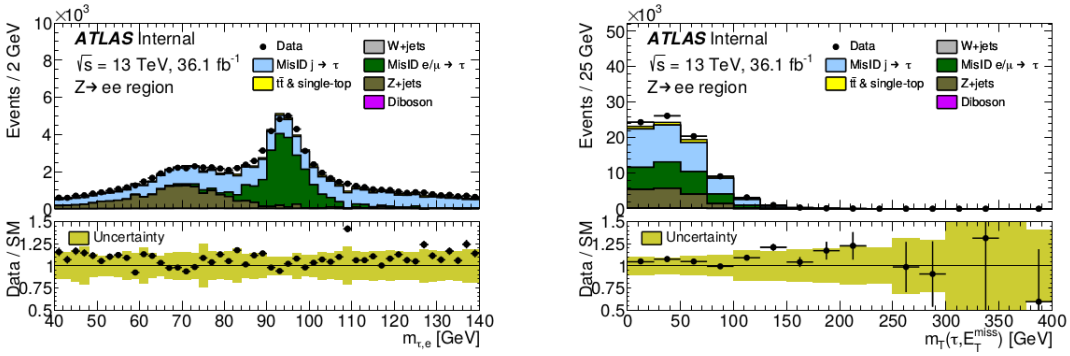

FIGURE 6.11: Distribution of the $e \to \tau_{\text{had-vis}}$ visible mass and transverse mass of the $\tau_{\text{had-vis}}$+ E_T^{miss} system. The uncertainty band in the ratio plots includes the total statistical and systematic uncertainty of the simulated events.

requirement instead of fulfilling it. Then in bin i, the number of events with a jet misidentified as τ is given by:

$$N^{\tau}_{\text{fakes}}(i) = (N^{\text{SR}}_{\text{anti}-\tau-ID}(\text{data})(i) - N^{\text{SR}}_{\text{anti}-\tau-ID}(\text{MC}, \tau \neq j)(i)) \times \text{FF}(i). \quad (6.4)$$

Note that the signal contamination to the $N^{\text{SR}}_{\text{anti}-\tau-ID}$ is expected to be negligable.

6.4.2 Considering quark/gluon jet composition

The fake factors in a selection region depend on the fraction of gluon- and quark-initiated jets, as the probability for a hadronic jet to fake a τ depends on its origin. Depending on the analysis, there can be one or several control regions where the fake factors are measured. If there is only one control region, one must ensure that the jet fractions are similar to what is found in the signal region. When two (or more [158]) control regions are used, and one is enriched with gluon-initiated jet, the FF for each bin can be calculated as follows:

$$\text{FF} = \alpha_g \times \text{FF}(g) + [1 - \alpha_g] \times \text{FF}(q) \quad (6.5)$$

where FF(g) and FF(q) are the fake factors in a control region dominated by gluon-initiated jets and other control regions (with a smaller fraction of gluon-initiated jets) respectively, and α is the fraction of gluon-initiated jets in the signal-like anti-τ region. Therefore, one needs to estimate the α_g.

6.4.3 Fake factor method in the $H^+ \to \tau\nu$ analysis

In the $H^+ \to \tau\nu$ analysis [32], the anti-τ control region is defined as a subset of reconstructed $\tau_{\text{had-vis}}$ candidates that fail the loose working point, with a lower cut on the transformed $\tau_{\text{had-vis}}$ BDT score at 0.02 in order to keep the $\tau_{\text{had-vis}}$ object and event topology similar to the signal region. For multijet events, the $\tau_{\text{had-vis}}$ candidates with a low value of the transformed $\tau_{\text{had-vis}}$ BDT score (below 0.02) typically are not representative of fake $\tau_{\text{had-vis}}$ objects in the signal region [159].

In order to account for different sources of misidentified hadronically decaying τ leptons [160] in the signal region, fake factors are calculated in two control regions of

Multijet CR	W+jets CR
number of jets ≥ 1	one electron or muon
$E_T^{miss} < 80$ GeV	at least one reconstructed $\tau_{\text{had-vis}}$ candidate
b-jet veto, electron and muon veto	b-jet veto
p_T of $\tau > 30$ GeV	p_T of electron or muon > 30 GeV
$m_T(\tau\ , E_T^{miss}) > 50$ GeV	$60 < m_T(\ell, E_T^{miss}) < 160$ GeV
transformed $\tau_{\text{had-vis}}$ BDT score > 0.02	transformed $\tau_{\text{had-vis}}$ BDT score > 0.02

TABLE 6.4: Control regions for fake factor measurement in $H^+ \to \tau\nu$ analysis [32].

the data with different fractions of quark- and gluon-initiated jets, and then they are combined. The first control region with a significant fraction of gluon-initiated jets (multijet CR) is defined as shown in Table 6.4 (left). Such events are collected using a combination of multijet triggers. The other control region enriched in quark-initiated jets (W+jets CR) is defined as shown in Table 6.4 (right) and uses a single lepton trigger. The transverse mass m_T is defined in Equation 6.1. In the second control region the transverse mass variable $m_T(\ell, E_T^{miss})$ is computed as in the previous case but using the lepton p_T and separation in the azimuthal angle from the missing transverse momentum of the event. In the multijet CR, the contamination arising from correctly reconstructed and identified $\tau_{\text{had-vis}}$ objects is small (5%). In the W+jets CR, this contamination is about 10%. In the corresponding anti-τ regions, the fraction of true $\tau_{\text{had-vis}}$ objects is negligible. When computing the fake factors, the contamination of such truth-matched objects is subtracted using the predictions from MC simulation. The fake factors for two control regions as a function of p_T^τ and number of tracks is presented in Figure 6.12 (a).

In the anti-$\tau_{\text{had-vis}}$ regions corresponding to the nominal event selections, the fraction of quark- and gluon-initiated jets misidentified as $\tau_{\text{had-vis}}$ candidates are then measured using a template-fit approach, based on variables that are sensitive to the jet origin. For 1-prong $\tau_{\text{had-vis}}$ candidates, the $\tau_{\text{had-vis}}$ jet width is used which is defined as:

$$w_\tau = \frac{\Sigma[p_T^{\text{track}} \times \Delta R(\tau_{\text{had-vis}}, \text{track})]}{\Sigma p_T^{\text{track}}}, \tag{6.6}$$

where the sum runs over the tracks satisfying $\Delta R(\tau_{\text{had-vis}}, track) < 0.4$. For 3-prong $\tau_{\text{had-vis}}$ candidates, the τ identification score (based on the multivariate BDT approach) is used as a template. In order to account for unknown gluon- and quark-initiated jet fraction in the signal region, a linear combination of the two templates is defined as :

$$f(x|\alpha_{MJ}) = \alpha_{MJ} \times f_{MJ}(x) + (1 - \alpha_{MJ}) f_{W+\text{jets}}(x), \tag{6.7}$$

with a free parameter α_{MJ} and where f_{MJ} and $f_{W+\text{jets}}$ are two binned templates of the $\tau_{\text{had-vis}}$ jet width and the $\tau_{\text{had-vis}}$ BDT score obtained in the multijet and W+jets control regions defined above, respectively. This linear combination is fitted to the normalized distribution measured in the signal region in every bin of p_T by minimizing the χ^2 with respect to the α_{MJ}. Finally, from the best fit values of α_{MJ}, combined fake factors are obtained by:

$$FF^{\text{combined}}(i) = \alpha_{MJ}(i) \times FF^{MJ}(i) + (1 - \alpha_{MJ}) \times FF^{W+jets}(i). \tag{6.8}$$

where i refers to the bin index in the parametrization of the fake factor. The combined fake factors, used in the $\tau_{\text{had-vis}}$+jets and $\tau_{\text{had-vis}}$+lepton signal regions are shown in Figure 6.12 (b).

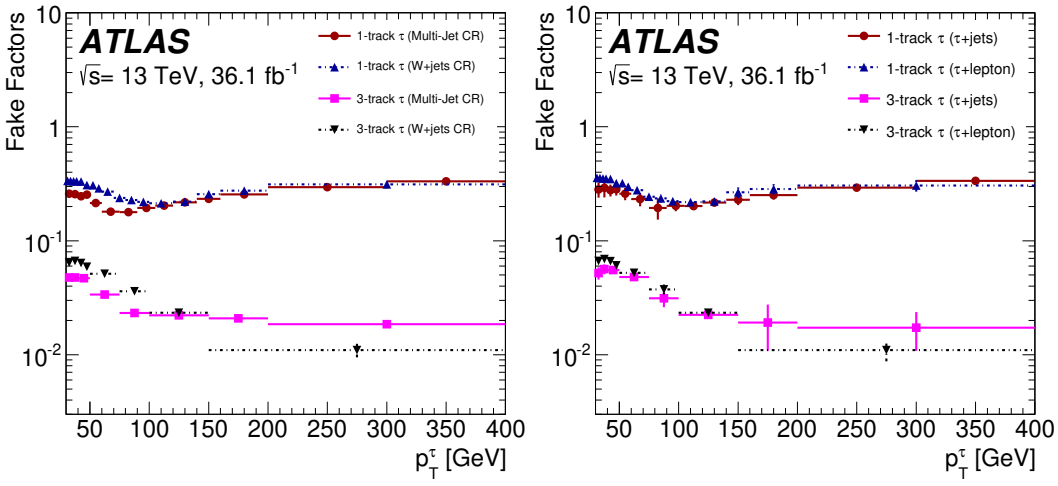

(a) (b)

FIGURE 6.12: Fake factors parameterized as a function of p_T^τ and the number of tracks. The fake factor in the multijet and W+jet CRs. Errors represent the statistical uncertainties (a). Fake factors after reweighting by α_{MJ} in the $\tau_{\text{had-vis}}$+jets and $\tau_{\text{had-vis}}$+lepton channel (b) [6].

Note that the anti-τ region used to obtain the template fits is defined with non-loose candidates, while the anti-$\tau_{\text{had-vis}}$ region used to obtain the fake factors is defined with non-loose candidates that also have a lower cut on the transformed $\tau_{\text{had-vis}}$ BDT score. Therefore, the α_{MJ} parameter obtained from fit gives the gluon-initiated jet fraction for a more inclusive sample. This looser selection was chosen to have a better separation between gluon- and quark-initiated jets and hence minimize the error on the fit. In order to correct for the gluon- and quark-initiated jet fractions of the actual anti-$\tau_{\text{had-vis}}$ region used for the fake-factor estimation, a corrected α_{MJ} is used, defined as:

$$\alpha_{\text{MJ}}^{\text{corr}} = \frac{\zeta_{\text{MJ}} \times \alpha_{\text{MJ}}}{\zeta_{\text{MJ}} \times \alpha_{\text{MJ}} + \zeta_{\text{W+jets}} \times (1 - \alpha_{\text{MJ}})} \tag{6.9}$$

where ζ_{MJ} and $\zeta_{\text{W+jets}}$ are fractions of events in the non-loose multijet and W+jets control regions, respectively, that pass the lower cut on the transformed $\tau_{\text{had-vis}}$ BDT score.

6.4.4 Validation of the fake τ background modeling

In order to validate fake τ background modeling, two additional validation regions are used: a $\tau_{\text{had-vis}}$+jet signal like region with a b-veto cut and a $\tau_{\text{had-vis}}$+lepton signal-like region with same sign charges. Figure 6.13 shows the distribution of p_T^τ and $m_T(\tau, E_T^{miss})$ obtained in these two regions: good modeling of fake $\tau_{\text{had-vis}}$ component can be observed.

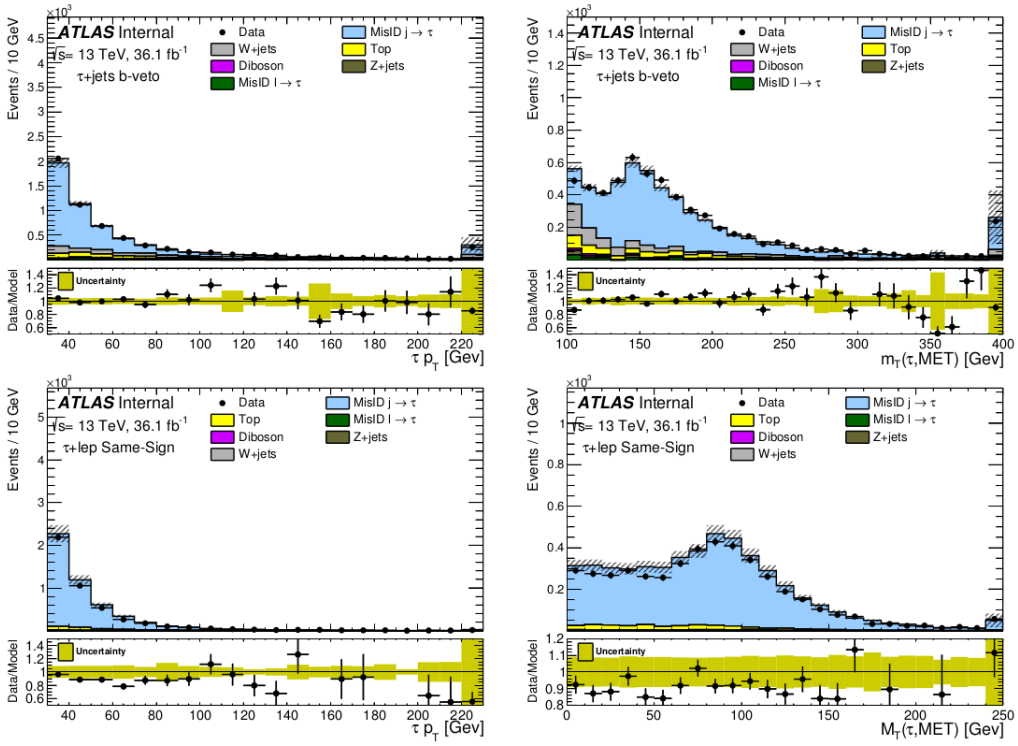

FIGURE 6.13: $j \rightarrow \tau_{\text{had-vis}}$ background validation plots of p_T^{τ} and $m_T(\tau, E_T^{miss})$ are obtained in $\tau_{\text{had-vis}}$+jet signal-like region with a b-veto cut (top) and same sign $\tau_{\text{had-vis}}$+lepton signal-like region (bottom) [6]. The uncertainty bands are statistical only.

6.4.5 The Υ correction for fake-$\tau_{\text{had-vis}}$ candidates

Hadronic τ decays are identified using a BDT, which is based on several input variables [160], where one of them, the leading-track momentum fraction, is strongly correlated with Υ. As a result, the distribution of the Υ variable significantly differs between $\tau_{\text{had-vis}}$ and anti-$\tau_{\text{had-vis}}$ candidates. Since the Υ variable is used as an input to the final BDT discriminant of the analysis, its shape should be modeled properly for the $\tau_{\text{had-vis}}$ candidates in the signal region. The Υ variable shows no correlation with any of the other variables that are used as input to the final BDT. Hence, its shape is corrected using inverse transform sampling (Smirnov transformation) [161]. The Smirnov transformation works as follows: shapes of the Υ variable are obtained for $\tau_{\text{had-vis}}$ and anti-$\tau_{\text{had-vis}}$ in the control region, then a cumulative distribution function (CDF) is calculated from these shapes (F(Υ)). Using an inverse transformation of F, the corrected value is obtained:

$$\Upsilon_{\text{corr}} = \text{F}_{\tau}^{-1}(\text{F}_{\text{anti}-\tau}(\Upsilon)) \tag{6.10}$$

where $\text{F}_{\tau}^{-1}(x)$ is the inverse of the cumulative distribution function of $\tau_{\text{had-vis}}$ candidates and $\text{F}_{\text{anti}-\tau}(x)$ is the cumulative distribution function of anti-$\tau_{\text{had-vis}}$ candidates. Figure 6.14 (a) shows the distribution of the Υ variable for $\tau_{\text{had-vis}}$ and anti-$\tau_{\text{had-vis}}$ 1-prong candidates in the W+jets control region and (b) shows the CDF of the Υ variable in the W+jets control region. The distribution of Υ before and after the Smirnov transformation is shown in Figure 6.15 for a $\tau_{\text{had-vis}}$+jet signal-like region with a b-jet veto.

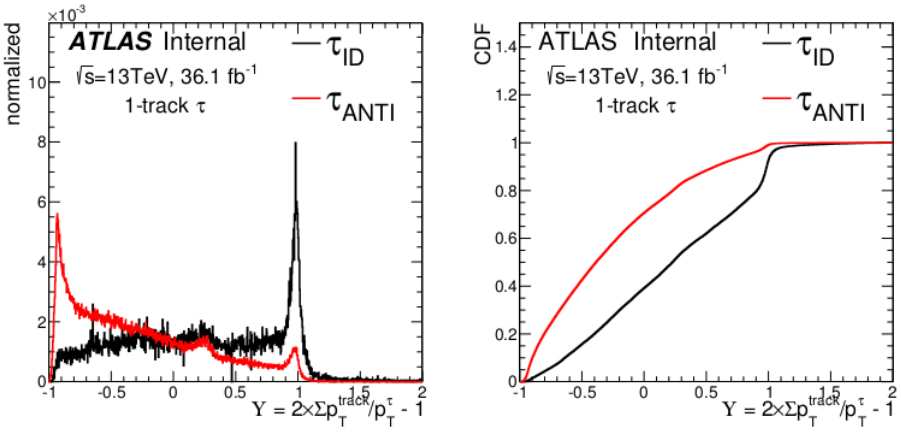

(a) (b)

FIGURE 6.14: Distribution of Y for $\tau_{\text{had-vis}}$(black) and anti-$\tau_{\text{had-vis}}$ (red) candidates in the W+jets control region (a). CDF of Y for $\tau_{\text{had-vis}}$(black) and anti-$\tau_{\text{had-vis}}$ (red) candidates in the W+jets control region (b) [32].

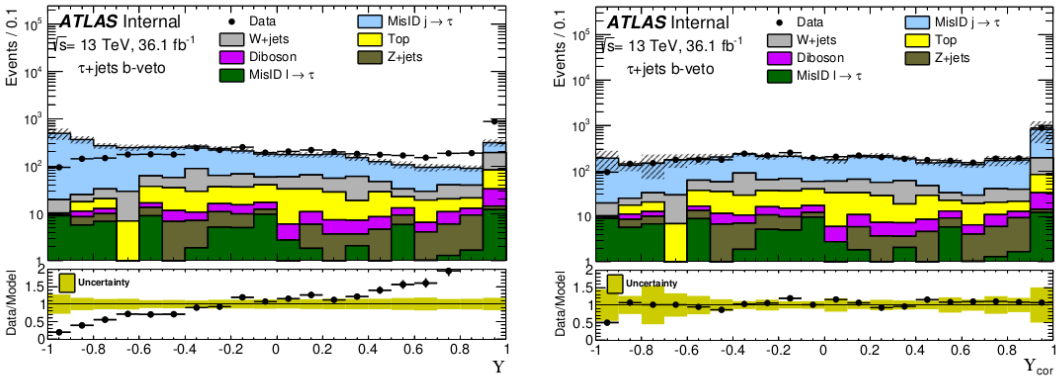

(a) (b)

FIGURE 6.15: Distribution of Y before (a) and after (b) Smirnov transformation in the signal-like region with a b-jet veto applied [32]

6.5 Systematic uncertainties

Several sources of systematic uncertainty affect the normalisation of the signal and background processes, as well as the shape of the final discriminant distribution. Individual sources of systematic uncertainty are assumed to be uncorrelated. However, when the systematic variations are applied to different samples of simulated events, correlations of a given systematic uncertainty are taken into account across processes. All sources of systematic uncertainty, i.e. the reconstruction and identification efficiencies, as well as the energy scales and resolutions of $\tau_{\text{had-vis}}$ candidates, electrons, muons and (b-tagged) jets are considered, including their impact on the reconstructed E_T^{miss}. The dominant experimental sources of systematic

uncertainties come from the data-driven fake τ estimation in both $\tau_{\text{had-vis}}$+jet and $\tau_{\text{had-vis}}$+lepton channel. The subdominant one is the jet energy scale uncertainty. For high m_{H^+} the largest uncertainty comes from signal modeling. The impact of various sources of systematic uncertainty is estimated by comparing 95% CL limits on $\sigma(pp \to tbH^+) \times \mathcal{B}(H^+ \to \tau\nu)$ taking only statistical uncertainties into account and obtained when a certain set of systematic uncertainties is added in the limit-setting procedure, as summarized in Table 6.5.

Source of systematic uncertainty	Impact on the expected limit (stat. only) in % M_{H^+} = 170 GeV	M_{H^+} = 1000 GeV
Experimental		
luminosity	2.9	0.2
trigger	1.3	<0.1
$\tau_{\text{had-vis}}$	14.6	0.3
jet	16.9	0.2
electron	10.1	0.1
muon	1.1	<0.1
E_T^{miss}	9.9	<0.1
Fake-factor methods	20.3	2.7
Υ modeling	0.8	-
Signal and background models		
$t\bar{t}$ modeling	6.3	0.1
W/Z+jets modeling	1.1	<0.1
cross-section(W/Z/VV/t)	9.6	0.4
H^+ signal modeling	2.5	6.4
All	52.1	13.8

TABLE 6.5: Impact of systematic uncertainties on the expected 95% CL limit on $\sigma(pp \to tbH^+) \times \mathcal{B}(H^+ \to \tau\nu)$, for two H^+ hypotheses: with mass of 170 GeV and 1000 GeV. The impact is obtained by comparing the expected limit considering only statistical uncertainties (stat. only) with the expected limit when a certain set of systematic uncertainties is added in the limit-setting procedure [6]

.

6.6 Statistical interpretation of results

The statistical interpretation of the result of the analysis is based on a simultaneous fit of the parameter of interest (signal strength), defined as $\mu \equiv \sigma(pp \to tbH^+) \times \mathcal{B}(H^+ \to \tau\nu)$.

The test statistic $\tilde{q}_\mu$ [162] computed from the profile likelihood ratio, is used to test the compatibility of the data with the background-only and signal+background hypotheses, and throughout the statistical analysis the asymptotic approximation is used. The nuisance parameters θ are from negative log-likelihood minimization which encode statistical and systematic uncertainties.

Three signal regions and one control region enriched in $t\bar{t}$ events are considered in the simultaneous fit:

1. For the BDT score distributions in the three signal regions of the $\tau_{\text{had-vis}}$+jets, $\tau_{\text{had-vis}}$+electron and $\tau_{\text{had-vis}}$+muon channels, binned likelihood functions are

used. The binning of the discriminating variable was optimized to maximize the sensitivity of the analysis prior to looking at the data in the signal regions.

2. In the control region enriched with $t\bar{t}$ events, a single-bin likelihood is used: this control region is defined with the same event selection as the $\tau_{\text{had-vis}}$+lepton signal region, but with the requirement of an $e\mu$ pair instead of the $e\mu$+$\tau_{\text{had-vis}}$.

The distributions of the BDT score in the five mass ranges of the charged Higgs boson which were used in the analysis are shown in Figure 6.16 for the $\tau_{\text{had-vis}}$+jets signal region, as well as Figures 6.17 and 6.18 for $\tau_{\text{had-vis}}$+electron and $\tau_{\text{had-vis}}$+muon signal regions, respectively. All plots are obtained from the statistical fitting procedure with the background-only hypothesis. The binning shown in the figures is also used in the statistical analysis.

It is found that data is consistent with the background-only hypothesis (the smallest p_0 value is 0.3 around 350 GeV). The signal+background hypothesis is excluded at the 95% confidence level (CL), by using the CL_s procedure [163] on $\sigma(pp \to tbH^+) \times \mathcal{B}(H^+ \to \tau\nu)$ for the full mass range investigated, as well as on $\mathcal{B}(t \to bH^+) \times \mathcal{B}(H^+ \to \tau\nu)$ in the low H^+ mass range.

The expected and observed exclusion limits as a function of the H^+ mass hypothesis are shown in Figure 6.19. In this search, the observed limits range from 4.2 pb to 2.5 fb considered over the mass range. The limits are interpolated between the H^+ mass regions which are tested explicitly. The bias in the expected limits from this interpolation is found to be smaller than the statistical uncertainty. The limits on $\sigma(pp \to tbH^+) \times \mathcal{B}(H^+ \to \tau\nu)$, for the mass range between 90 to 160 GeV, translate into observed limits between 0.25% and 0.031% for the branching fraction $\mathcal{B}(t \to bH^+) \times \mathcal{B}(H^+ \to \tau\nu)$ with the assumption that the production cross-section is equal to that of $t\bar{t}$ pairs. For H^+ masses of 170 GeV and 1 TeV, the 95% CL exclusion limits on tanβ as a function of the H^+ mass in the context of the hMSSM scenario are shown in Figure 6.20. All tanβ values are excluded for $m_{H^+} \lesssim 160$ GeV. At tanβ=60, above which no reliable theoretical calculations exist, the charged Higgs boson mass range up to 1100 GeV is excluded, therefore significantly improving on the limits set based on data collected in 2015 with integrated luminosity of 3.2 fb^{-1}.

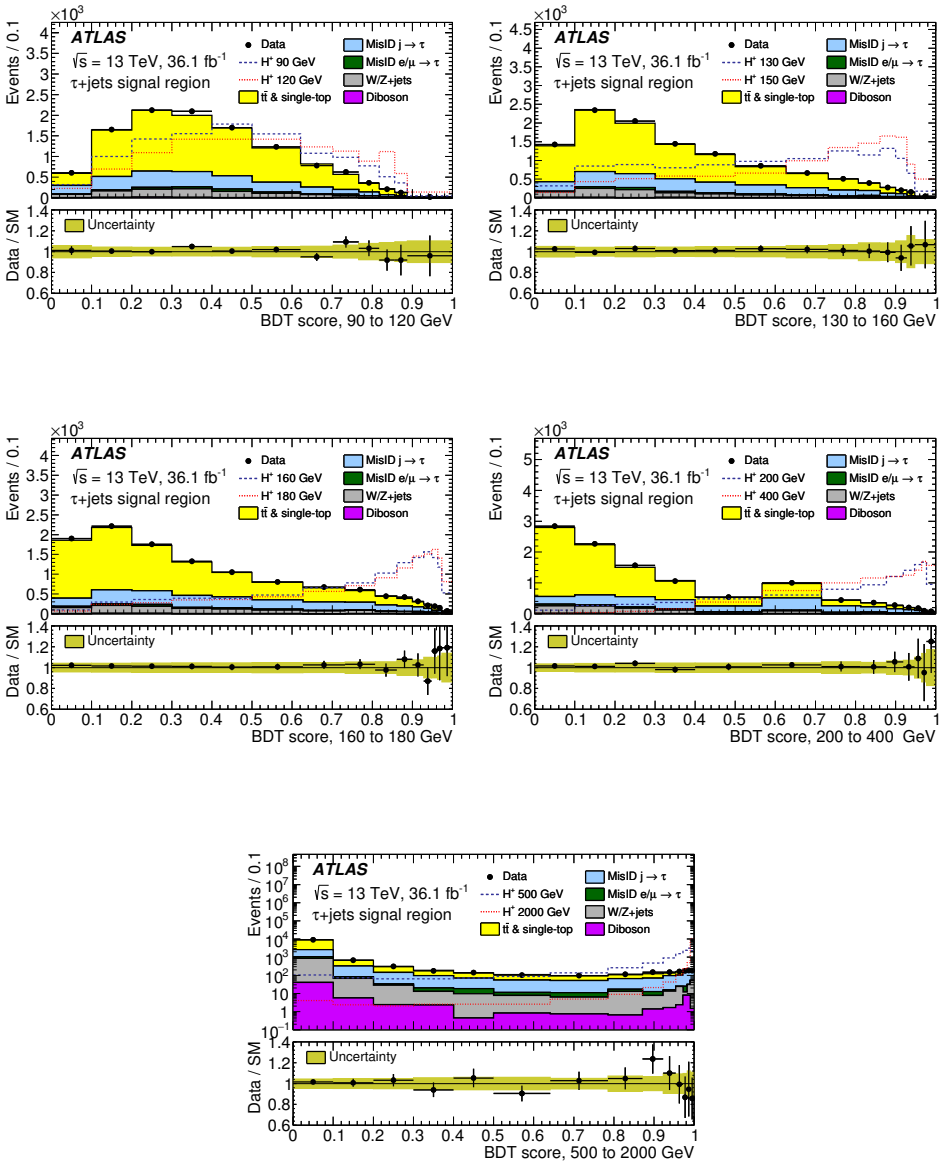

FIGURE 6.16: Distributions of the BDT score in the the $\tau_{\text{had-vis}}$+jets signal region, in the five mass ranges used for BDT training, after a fit to the data with the background-only hypothesis. The lower panel of each plot shows the ratio of data to the SM background prediction. The uncertainty bands include all statistical and systematic uncertainties. The normalization of the signal (shown for illustration) corresponds to the integral of the background [6].

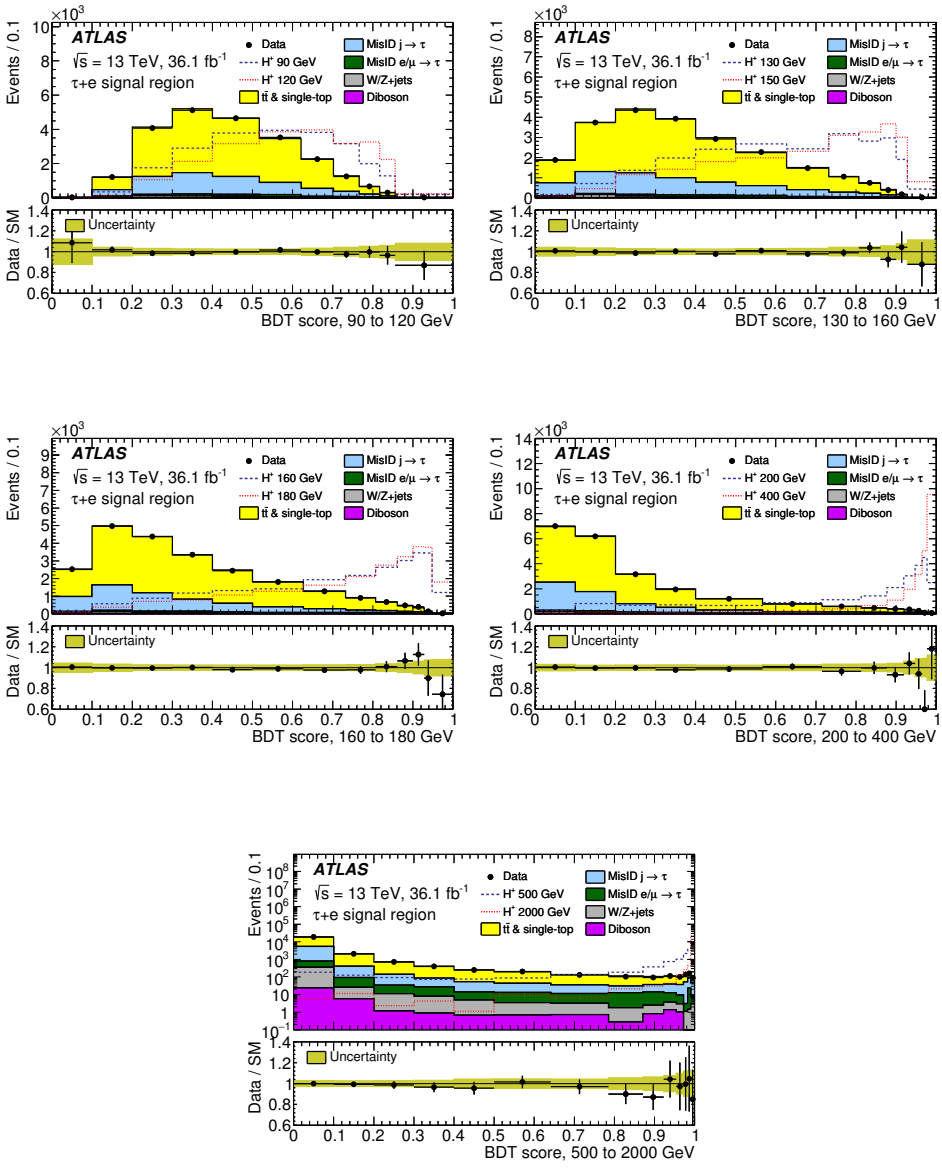

FIGURE 6.17: Distributions of the BDT score in the the $\tau_{\text{had-vis}}$+electron signal region, in the five mass ranges used for BDT training, after a fit to the data with the background-only hypothesis. The lower panel of each plot shows the ratio of data to the SM background prediction. The uncertainty bands include all statistical and systematic uncertainties. The normalization of the signal (shown for illustration) corresponds to the integral of the background [6].

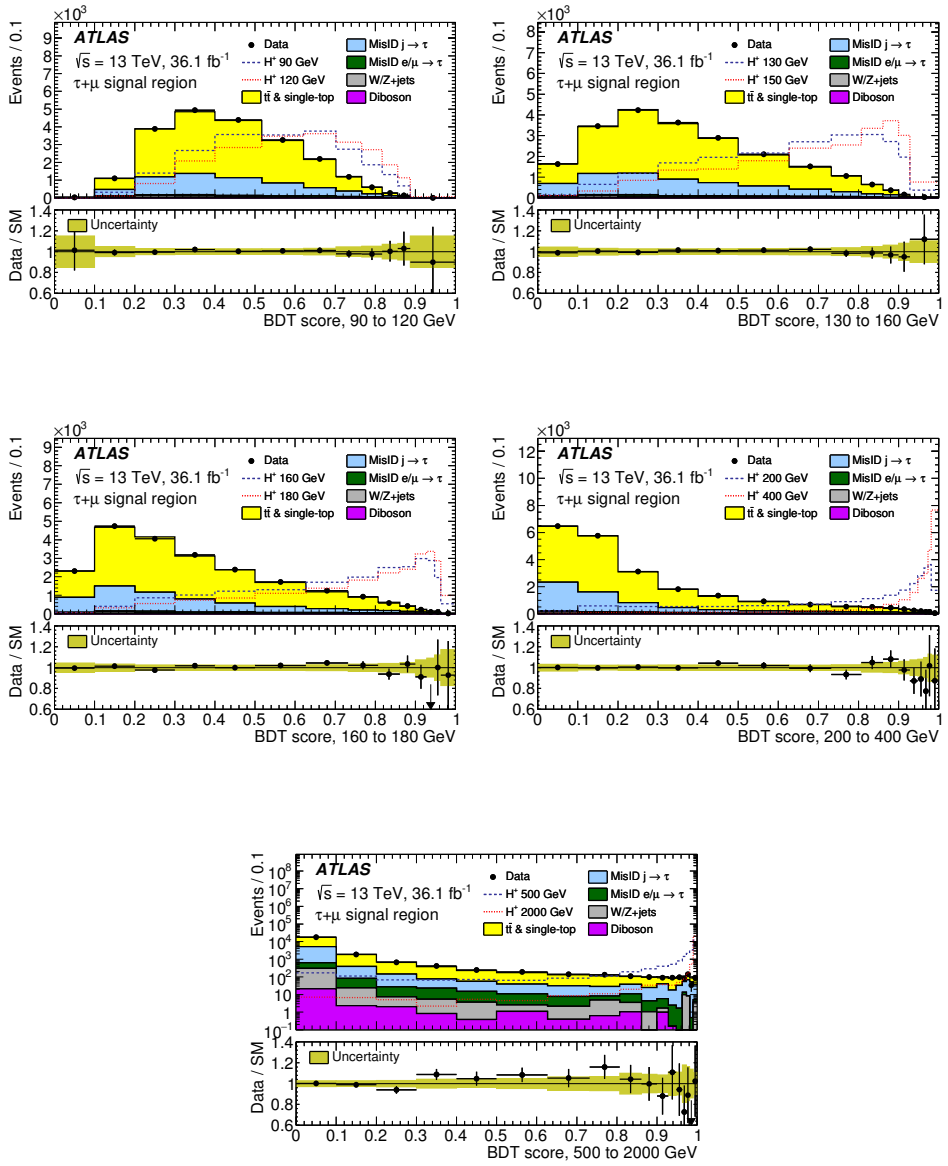

FIGURE 6.18: Distributions of the BDT score in the the $\tau_{\text{had-vis}}$+muon signal region, in the five mass ranges used for BDT training, after a fit to the data with the background-only hypothesis. The lower panel of each plot shows the ratio of data to the SM background prediction. The uncertainty bands include all statistical and systematic uncertainties. The normalization of the signal (shown for illustration) corresponds to the integral of the background [6].

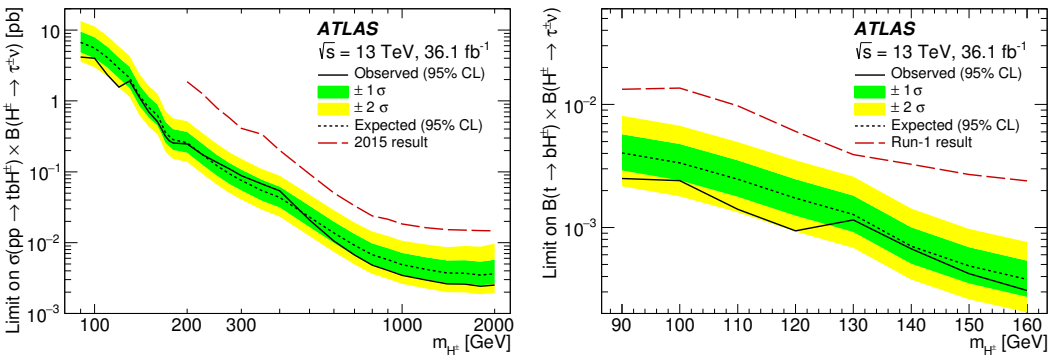

(a) (b)

FIGURE 6.19: 95% CL exclusion limits observed and expected on (a) $\sigma(pp \to tbH^+) \times \mathcal{B}(H^+ \to \tau\nu)$ and (b) $\mathcal{B}(t \to bH^+) \times \mathcal{B}(H^+ \to \tau\nu)$ as a function of the charged Higgs boson mass in 36.1 fb^{-1} of pp collision data at $\sqrt{s}$ =13 TeV, after combination of the $\tau_{\text{had-vis}}$+jets and $\tau_{\text{had-vis}}$+lepton channels. In the case of the expected limits, one- and two-standard-deviation uncertainty bands are also shown. As a comparison, the observed exclusion limits on $\mathcal{B}(t \to bH^+) \times \mathcal{B}(H^+ \to \tau\nu)$ obtained with Run-I data at $\sqrt{s}$ = 8 TeV [117] and on $\sigma(pp \to tbH^+) \times \mathcal{B}(H^+ \to \tau\nu)$ obtained with data collected in 2015 at $\sqrt{s}$ =13 TeV [123] are also shown [6].

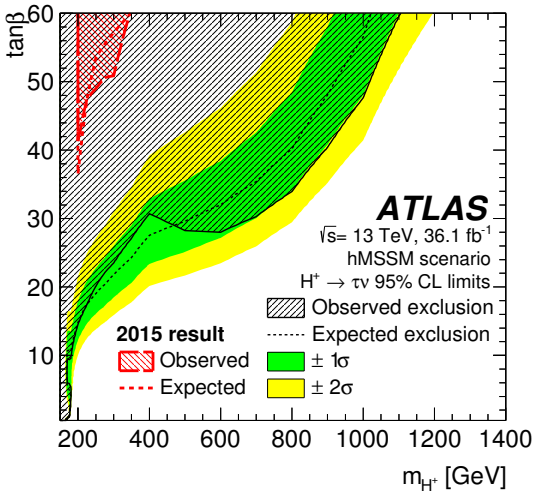

FIGURE 6.20: 95% CL exclusion limits on tanβ as a function of m_{H^+}, shown in the context of the hMSSM, for the regions in which theoretical predictions are available ($0.5 \leq \tan\beta \leq 60$). In the case of the expected limits, one- and two-standard-deviation uncertainty bands are also shown. As a comparison, the red curves near the upper-left corner show the observed and expected exclusion limits based on 3.2 fb^{-1} of data collected in 2015 at $\sqrt{s}$ =13 TeV [6].

Chapter 7

Fake τ background estimation in the full Run-II data analysis

7.1 Introduction

The search for a charged Higgs boson using the $H^+ \to \tau\nu$ decay for data collected with the ATLAS experiment at the LHC in 2015 and 2016 has been presented in the previous Chapter. Here, the background modeling of jets misidentified as τ leptons for the entire Run-II data set collected in the years 2015-2018, and corresponding to integrated luminosity of 138.9 fb^{-1}, is presented. For this round of analysis, data has been reprocessed using improved reconstruction and identification algorithms. Likewise, new Monte Carlo samples, called the MC16 campaign, have been produced. Samples MC16a are to be compared with 2015 and 2016 data, MC16d to be compared with 2017 data and MC16e to be compared with 2018 data. The MC generators used for the SM background samples in MC15 campaign are listed in Table 6.1. With respect to MC15, in MC16 `Powheg & Pythia8` were used for the production of single top-quark and $t\bar{t}$ samples; additionally the `A14` PDFset was used for the latter. As mentioned in the previous Chapter, the dominant background processes can be categorized based on the object that gives rise to the reconstructed and identified hadronically decaying τ candidate. Apart from true τ leptons, these objects are mostly quark- or gluon-initiated jets passing the selection criteria of the signal region. The fake τ background estimation using the data-driven fake factor method described in Section 6.4.3 is presented in the Section 7.2. Additionally, in Section 7.3 the possibility of using MVA trained variables sensitive to jet composition is explored. Section 7.5 is dedicated to the validation of the fake factor method using MC generated samples. The systematic uncertainties of the fake factor method are presented in Section 7.6. Finally, the modified discriminant in the full Run-II analysis and the expected sensitivity are presented in Section 7.7.

7.2 Fake factor estimation

The fake factors are extracted in the control regions enriched in either gluon-initiated or quark-initiated jets. The baseline fake factors are extracted by using the same control regions as defined in Table 6.4 and the anti-τ region defined in Section 6.4.3.

The estimation of α_{MJ} is done in the following way:

- The normalized distributions of templates for anti-$\tau_{\text{had-vis}}$ candidates are obtained in the multijet (MJ) and W+jet control regions, for different bins of p_T^{τ} and the number of associated tracks (hereafter called tracks or prongs) of the fake $\tau_{\text{had-vis}}$ ($\mathrm{P}_{\text{bin}}^{\mathrm{MJ}}(\mathrm{x})$ and $\mathrm{P}_{\text{bin}}^{\mathrm{W+jet}}(\mathrm{x})$).

- The weighted combination of the two shapes is:

$$P_{bin}^{\alpha_{MJ}}(x) = \alpha_{MJ} \times P_{bin}^{MJ}(x) + (1 - \alpha_{MJ}) \times P_{bin}^{W+jet}(x). \tag{7.1}$$

- The fit is done to the shape measured for anti-$\tau_{\text{had-vis}}$ candidates in the region of interest $P_{bin}^{ROI}(x)$, e.g. the signal region, by minimizing χ^2 as a function of α_{MJ}, where $\sigma_{bin}(x)$ is the statistical uncertainty on the bin content and K+1 is the number of bins in the template distribution (later denoted as number of degrees of freedom, or ndf):

$$\chi^2_{bin}(\alpha_{MJ}) = \sum_{x=0}^{K+1} \frac{(P_{bin}^{\alpha_{MJ}}(x) - P_{bin}^{ROI}(x))^2}{(\sigma_{bin}^{template}(x))^2 + (\sigma_{bin}^{ROI}(x))^2}. \tag{7.2}$$

The distribution of χ^2_{bin} can be described by the χ^2-function with K degrees of freedom, which has a mean and a variance of K and 2K, respectively. For 1-prong $\tau_{\text{had-vis}}$ candidates, the variable sensitive to the jet origin and used for the template is τ jet width, while for 3-prong candidates the variable is the transformed $\tau_{\text{had-vis}}$ BDT score.

The fit of α_{MJ} in the $\tau_{\text{had-vis}}$+jets and $\tau_{\text{had-vis}}$+lepton signal regions for 1-prong $\tau_{\text{had-vis}}$ candidates is illustrated in Figures 7.1, 7.2 and 7.3, respectively. Left plots show the template distributions of the τ jet width for the two control regions. The τ jet width discriminant in the signal region overlaid with the fitted shape using the templates from the control regions are shown in the middle. The right plots are the profile of χ^2/ndf of the fit as a function of α_{MJ}. The minimum value of χ^2/ndf is the fitted value of α_{MJ} for the corresponding bin. The error on α_{MJ} is defined by the band at $\chi^2_{min}/ndf + \sqrt{\frac{2}{ndf}}$.

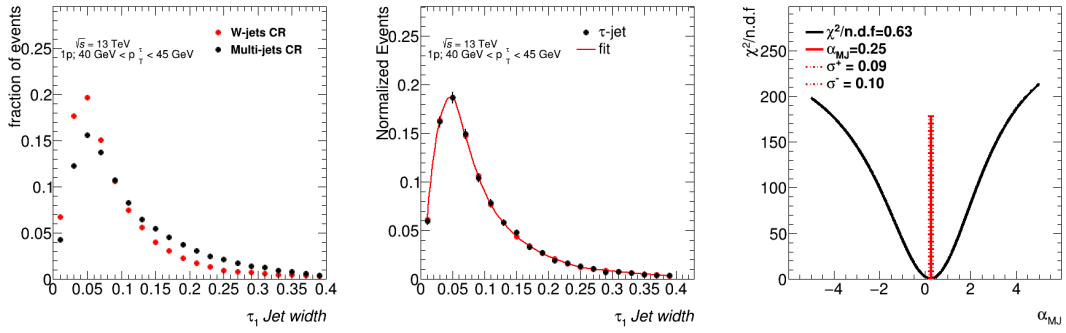

FIGURE 7.1: Estimation of α_{MJ} in the $\tau_{\text{had-vis}}$+jets signal region for 1-prong $\tau_{\text{had-vis}}$ candidates and anti-$\tau_{\text{had-vis}}$ region defined with not-loose working point. Left: templates of discriminating variables for different values of p_T^{τ} . Middle: shape of the discriminating variable obtained in the signal region and shape fitted using the templates measured in the control regions. Right: χ^2/ndf of the fit as a function of α_{MJ}, the error on α_{MJ} is defined by the band at $\chi^2_{min}/ndf + \sqrt{\frac{2}{ndf}}$.

Analogous template fits of α_{MJ} for 3-prong candidates are illustrated in Figures 7.4 and 7.5. Here, the variable used for the template is the transformed $\tau_{\text{had-vis}}$ BDT

score. It is worth to mention that, as long as the fake factors from quark- and gluon-initiated jets are substantially different, the accurate knowledge of α_{MJ} is very important. However, as soon as the values of fake factors become similar in the two control regions, the precise extraction of α_{MJ} is not essential anymore.

The fake factors for each control region and the combined fake factors are illustrated in Figures 7.6 and 7.7. One can see that for larger p_T^τ the fake factors for multijet and W+jet control regions are getting similar, thus the precise estimation of alpha becomes less relevant for the last p_T^τ bin.

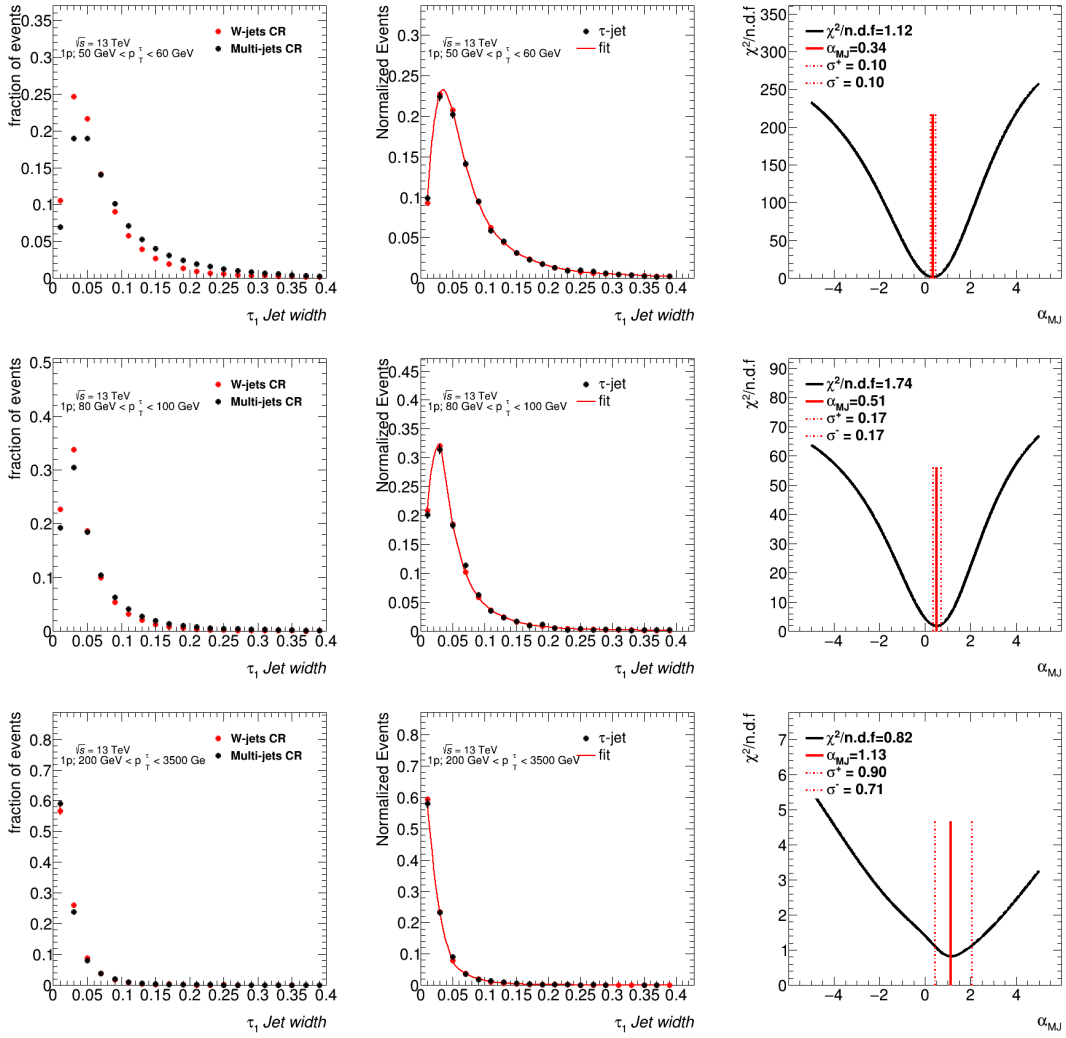

FIGURE 7.2: Estimation of α_{MJ} in the $\tau_{\text{had-vis}}$+jets signal region and in the anti-$\tau_{\text{had-vis}}$ region defined with not-loose working point for 1-prong $\tau_{\text{had-vis}}$ candidates. Left: templates of discriminating variables for different values of p_T^τ . Middle: shape of the discriminating variable obtained in the signal region and shape fitted using the templates measured in the control regions. Right: χ^2/ndf of the fit as a function of α_{MJ}, the error on α_{MJ} is defined by the band at $\chi^2_{min}/ndf + \sqrt{\frac{2}{ndf}}$.

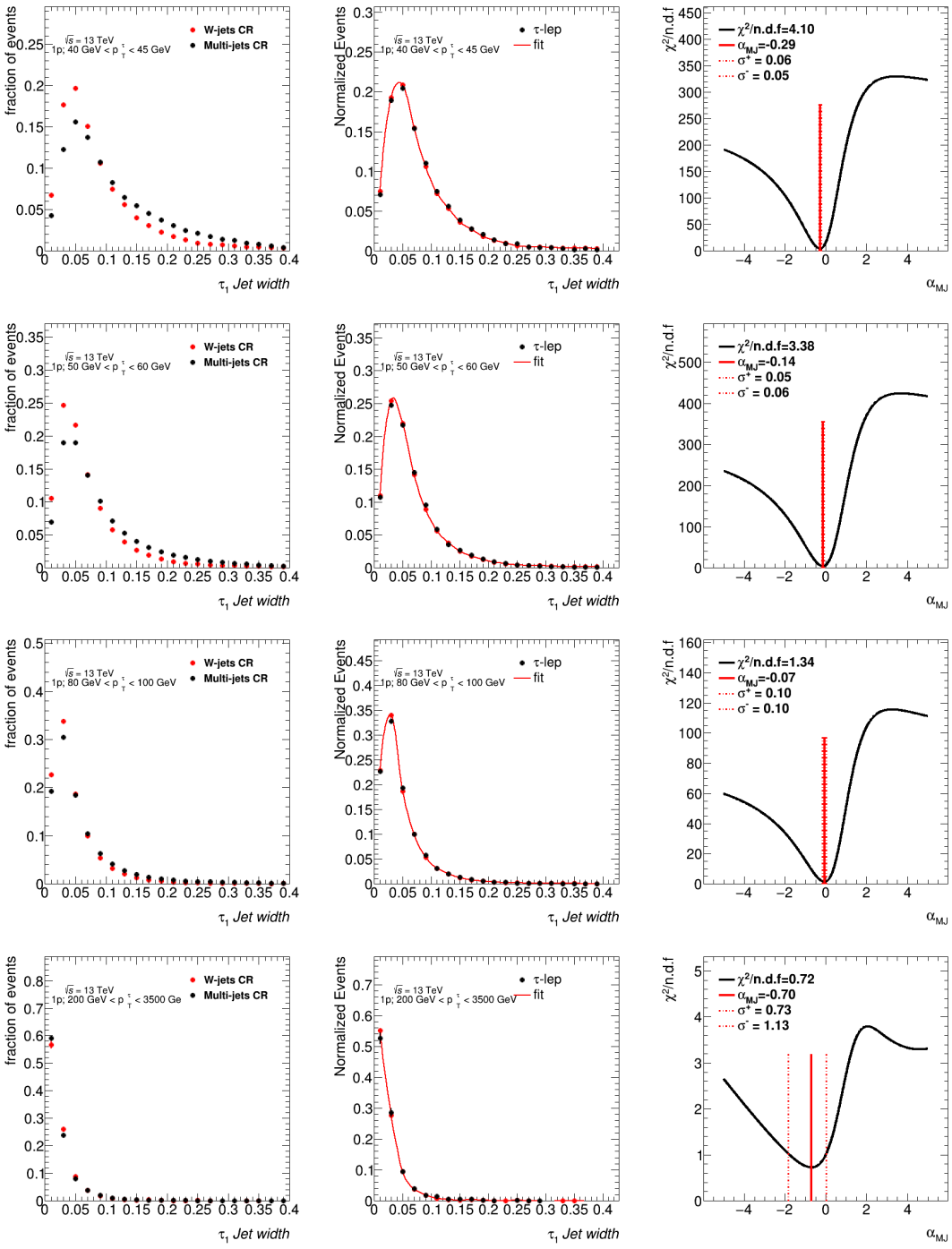

FIGURE 7.3: Estimation of α_{MJ} in the $\tau_{\text{had-vis}}$+lepton signal region and in the anti-$\tau_{\text{had-vis}}$ region defined with not-loose working point for 1-prong $\tau_{\text{had-vis}}$ candidates. Left: templates of discriminating variables for different p_T^{τ} . Middle: shape of the discriminating variable obtained in the signal region and shape fitted using the templates measured in the control regions. Right: χ^2/ndf of the fit as a function of α_{MJ}, the error on α_{MJ} is defined by the band at $\chi^2_{min}/ndf + \sqrt{\frac{2}{ndf}}$.

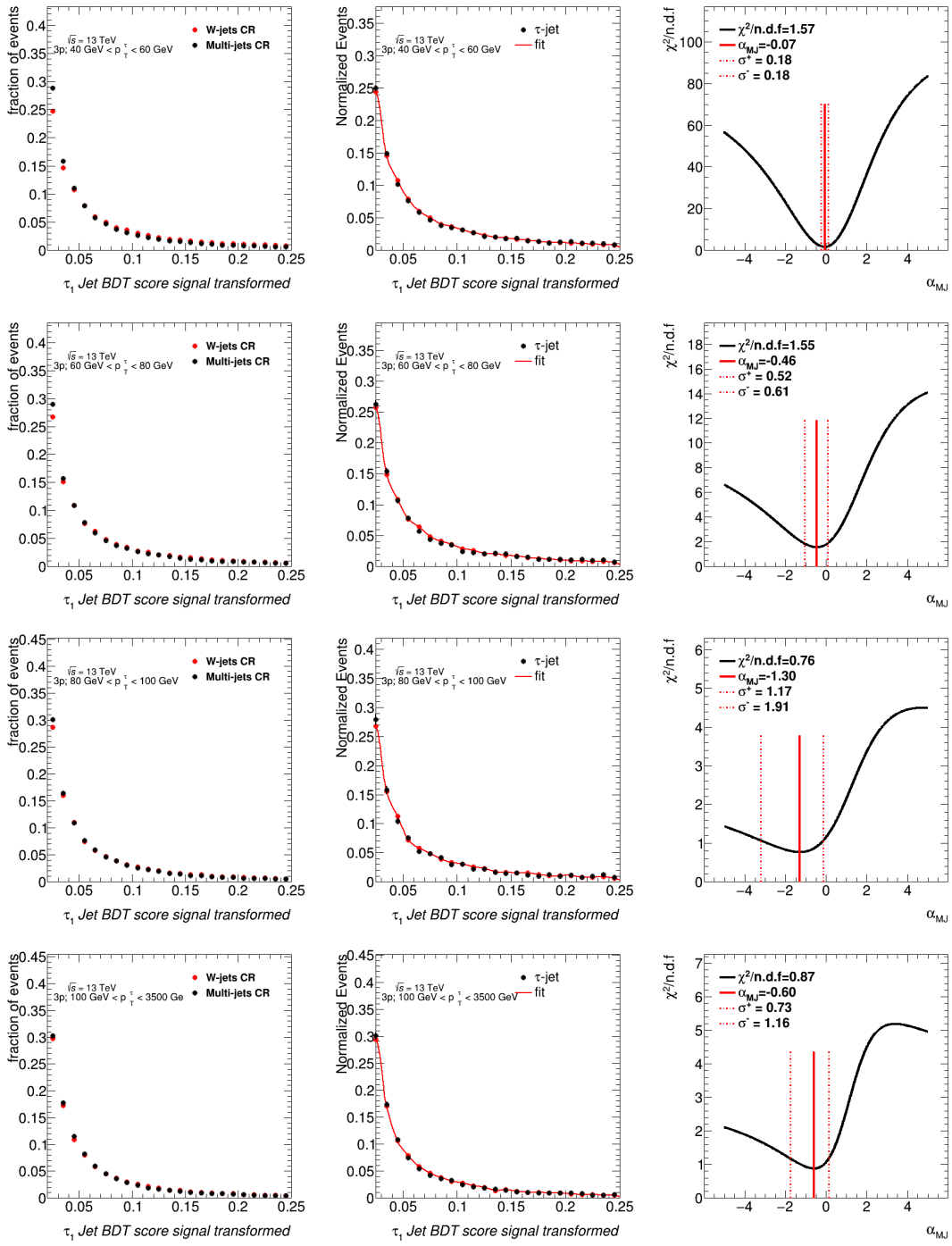

FIGURE 7.4: Estimation of α_{MJ} in the $\tau_{\text{had-vis}}$+jets signal region and in the anti-$\tau_{\text{had-vis}}$ region defined with not-loose working point for 3-prong $\tau_{\text{had-vis}}$ candidates. Left: templates of discriminating variables for different values of p_T^{τ}. Middle: shape of the discriminating variable obtained in the signal region and fitted shape using the templates measured in the control regions. Right: χ^2/ndf of the fit as a function of α_{MJ}, the error on α_{MJ} is defined by the band at $\chi^2_{min}/ndf + \sqrt{\frac{2}{ndf}}$.

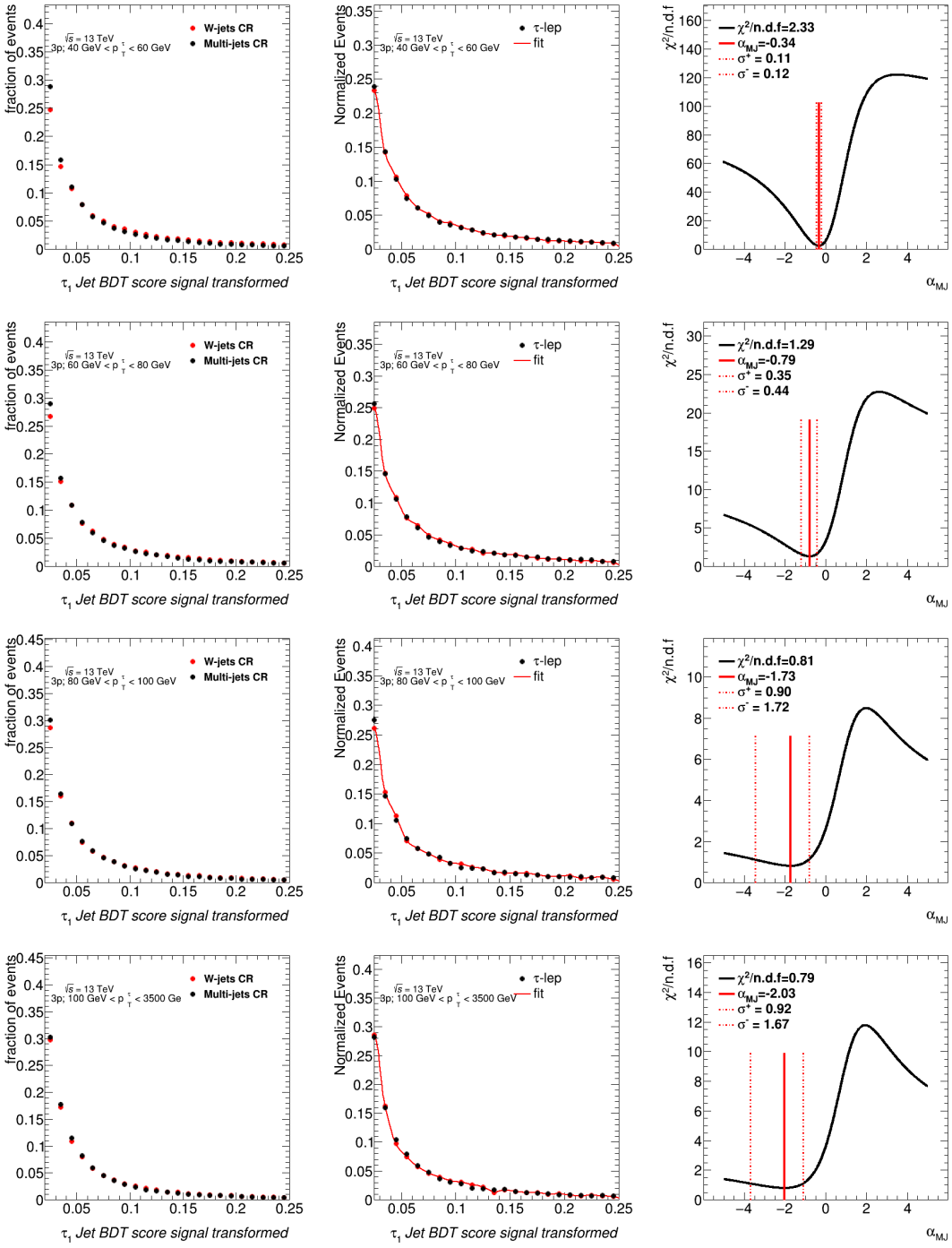

FIGURE 7.5: Estimation of α_{MJ} in the $\tau_{\text{had-vis}}$+lepton signal region and in the anti-$\tau_{\text{had-vis}}$ region defined with not-loose working point for 3-prong $\tau_{\text{had-vis}}$ candidates. Left: templates of discriminating variables for different values of p_T^τ. Middle: shape of the discriminating variable obtained in the signal region and fitted shape using the templates measured in the control regions. Right: χ^2/ndf of the fit as a function of α_{MJ}, the error on α_{MJ} is defined by the band at $\chi^2_{min}/ndf + \sqrt{\frac{2}{ndf}}$.

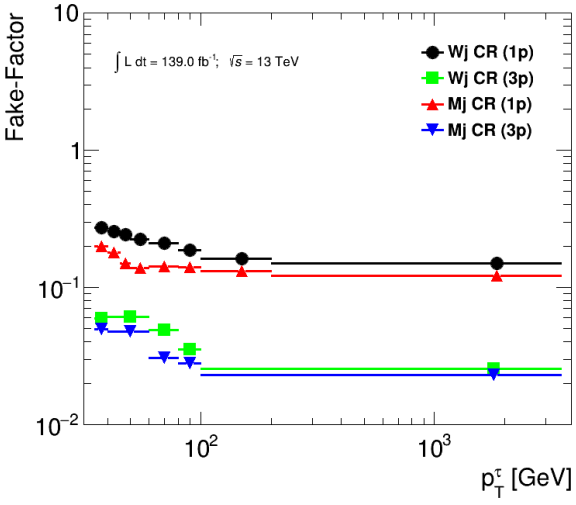

FIGURE 7.6: Fake factors parameterized as a function of p_T^τ and number of tracks. The plots show the fake factor in the multi-jet and W+jet control regions. Errors represent the statistical uncertainties.

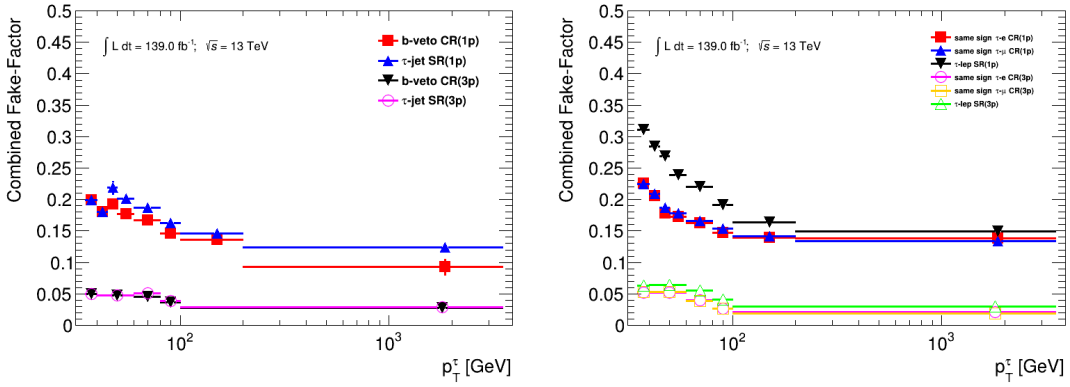

(a) (b)

FIGURE 7.7: Fake factors after reweighting by α_{MJ} in the (a) $\tau_{\text{had-vis}}$+jets channel (b) $\tau_{\text{had-vis}}$+lepton channel. The uncertainties include the uncertainty on the template fit and the statistical uncertainties of fake factor extraction.

7.3 Test of an alternative variable for the determination of jet composition

The estimation of α_{MJ} would benefit from using a variable which demonstrates the best discrimination of jet composition in all considered bins of p_T^τ and the number of tracks. In this section, MVA analysis is employed to define an improved discriminant. A simple Neural Network (MLP) was trained on 2018 data in the W+jets and multi-jet control regions defined in Table 6.4. The anti-$\tau_{\text{had-vis}}$ selection used as for the standard template fit in the nine p_T^τ bins, 30-35, 35-40, 45-50, 50-60, 60-80, 80-100, 100-200, 200-3500 [GeV]. Three variables, the $\tau_{\text{had-vis}}$ jet width, the transformed

BDT score and p_T^τ were used for training as illustrated in Figures 7.8 and 7.9. The MLP combines the standard two variables, which are used as the discriminant of the quark- and gluon-initiated jet fraction in the analysis, while p_T^τ of the $\tau_{\text{had-vis}}$ candidate is used only as an additional parameter that should not itself contribute to the discrimination. Therefore, two samples have to be reweighted to have same p_T^τ distribution to avoid any possible bias due to the actual p_T^τ at the evaluation stage. The reweighting is done in the following way:

- Histograms of p_T^τ for W+jet and multijet regions are created.
- The content of the W+jet p_T^τ histogram, which is smoothed by interpolation between bins for a given p_T^τ is attributed as an event-by-event weight for multijet region, and vice versa.

Thus, we obtain statistically compatible p_T^τ distributions in these two regions as illustrated in the right plots of Figures 7.8 and 7.9. After reweighting, the goal has been achieved, as p_T^τ, which was meant to be a parameter in the training and not a discriminant, ranks the lowest as listed in Table 7.1.

The MLP responses for each p_T^τ bin are shown in Figures 7.10 and 7.11. It can be seen that the discrimination for the last bin is generally poor, since for large p_T^τ the quark- and gluon-initiated jet fractions are becoming similar in the two control regions, unlike for low and intermediate p_T^τ. It can also be seen from Figure 7.6 that in high p_T^τ bins values of fake factors for both multijet and W+jet control regions become compatible within the uncertainty.

The estimation of α_{MJ} was done for 1-prong $\tau_{\text{had-vis}}$ using the MLP response for the $\tau_{\text{had-vis}}$+jet and $\tau_{\text{had-vis}}$+lepton signal regions as illustrated in Figures 7.12, 7.13 and 7.14, respectively. Note that, for removing p_T^τ difference of control regions and signal region, a weight defined as ratio of normalized p_T^τ histograms of the signal to the control regions, was attributed event-by-event to the template distributions.

Variable	30-35 GeV Rank-Importance	35-40 GeV Rank-Importance	40-45 GeV Rank-Importance	45-50 GeV Rank-Importance	50-60 GeV Rank-Importance
Tau_jet_width	1- 5.284e+00	1- 3.142e+00	1- 4.068e+00	1- 5.705e+00	1- 2.942e+00
Tau_BDT_score	2- 7.306e-02	2- 1.444e+00	2- 1.321e+00	2- 5.284e-01	2- 3.144e-02
p_T^τ	3- 4.529e-02	3- 6.755e-02	3- 9.606e-03	3- 3.113e-03	3- 2.188e-02
ROC-integral	0.589	0.601	0.614	0.621	0.606

Variable	60-80 GeV Rank-Importance	80-100 GeV Rank-Importance	100-200 GeV Rank-Importance	200-3500 GeV Rank-Importance
Tau_jet_width	1- 1.743e+00	1- 1.964e+00	1- 2.918e+00	1- 7.906e+00
Tau_BDT_score	2- 4.537e-01	2- 2.122e-02	2- 1.990e-02	3- 2.337e-01
p_T^τ	3- 3.805e-02	3- 2.221e-03	3- 1.371e-02	2- 5.164e+00
ROC-integral	0.582	0.573	0.557	0.522

TABLE 7.1: Ranking of variables and their importance used in the BDT training for the entire p_T^τ range. The ranking is shown for events with 1-prong $\tau_{\text{had-vis}}$ candidates. The values of the ROC-integral are also presented.

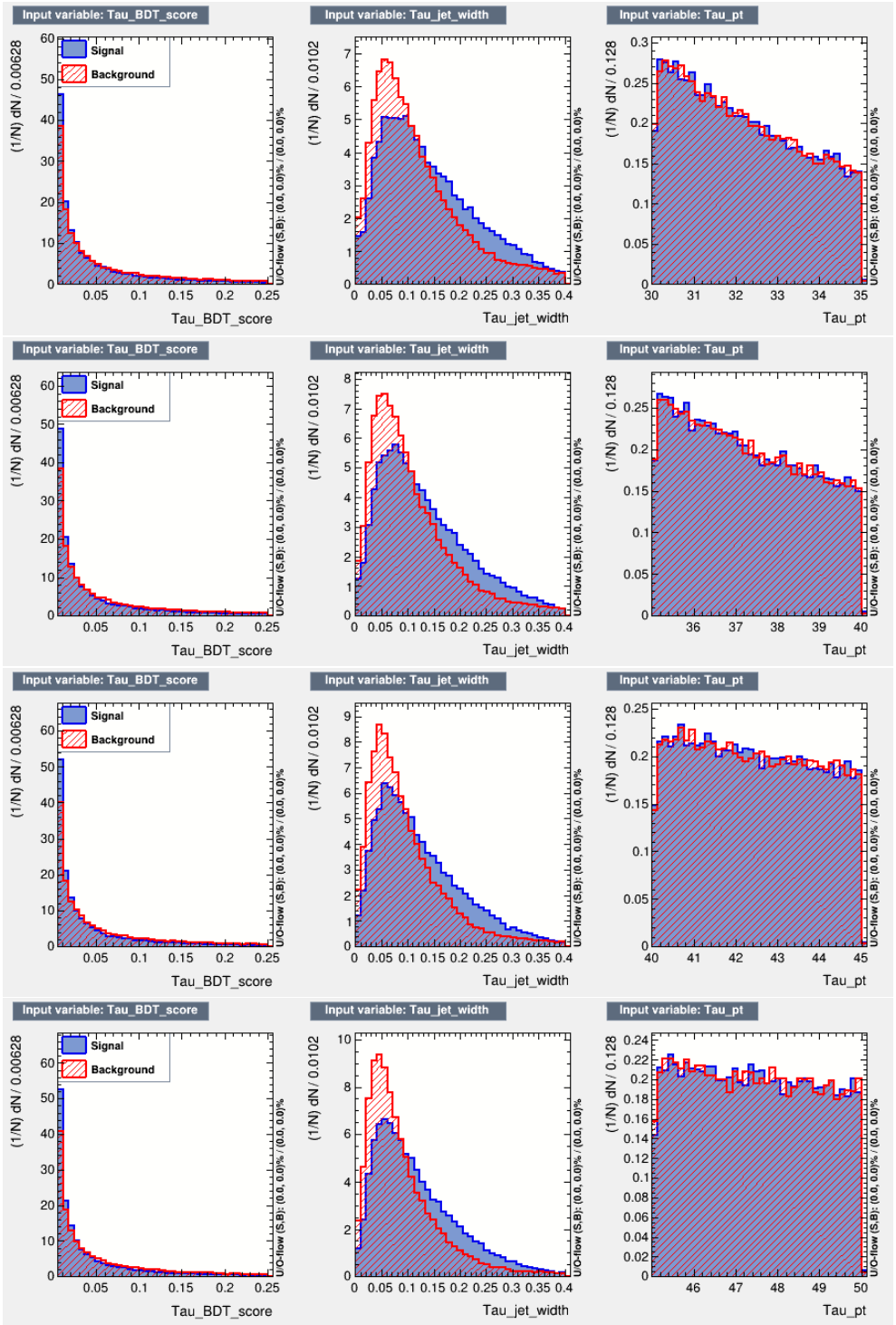

FIGURE 7.8: Distribution of input variables for 1-prong τ candidates in five p_T^τ bins, 30-35, 35-40, 40-45 and 45-50 GeV from top to bottom, respectively. The signal is multi-jet control region and the background is W+jet control regions.

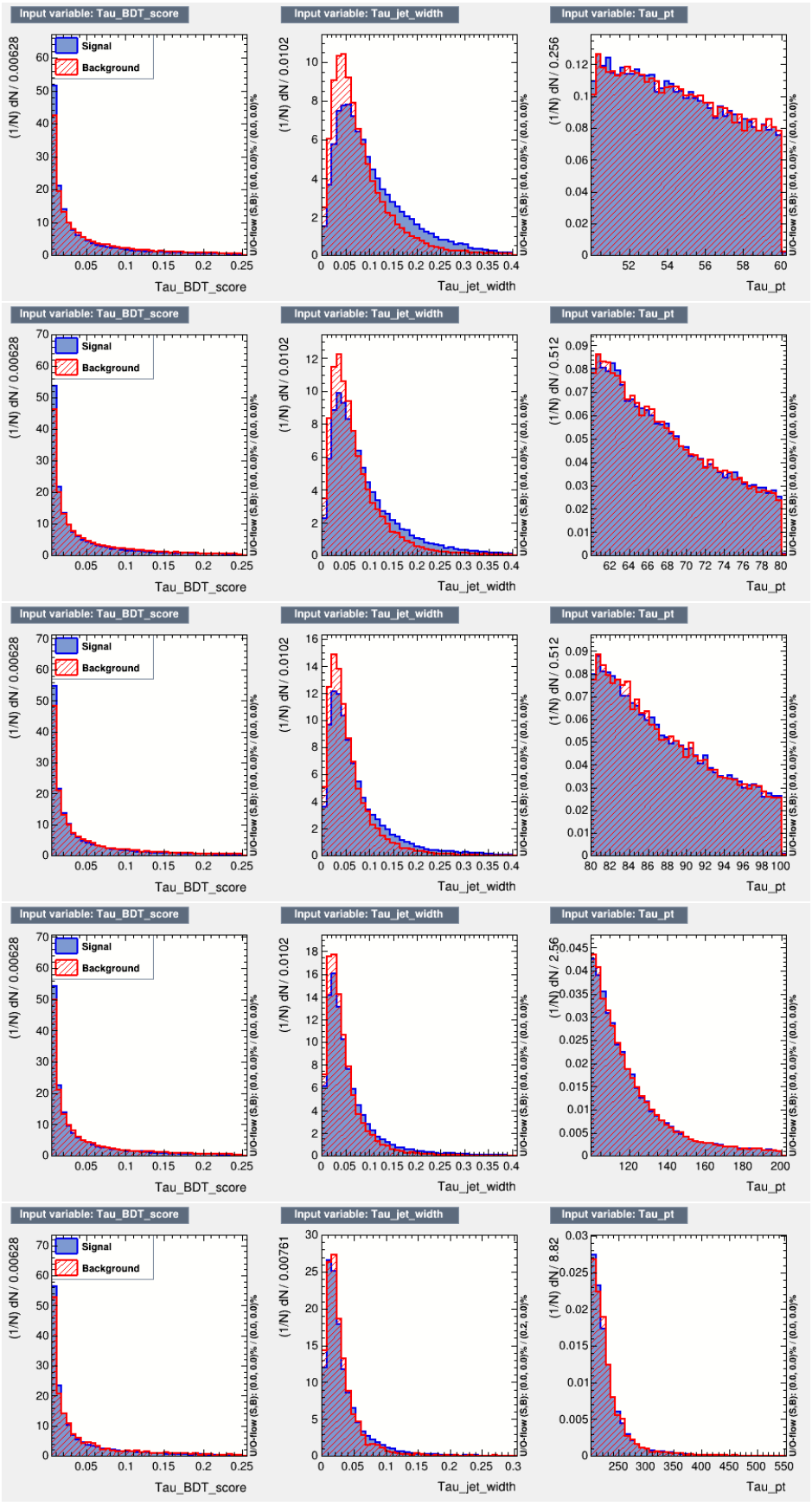

FIGURE 7.9: Distribution of input variables for 1-prong τ candidates in five p_T^τ bins, 50-60, 60-80, 80-100, 100-200 and 200-3500 GeV from top to bottom, respectively. The signal is multi-jet control region and the background is W+jet control regions.

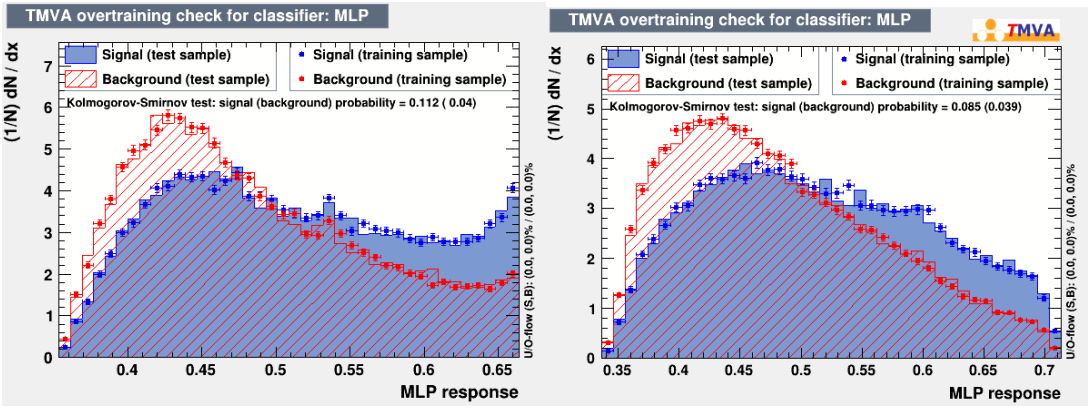

(a) ROC-integral= 0.589

(b) ROC-integral= 0.601

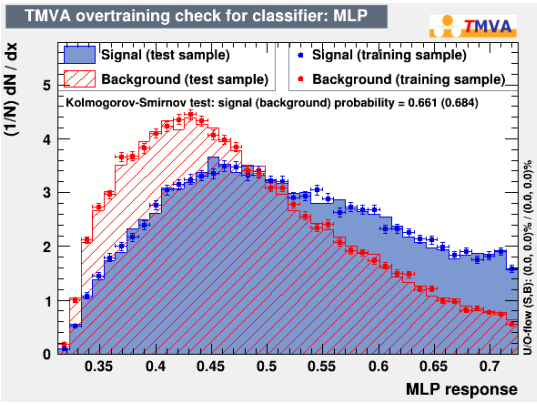

(c) ROC-integral= 0.614

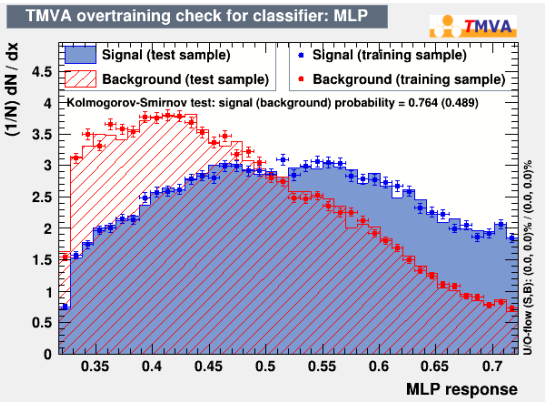

(d) ROC-integral= 0.621

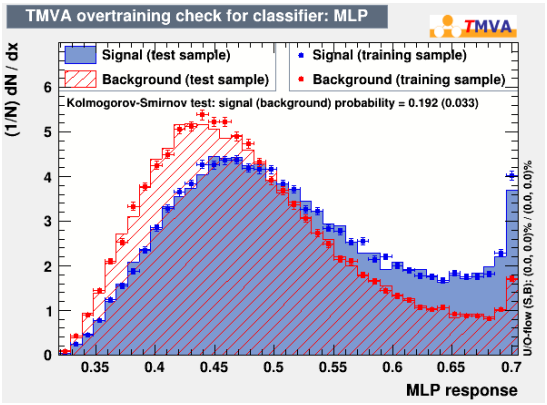

(e) ROC-integral= 0.606

FIGURE 7.10: Distribution of MLP response for 1-prong τ candidates in five p_T^τ bins, (a) 30-35, (b) 35-40, (c) 40-45, (d) 45-50 and (e) 50-60 GeV. The signal is multi-jet control region and the background is W+jet control regions.

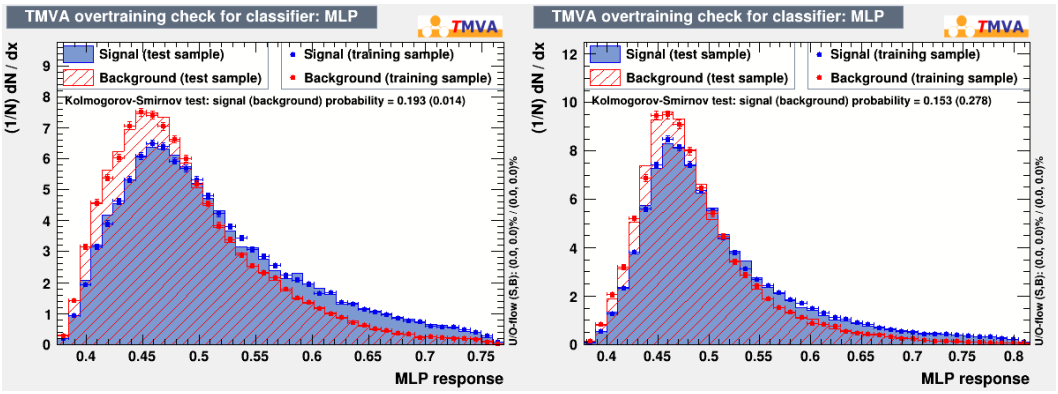

(a) ROC-integral= 0.582 (b) ROC-integral= 0.573

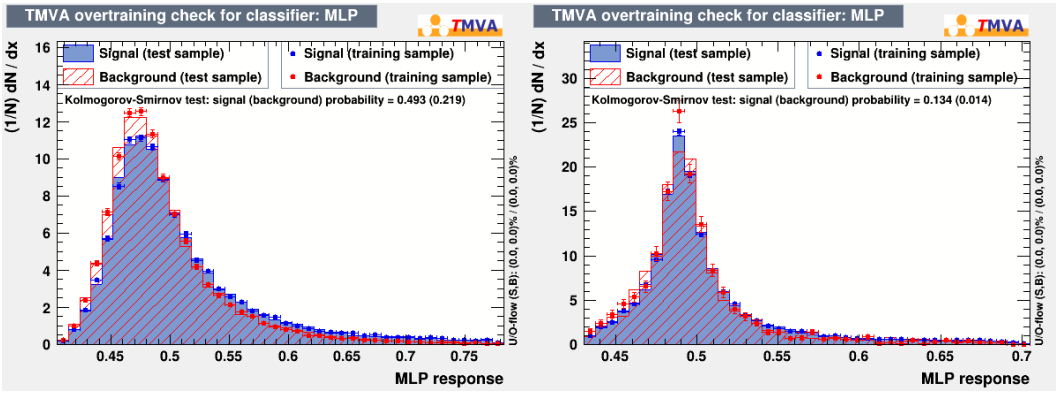

(c) ROC-integral= 0.557 (d) ROC-integral= 0.522

FIGURE 7.11: Distribution of MLP response for 1-prong τ candidates in five p_T^τ bins, (a) 60-80, (b) 80-100, (c) 100-200 and (d) 200-3500 GeV. The signal is multi-jet control region and the background is W+jet control regions.

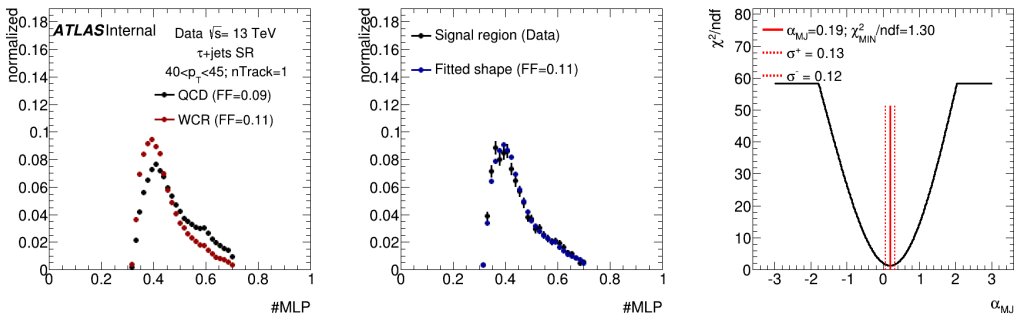

FIGURE 7.12: Estimation of α_{MJ} in the $\tau_{\text{had-vis}}$+jets signal region and in the anti-$\tau_{\text{had-vis}}$ region defined with not-loose working point for 1-prong $\tau_{\text{had-vis}}$ candidates. Left: templates of the MLP response for p_T^τ between 40 and 45 GeV. Middle: shape of the discriminating variable obtained in the signal region and fitted shape using the templates measured in the control regions. Right: χ^2/ndf of the fit as a function of α_{MJ}, the error on α_{MJ} is defined by the band at $\chi^2_{min}/ndf + \sqrt{\frac{2}{ndf}}$.

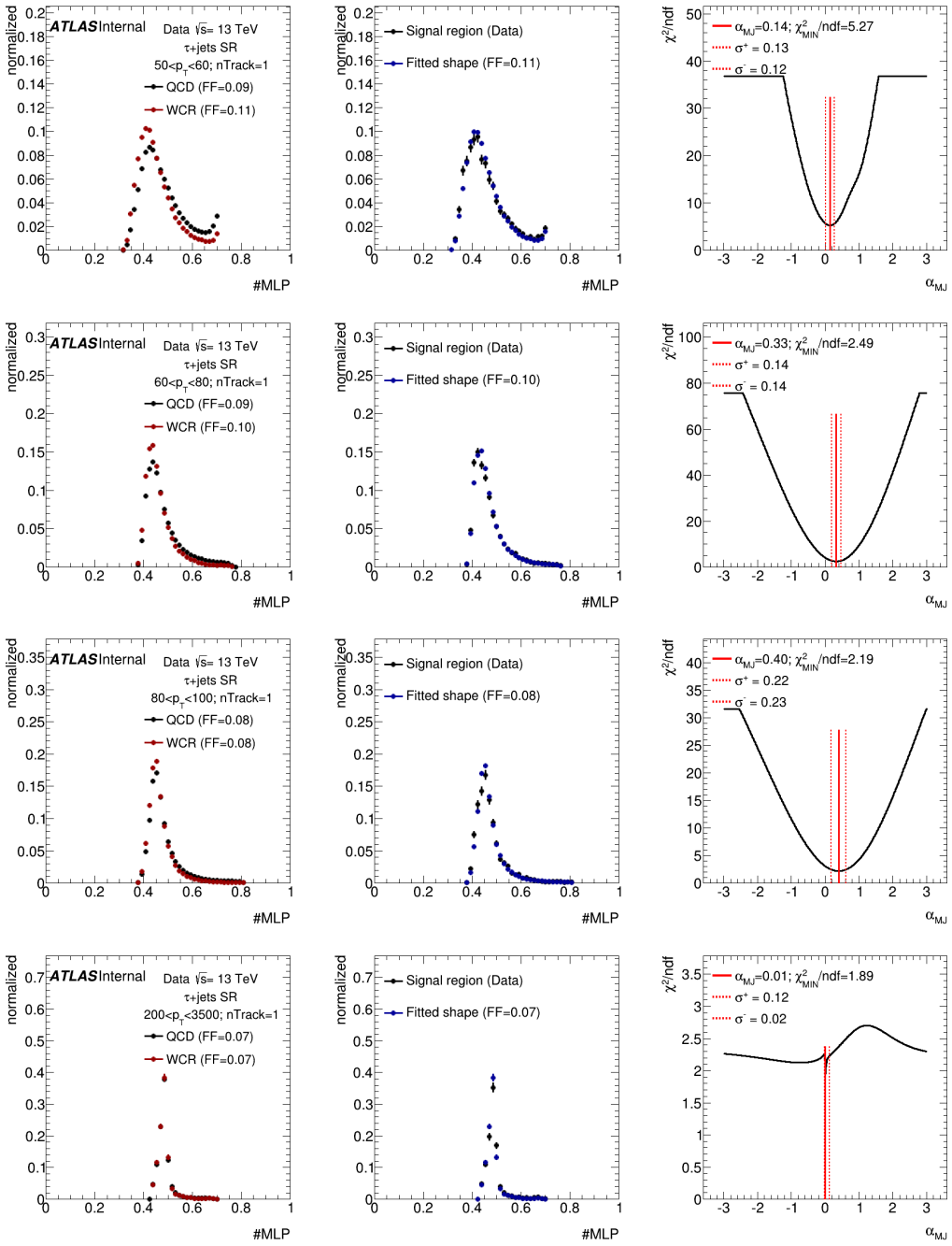

FIGURE 7.13: Estimation of α_{MJ} in the $\tau_{\text{had-vis}}$+jets signal region and in the anti-$\tau_{\text{had-vis}}$ region defined with not-loose working point for 1-prong $\tau_{\text{had-vis}}$ candidates. Left: templates of the MLP response for different p_T^{τ} slices. Middle: shape of the discriminating variable obtained in the signal region and fitted shape using the templates measured in the control regions. Right: χ^2/ndf of the fit as a function of α_{MJ}, the error on α_{MJ} is defined by the band at $\chi^2_{min}/ndf + \sqrt{\frac{2}{ndf}}$.

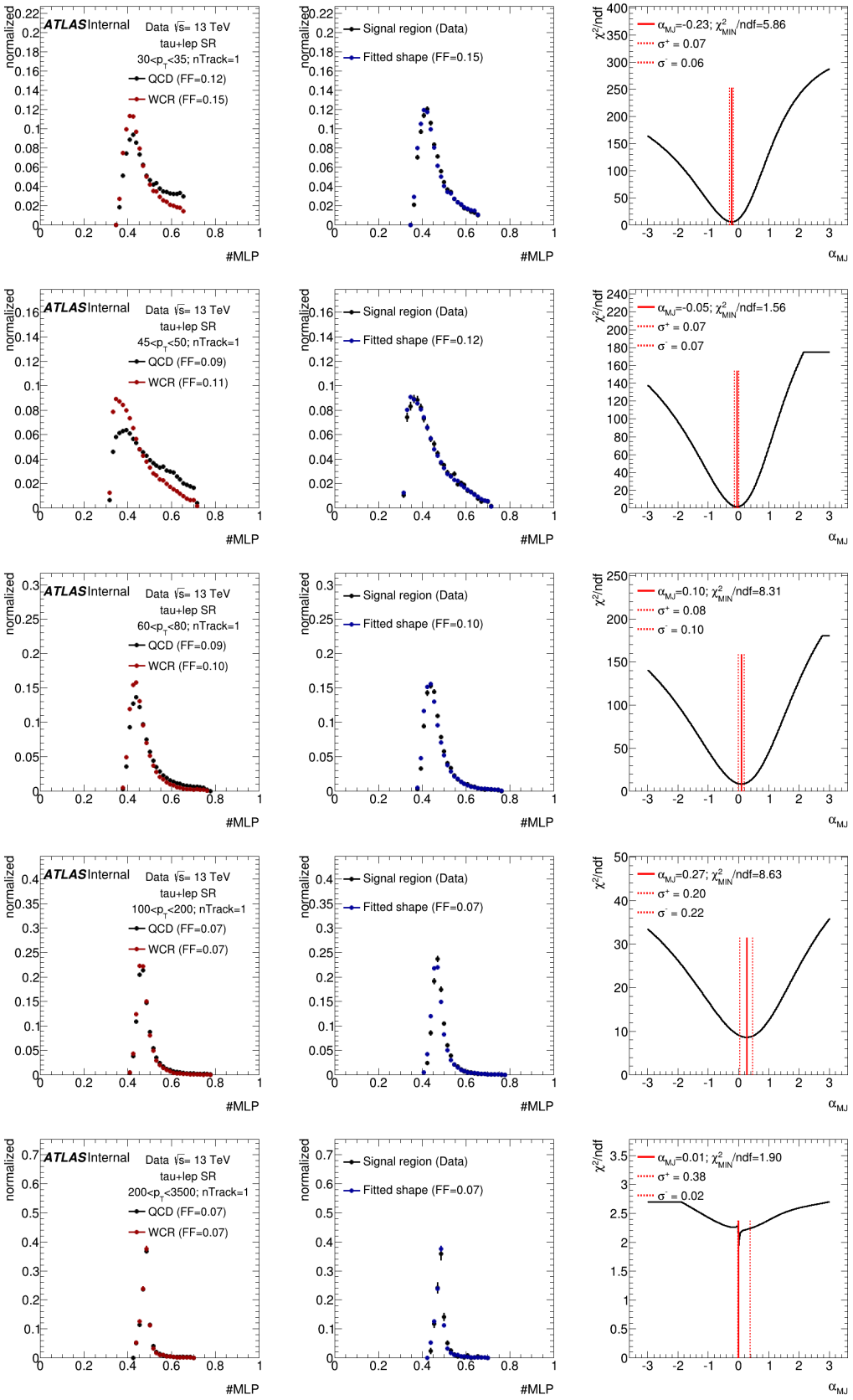

FIGURE 7.14: Estimation of α_{MJ} in the $\tau_{\text{had-vis}}$+lepton signal region and in the anti-$\tau_{\text{had-vis}}$ region defined with not-loose working point for 1-prong $\tau_{\text{had-vis}}$ candidates . Left: templates of discriminating variables MLP for different p_T^{τ} slices. Middle: shape of the discriminating variable obtained in the signal region and fitted shape using the templates measured in the control regions. Right: χ^2/ndf of the fit as a function of α_{MJ}, the error on α_{MJ} is defined by the band at $\chi^2_{min}/ndf + \sqrt{\frac{2}{ndf}}$.

Altogether three variables were considered as discriminants to estimate α_{MJ} in the signal region. The τ jet width, the MLP response and the transformed $\tau_{\text{had-vis}}$ BDT score were used for 1-prong and 3-prong $\tau_{\text{had-vis}}$ candidates in the template fit approach for τ+jet and τ+lepton signal regions. For 3-prong candidates the estima-

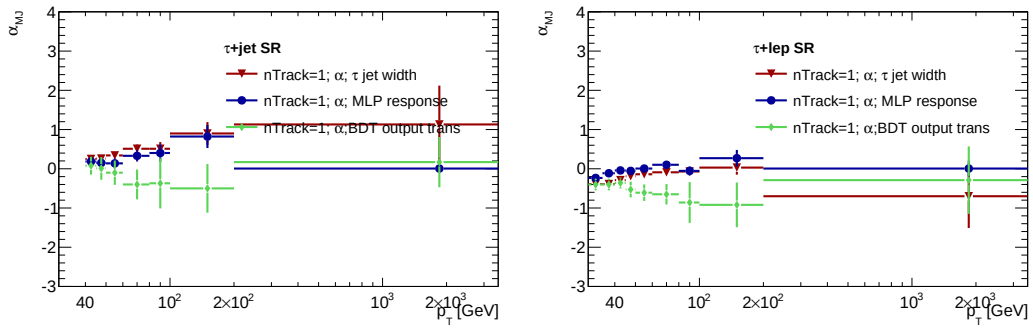

(a) (b)

FIGURE 7.15: α_{MJ} as a function of p_T^τ for 1-prong $\tau_{\text{had-vis}}$ candidates estimated by template fit method using χ^2 with τ jet width, MLP response and transformed $\tau_{\text{had-vis}}$ BDT score, red, blue and green lines respectively for (a) τ+jet signal region and (b) τ+lepton signal region.

tion of α_{MJ} from τ jet width in the last two bins is very poor; however the uncertainty on the first bins is smaller than the fit from using the transformed $\tau_{\text{had-vis}}$ BDT score. One could consider fitting α_{MJ} using τ jet width for lower p_T^τ bins and transformed $\tau_{\text{had-vis}}$ BDT score for higher bins. Alternatively, using the MLP response would make it possible to cover entire p_T^τ range. Moreover, the final fake factors obtained by using the MLP response have smaller uncertainties.

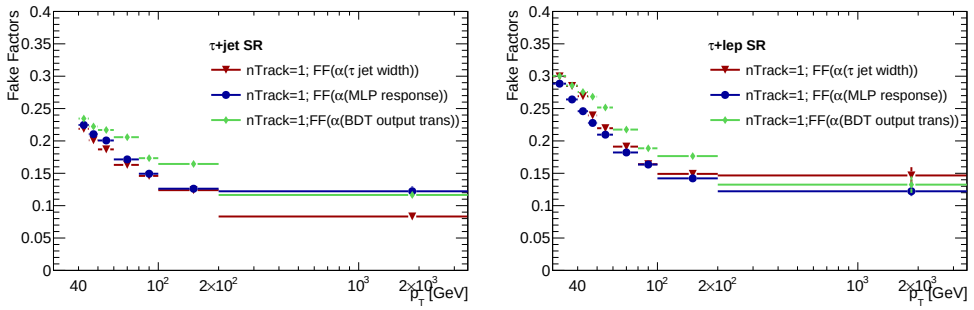

(a) (b)

FIGURE 7.16: Combined fake factors for 1-prong $\tau_{\text{had-vis}}$ candidates estimated by the template fit method using χ^2 with τ jet width, the MLP response and the transformed BDT score (red, blue and green lines respectively) for (a) the $\tau_{\text{had-vis}}$+jet signal region and (b) the $\tau_{\text{had-vis}}$+lepton signal region.

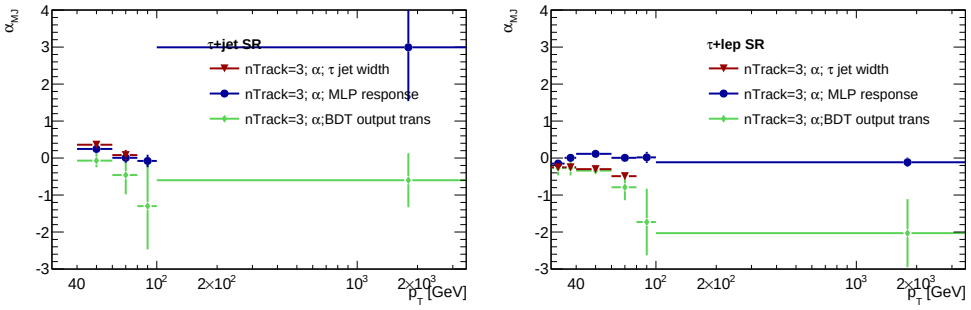

(a) (b)

FIGURE 7.17: α_{MJ} as a function of p_T^{τ} for 3-prong $\tau_{\text{had-vis}}$ candidates estimated by the template fit method using χ^2 with the τ jet width, the MLP response and the transformed BDT score (red, blue and green lines respectively) for (a) $\tau_{\text{had-vis}}$+jet signal region and (b) $\tau_{\text{had-vis}}$+lepton signal region.

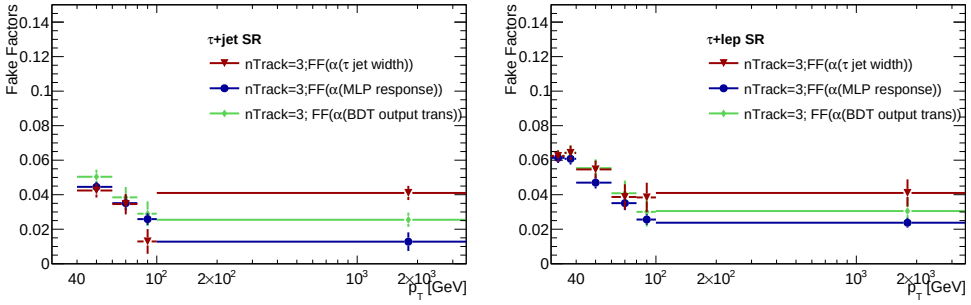

(a) (b)

FIGURE 7.18: Combined fake factors for for 3-prong $\tau_{\text{had-vis}}$ candidates estimated by the template fit method using χ^2 with the τ jet width, the MLP response and the transformed BDT score (red, blue and green lines respectively) for (a) $\tau_{\text{had-vis}}$+jet signal region and (b) $\tau_{\text{had-vis}}$+lepton signal region.

The α_{MJ} distribution as a function of p_T^{τ}, fitted using these variables is presented in Figure 7.15 for 1-prong and in Figure 7.17 for 3-prong candidates in (a) $\tau_{\text{had-vis}}$+jet and (b) $\tau_{\text{had-vis}}$+lepton signal regions. The combined fake factors obtained with the fitted α_{MJ} are shown for 1-prong and 3-prong candidates in Figures 7.16 and 7.18. It can be seen that the final fake factors do not show significant difference within the uncertainty bands for 1-prong candidates from τ jet width and the MLP response. The transformed BDT score shows better agreement for 3-prong candidates. In all, one can see that the final combined fake factors obtained by α_{MJ} fitted using τ jet width are suitable for 1-prong candidates while the ones obtained by using the transformed $\tau_{\text{had-vis}}$ BDT score are suitable for 3-prong candidates. The ones obtained using the MLP response could be universally applicable.

7.4 Validating the fake τ background estimation using signal-like control regions

In order to validate the estimation of τ background arising from jet misidentified as τ leptons, two validation regions are used: a $\tau_{\text{had-vis}}$ +jets signal-like region with a b-veto requirement (no jets passing the b-tag requirement) and a $\tau_{\text{had-vis}}$ +electron or muon signal-like region with same-sign charges of the lepton and τ candidates. Figures 7.19, 7.20 and 7.21 show the distribution of the $\tau_{\text{had-vis}}$ transverse momentum and the transverse mass of the τ and E_T^{miss} in the above validation regions.

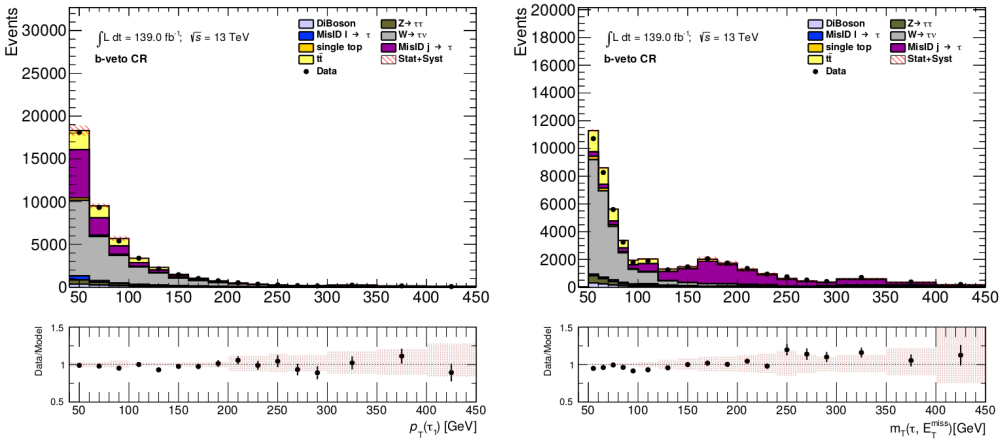

(a) (b)

FIGURE 7.19: $j \rightarrow \tau_{\text{had-vis}}$ background validation plots: $\tau_{\text{had-vis}}$ +jets signal-like region with b-veto for anti-$\tau_{\text{had-vis}}$ candidates not passing loose (a) p_T^{τ} (b) $m_T(\tau, E_T^{miss})$. The uncertainty band in the ratio plots includes both statistical and fake factor method systematic uncertainty.

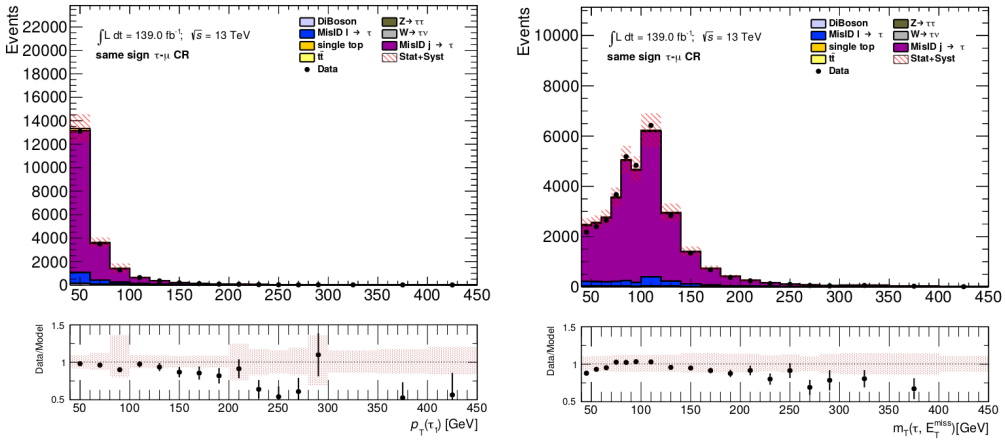

(a) (b)

FIGURE 7.20: $j \rightarrow \tau_{\text{had-vis}}$ background validation plots: $\tau_{\text{had-vis}}$ + muon signal-like region with same-sign charges for anti-$\tau_{\text{had-vis}}$ candidates not passing loose (a) p_T^{τ} (b) $m_T(\tau, E_T^{miss})$. The uncertainty band in the ratio plots include both statistical and fake factor method systematic uncertainty.

Data points are overlaid with the SM processes estimated using MC simulated samples for true τ and lepton faking $\tau_{\text{had-vis}}$ and the fake factor data-driven estimation for jets faking $\tau_{\text{had-vis}}$. A good modeling of the background is observed. The systematic uncertainties included in the ratio plots are due to the fake factor method and are assessed as described in Section 7.6.

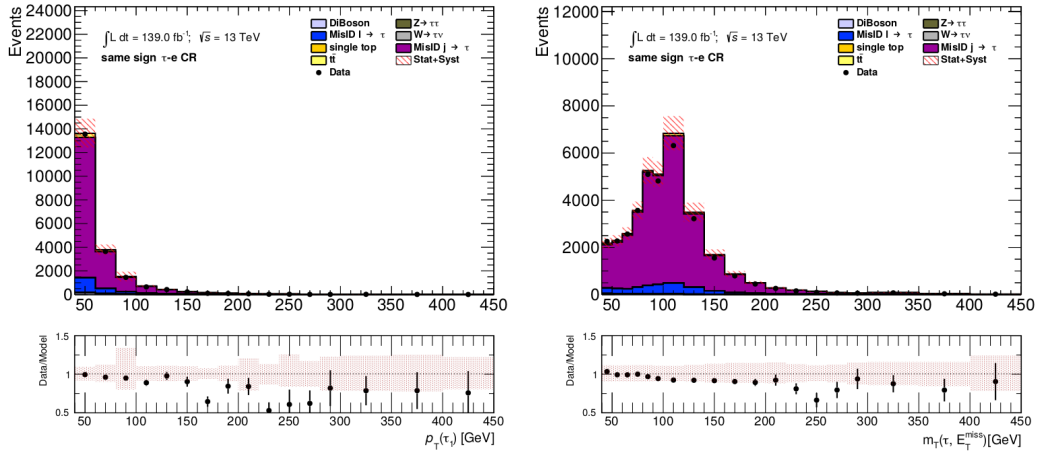

(a) (b)

FIGURE 7.21: $j \to \tau_{\text{had-vis}}$ background validation plots: $\tau_{\text{had-vis}}$ + electron signal-like region with same-sign charges for anti-$\tau_{\text{had-vis}}$ candidates not passing loose (a) p_T^{τ} (b) $m_T(\tau, E_T^{miss}$. The uncertainty band in the ratio plots include both statistical and fake factor method systematic uncertainty.

7.5 Study of the fake factor method using MC samples

In the data-driven fake factor method discussed in the previous chapter, two control regions based on their jet origin composition were defined, for estimating the misidentified hadronic τ candidates in signal regions. In this section, the fake factor method is studied directly on simulated events. The determination of fake factors and the estimation of the parameter α_g as well as extraction of potential systematic uncertainties due to the extrapolation of fake factors between different selection regions are the main goals of this study. Unfortunately the multijet events are generally not well-modeled by MC generators and we do not have sufficiently large MC samples for the study. Instead, the W+jet control region defined in Table 6.4 is split in two sub regions, one with τ candidates originating from gluon- and other from quark-initiated jets (hereafter they are called W+jet(g) and W+jet(q)), based on the MC truth information. In both cases the reconstructed candidate is required not to match any true τ, electron or muon from the simulation. Then the fake factor is defined as the number of fake candidates passing the identification requirement over number of those failing it.

The regions under study are the $\tau_{\text{had-vis}}$+jet signal region, the $\tau_{\text{had-vis}}$+jet b-veto region, the $\tau_{\text{had-vis}}$+jet preselection region, $\tau_{\text{had-vis}}$+lepton signal region, the $\tau_{\text{had-vis}}$+lepton

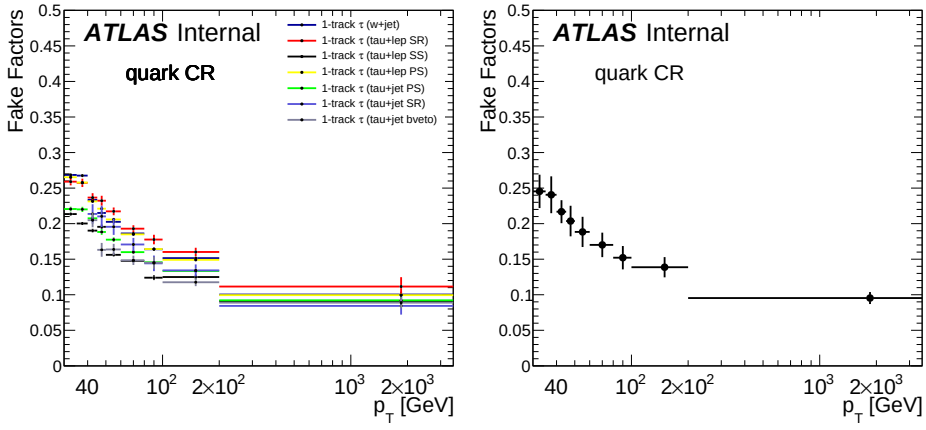

(a) (b)

FIGURE 7.22: The fake factors as a function of p_T^τ for 1-prong fake τ candidates from quark-initiated jets for control regions (a) and the mean value of fake factor from all those regions and the RMS of the spread (b).

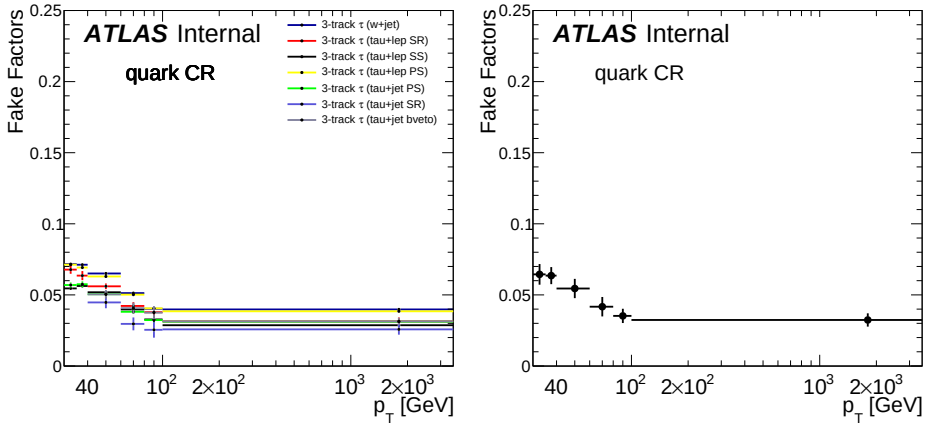

(a) (b)

FIGURE 7.23: The fake factors as a function of p_T^τ for 3-prong fake τ candidates from quark-initiated jets for control regions (a) and the mean value of fake factor from all those regions and the RMS of the spread (b).

same sign signal-like region and the τ+lepton preselection region as defined in Table 7.2. The fake factors for the region with τ candidates originating from quark-initiated jets, their mean values and RMS of the spread for 1- and 3-prong τ candidates, are shown in Figures 7.22 and 7.23. Figures 7.24 and 7.25 show analogous plots for τ candidates originating from gluon-initiated jets. In each region the fraction of τ candidates originating from quark- and gluon-initiated jets in a given p_T^τ bin are used for the estimation of the combined fake factor as:

$$\mathrm{FF}_{\mathrm{combined}} = f_g * \mathrm{FF}_{\mathrm{W+jet(g)}} + f_q * \mathrm{FF}_{\mathrm{W+jet(q)}} \tag{7.3}$$

where f_g and f_q are the fractions of gluons and quarks, and $\mathrm{FF}_{\mathrm{W+jet(g)}}$ and $\mathrm{FF}_{\mathrm{W+jet(q)}}$ are fake factors for W+jet with gluon- and quark-initiated jets, respectively.

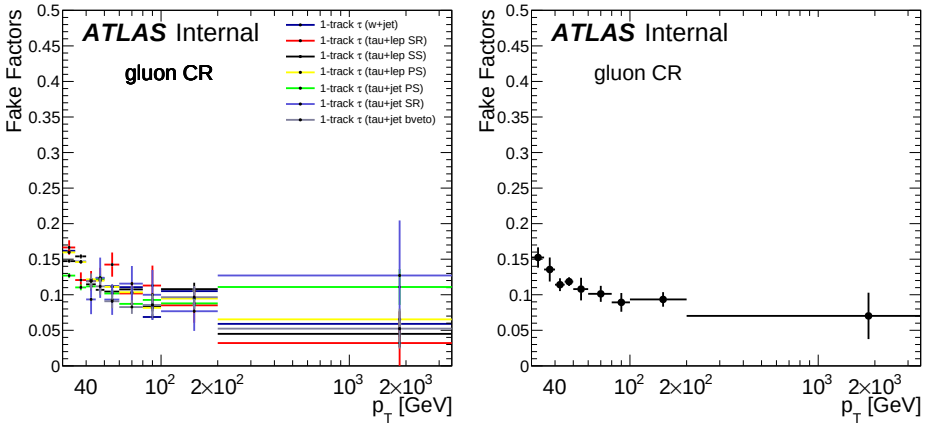

FIGURE 7.24: The fake factors as a function of p_T^τ for 1-prong fake τ candidates from gluon-initiated jets for control regions (a) and the mean value of fake factors from all those regions and the RMS of spread (b).

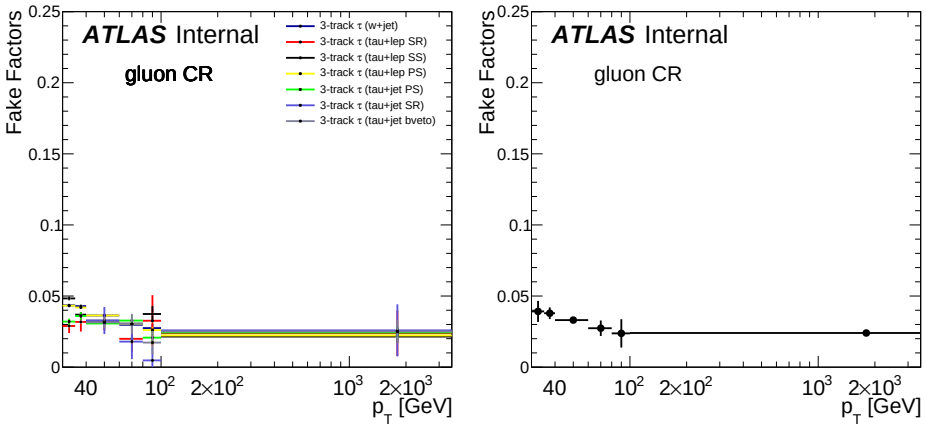

FIGURE 7.25: The fake factors as a function of p_T^τ for 3-prong fake τ candidates from gluon-initiated jets for control regions (a) the mean value of fake factor from all those regions and the RMS of spread (b).

A template fit is preformed in the validation region to estimate the fraction of gluon-originating jets α_g. The τ jet width is used as the discriminant of the jet composition.

Also, an MLP is trained with the following input variables: τ jet width, the transformed $\tau_{\text{had-vis}}$ BDT score and p_T^τ on the W+jet(q) and W+jet(g) control regions. The MC16e W+jets samples are used. The reweighting on p_T^τ is preformed as it was done for data in Section 7.3. The values of the ROC-integral for each p_T^τ bin are shown in Table 7.3. By comparing the values with the corresponding result from data in Table 7.1, it can be seen that MC features a better separation. This is expected because in MC the jet composition is known, and the training was done on pure quark and

gluon categories, while in data the multijet and W+jet selections have barely different admixtures of the two categories. In higher p_T^τ bins the jet composition becomes more similar in the two control regions in data, therefore the separation gets worse.

τ+jet signal region	τ+lepton signal region
$p_T^\tau > 40$ GeV $p_T^{jet} > 25$ GeV $m_T(\tau\ ,\ E_T^{miss})$ >50 GeV at least 3 jets and 1 b-jet lepton veto E_T^{miss} >150 GeV	$p_T^\tau > 30$ GeV one lepton with $p_T^l > 30$ GeV at least 1 jet and 1 b-jet lepton charge opposite than τ charge E_T^{miss} >50 GeV
τ+jet preselection	τ+lepton preselection
$p_T^\tau > 30$ GeV $m_T(\tau\ ,\ E_T^{miss})$ >50 GeV E_T^{miss} >100 GeV lepton veto at least 3 jets	one lepton with $p_T^l > 30$ GeV $p_T^\tau > 30$ GeV $p_T^{jet} > 25$ GeV at least 1 jet
τ+jet b-veto	τ+lepton same sign
$p_T^\tau > 40$ GeV $m_T(\tau\ ,\ E_T^{miss})$ >50 GeV at least 3 jets b-jet veto lepton veto E_T^{miss} >150 GeV $p_T^{jet} > 25$ GeV	one lepton with $p_T^l > 30$ GeV $p_T^\tau > 30$ GeV at least 1 jets $p_T^{jet} > 25$ GeV lepton charge same as τ charge E_T^{miss} >50 GeV

TABLE 7.2: Validation region used for MC study for τ+jet and τ+lepton channel.

p_T^τ	30-35	35-40	40-45	45-50	50-60	60-80	80-100	100-200	200-3500
ROC-integral	0.612	0.612	0.617	0.623	0.613	0.621	0.621	0.628	0.656

TABLE 7.3: The values of the ROC-integral for each p_T^τ bin, for an MLP trained on the MC16e W+jets samples.

The validation plots for the $\tau_{\text{had-vis}}$+jet signal region and the $\tau_{\text{had-vis}}$+lepton signal region are shown in Figures 7.26 and 7.27. The systematic uncertainty from the fake factor method discussed in Section 7.6 is applied on the ratio plot as the dashed band.

In order to validate the α_g estimation by the template fit, we preformed an exercise on a region with a sufficiently large number of events. A minimal selection was applied on the fake τ samples (requiring the $p_T^\tau > 30$ GeV, hereafter called inclusive τ selection) in order to define a region with sufficient statistics. Then, by considering the same W+jets(q/g) regions for the template, α_g was estimated using τ jet width and the MLP response. In Figure 7.28, the distribution of α_g estimated by the template fit from τ jet width and the MLP response is compared with the actual number of gluons in the inclusive τ region and their corresponding combined fake factors. One can see that the values of α_g from the template fit for different approach do not cause a significant difference in the final fake factors.

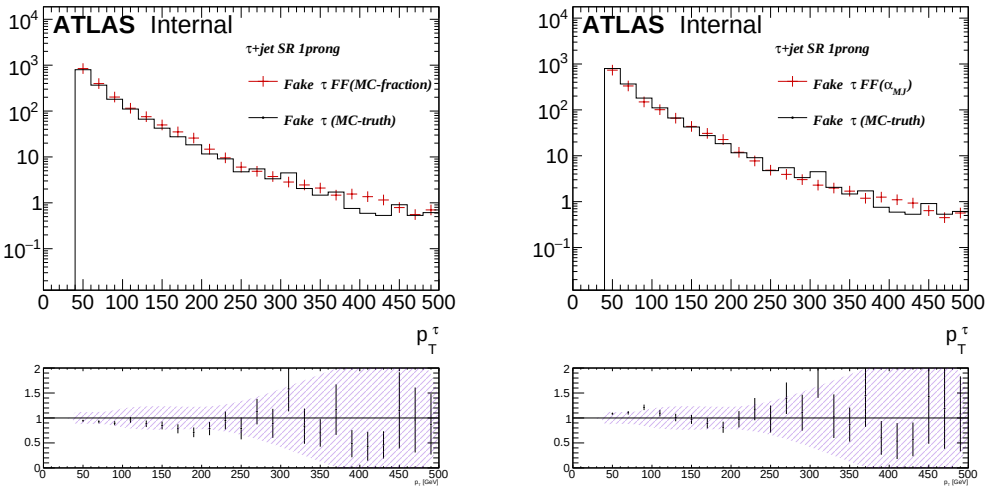

(a) (b)

FIGURE 7.26: Distribution of p_T^τ for τ+jet signal region, the red crosses correspond to the distribution of anti-$\tau_{\text{had-vis}}$ candidate after applying the fake factors corresponding to (a) the fraction of quark- and gluon-initiated jets (b) fraction estimated using the τ jet width template fit. The black curve corresponds to the fake τ candidates which passed the identification. The band on the ratio plot is the fake factor estimation systematic uncertainty.

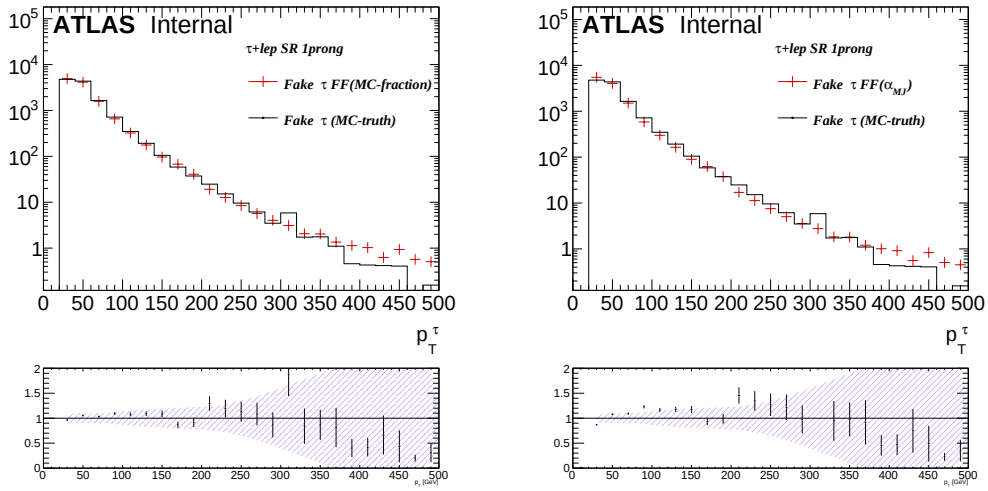

(a) (b)

FIGURE 7.27: Distribution of p_T^τ for τ+lepton signal region,the red crosses correspond to the distribution of anti-$\tau_{\text{had-vis}}$ candidate after applying the fake factors corresponding to (a) the fraction of quark- and gluon-initiated jets (b) fraction estimated using the τ jet width template fit. The black curve corresponds to the fake τ candidates which passed the identification. The band on the ratio plot is the fake factor estimation systematic uncertainty.

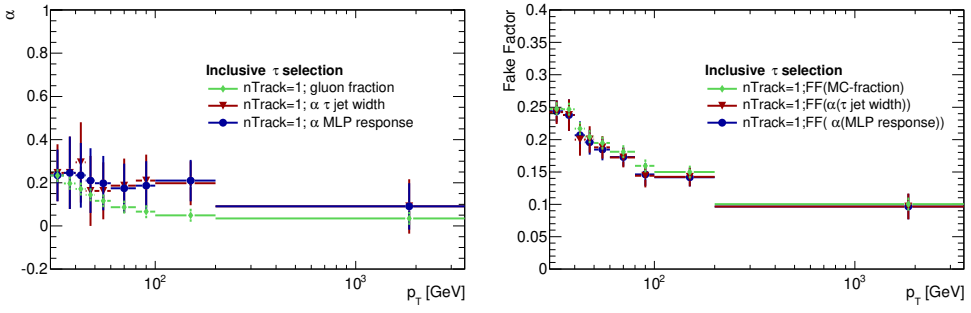

(a) (b)

FIGURE 7.28: The distribution of α_g estimated by the template fit from τ jet width and the MLP response in comparison with the real number of gluons in the $\tau_{\text{had-vis}}$+lepton signal region (a) and the combined fake factors estimated by corresponding α_g estimation (b).

7.6 Systematic uncertainties of the fake factor method

In the estimation of backgrounds with jets misidentified as $\tau_{\text{had-vis}}$, one must account for various sources of systematic uncertainties:

- Statistical uncertainty in the bins of the fake factors, due to the limited size of the control sample.
- Jet composion uncertainty due to the choice of the lower $\tau_{\text{had-vis}}$ BDT requirement in the anti-$\tau_{\text{had-vis}}$ control sample. For different choices of this requirement, different fractions of gluon- and quark-initiated jets populate the anti-$\tau_{\text{had-vis}}$ control region. Furthermore, it has been shown that reconstructed $\tau_{\text{had-vis}}$ objects may have different topologies depending on the choice of the lower cut on the $\tau_{\text{had-vis}}$ BDT score [159]. In order to assess the systematic uncertainty related to this choice, the lower cut on the $\tau_{\text{had-vis}}$ BDT score was varied in the anti-$\tau_{\text{had-vis}}$ region definition, between 0.01 and 0.03.
- Uncertainty of 50% is applied on the number of $\tau_{\text{had-vis}}$ candidates from true hadronic τ decays that must be subtracted when computing number of fakes in the anti-$\tau_{\text{had-vis}}$ region denoted as $N_{\text{fakes}}^{\text{anti}-\tau}$, which is called true $\tau_{\text{had-vis}}$ in the anti-$\tau_{\text{had-vis}}$ control region (the number of true $\tau_{\text{had-vis}}$ was increased and decreased by 50%):

$$N_{\text{fakes}}^{\text{anti}-\tau}(i) = N^{\text{anti}-\tau}(\text{data}) - [0.5, 1.5] \times N_{\text{true}}^{\text{anti}-\tau}(\text{MC}), \tag{7.4}$$

  Note that the MC modeling of true τ identification in the identified region is assured by appropriate scale factors, while in the anti-τ region it may be substantially mismodeled.
- The error on α_{MJ} in the template-fit method. The systematic uncertainty of the template fit has to be estimated for each p_T^τ bin, since α_{MJ} is estimated independently for each p_T^τ bin. The uncertainty of α_{MJ} fit as detailed in Section 7.2 denoted as σ_α, for bin i is derived as follows:

$$\sigma_\alpha(\text{FF}^i) = \sqrt{(\text{FF}^2_{\text{multijet}} - \text{FF}^2_{\text{W+jet}})\sigma_\alpha^2} \tag{7.5}$$

where the $FF_{multijet}$ and FF_{W+jet} are the multijet and W+jet fake factors for the bin i respectively. The uncertainty on the total yield of the fake τ leptons is given by:

$$\frac{\sigma(N_{fakes})}{N_{fakes}} = \frac{\sqrt{\sum_i \sigma_\alpha^2 (FF^i)^2 n_i^2}}{N_{fakes}} \tag{7.6}$$

where

$$N_{fakes} = \sum_i n_i FF^i_{combined} \tag{7.7}$$

and $FF^i_{combined}$ is the combined fake factor for the corresponding bin in the signal region.

- The choice of the control region, i.e. the extrapolation from the control region to the signal region. It is estimated by using the study on the MC samples described in Section 7.5. In this case the uncertainties on the p_T^τ bins appear correlated. Therefore, the systematic uncertainty on the total yield due to the control region choice is derived with the allowing formula:

$$\frac{\sigma(N_{fakes})}{N_{fakes}} = \frac{\sum_i \sigma_\alpha (FF^i) n_i}{N_{fakes}}. \tag{7.8}$$

A summary of the effect of the systematic uncertainties on the total yield of the estimated fake τ contribution in the signal regions is given in Table 7.4 The impact

	$\tau_{had\text{-}vis}$+jets		$\tau_{had\text{-}vis}$+lepton	
Source of uncertainty on fake factors	Effect on yield	Shape	Effect on yield	Shape
Jet composition	4.6%	✓	2.8%	✓
Statistical uncertainties	0.62 %	✗	0.73%	✗
True $\tau_{had\text{-}vis}$ in the anti-$\tau_{had\text{-}vis}$ CR	3.0%	✓	4.5%	✓
α_{MJ} uncertainty	1.60%	✓	4.20%	✓
Control region choice	8.4 %	✓	7.9%	✓
Smirnov transform.	0%	✓	0%	✓

TABLE 7.4: Effect on the shape variation and the yields of systematic uncertainties associated with the data-driven fake factor method, used to estimate the $j \to \tau_{had\text{-}vis}$ background in the $\tau_{had\text{-}vis}$+jets and $\tau_{had\text{-}vis}$+lepton channel.

of systematic uncertainties on the normalization and shape of the BDT discriminant trained on the H^+ mass range 130–160 GeV for the $j \to \tau_{had\text{-}vis}$ background is illustrated in Figure 7.29.

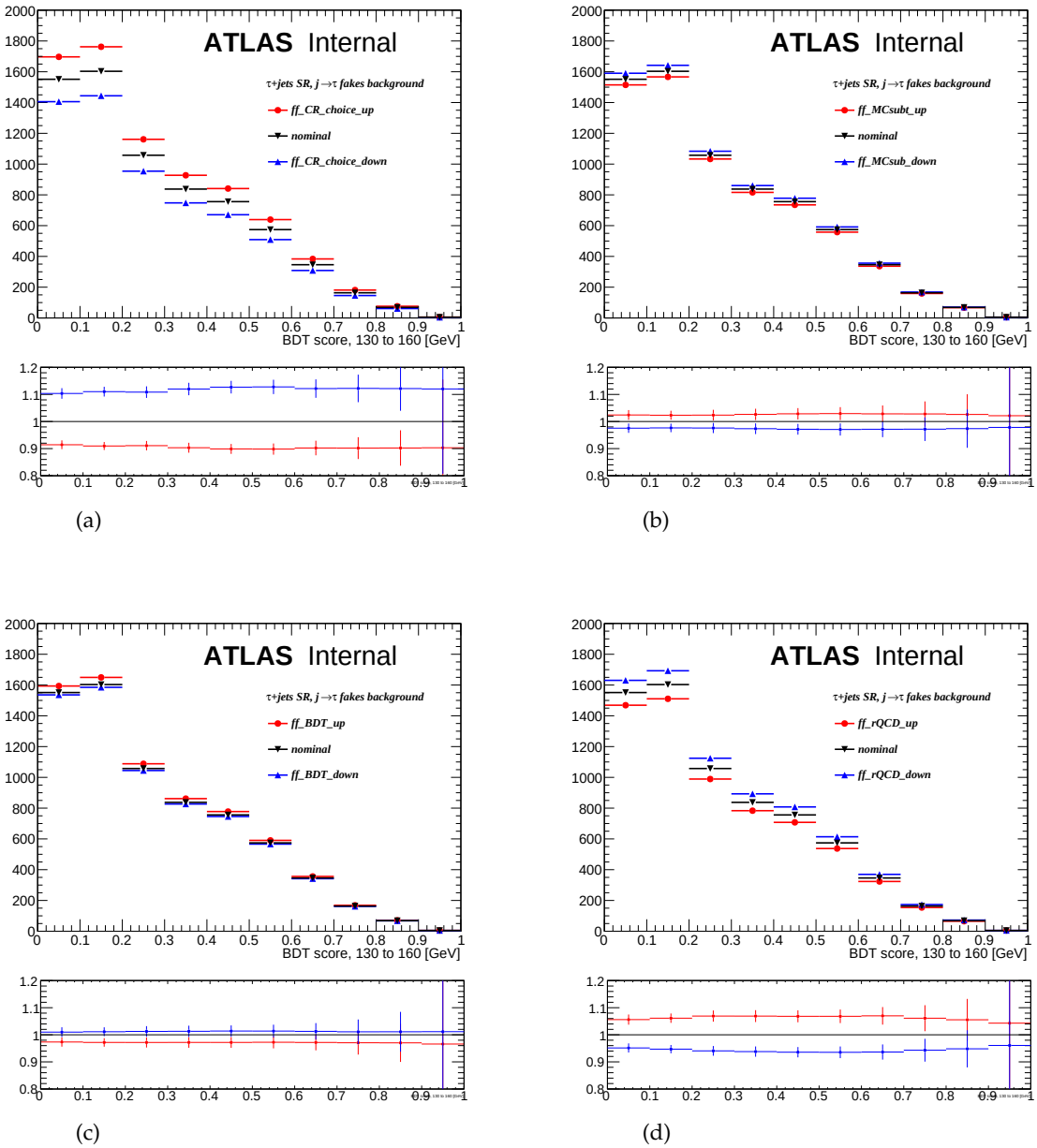

FIGURE 7.29: Effect of systematic variations on the BDT score in the H^+ mass range 130–160 GeV in the $\tau_{\text{had-vis}}$+jets signal region: choice of control region (a) true τ contamination in the anti-$\tau_{\text{had-vis}}$ control region (b), lower cut of the transformed $\tau_{\text{had-vis}}$ BDT score (c) and α_{MJ} uncertainty (d).

As mentioned in section 6.4.5 the correction to the $\mathcal{Y}$ variable calculated for the fake-$\tau_{\text{had-vis}}$ candidates is mandatory. Figure 7.30 shows distributions of $\mathcal{Y}$ for $\tau_{\text{had-vis}}$ and anti-$\tau_{\text{had-vis}}$ candidates in the W+jets control region and their CDFs. The shape of the $\mathcal{Y}$ variable obtained from different control regions is different. One can obtain the $\mathcal{Y}$ correction from each control region separately. This shape variation is considered as the source of systematic uncertainty. The distribution of the $\mathcal{Y}$ variable after Smirnov transformation in the signal-like region and the Shape variation of $\mathcal{Y}$ after

correction obtained by multijet and W+jet control regions are shown in Figure 7.31. The systematic uncertainty of Smirnov transform is not included in the uncertainty band of ratio plots. However, it will contribute to the final statistical analysis of the result.

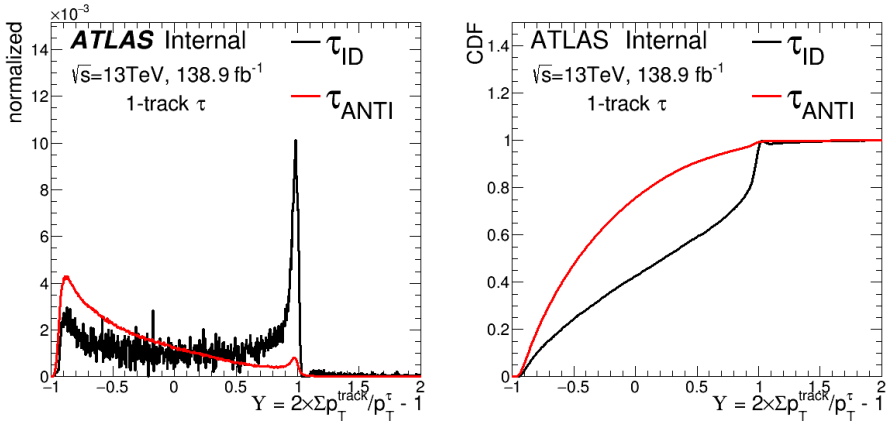

(a) (b)

FIGURE 7.30: Distribution of the Υ for $\tau_{\text{had-vis}}$(black) and anti-$\tau_{\text{had-vis}}$ (red) candidates in the W+jets control region (a). CDF of Υ for $\tau_{\text{had-vis}}$(black) and anti-$\tau_{\text{had-vis}}$ (red) candidates in the W+jets control region (b).

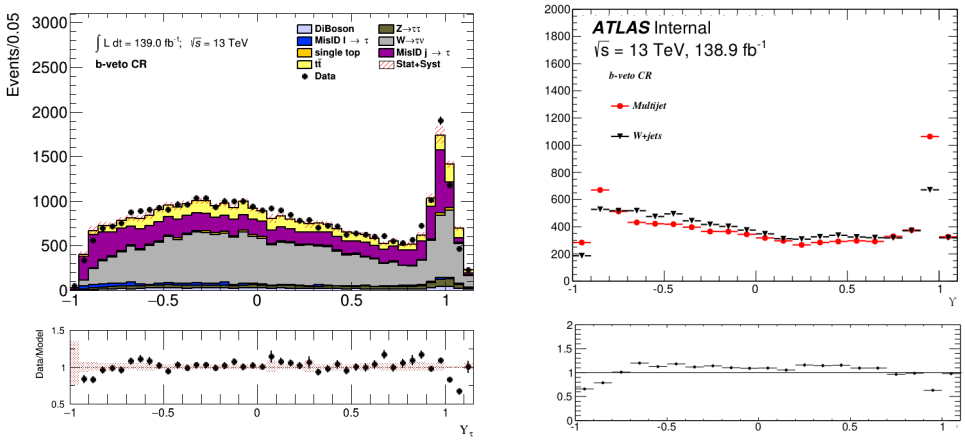

(a) (b)

FIGURE 7.31: Distribution of Υ variable after the Smirnov transformation in the signal-like region with a *b*-jet veto applied (a). The shape variation of Υ variable after a correction obtained from multijet and W+jet control regions (b). The uncertainty band in the ratio plots includes both statistical and fake factor method systematic uncertainty.

7.7 Modified discriminant in the full Run-II analysis and expected sensitivity

The output of the Boosted Decision Tree classifier is used to separate H^+ signal from SM background processes, following the same event selection as the one used in the previous round of analysis in Section 6.3. The training of the BDT is preformed using the Scikit learning tool [103], the setting of parameters is presented in Appendix B.1. A new variable $\Delta\phi_{\tau,miss}$ / $\Delta\phi_{jets,miss}$, where $\Delta\phi_{x,miss}$ is the difference in azimuthal angle between a detector object x and the direction of the missing transverse momentum, is introduced for both channels. Two hardest jets are considered. Training is done in five mass bins: 80-120, 130-160, 160-200, 200-400, 500-3000 GeV. The k-fold strategy with k=5 is used. The modeling of input variables for $\tau_{\text{had-vis}}$+jet channel in the b-veto control region is shown in Figures 7.32 and 7.33. For the $\tau_{\text{had-vis}}$+lepton channel, the corresponding plots are presented in Appendix B.2. The observed modeling of all input variables contributing to the MVA discriminant output appears satisfactory within the attributed systematic uncertainty. At the time of writing, signal regions are still blinded i.e. any data distributions in signal regions can not yet be directly inspected. The $\tau_{\text{had-vis}}$+jet and $\tau_{\text{had-vis}}$+lepton signal regions blinded distribution of input variables are shown in Appendix B.2. The BDT score distributions in the b-veto control region for five H^+ mass regions are shown in Figures 7.34 and 7.35. In Figures 7.32, 7.33, 7.34 and 7.35, the uncertainty bands in the ratio plots include both statistical and fake factor method systematic uncertainty. One can see good modeling of the background.

A comparison of the analysis sensitivity for the full Run-II and 2015 and 2016 analysis presented in Chapter 6 is shown in Figure 7.36. The expected limit is obtained using exactly the same statistical analysis as the one used in the previous round described in Section 6.6.

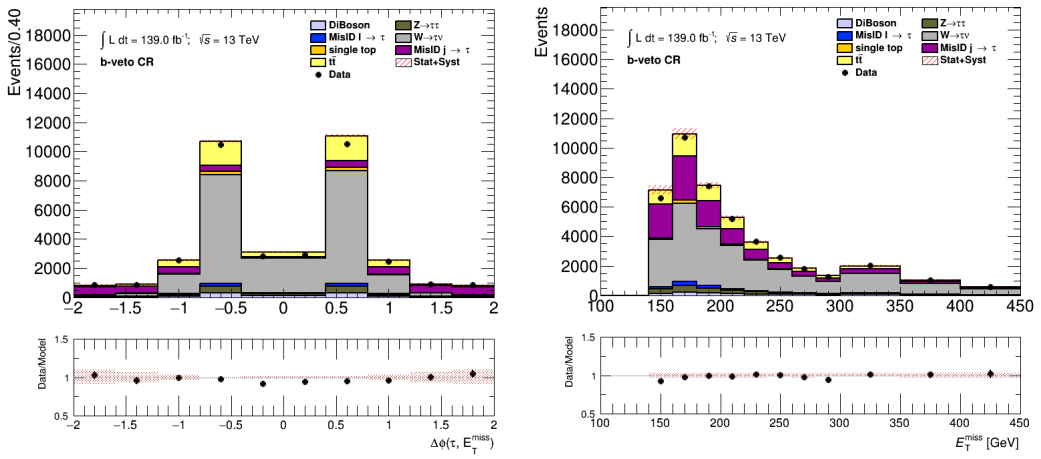

(a) (b)

FIGURE 7.32: Distributions of input variables for BDT training for the $\tau_{\text{had-vis}}$+jet channel in b-veto control region, $\Delta\phi_{\tau,miss}$ (a) E_T^{miss} (b). The uncertainty band in the ratio plots includes both statistical and fake factor method systematic uncertainty.

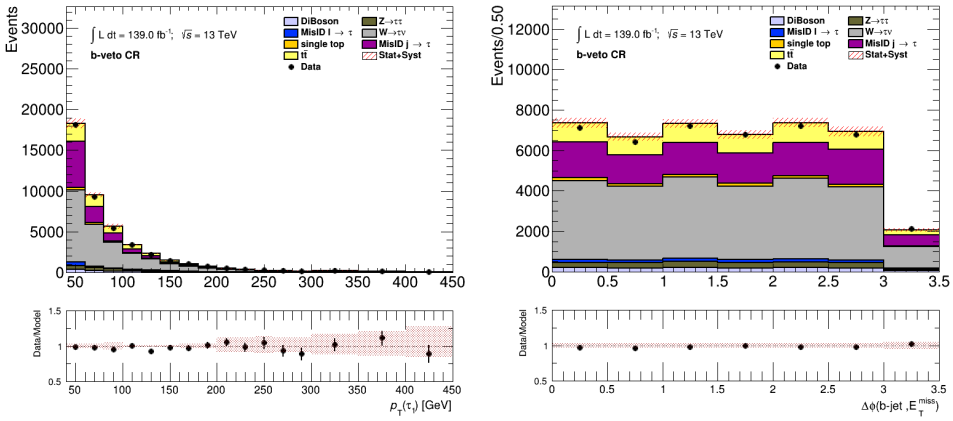

(c) (d)

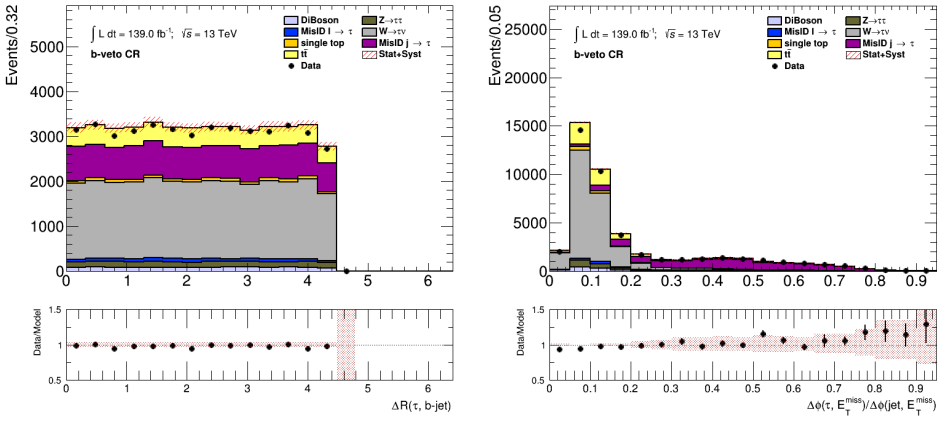

(e) (f)

FIGURE 7.33: Distributions of input variables for BDT training for $\tau_{\text{had-vis}}$+jet channel in the b-veto control region, p_T^τ (c) $\Delta\phi_{bjet,miss}$ (d) $\Delta R_{bjet,\tau}$ (e) $\Delta\phi_{\tau,miss}/\Delta\phi_{jets,miss}$ (f) where the jets are two hardest jets, the distribution of Y is shown in Figure 7.31 (a). The uncertainty band in the ratio plots includes both statistical and fake factor method systematic uncertainty.

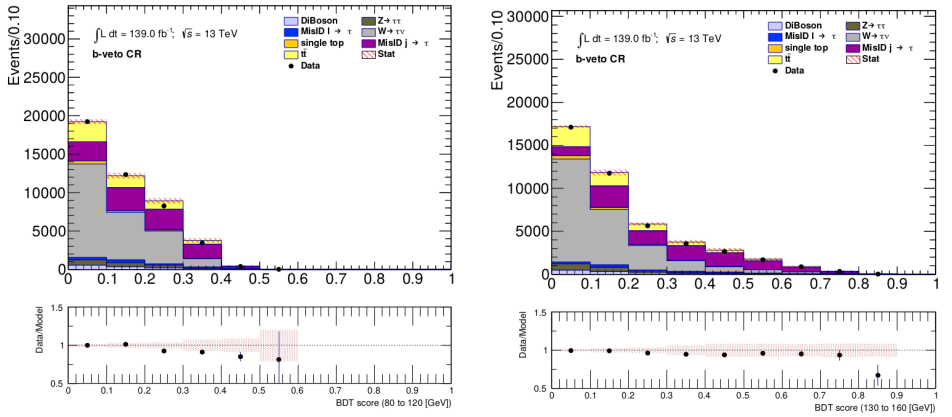

(a) (b)

FIGURE 7.34: BDT score distribution in the b-veto control region for five H^+ mass ranges 80-120 (a) 130-160 (b) GeV. The uncertainty band in the ratio plots includes both statistical and fake factor method systematic uncertainty.

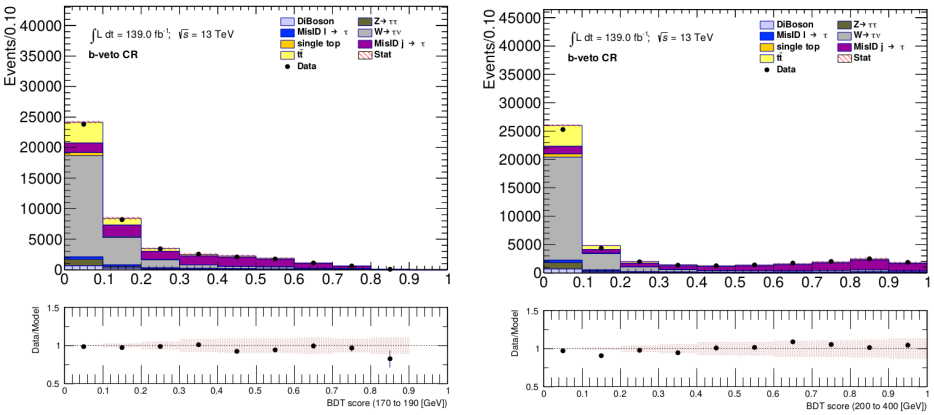

(c) (d)

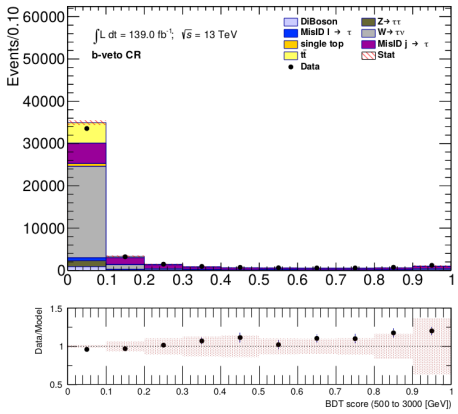

(e)

FIGURE 7.35: BDT score distribution in b-veto control region for five H^+ mass ranges 170-190 (c) 200-400 and (d) 500-3000 (e) GeV. The uncertainty band in the ratio plots includes both statistical and fake factor method systematic uncertainty.

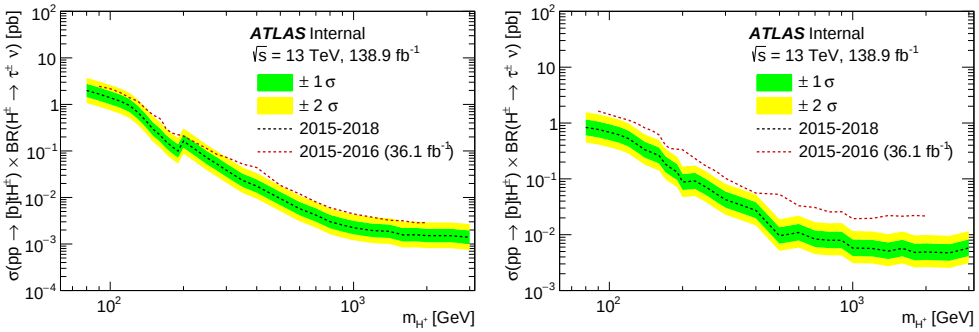

(a) (b)

FIGURE 7.36: The comparison of expected limit for the full Run-II and 2015 and 2016 analysis for $\tau_{\text{had-vis}}$+jet (a) for $\tau_{\text{had-vis}}$+lepton (b) channel. The shown limits include statistical uncertainty only.

At the current stage, the sensitivity gain in the $\tau_{\text{had-vis}}$+jet channel seems consistent with the increased statistics. In the $\tau_{\text{had-vis}}$+lepton, there is a visible additional gain, due to the analysis improvement. The present limits are very preliminary. Further improvement of sensitivity especially, in the $\tau_{\text{had-vis}}$+jet channel, should be expected. The shown limits include statistical uncertainty only, as for technical reasons the proper treatment of systematics could not yet be included.

7.8 Summary

In this chapter the estimation of the background resulting from jet misidentified as $\tau_{\text{had-vis}}$ candidates for full Run-II data is presented. The fake factor data-driven method is used to estimate the number of jets misidentified as hadronically decaying τ leptons. In Section 7.2 the standard fake factor method is used. It is shown that in the low and intermediate p_T^τ region, the jet fractions of control regions are different, therefore as it is discussed in Section 7.3 a template fit approach is used with τ jet width, the MLP response and the transformed $\tau_{\text{had-vis}}$ BDT score for 1-prong and 3-prong τ candidates in order to estimate α_{MJ} used for the combined fake factors. The results show that the transformed $\tau_{\text{had-vis}}$ BDT score is not an optimal discriminant for 1-prong candidate and τ jet width is not an optimal discriminant for 3-prong candidates. However, the fake factors estimated from different approaches are typically consistent within the attributed uncertainties. For large p_T^τ candidates, the fake factors are similar in the two control regions; therefore, the template fit, although not preforming as well as lower p_T^τ bins, does not have a large effect on the final fake factors. Validation of the fake τ background estimation using signal-like control regions is presented in Section 7.4. In Section 7.5, a study based on MC samples was preformed in order to validate the fake factor method in particular the estimation of α_g and the extraction of the potential systematic due to the extrapolation of fake factors from control regions to the signal region. In Section 7.6, a detailed analysis of the systematic uncertainties related to the fake factor method is presented. Section 7.7 presents the modified BDT discriminant used for full Run-II analysis and the expected limit, which shows improvement of sensitivity in the full Run-II analysis. The results of this section are preliminary, and they are subject to further improvement. The main goal ofthis part of the thesis was to assure good modeling of the background arising from jets misidentified as $\tau_{\text{had-vis}}$. This goal has been achieved.

Chapter 8

Conclusions

This thesis presents a selection of studies dedicated to the search for extended scenarios of electroweak symmetry breaking. It consists of two parts.

The first part is dedicated to the development of tools used for high precision predictions for τ physics, including signal, background and their interference in the SM and BSM electroweak symmetry breaking scenarios. The studies were dedicated to `TauSpinner`. `TauSpinner` is a program that allows for modifying the physics model of Monte Carlo generated samples in the case of the changed assumptions about event production dynamics without the need to re-generate events. With the help of weights τ-lepton production or decay processes can be modified according to a new physics model. In this study a new version of `TauSpinner` which includes a provision for introducing non-standard matrix element and couplings together with tests of its effect on the vector-boson-fusion processes is presented. It exploits the spin correlations of τ-lepton pair decay produced in processes where final states include also two hard jets, so-called $2 \to 4$ processes. The results of this work are presented in Chapter 3, which contains the evaluation of systematic uncertainties of `TauSpinner` for variation of its input parameters and a study on the effect of interference between QCD and electroweak subprocesses in `TauSpinner`. The results were published in Ref. [4]. Moreover, the `TauSpinner` was developed to allow for the implementation of new matrix elements in non-SM scenarios and the new feature was tested for an example case of a generic spin-2 boson. This results also presented in Chapter 3, were published in Ref. [5].

The second part of the thesis is dedicated to the search for charged Higgs bosons produced in top quark decays or in association with a top quark and eventually decaying to a $\tau\nu$ pair in the $\tau_{\text{had-vis}}$+jets and $\tau_{\text{had-vis}}$+lepton final states. The result is published in Ref. [6] is described in Chapter 6. The investigation was based on 36 fb^{-1} of data produced with the ATLAS detector at center-of-mass energy $\sqrt{s} = 13$ TeV in the years 2015 and 2016. The data is found to be in agreement with the background-only hypothesis. Upper limits at 95% confidence level are set on the H^+ production cross-section times the branching fraction $\mathcal{B}(H^+ \to \tau\nu)$ between 4.2 pb and 2.5 fb for charged Higgs boson mass range 90-2000 GeV, corresponding to upper limits between 0.25% and 0.031% for the branching fraction $\mathcal{B}(t \to bH^+) \times \mathcal{B}(H^+ \to \tau\nu)$ in the mass range 90-160 GeV. In this round of analysis the author contributed to study of adding the polarization sensitive variable Y in the BDT discriminant, setting up the BDT training for the $\tau_{\text{had-vis}}$+jets channel and evaluation of selected systematic uncertainties.

The fake τ background estimation for the full Run-II, 139 fb^{-1} of data recorded by the ATLAS detector in the years 2015-2018 is presented in Chapter 7. The study presents the complete evaluation of the critical background arising from quark- and gluon-initiated jets misidentified as hadronically decaying τ leptons performed on the new reprocessing of ATLAS data and MC samples. The fake factors extracted

in the two different control regions, were combined according to the composition of quark- or gluon-initiated jets faking τ leptons in the signal region. The composition was estimated using a template fit to a variable sensitive to the jet origin (quark or gluon). Special attention was paid to the optimal choice of the discriminant.

The results indicate that based on MLP training, the newly proposed variable, can be a universally good discriminant candidate for determining the jet composition structure. Nonetheless, the τ jet width variable as discriminant shows compatible results for 1-prong candidates, and transformed $\tau_{\text{had-vis}}$ BDT score for 3-prong candidates. A detailed analysis of systematic uncertainties of the fully data-driven fake factor method for full Run-II analysis was presented. The modified BDT discriminant used for the full Run-II analysis and the expected limit were also presented. The observed modeling of all input variables appeared satisfactory within attributed uncertainties. So does the modeling of the resulting BDT score discriminant in the full Run-II analysis. The analysis sensitivity in the $\tau_{\text{had-vis}}$+jet and $\tau_{\text{had-vis}}$+ lepton channels was presented. The expected limits show improvement with respect to the published result. It should be kept in mind that these results are early-stage and subject to further improvement.

Appendix A

TauSpinner $2 \to 4$ technical details

A.1 Topologies and the dynamical strauctures of subprocesses

There are automated programs for generating codes of spin amplitudes calculation. In the development of TauSpinner $2 \to 4$ MadGraph5 was used. The number of contributing processes in the TauSpiner $2 \to 4$ is very large. For the case of the non-Higgs Drell-Yan–type background processes, in which the τ-pair originates either from the vector boson decay (including also cascade decays) or from multi-peripheral vector-boson fusion processes, MadGraph5 generates 82 subprocesses with partons belonging to the first two generations of quarks, or gluons. Subprocesses in which all partons are of the same flavour, receive contributions from 64 Feynman diagrams, subprocesses with two pairs of flavours – either 43 diagrams or 32 diagrams (if both pairs are either down- or up-type), subprocesses with three or four different flavours – 11 diagrams, and subprocesses with two quarks and two gluons 16 diagrams. As far as the dynamical structure of the amplitudes is concerned, there are in general, seven different topologies of Feynman diagrams, shown in Figure A.1. Each of them contribute to a given subprocess depends on flavours of incoming and outgoing partons. It is worth to mention that, independent of their origin, in all processes the polarization of τ leptons are strongly correlated due to the helicity-conserving couplings to the vector bosons. The spin correlations of the τ pair depend on the relative size of the subprocesses with vector and pseudo-vector coupling contributing to the given final state configuration. For example, in the case of $q\bar{q} \to \tau^+\tau^- q\bar{q}$, in Figure A.1 diagram(d) contributes with 100% polarized τ's since they couple directly to $W^\pm$. In diagram (g), the polarization of $Z\gamma^*$ is different than in the Born-like production because $Z\gamma^*$ decaying to $\tau^+\tau^-$ originates from $WWZ\gamma^*$ vertex. This leads to a distinct polarization of τ lepton.

For the Higgs signal processes the τ pairs originate from the Higgs boson decay, which is imposed at the generation level, and the number of subprocesses is reduced to 67. Each subprocess receives contributions from at most two Feynman diagrams, since with massless quarks of the first two generations, the Higgs boson can originate either from the vector boson fusion or from Higgs-strahlung diagrams, as illustrated in Figure A.2. Depending on the flavour configuration of incoming partons, mediating boson is W or Z, which causes almost 10 GeV shift betweeen resonance invariant mass of the outgoing pair of jets in case of Higgs-strahlung process. The helicity-flipping scalar coupling to the Higgs boson results in the opposite spin correlation as compared to the case of the Drell-Yan-process. The individual τ polarization is absent. Concerning the analytic structure of the differential cross sections, it is determined by topologies of contributing diagrams to a particular subprocess. For example, s-channel propagators will result in a resonance enhancement, (in the limit $m_W^2/s \ll 1$, $m_Z^2/s \ll 1$) regulated either by the phase space cuts or by the virtuality of the attached boson line. Technically speaking, the sum in Equation 3.8 defining

the production weights used in `TauSpinner` consist of 9^4(11^4 if b-quark are allowed) elements, which are poteintially distinct and require thier own subroutines for the matrix elements. Since most of the elements are equal zero, or some matrix elements are related to others by permutation of partons and/or CP symmetries, special interfacing procedure is prepared to exploit those relations. It reduces significantly the computation time and size of the program code. Details can be found in [3].

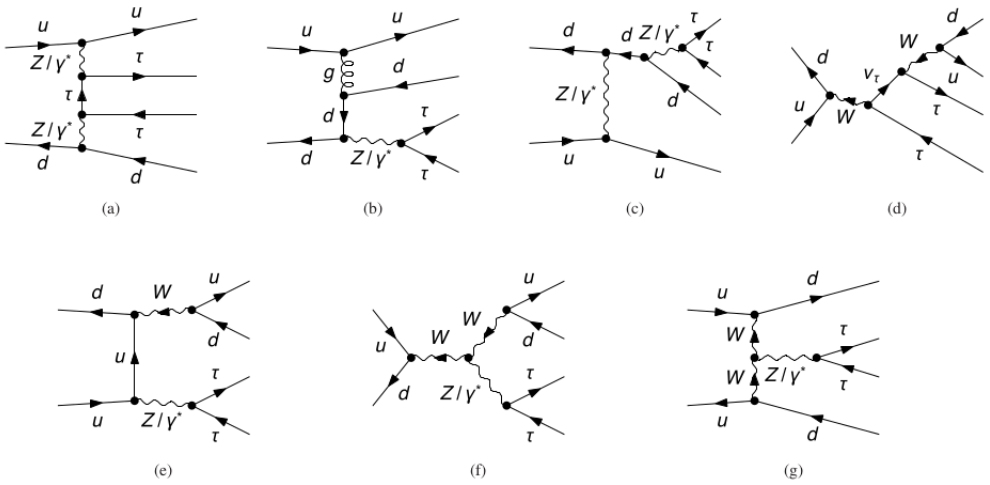

FIGURE A.1: Typical topologies of diagrams contributing to the Drell-Yan–type SM process in $u\bar{d} \to \tau^+\tau^- u\bar{d}$:multi-pheripheral(a), double-t(b), t-cascade(d), double-s(e), mercedes(f) and fusion(g) type of diagrams.

FIGURE A.2: Topologies of diagrams contributing to the Higgs production process $u\bar{d} \to H(\to \tau^+\tau^- u\bar{d}$: vector boson fusion(a), Higgs-struhlung(b). In general, depending on the flavour of incoming partons, mediating boson could be W or Z.

A.1.1 Kinematical distribution for tests of implementation of external matrix elements

In this section all kinematical distributions that is used for testing of implementation in the `TauSpinner` have been shown. The distributions are :

- η^{τ} : pseudorapidity of τ;
- η^{jet} : pseudorapidity of jet;
- $\Delta\eta^{jj}$: pseudorapidity gap between two jets;

- $Y^{\tau,\tau}$: rapidity of $\tau\tau$ system;
- m^{jj} : invariant mass of jj system;
- p_T^{jj} : transverse momenta of the jj system;
- Y^{jj} : rapidity of jj system;
- $m^{\tau\tau\,jj}$: invariant mass of $\tau\tau$ jj system;
- $p_T^{\tau\tau}$: transverse momentum of the $\tau\tau$ system;
- $p_z^{\tau\tau jj}$: longitudinal momentum of the $\tau\tau$ jj system;

VBF selection

- $100 < m^{jj} < 800$ GeV
- $p_T^{\tau\tau}$ <600 GeV
- $m^{\tau\tau\,jj} < 1500$ GeV

Normalization

- X sample : σ= 0.90614 e+03 (pb)
- Higgs sample : σ= 0.20431 e+00 (pb)

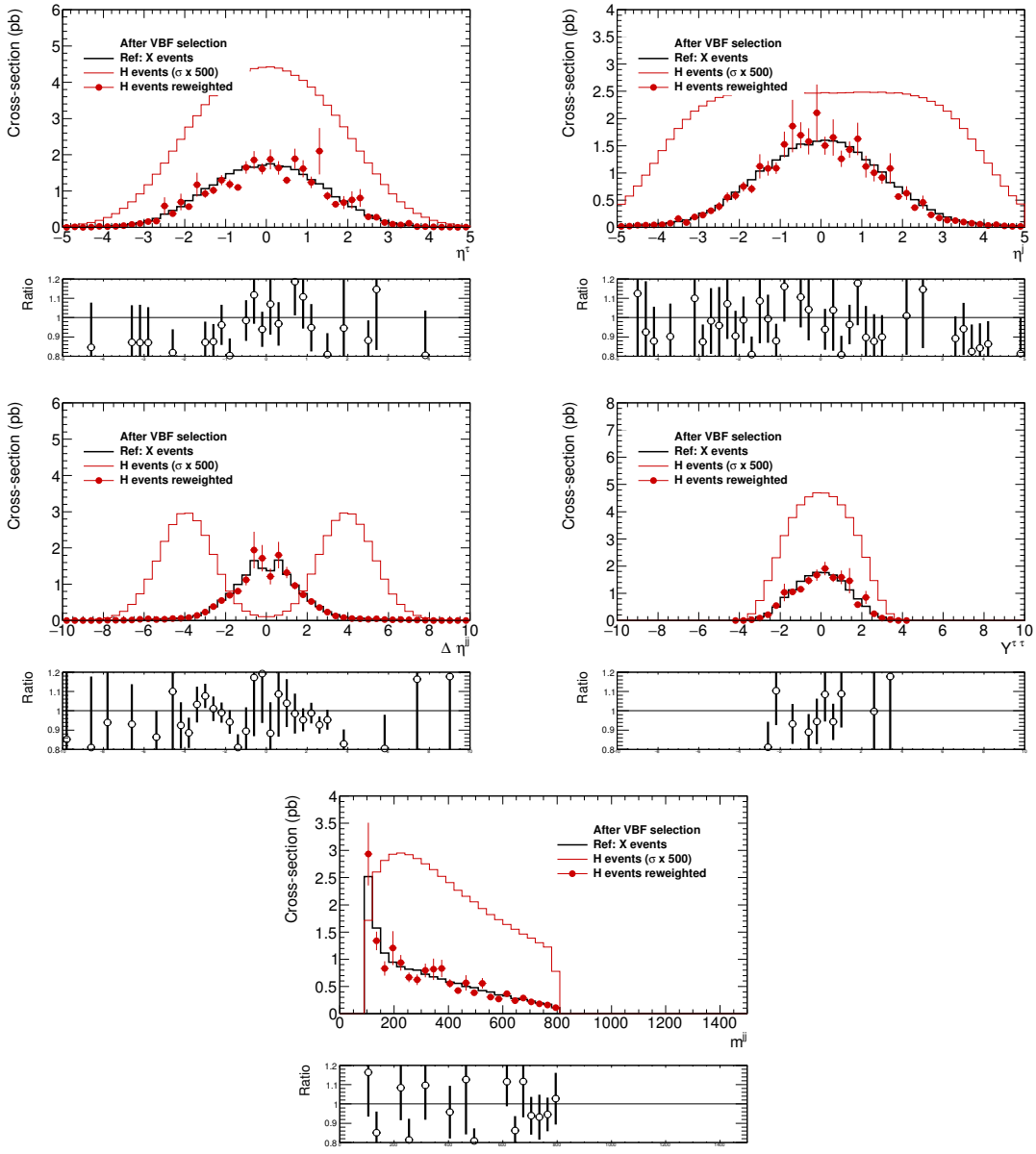

Figure 1: The Higgs sample reweighted to X and compared to X sample. After VBF selection.

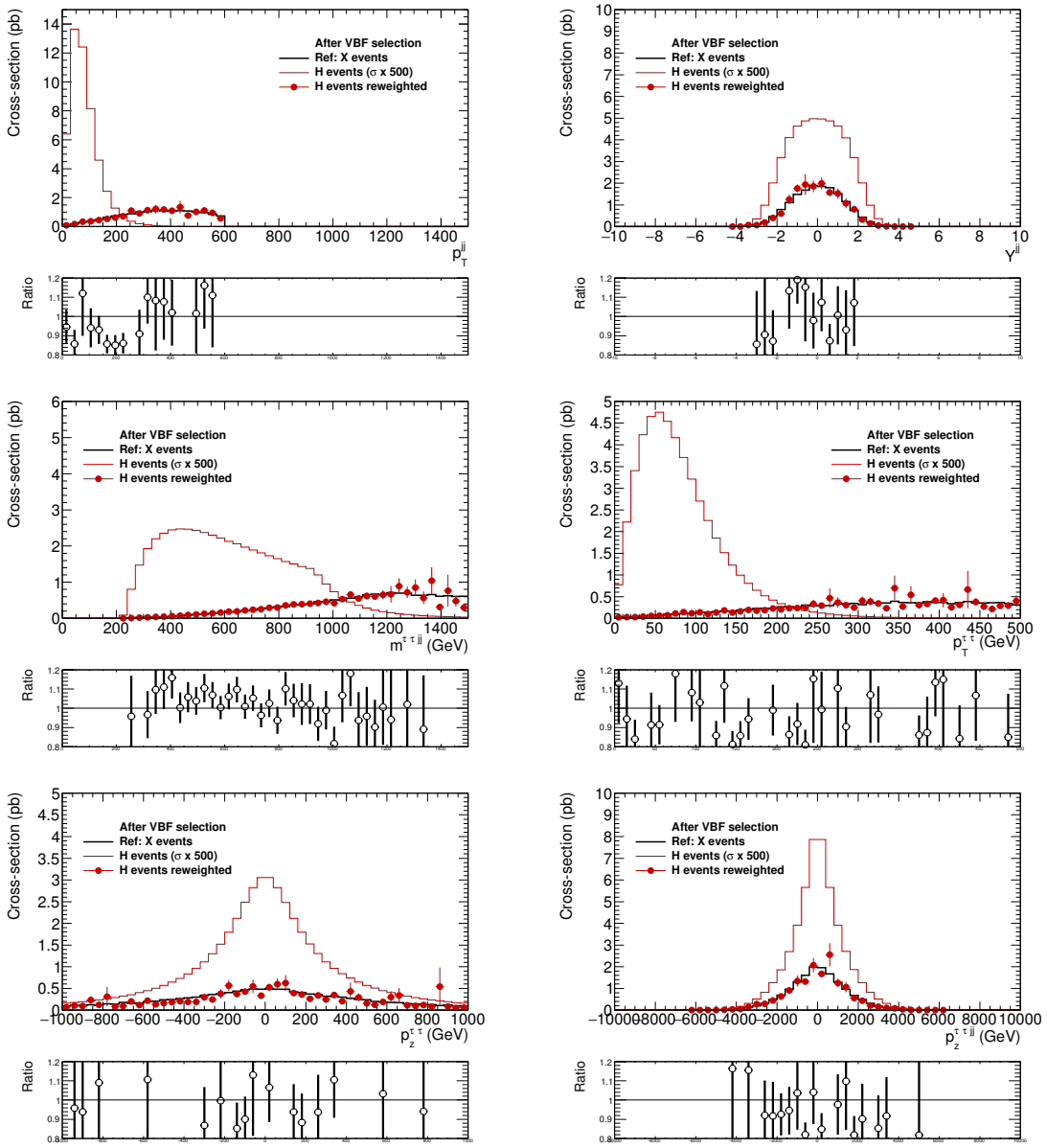

Figure 2: The Higgs sample reweighted to X and compared to X sample. After VBF selection.

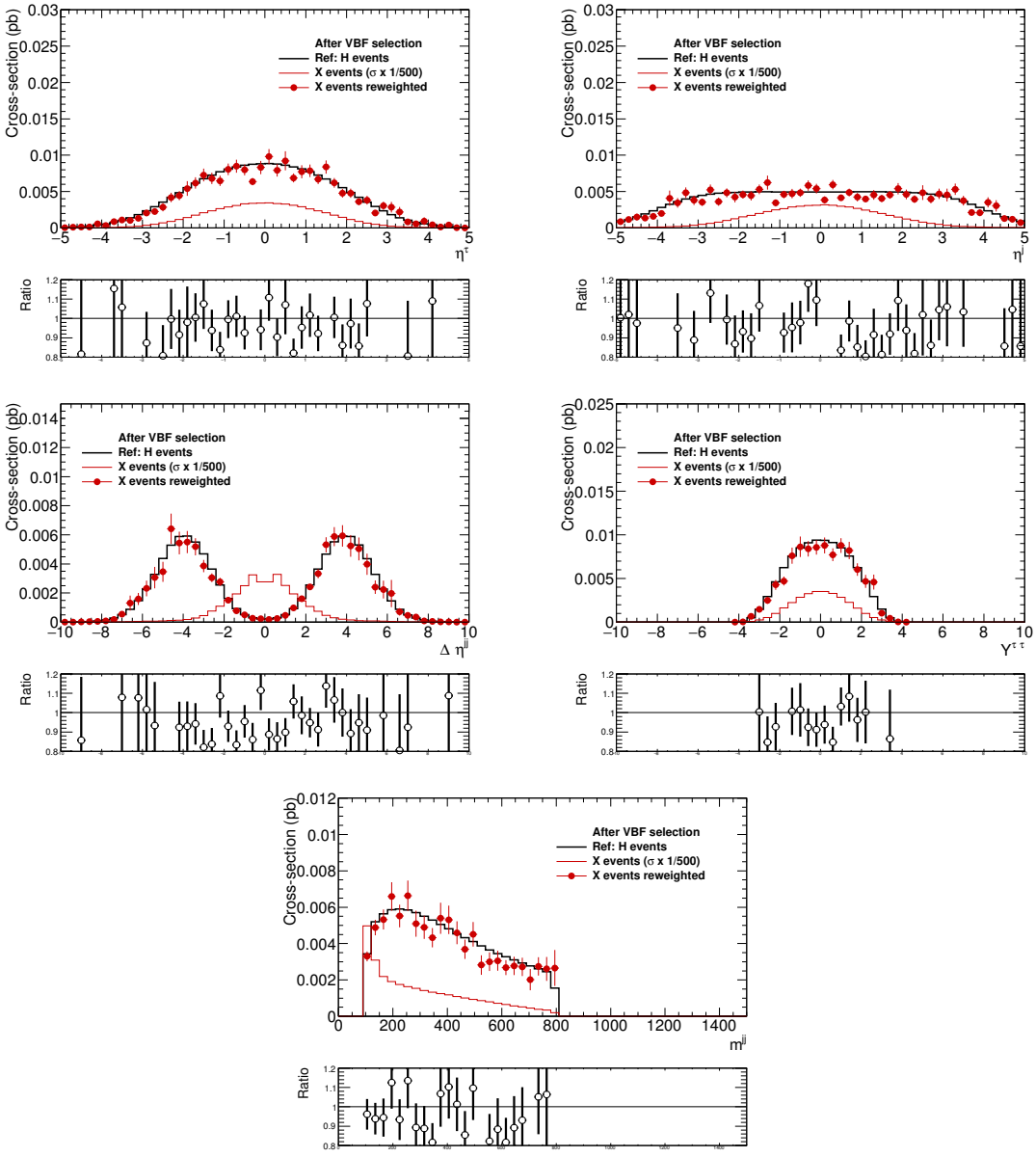

Figure 3: The X sample reweighted to the Higgs. After VBF selection.

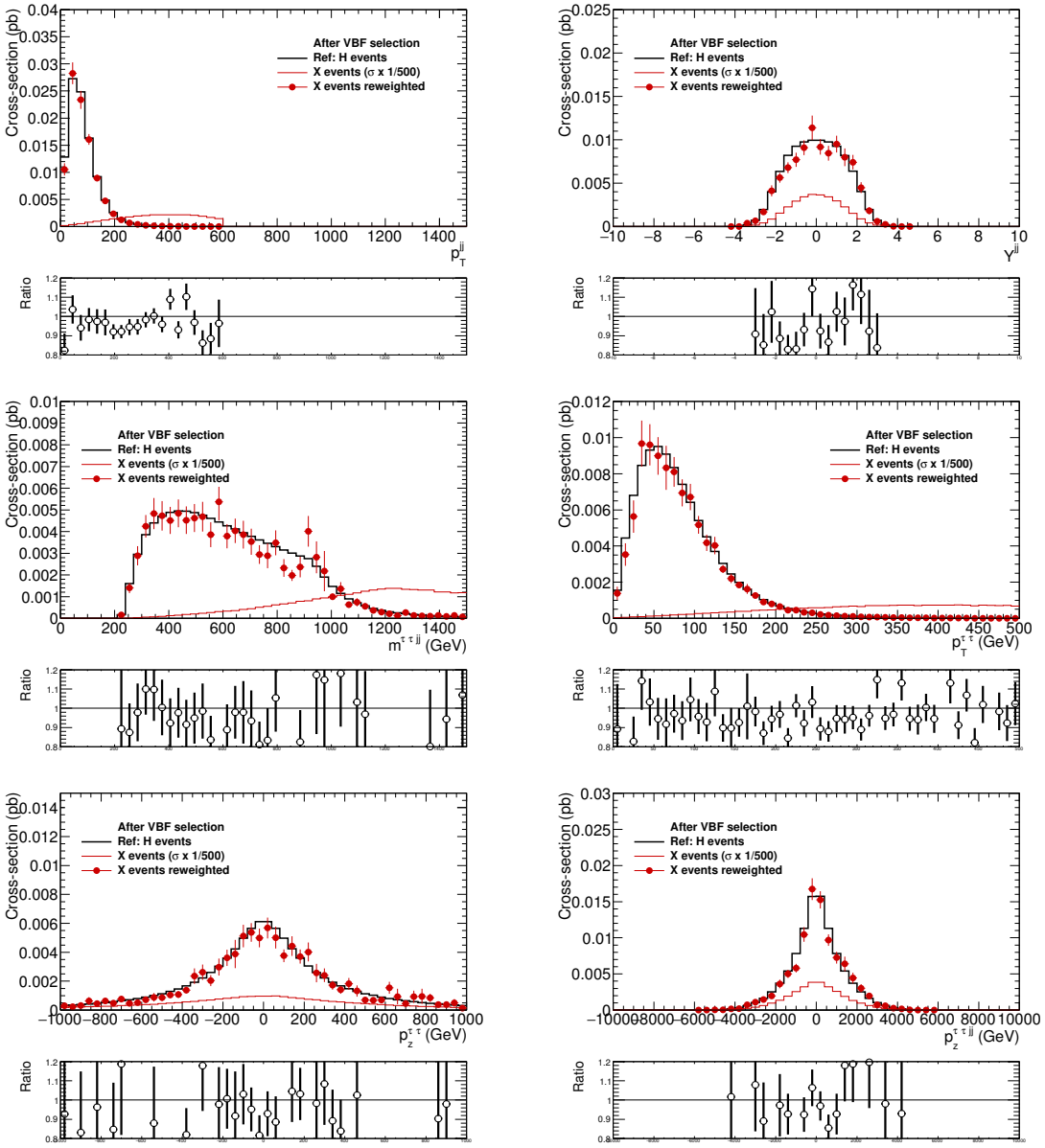

Figure 4: The X sample reweighted to the Higgs. After VBF selection.

Appendix B

Fake factor method full Run-II

B.1 BDT tarining setup for full Run-II

The hyperparameter of BDT training for $\tau_{\text{had-vis}}$+jet and $\tau_{\text{had-vis}}$+lepton channels are shown in Tables B.1 and B.2, respectively.

mass range [GeV]	80-120	130-160	170-190	200-400	500-3000
number of estimators	100	100	100	200	200
learning rate	0.1	0.1	0.1	0.1	0.1
max depth	10	10	10	20	20
min samples leaf	0.005	0.005	0.005	0.002	0.001
min samples split	0.01	0.01	0.01	0.004	0.002

TABLE B.1: The hyperparameter of BDT training used in five H^+ mass bins for $\tau_{\text{had-vis}}$+jet channel.

mass range [GeV]	80-120	130-160	170-190	200-400	500-3000
number of estimators	200	200	200	200	200
learning rate	0.1	0.1	0.1	0.1	0.1
max depth	12	12	12	20	20
min samples leaf	0.005	0.005	0.005	0.002	0.002
min samples split	0.01	0.01	0.01	0.004	0.002

TABLE B.2: The hyperparameter of BDT training used in five H^+ mass bins for $\tau_{\text{had-vis}}$+lepton channel.

B.2 Input variables for BDT-training for different regions

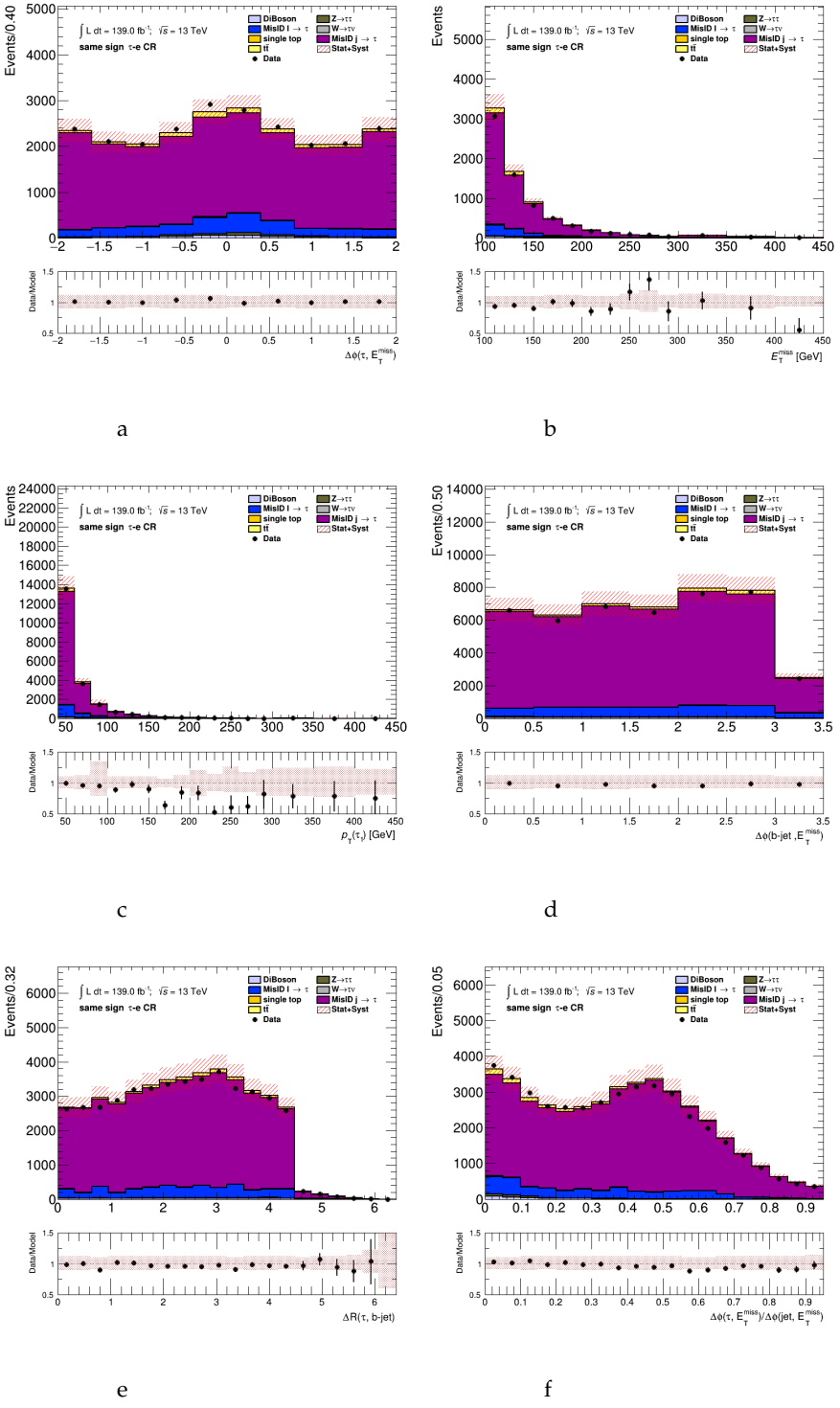

FIGURE B.1: Distributions of input variables for BDT-training for $\tau_{\text{had-vis}}$+lep channel in τ+electron same sign control region (a) $\Delta\phi_{\tau,miss}$ (b) E_T^{miss} (c) p_T^{τ} (d) $\Delta\phi_{bjet,miss}$ (e) $\Delta R_{bjet,\tau}$ (f) $\Delta\phi_{\tau,miss}/\Delta\phi_{jets,miss}$ where the jets are two hardest jets, the distribution of Y is already shown in Figure 7.31 (a).

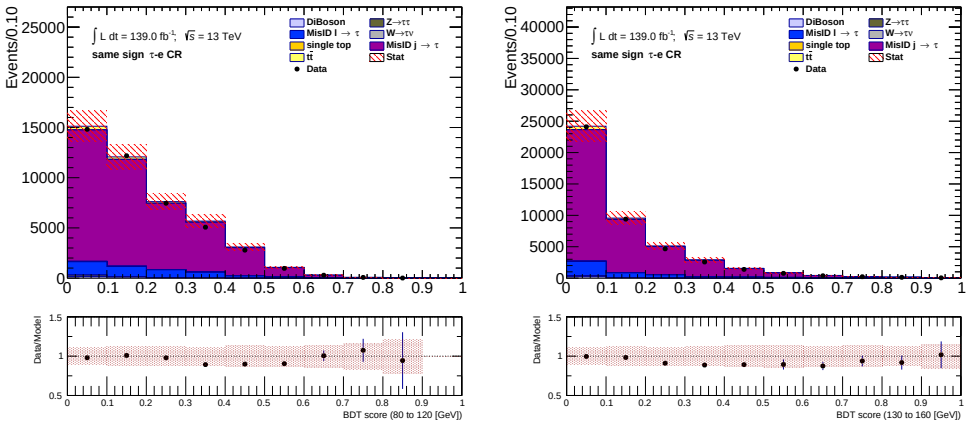

a b

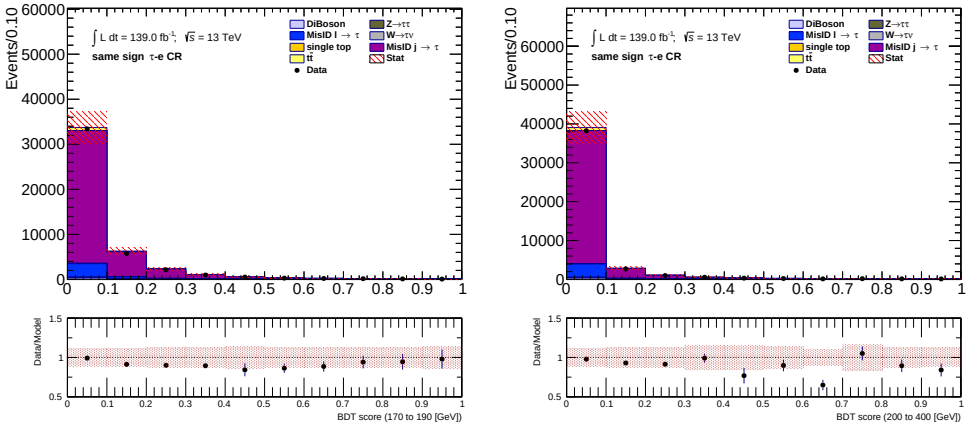

c d

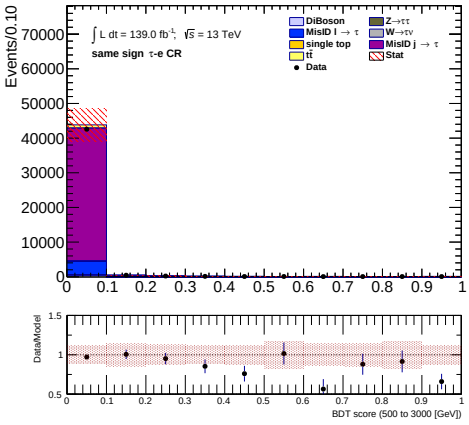

e

FIGURE B.2: BDT score distribution in τ+electron same sign control region for five H^+ mass range training, the uncertainty band in the ratio plots include both statistical and fake factor method systematic uncertainty.

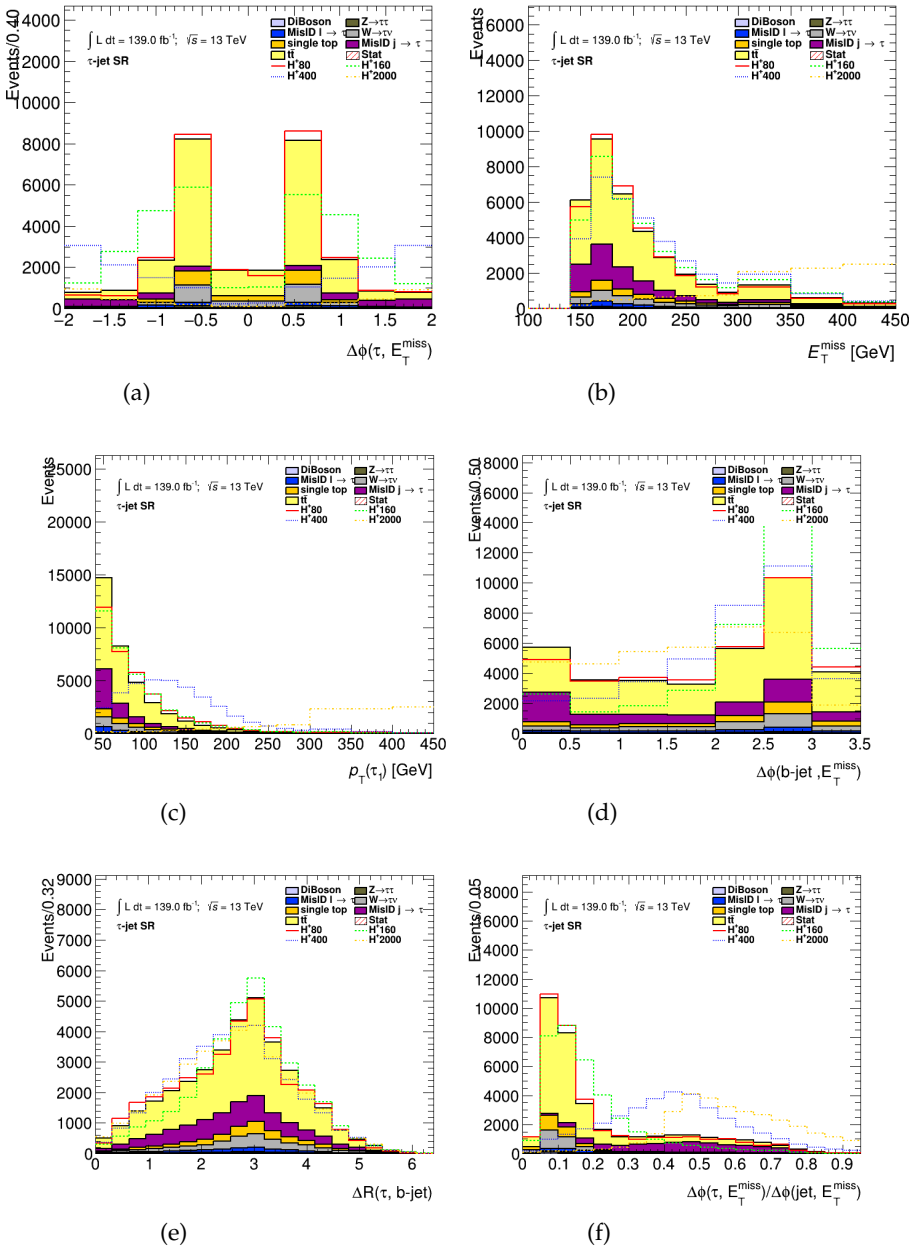

(a) (b)

(c) (d)

(e) (f)

FIGURE B.3: Distributions of input variables for BDT training for $\tau_{\text{had-vis}}$+jet signal region, $\Delta\phi_{\tau,miss}$ (a) E_T^{miss} (b), p_T^{τ} (c) $\Delta\phi_{bjet,miss}$ (d) $\Delta R_{bjet,\tau}$ (e) $\Delta\phi_{\tau,miss}/\Delta\phi_{jets,miss}$ (f) where the jets are two hardest jets.

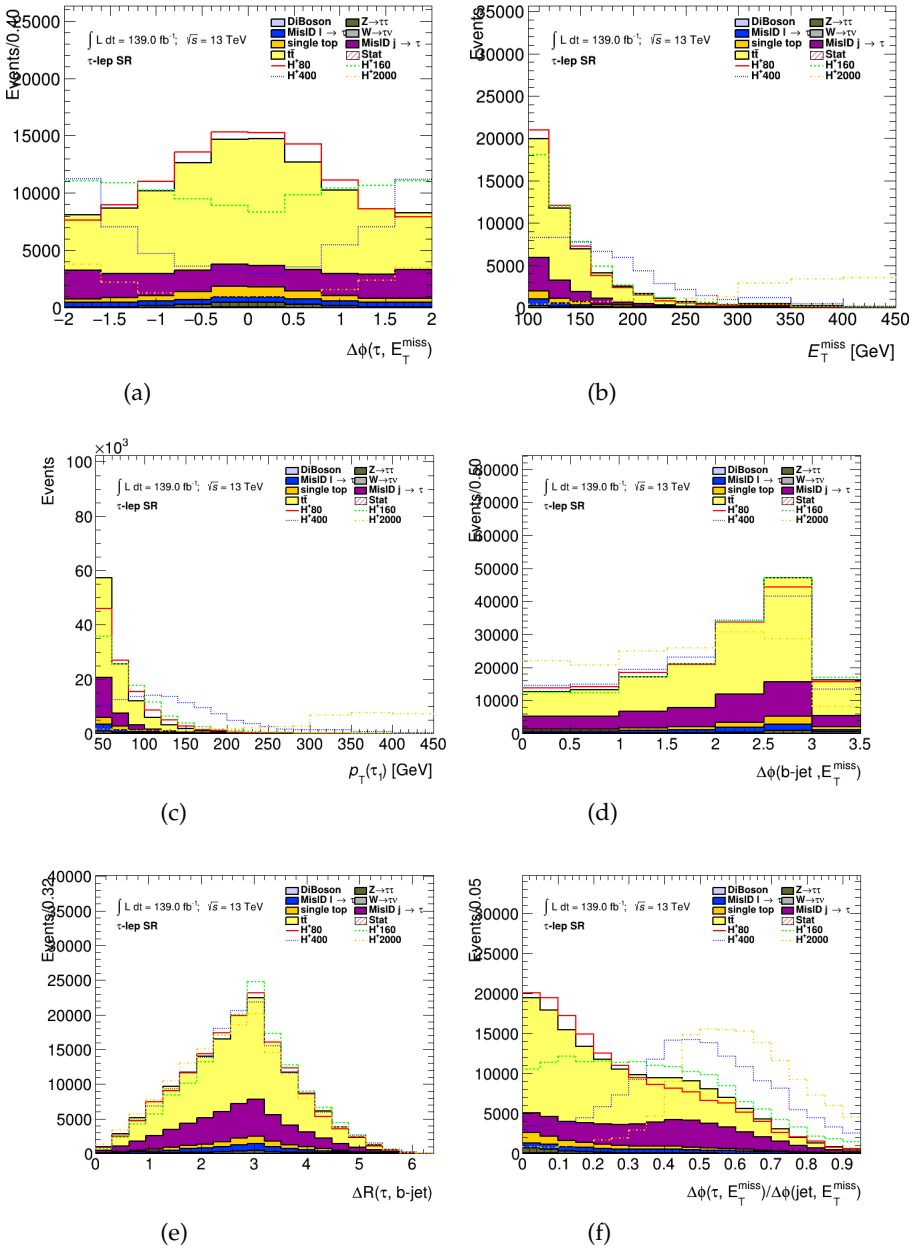

(a) (b) (c) (d) (e) (f)

FIGURE B.4: Distributions of input variables for BDT training for $\tau_{\text{had-vis}}$+lepton signal region, $\Delta\phi_{\tau,miss}$ (a) E_T^{miss} (b), p_T^{τ} (c) $\Delta\phi_{bjet,miss}$ (d) $\Delta R_{bjet,\tau}$ (e) $\Delta\phi_{\tau,miss}/\Delta\phi_{jets,miss}$ (f) where the jets are two hardest jets.

B.3 Test of alternative working point for the fake factor estimation for full Run-II

In this Section, we study the effect of using different working point for the fake factor extraction. In this exercise, a subset of reconstructed $\tau_{\text{had-vis}}$ candidates that fail the medium working point is considered. Note that, the reason for study the anti-$\tau_{\text{had-vis}}$ region with not medium identification is related to the fake factor extraction, as one can see from Equation 6.3 in Section 6.4, the fake factor is the number of $\tau_{\text{had-vis}}$ candidates which pass the identification criteria over the ones which fail it.

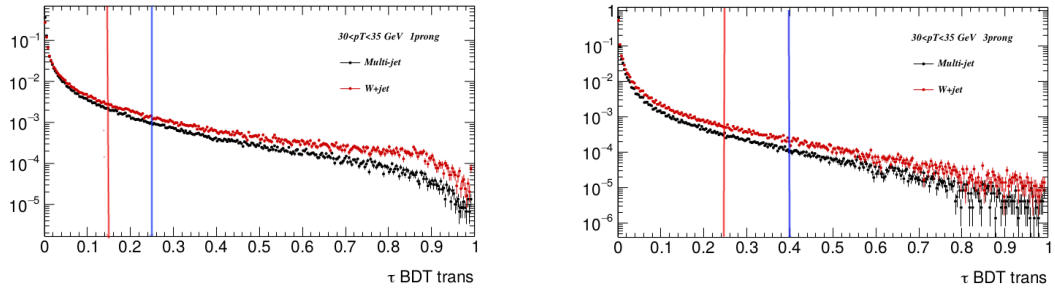

(a) (b)

FIGURE B.5: The distribution of BDT output transformed in $30 < P_T^\tau < 35$ GeV, for (a) 1-prong and (b) 3-prong τ candidates in the W+jet and multijet control regions, the blue line indicates the medium and the red line the loose working points.

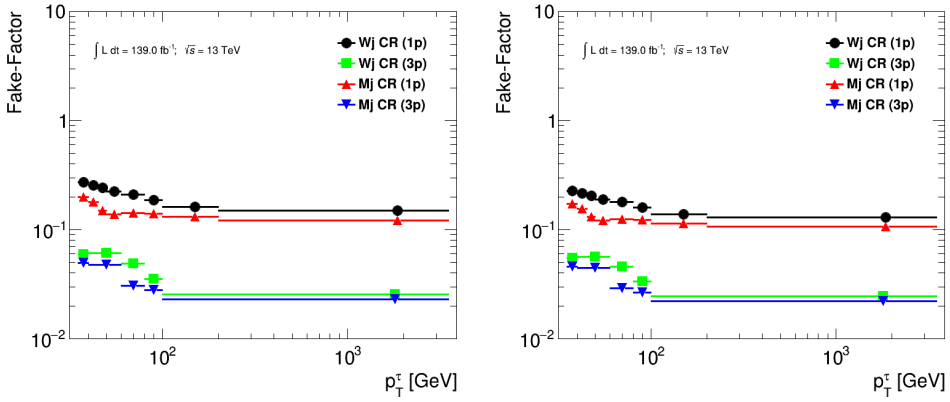

(a) (b)

FIGURE B.6: Fake factors parameterized as a function of p_T^τ and number of tracks. The plots show the fake factor in the multi-jet and W+jet control regions. Errors represent the statistical uncertainties, (a) anti-$\tau_{\text{had-vis}}$ for candidates not passing loose (b) anti-$\tau_{\text{had-vis}}$ for candidates not passing medium working point.

Since the medium identification for the numerator (passing) and loose identification for denominator (not passing) were considered, there was a gap between these two categories as illustrated in Figure B.5 (a) for 1-prong and (b) for 3-prong candidates (the first p_T^τ bin). Therefore by considering not medium identification

the number of events in the denominator increases and the statistical uncertainty on fake factor becomes smaller.

Figure B.6 shows the fake factors for multi-jet and W+jet control regions for (a) definition of denominator not passing loose criteria and (b) not passing medium criteria. One can see a small decrease of fake factors by changing to medium criteria for anti-$\tau_{\text{had-vis}}$ candidates.

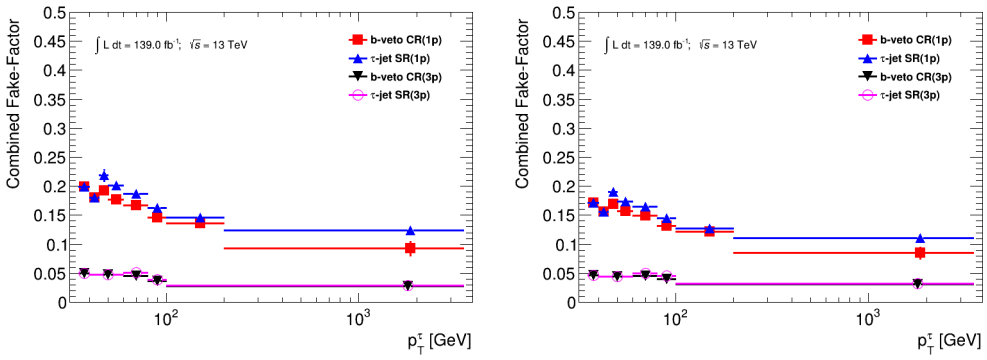

(a) (b)

FIGURE B.7: Fake factors after reweighting by α_{MJ} in the $\tau_{\text{had-vis}}$+jets channel for anti-$\tau_{\text{had-vis}}$ for candidates not passing loose (a) and anti-$\tau_{\text{had-vis}}$ for candidates not passing medium working points(b).

The combined fake factor after estimation of α_{MJ} in the $\tau_{\text{had-vis}}$+jets channel is shown in Figure B.7, and in the $\tau_{\text{had-vis}}$+lepton channel in Figure B.8 for anti-$\tau_{\text{had-vis}}$ candidates not passing loose (a) and for candidates not passing medium (b). There is a small decrease of the fake factors for anti-$\tau_{\text{had-vis}}$ candidates not passing medium. Note that, the uncertainty of the template fit is included in the uncertainties of fake factors. The result of estimation of α_{MJ} for anti-$\tau_{\text{had-vis}}$ for candidates not passing medium can be found in the Appendix B Section **??**.

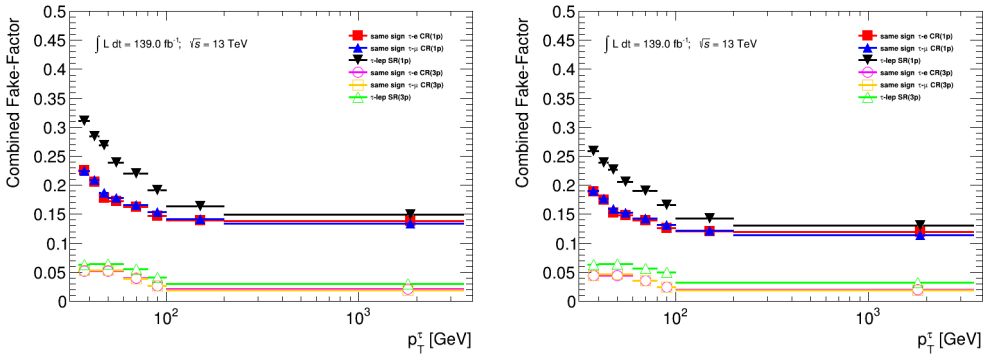

(a) (b)

FIGURE B.8: Fake factors after reweighting by α_{MJ} in the $\tau_{\text{had-vis}}$+lepton channel for anti-$\tau_{\text{had-vis}}$ with not loose (a) and anti-$\tau_{\text{had-vis}}$ with not medium working points(b).

Bibliography

[1] ATLAS Collaboration. "The ATLAS Experiment at the CERN Large Hadron Collider". In: *JINST* 3 (2008), S08003.

[2] CMS Collaboration. "The CMS Experiment at the CERN LHC". In: *JINST* 3 (2008), S08004.

[3] J. Kalinowski et al. "Production of τ lepton pairs with high p_T jets at the LHC and the TauSpinner reweighting algorithm". In: *Eur. Phys. J* C76 (2016), p. 540.

[4] M. Bahmani, J. Kalinowski, W. Kotlarski, E. Richter-Was, and Z. Was. "Systematic of TauSpinner for τ Pairs With Two Hard Jets and Its Recent Development". In: *Acta Phys. Polon.* B48 (2017), pp. 903–911.

[5] M. Bahmani, J. Kalinowski, W. Kotlarski, E. Richter-Was, and Z. Was. "Production of $\tau\tau jj$ final states at the LHC and the TauSpinner algorithm: the spin-2 case". In: *Eur. Phys. J.* C78.1 (2018), p. 10.

[6] ATLAS Collaboration. "Search for charged Higgs bosons decaying via $H^{\pm} \to \tau^{\pm}\nu$ in the τ+jets and τ+lepton final states with 36 fb^{-1} of pp collision data recorded at $\sqrt{s}$=13 TeV with the ATLAS experiment". In: *JHEP* 09 (2018), p. 139.

[7] S.L. Glashow. "Partial Symmetries of Weak Interactions". In: *Nucl. Phys.* 22 (1961), pp. 579–588.

[8] S. Weinberg. In: *Phys. Rev. Lett* 19 (1967), pp. 1264–1266.

[9] A. Salam. "Weak and Electromagnetic Interactions". In: *Conf. Proc. C680519* (1968), pp. 367–377.

[10] C.N. Yang and R.L. Mills. "Conservation of Isotopic Spin and Isotopic Gauge Invariance". In: *Phys. Rev.* 96 (1954), p. 191.

[11] N. Straumann L. O'Raifeartaigh. "Gauge theory: Historical origins and some modern developments". In: *Rev. Mod. Phys.* 72 (2000), p. 1.

[12] D. J. Griffiths. "Introduction to elementary particles". In: *Wiley, New York, NY* (2008).

[13] M. Tanabashi et al. "Particle Data Group". In: *Phys. Rev* D 98 (2018), p. 030001.

[14] L. H. Ryder. "Quantum Field Theory, Second Edition." In: *Cambridge University Press* Chapter 9 (1986).

[15] E. Noether. "Invariant variation problems". In: *Transport Theory and Statistical Physics* (1971), pp. 186–207.

[16] S. Schramm W. Greiner and E. Stein. "Quantum Chromodynamics". In: *Springer* (2007).

[17] G. P. Salam. "Elements of QCD for hadron colliders". In: *CERN Yellow Report CERN-2010-002* (2010), pp. 45–100. URL: arXiv:1011.5131v2[hep-ph].

[18] Michael E. Peskin and Daniel V. Schroeder. "An Introduction to quantum field theory". In: *Reading, MA, United States* (1997).

[19] P. Lipari. "Introduction to neutrino physics". In: *CERN-CLAF School of Conference* (2001). URL: https://cds.cern.ch/record/677618/files/p115.pdf.

[20] R. N. Mohapatra and G. Senjanovic. "Neutrino Masses and Mixings in Gauge Models with Spontaneous Parity Violation". In: *Phys. Rev* D23 (1981), p. 165.

[21] M. Fukugita and T. Yanagida. "Baryogenesis Without Grand Unification". In: *Phys. Lett* B174 (1986), p. 45.

[22] ATLAS Collaboration. "Observation of a new particle in the search for the Standard Model Higgs boson with the ATLAS detector at the LHC". In: *Phys. Lett. B* 716 (2012), pp. 1–29.

[23] CMS Collaboration. "Observation of a new boson at a mass of 125 GeV with the CMS experiment at the LHC". In: *Phys. Lett. B* 716 (2012), pp. 30–61.

[24] L. Evans and P. Bryant. "LHC Machine". In: *JINST* 3 (2008), S08001.

[25] G.C. Branco et al. "Theory and phenomenology of two-Higgs-doublet models". In: *Phys.Rept* 516 (2012), pp. 1–102.

[26] A. Djouadi. "The Anatomy of electro-weak symmetry breaking. II. The Higgs bosons in the minimal supersymmetric model". In: *Phys. Rept.* 459 (2008), p. 1.

[27] M. Ibe, A. Rajaraman, and Z. Surujon. "Does Supersymmetry Require Two Higgs Doublets?" In: *arXiv1012.5099[hep-ph]* (2011). URL: https://arxiv.org/abs/1012.5099.

[28] R. D. Peccei. "QCD, strong cp and axions". In: *J.Korean Phys.Soc.* 29 (1996), S199–S208. URL: https://cds.cern.ch/record/306320/files/9606475.pdf.

[29] Ning Chen and Hong-Jian He. "LHC Signatures of Two-Higgs-Doublets with Fourth Family". In: *JHEP* 04 (2012), p. 062.

[30] M. Flechl et al. "Improved cross-section predictions for heavy charged Higgs boson production at the LHC". In: *Phys. Rev.* D91 (2015), p. 075015.

[31] M. Flechl. "Charged Higgs boson production around the top quark mass threshold". In: *PoS CHARGED2016* (2016), p. 013. URL: https://pos.sissa.it/286/013.

[32] M. Pitt et al. "Search for charged Higgs bosons in the τ+jets and τ+lepton final states with 36.1 fb^{-1} of pp collision data recorded at $\sqrt{s}$ = 13 TeV with the ATLAS experiment". In: *ATL-COM-PHYS-2016-1452* (2018). URL: https://cds.cern.ch/record/2222104.

[33] M. Carena et al. "MSSM Higgs Boson Searches at the LHC: Benchmark Scenarios after the Discovery of a Higgs-like Particle". In: *Eur. Phys. J.* C 73 (2013), p. 2552.

[34] A. Djouadi et al. "The post-Higgs MSSM scenario: Habemus MSSM". In: *Eur. Phys. J.* C 73 (2013), p. 2650.

[35] S. Dittmaier et al. "Handbook of LHC Higgs Cross Sections: 1. Inclusive Observables". In: *CERN-2011-002* (2011). URL: https://cds.cern.ch/record/1318996.

[36] M. L. Perl. "The Discovery of the tau lepton, in The Rise of the standard model: Particle physics in the 1960s and 1970s." In: *Proceedings, Conference, Stanford, USA* (1992), pp. 79–100. URL: https://www.slac.stanford.edu/pubs/slacpubs/10000/slac-pub-10150.pdf.

[37] Yung-Su Tsai. "Decay Correlations of Heavy Leptons in $e^+ + e^- \to l^+ + l^-$". In: *Phys. Rev D4* 9 (1971), pp. 2821–2837.

[38] ALEPH collaboration. "Branching ratios and spectral functions of tau decays: Final ALEPH measurements and physics implications". In: *Phys.Rept. 421* (2005), pp. 139–248.

[39] S. Bedikian. "A Search for the Charged Higgs: Using Tau Polarimetry with Proton-Proton Collisions at the ATLAS Detector". In: *Yale U. ,Ph.D. thesis* (2013-03-14).

[40] A. Rouge. "Tau decays as polarization analysers". In: *1st Workshop on Tau lepton Physics, Orsay, France.* (1991), pp. 213–222. URL: https://cds.cern.ch/record/218082.

[41] T. Przedzinski, E. Richter-Was, and Z. Was. "TauSpinner: a Tool for simulating CP effects in H to tau tau decays at LHC". In: *Eur.Phys.J.* C74 (2014), p. 3177.

[42] J. C. Collins, D. E. Soper, and G. F. Sterman. "Factorization of Hard Processes in QCD". In: *Adv.Ser.Direct.High Energy Phys* 5 (1998), pp. 1–91.

[43] M. Dobbs and J. B. Hansen. "The HepMC C++ Monte Carlo Event Record for High Energy Physics". In: *Comput.Phys.Commun* 134 (2001), pp. 41–46.

[44] S. Banerjee et al. "Ascertaining the spin for new resonances decaying into $\tau^+\tau^-$ at Hadron Colliders". In: *Eur.Phys.J* C73 (2013).

[45] T. Przedzinski, E. Richter-Was, and Z. Was. "Documentation of TauSpinner algorithms: program for simulating spin effects in τ -lepton production at LHC". In: *Eur. Phys. J. C* 2 (2019), p. 91.

[46] S. Jadach and Z. Was. "Qed O (α^3) Radiative Corrections To The Reaction $E^+E^- \to \tau^+\tau^-$ Including Spin And Mass Effects". In: *Acta Phys. Polon* B15 (1984), p. 1151.

[47] S. Jadach et al. "The τ decay library TAUOLA, version 2.4". In: *Comput. Phys. Commun* 76 (1993), p. 361.

[48] Z. Czyczula et al. "TauSpinner Program for Studies on Spin Effect in tau Production at the LHC". In: *Eur. Phys. J.* C72 (2012).

[49] SLD Electroweak Group, DELPHI, ALEPH, SLD, SLD Heavy Flavour Group, OPAL, LEP Electroweak Working Group, L3 Collaboration, and S. Schael et al. "Precision Electroweak Measurements on the Z Resonance". In: *Phys. Rept* 427 (2006), pp. 257–454.

[50] A. Buckley et al. "LHAPDF6: parton density access in the LHC precision era". In: *Eur. Phys. J.* C75 (2015), p. 132.

[51] J. Alwall et al. "The automated computation of tree-level and next-to-leading order differential cross sections, and their matching to parton shower simulations". In: *JHEP* 07 (2014), p. 079.

[52] ATLAS Collaboration. "Search for neutral Higgs bosons of the minimal supersymmetric standard model in pp collisions at $\sqrt{s} = 8$ TeV with the ATLAS detector". In: *JHEP* 11 (2014), p. 056.

[53] CMS Collaboration. "Search for additional neutral Higgs bosons decaying to a pair of tau leptons in pp collisions at $\sqrt{s} = 7$ and 8 TeV". In: *CMS-PAS-HIG-14-029* (2015). URL: https://cds.cern.ch/record/2041463.

[54] ATLAS Collaboration. "Measurement of τ polarization in $W \to \tau\nu$ decays with the ATLAS detector in pp collisions at sqrt(s) = 7 TeV". In: *Eur. Phys. J.* C72 (2012), p. 2062.

[55] CMS Collaboration. "Model independent search for Higgs boson pair production in the $b\bar{b}\,\tau^+\tau^-$ final state". In: *CMS-PAS-HIG-15-013* (2016). URL: https://cds.cern.ch/record/2139335.

[56] V. Cherepanov. "Measurement of the polarization of τ-leptons produced in Z decays at CMS and determination of the effective weak mixing angle". In: *Aachen, Tech. Hochsch. PhD thesis* (2016).

[57] ATLAS Collaboration. "Evidence for the Higgs-boson Yukawa coupling to tau leptons with the ATLAS detector". In: *JHEP* 04 (2015), p. 117.

[58] ATLAS Collaboration. "Measurement of τ polarisation in $Z/\gamma^* \to \tau\tau$ decays in proton proton collisions at $\sqrt{s} = 8$ TeV with the ATLAS detector". In: *Eur. Phys. J.* C78 (2018), p. 163.

[59] K. Hagiwara et al. "HELAS and MadGraph/MadEvent with spin-2 particles". In: *Eur. Phys. J.* C56 (2008), pp. 435–447.

[60] N. Davidson et al. "Universal Interface of TAUOLA Technical and Physics Documentation". In: *Comput. Phys. Commun.* 183 (2012), pp. 821–843.

[61] A. Kaczmarska et al. "Application of TauSpinner for Studies on τ-Lepton Polarization and Spin Correlations in Z, W and H Decays at the LHC". In: *Acta Phys. Polon* B45.10 (2014), pp. 1921–1946.

[62] S. Alioli, P. Nason, C. Oleari, and E. Re. "Vector boson plus one jet production with decay". In: *JHEP* 1101 (2011), p. 095.

[63] L. M. Michelangelo et al. "ALPGEN, a generator for hard multiparton processes in hadronic collisions". In: *JHEP* 07 (2003), p. 001.

[64] ATLAS Collaboration. "ATLAS Run 1 Pythia8 tunes". In: *ATL-PHYS-PUB-2014-021* (2014). URL: https://cds.cern.ch/record/1966419.

[65] D. B. Richard et al. "Parton distributions with LHC data". In: *Nucl. Phys* B 867 (2013), p. 244.

[66] T. Gleisberg et al. "Event generation with SHERPA 1.1". In: *JHEP* 02 (2009), p. 007.

[67] T. Gleisberg and S. Hoche. "Comix, a new matrix element generator". In: *JHEP* 0812 (2008), p. 039.

[68] Cascioli, Fabio, Maierhofer, Philipp, Pozzorini, and Stefano. "Scattering Amplitudes with Open Loops". In: *Phys. Rev. Lett.* 108 (2012), p. 111601.

[69] S. Schumann and F. Krauss. "A Parton shower algorithm based on Catani-Seymour dipole factorisation". In: *JHEP* 0803 (2008), p. 038.

[70] S. Hoeche, F. Krauss, M. Schonherr, and F. Siegert. "QCD matrix elements + parton showers: The NLO case". In: *JHEP* 04 (2013), p. 027.

[71] LHCb Collaboration. "The LHCb Detector at the LHC". In: *JINST* 3 (2008), S08005.

[72] ALICE Collaboration. "The ALICE experiment at the CERN LHC". In: *JINST* 3 (2008), S08002.

[73] M. Albrow et al. "CMS-TOTEM Precision Proton Spectrometer". In: *Tech. rep. CERN-LHCC-2014-021.TOTEM-TDR-003. CMS-TDR-13.* (2014). URL: https://cds.cern.ch/record/1753795.

[74] O. Adriani et al. "LHCf experiment: Technical Design Report". In: *Technical Design Report LHCf. Geneva:CERN* (2006). URL: https://cds.cern.ch/record/926196.

[75] J. Pinfold et al. "Technical Design Report of the MoEDAL Experiment". In: *Tech. rep. CERN-LHCC-2009-006. MoEDAL-TDR-001* (2009). URL: https://cds.cern.ch/record/1181486.

[76] ATLAS Collaboration. "ATLAS experiment- Public results". In: *CERN* (2019). URL: https://twiki.cern.ch/twiki/bin/view/AtlasPublic/LuminosityPublicResultsRun2.

[77] ATLAS Collaboration. "ATLAS inner detector: Technical Design Report". In: *Technical Design Report ATLAS. Geneva: CERN* (1997). URL: https://cds.cern.ch/record/331063.

[78] K. Potamianos. "The upgraded Pixel detector and the commissioning of the Inner Detector tracking of the ATLAS experiment for Run-2 at the Large Hadron Collider". In: *PoS EPS-HEP2015* (2015), p. 261. URL: https://arxiv.org/abs/1608.07850.

[79] ATLAS Collaboration. "ATLAS Insertable B-Layer Technical Design Report." In: *CERN-LHCC-2010-013,ATLAS-TDR-19* (2010). URL: https://cds.cern.ch/record/1291633.

[80] A. Vogel. "ATLAS Transition Radiation Tracker (TRT): Straw Tube Gaseous Detectors at High Rates. Tech. rep." In: *ATL-INDET-PROC-2013-005. Geneva: CERN* (2013). URL: https://cds.cern.ch/record/1537991.

[81] ATLAS Collaboration. "Performance of the ATLAS Trigger System in 2015". In: *Eur. Phys. J.* C77 (2017).

[82] S. Agostinelli et al. "GEANT4: A Simulation toolkit". In: *Nucl.Instrum.Meth* A506 (2003), pp. 250–303.

[83] J. Allison and K. Amako et al. "Geant4 developments and applications". In: *IEEE Trans.Nucl.Sci.* 53 (2006), p. 270.

[84] The ATLAS Collaboration. "The ATLAS Simulation Infrastructure". In: *Eur. Phys. J.* C70 (2010), p. 823.

[85] ATLAS Collaboration. "Electron reconstruction and identification efficiency measurements with the ATLAS detector using the 2011 LHC proton-proton collision data". In: *Eur. Phys. J* C74 (2014), p. 2941.

[86] ATLAS Collaboration. "Electron and photon energy calibration with the ATLAS detector using LHC Run 1 data". In: *Eur. Phys. J* C74 (2014), p. 3071.

[87] ATLAS Collaboration. "Muon reconstruction performance of the ATLAS detector in proton-proton collision data at $\sqrt{s}$ =13 TeV". In: *Eur. Phys. J.* C76 (2016), p. 292.

[88] M. Cacciari, G. P. Salam, and G. Soyez. "The anti-k_t jet clustering algorithm," in: *JHEP* 04 (2008), p. 063.

[89] M. Cacciari, G. P. Salam, and G. Soyez. "FastJet User Manual". In: *Eur. Phys. J.* C72 (2012), p. 1986.

[90] ATLAS Collaboration. "Jet energy scale measurements and their systematic uncertainties in proton-proton collisions at $\sqrt{s}$= 13 TeV with the ATLAS detector". In: *Phys. Rev.* D96 (2017), p. 072002.

[91] ATLAS Collaboration. "Tagging and suppression of pileup jets with the ATLAS detector". In: *ATLAS-CONF-2014-018* (2014). URL: https://cds.cern.ch/record/1700870.

[92] ATLAS Collaboration. "Reconstruction, Energy Calibration, and Identification of Hadronically Decaying Tau Leptons in the ATLAS Experiment for Run-2 of the LHC". In: *ATL-PHYS-PUB-2015-045* (2015). URL: https://cds.cern.ch/record/2064383.

[93] P. Giovannini. "Local hadron calibration with ATLAS". In: *ATL-LARG-PROC-2010-008* (210). URL: https://cds.cern.ch/record/1284955/.

[94] CMS and ATLAS Collaborations. "Hadronic tau reconstruction and identification performance in ATLAS and CMS". In: *PoS LHCP2018* (2018), p. 228. URL: http://inspirehep.net/record/1713242.

[95] ATLAS Collaboration. "Performance of b-Jet Identification in the ATLAS Experiment". In: *JINST* 11 (2016), P04008.

[96] ATLAS Collaboration. "Optimisation of the ATLAS b-tagging performance for the 2016 LHC Run". In: *ATL-PHYS-PUB-2016-012* (2016). URL: https://cds.cern.ch/record/2160731.

[97] P. C. Bhat. "Advanced analysis methods in high-energy physics". In: *AIP Conf. Proc* 583 (2001), p. 22.

[98] D0 Collaboration. "Search for single top quarks in the tau+jets channel using 4.8 fb^{-1} of p p-bar collision data". In: *Phys. Lett* B690 (2010), p. 5.

[99] ATLAS Collaboration. "Measurement of the top quark pair cross section with ATLAS in pp collisions at $\sqrt{s}$ = 7 TeV using final states with an electron or a muon and a hadronically decaying τ lepton". In: *Phys. Lett* B717 (2012), p. 89.

[100] ATLAS Collaboration. "Evidence for the associated production of a W boson and a top quark in ATLAS at $\sqrt{s}$ = 7 TeV". In: *Phys. Lett* B716 (2012), p. 142.

[101] O. Behnke, K. Krninger, T. Schrner-Sadenius, and G. Schott. "Data analysis in high energy physics". In: *Wiley-VCH, Weinheim, Germany* (2013).

[102] C. Peterson, T. Rognvaldsson, and L. Lonnblad. "Jetnet 3.0: A versatile artificial neural network package." In: *Comput. Phys. Commun.* 81 (1994), p. 185.

[103] F. Pedregosa, G. Varoquaux, A. Gramfort, and et al. "Scikit-learn: Machine Learning in Python". In: *Journal of Machine Learning Research* (2018), p. 1. URL: arXiv:1201.0490.

[104] A. Hocker et al. "TMVA: Toolkit for multivariate data analysis". In: *PoS, ACAT* 40 (2007). URL: arXiv:physics/0703039.

[105] T. Kohonen. "Self-organized formation of topologically correct feature maps". In: *Biol. Cybern* 43 (1982), p. 59.

[106] P. Liang and S. Ermo. "Machine learning, Lectures". In: *Stanford University, California* (2017).

[107] P. Baldi and K. Hornik. "Neural networks and principal component analysis: learning from examples without local minima". In: *Neural Network* 2 (1989), pp. 53–58.

[108] Y. Bengio. "Artificial neural networks and their application to sequence recognition, (Ph.D. thesis)". In: *McGill University* (1991).

[109] R. E. David et al. "Learning representations by back-propagating errors". In: *Nature* 323.6088 (1986), 533–536.

[110] L. Breiman. "Arcing classifiers". In: *Ann. Stat* 26(3) (1998), p. 801.

[111] T. Hastie, R. Tibshirani, and J. Friedman. "The Elements of Statistical Learning, Springer Series in Statistics". In: *Springer New York Inc, New York, NY, USA* (2001).

[112] G. Prashant. In: *Data science webpage* (2017). URL: https://towardsdatascience.com/cross-validation-in-machine-learning-72924a69872f.

[113] ATLAS Collaboration. "Observation of a new particle in the search for the Standard Model Higgs boson with the ATLAS detector at the LHC". In: *Phys. Lett.* B 716 (2012), p. 1.

[114] CMS Collaboration. "Observation of a new boson at a mass of 125 GeV with the CMS experiment at the LHC". In: *Phys. Lett.* B 716 (2012), p. 30.

[115] ATLAS Collaboration. "Search for charged Higgs bosons decaying via $H^+ \to \tau\nu$ in top quark pair events using pp collision data at $\sqrt{s}$ = 7 TeV with the ATLAS detector". In: *JHEP* 06 (2012), p. 039.

[116] ATLAS Collaboration. "Search for charged Higgs bosons through the violation of lepton universality in $t\bar{t}$ events using pp collision data at $\sqrt{s}$= 7 TeV with the ATLAS experiment". In: *JHEP* 03 (2013), p. 076.

[117] ATLAS Collaboration. "Search for charged Higgs bosons decaying via $H^\pm \to \tau^\pm\nu$ in fully hadronic final states using pp collision data at $\sqrt{s}$ = 8 TeV with the ATLAS detector". In: *JHEP* 03 (2015), p. 088.

[118] CMS Collaboration. "Search for a light charged Higgs boson in top quark decays in pp collisions at $\sqrt{s}$= 7 TeV". In: *JHEP* 07 (2012), p. 143.

[119] CMS Collaboration. "Search for a charged Higgs boson in pp collisions at $\sqrt{s}$= 8 TeV". In: *JHEP* 11 (2015), p. 018.

[120] ATLAS Collaboration. "Search for a light charged Higgs boson in the decay channel $H^+ \to c\bar{s}$ in $t\bar{t}$ events using pp collisions at $\sqrt{s}$ = 7 TeV with the ATLAS detector". In: *Eur. Phys. J* C73 (2013), p. 2465.

[121] CMS Collaboration. "Search for a light charged Higgs boson decaying to cs in pp collisions at $\sqrt{s}$ = 8 TeV". In: *JHEP* 12 (2015), p. 178.

[122] ATLAS Collaboration. "Search for charged Higgs bosons in the $H^\pm \to tb$ decay channel in pp collisions at $\sqrt{s}$ = 8 TeV using the ATLAS detector". In: *JHEP* 03 (2016), p. 127.

[123] ATLAS Collaboration. "Search for charged Higgs bosons produced in association with a top quark and decaying via $H^\pm \to \tau\nu$ using pp collision data recorded at $\sqrt{s}$ = 13 TeV by the ATLAS detector". In: *Phys. Lett.* B759 (2016), p. 555.

[124] CMS Collaboration. "Search for charged Higgs bosons with the $H^\pm \to \tau^\pm\nu_\tau$ decay channel in the fully hadronic final state at $\sqrt{s} = 13$ TeV". In: CMS-PAS-HIG-16-031 (2016). URL: https://cds.cern.ch/record/2223865.

[125] ATLAS Collaboration. "Search for a Charged Higgs Boson Produced in the Vector-Boson Fusion Mode with Decay $H^\pm \to W^\pm Z$ using pp Collisions at $\sqrt{s}$ = 8 TeV with the ATLAS Experiment". In: *Phys. Rev. Lett.* 114 (2015), p. 231801.

[126] CMS Collaboration. "Search for charged Higgs bosons produced via vector boson fusion and decaying into a pair of W and Z bosons using pp collisions at $\sqrt{s}$ = 13 TeV". In: *Phys. Rev. Lett* 119 (2017), p. 141802.

[127] CMS Collaboration. "Search for charged Higgs bosons in the $H^{\pm} \to \tau\nu$ decay channel in proton-proton collisions at $\sqrt{s}$=13 TeV". In: *High Energ. Phys* (2019), p. 142.

[128] ATLAS Collaboration. "Measurement of the tau lepton reconstruction and identification performance in the ATLAS experiment using pp collisions at $\sqrt{s}$ = 13 TeV". In: *ATLAS-CONF-2017-029* (2017).

[129] ATLAS Collaboration. "Luminosity determination in pp collisions at $\sqrt{s}$ = 8 TeV using the ATLAS detector at the LHC". In: *Eur. Phys. J* C76 (2016), p. 653.

[130] T. Sjostrand, S. Mrenna, and P. Z. Skands. "A Brief Introduction to PYTHIA 8.1". In: *Comput. Phys. Commun* 178 (2008), p. 852.

[131] R. D. Ball et al. "Parton distributions with LHC data". In: *Nucl. Phys* B867 (2013), p. 244.

[132] P. Nason. "A New method for combining NLO QCD with shower Monte Carlo algorithms". In: *JHEP* 11 (2004), p. 040.

[133] P. Nason S. Frixione and C. Oleari. "Matching NLO QCD computations with Parton Shower simulations: the POWHEG method". In: *JHEP* 11 (2007), p. 070.

[134] S. Alioli, P. Nason, C. Oleari, and E. Re. "A general framework for implementing NLO calculations in shower Monte Carlo programs: the POWHEG BOX". In: *JHEP* 06 (2010), p. 043.

[135] H. L. Lai et al. "New parton distributions for collider physics". In: *Phys. Rev* D82 (2010), p. 074024.

[136] S. Dulat et al. "New parton distribution functions from a global analysis of quantum chromodynamics". In: *Phys. Rev.* D93 (2016), p. 033006.

[137] P. Artoisenet, R. Frederix, O. Mattelaer, and R. Rietkerk. "Automatic spin-entangled decays of heavy resonances in Monte Carlo simulations". In: *JHEP* 03 (2013), p. 015.

[138] T. Sjostrand, S. Mrenna, and P. Z. Skands. "PYTHIA 6.4 Physics and Manual". In: *JHEP* 05 (2006), p. 026.

[139] J. Pumplin et al. "New generation of parton distributions with uncertainties from global QCD analysis". In: *JHEP* 07 (2002), p. 012.

[140] P. Z. Skands. "Tuning Monte Carlo Generators: The Perugia Tunes". In: *Phys. Rev* D82 (2010), p. 074018.

[141] M. Czakon and A. Mitov. "Top++: A Program for the Calculation of the Top-Pair Cross-Section at Hadron Colliders". In: *Comput. Phys. Commun* 185 (2014), p. 2930.

[142] P. Kant et al. "HatHor for single top-quark production: Updated predictions and uncertainty estimates for single top-quark production in hadronic collisions". In: *Comput. Phys. Commun* 191 (2015), p. 74.

[143] M. Aliev et al. "HATHOR: HAdronic Top and Heavy quarks cross section calculatoR". In: *Comput. Phys. Commun* 182 (2011), p. 1034.

[144] N. Kidonakis. "Two-loop soft anomalous dimensions for single top quark associated production with a W^- or H^-". In: *Phys. Rev* D82 (2010), p. 054018.

[145] R. D. Ball et al. "Parton distributions for the LHC Run II". In: *JHEP* 04 (2015), p. 040.

[146] F. Cascioli, P. Maierhofer, and S. Pozzorini. "Scattering Amplitudes with Open Loops". In: *Phys. Rev. Lett* 108 (2012), p. 111601.

[147] C. Anastasiou, L. J. Dixon, K. Melnikov, and F. Petriello. "High precision QCD at hadron colliders: Electroweak gauge boson rapidity distributions at NNLO". In: *Phys. Rev* D69 (2004), p. 094008.

[148] K. Melnikov and F. Petriello. "Electroweak gauge boson production at hadron colliders through $O(\alpha(s)^2)$". In: *Phys. Rev* D74 (2006), p. 114017.

[149] R. Gavin, F. Petriello Y. Li, and S. Quackenbush. "FEWZ 2.0: A code for hadronic Z production at next-to-next-to-leading order". In: *Comput. Phys. Commun* 182 (2011), p. 2388.

[150] ATLAS Collaboration. "Measurement of the Z/γ^* boson transverse momentum distribution in pp collisions at$\sqrt{s}$ = 7 TeV with the ATLAS detector". In: *JHEP* 09 (2014), p. 145.

[151] D. J. Lange. "The EvtGen particle decay simulation package". In: *Nucl. Instrum. Meth.* A462 (2011), p. 152.

[152] ATLAS Collaboration. "Summary of ATLAS Pythia 8 tunes". In: *ATL-PHYS-PUB-2012-003* (2012). URL: https://cds.cern.ch/record/1474107.

[153] A. D. Martin, W. J. Stirling, R. S. Thorne, and G. Watt. "Parton distributions for the LHC". In: *Eur. Phys. J.* C63 (2009), p. 189.

[154] ATLAS Collaboration. "The ATLAS Simulation Infrastructure". In: *Eur. Phys. J.* C70 (2010), p. 823.

[155] S. Agostinelli et al. "GEANT4: A Simulation toolkit". In: *Nucl. Instrum. Meth* A506 (2003), p. 250.

[156] J. Griffiths et al. "Search for charged Higgs bosons in the τ+jets final state using 14.7 fb^{-1} of pp collision data recorded at $\sqrt{s}$ = 13 TeV with the ATLAS experiment". In: *ATL-COM-PHYS-2016-501* (2016). URL: https://cds.cern.ch/record/2206282.

[157] Keck T. "Fastbdt: A speed-optimized and cache-friendly implementation of stochastic gradient-boosted decision trees for multivariate classification". In: *CoRR* 1609.06119 (2016).

[158] ATLAS Collaboration. "Search for resonant and nonresonant Higgs boson pair production in the bbar tau tau decay channel in pp collisions at $\sqrt{s}$=13 TeV with the ATLAS detector". In: *Phys. Rev. Lett.* 121 (2018), p. 191801.

[159] ATLAS Collaboration. "Search for charged Higgs bosons in the τ+jets final state with 3.2 fb^{-1} of pp collision data recorded at $\sqrt{s}$ = 13 TeV with the ATLAS experiment". In: *ATL-PHYS-INT-2016-006* (2016). URL: https://cds.cern.ch/record/2161559.

[160] ATLAS Collaboration. "Identification and energy calibration of hadronically decaying tau leptons with the ATLAS experiment in pp collisions at $\sqrt{s}$=8 TeV". In: *Eur.Phys.J.* C75.7 (2015), p. 303.

[161] L. Devroye. "Non-Uniform Random Variate Generation". In: *Springer* (1986).

[162] G. Cowan, K. Cranmer, E. Gross, and O. Vitells. "Asymptotic formulae for likelihood-based tests of new physics". In: *Eur. Phys. J* C71 (2011), p. 1554.

[163] A. L. Read. "Presentation of search results: the CL s technique". In: *J. Phys. G* 28 (2003), p. 2693.